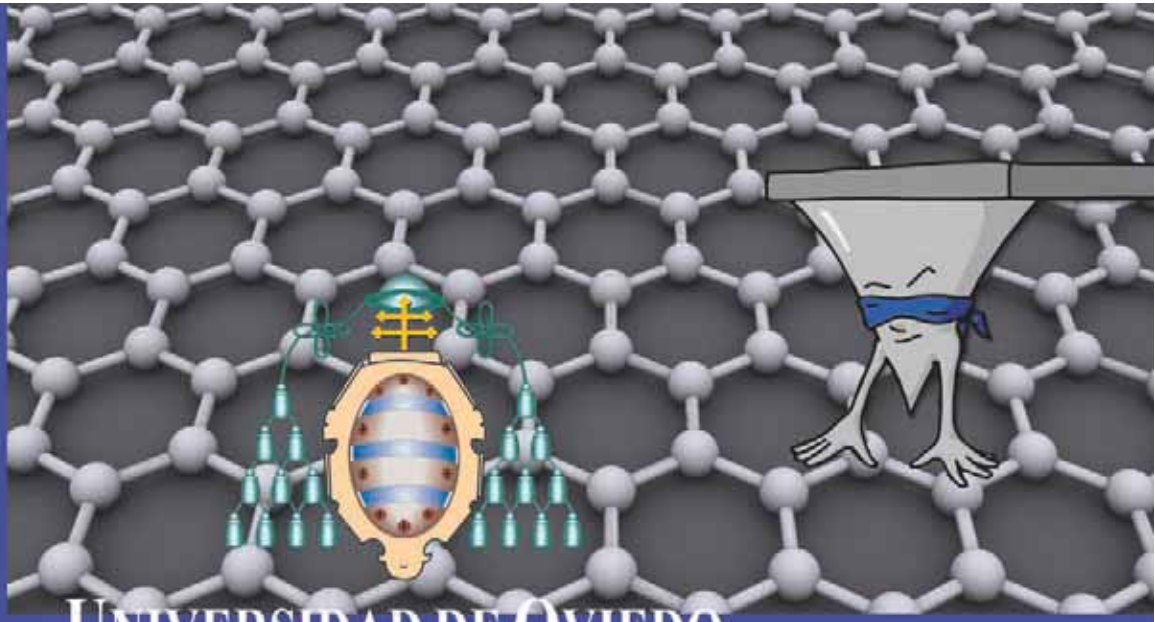

UNIVERSIDAD DE OVIEDO

Departamento de Ciencia de los Materiales e Ingenieria Metalúrgica

Modificación superficial de materiales de carbono: grafito y grafeno

Memoria de Tesis Doctoral
Pablo Solís Fernández
2011

UNIVERSIDAD DE OVIEDO

Departamento de Ciencia de los Materiales e Ingeniería Metalúrgica

Modificación superficial de materiales de carbono: grafito y grafeno

Memoria de Tesis Doctoral

Pablo Solís Fernández

2011

Índice

Agradecimientos

Quisiera expresar mi más sincero agradecimiento a una serie de personas y a una agencia estatal:

A los doctores Juan Ignacio Paredes Nachón, Amelia Martínez Alonso y Juan Manuel Diez Tascón, por toda la confianza depositada en mí. Sin ellos esta Memoria no sería lo que es.

A la doctora Blanca Hernando Grande, tutora durante todos estos años y que siempre ha demostrado ser una gran persona.

Al Consejo Superior de Investigaciones Científicas por las facilidades recibidas para la realización del presente trabajo y por la concesión de una beca predoctoral I3P.

A toda la gente que ha estado, en mayor o menor medida, directamente implicada en el trabajo incluido en esta Memoria: Susi, Laura, Silvia y Ana del Incar; Iván, Maria Jesús y Julio de Valladolid; László P. Biró y Gergely de Budapest.

A todos los compañeros de laboratorio que he tenido durante estos años, tanto a los "permanentes" (Alberto, Fabián, Katia, Ramón, Tomás, Bea, Marina, Rubén, Marley y Ángela), como a los que estuvieron de visita (Sami, Mélanie, Merce, Sigrid, Pedro y Sergio).

A la gente que me acogió en mis pequeñas emigraciones, y que hizo las estancias mucho más agradables: Ricky, Cliodhna, Camilo y Cristina en Belfast; Peter, Istvan, Ana y Gergely en Budapest; a todo el grupo del profesor Kyotani en Sendai, incluido Raúl.

A todo el personal laboral del centro, y muy especialmente a Josefina, Rosi, Mar, Carmen, Ismael, Tino, Carmen (no es un error, es que hay dos) y Manuela.

Por último, un agradecimiento muy especial a todos los que durante estos años me recordaron constantemente que existe un mundo fuera del Incar, y aquí se incluyen amigos, familia, compañeros de grupo y demás calamidades. No me olvido de ti, Victoria.

Resumen

El objetivo principal del presente trabajo es el estudio a escalas atómica y nanométrica de los efectos de diferentes tipos de oxidación sobre grafito y láminas de grafeno preparadas por métodos químicos. La herramienta fundamental de caracterización han sido las microscopías de efecto túnel (STM) y de fuerza atómica (AFM), que en combinación con diferentes técnicas complementarias (como espectroscopia Raman y fotoelectrónica de rayos X) han permitido analizar en detalle la morfología, estructura y química superficial de los distintos materiales oxidados.

Se empleó grafito pirolítico altamente orientado (HOPG) como material carbonoso modelo para el estudio de oxidación mediante plasma de descarga de barrera dieléctrica (DBD) y mediante ozono generado por radiación ultravioleta. Se pudieron establecer las diferencias esenciales entre los dos mecanismos básicos (físico y químico) que rigen el ataque oxidativo de los materiales carbonosos. En las muestras oxidadas por plasma DBD se observó mediante STM un tipo de defecto a escala atómica que no había sido documentado con anterioridad en materiales carbonosos. Estudios experimentales y teóricos detallados permitieron atribuir dicho defecto a clusters intersticiales bidimensionales de oxígeno atrapados bajo el grafeno superficial del HOPG.

Se estudió en detalle la estructura de las láminas de grafeno y de sus precursoras (óxido de grafeno) mediante STM y AFM. Se constató el alto nivel de desorden estructural que presenta este tipo de grafeno. Asimismo, se llevó a cabo un estudio sobre la determinación precisa del grosor de láminas de grafeno mediante estas microscopías. Por último, los estudios de oxidación de las láminas de grafeno revelaron su gran reactividad en comparación con la de materiales grafíticos de estructura más perfecta (HOPG y grafeno prístino). Estos estudios mostraron evidencia de una estructura heterogénea de las láminas a escalas de unos pocos nanómetros, de manera que coexisten zonas relativamente prístinas junto con otras en las que se concentran la mayor parte de los defectos.

Abstract

The present work mainly aims at investigating, both on the nanometer and atomic scales, the effect of different types of oxidation on graphite as well as on graphene sheets prepared by chemical methods. The basic characterization tools have been scanning tunneling and atomic force microscopies (STM/AFM), which in combination with several complementary techniques (e.g., Raman and X-ray photoelectron spectroscopies) have afforded a detailed knowledge of the surface morphology, structure and chemistry of the different oxidized materials.

Highly oriented pyrolytic graphite (HOPG) was employed as a model carbon material for studies of oxidation by dielectric barrier discharge (DBD) plasma and ultraviolet-generated ozone. The main differences between the two basic (physical and chemical) mechanisms that drive the oxidative etching of carbon materials could be established. For DBD plasma-oxidized samples, a type of atomic-scale defect hitherto unreported on carbon materials was observed by STM. A combination of experimental and theoretical work indicated that such type of defect could be attributed to two-dimensional interstitial clusters of oxygen trapped beneath the surface graphene of HOPG.

The structure of the graphene sheets and their precursor (graphene oxide) was examined in detail by STM and AFM. These sheets exhibited a large degree of structural disorder. Likewise, an in-depth study concerning the accurate measurement of sheet thickness by AFM/STM was carried out. Finally, studies on the oxidation of graphene sheets revealed their high reactivity compared with that of graphitic materials with more perfect structure (HOPG and pristine graphene). Such studies showed evidence of the heterogeneous structure that this type of graphene is believed to exhibit on a scale of just a few nm, so that relatively pristine regions coexist with areas where the large majority of the defects are located.

Lista de abreviaturas

AFM	Microscopía de fuerza atómica (*Atomic Force Microscopy*)
AM-AFM	Modo AFM de modulación de amplitud
CAFM	*Conductive Atomic Force Microscopy*
CCG	Grafeno químicamente convertido (*Chemically Converted Graphene*)
CDG	Grafeno químicamente derivado (*Chemically Derived Graphene*)
CMG	Grafeno químicamente modificado (*Chemically Modified Graphene*)
CRGO	Óxido de grafeno químicamente reducido (*Chemically Reduced Graphene Oxide*)
CVD	Depósito químico en fase vapor (*Chemical Vapor Deposition*)
DBD	(Plasma generado mediante) descarga de barrera dieléctrica (*Dielectric Barrier Discharge*)
DFT	Teoría del funcional de la densidad (*Density Functional Theory*)
DOS	Densidad de estados electrónicos (*Density Of States*)
DTG	Termogravimetría diferencial (*Differential ThermoGravimetry*)
EFM	Microscopía de fuerza electrostática (*Electrostatic Force Microscopy*)
FET	Transistor de efecto campo (*Field Effect Transistor*)
FM-AFM	Modo AFM de modulación de frecuencia
GNR	*Graphene NanoRibbon*
GO	Óxido de grafeno (*Graphene Oxide*)
HOPG	Grafito pirolítico altamente orientado/ordenado (*Highly Oriented/Ordered Pyrolytic Graphite*)
ITO	*Indium Tin Oxide*
LDOS	Densidad local de estados electrónicos (*Local Density Of States*)
LED	Diodo emisor de luz (*Light-Emitting Diode*)

LFM	Microscopía de fuerza lateral (*Lateral Force Microscopy*)
MFM	Microscopía de fuerza magnética (*Magnetic Force Microscopy*)
MW	(Plasma generado mediante) microondas
NC-AFM	Modo AFM de no-contacto
NMR	Resonancia magnética nuclear (*Nuclear Magnetic Resonance*)
QFT	Teoría cuántica de campos (*Quantum Field Theory*)
QHE	Efecto Hall cuántico (*Quantum Hall Effect*)
rGO	Óxido de grafeno reducido (*Reduced Graphene Oxide*)
SET	Transistor de electrón único (*Single Electron Transistor*)
SPL	Litografía SPM
SPM	Microscopías de campo cercano o de proximidad (*Scanning Probe Microscopy*)
STS	Espectroscopía de efecto túnel (*Scanning Tunneling Spectroscopy*)
TEM	Microscopía electrónica de transmisión (Transmission Electron Microscopy)
STM	Microscopía de efecto túnel (*Scanning Tunneling Microscopy*)
TG/TGA	Termogravimetría/Análisis termogravimétrico
UVO	Ultravioleta/Ozono
UV-vis	Espectroscopía de absorción ultravioleta-visible
XPS	Espectroscopía fotoelectrónica de rayos X (*X-Ray Photoelectron Spectroscopy*)

Introducción 1

1. Materiales de carbono

1.1 Carbono. Hibridaciones y formas alotrópicas

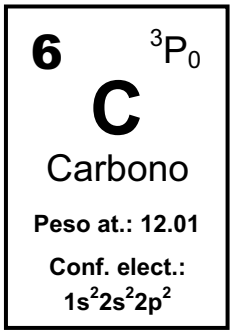

El carbono es el elemento químico de número atómico 6 y se encuentra representado por el símbolo *C*. Es uno de los elementos más abundantes tanto del universo [1] como de la corteza terrestre [2] y gracias a sus singulares propiedades juega un importante papel en la química de los procesos biológicos, encontrándose presente en todas las formas de vida conocidas [3].

Hibridaciones

Una de las peculiaridades que distingue al carbono del resto de elementos es su flexibilidad a la hora de formar enlaces químicos. La configuración electrónica del átomo de carbono es $1s^2\ 2s^2\ 2p^2$ cuando el átomo se encuentra aislado y en su estado fundamental de mínima energía (*tabla I*). En principio, solo los dos electrones que ocupan el orbital *2p* están disponibles para formar enlaces, por lo que el carbono sería divalente. Sin embargo, debido a que la diferencia de energía entre el orbital *2s* y los *2p* es muy pequeña, son posibles distintos tipos de hibridación cuando se produce una interacción del átomo de carbono con otros átomos cercanos, dado que la energía total al formarse los enlaces resulta menor que la del átomo aislado. El proceso de hibridación se inicia cuando uno de los electrones del orbital *2s* resulta promocionado a un orbital *2p*, de modo que el átomo de carbono se encuentra en un estado excitado previo a la hibridación (*tabla I*). Por último, se produce una mezcla de orbitales puros en un estado excitado formando orbitales híbridos equivalentes. Dependiendo de la cantidad de orbitales que intervengan en el proceso de mezcla existen varios tipos de hibridación posibles, en los que los orbitales híbridos resultantes poseen orientaciones espaciales muy bien definidas, dando lugar a fuertes enlaces covalentes denominados σ [4]. En la denominada hibridación sp^3 o tetragonal, se forman cuatro orbitales híbridos orientados en el espacio formando un tetraedro para minimizar la repulsión (*tabla I*). Esta hibridación es la base de la formación de compuestos alifáticos y de la estructura del diamante, una de las formas alotrópicas del carbono. A la segunda forma de hibridación se la conoce como sp^2 o trigonal, e involucra la formación de tres orbitales híbridos (*tabla I*). Éstos se encuentran formando un plano con una separación angular de 120° entre sí, origen de la estructura en forma de panal de abeja característica de los materiales grafíticos. El electrón *p* deslocalizado que permanece sin hibridar ocupa un orbital perpendicular al plano formado por los orbitales hibridados, y se halla disponible para la formación de un enlace π con otros átomos. La hibridación sp^2 da lugar a la estructura más estable del carbono a temperatura y presión ambiente, el grafito [5], siendo además la base de todas las estructuras grafíticas y compuestos aromáticos. En un tercer tipo de hibridación, conocido como *sp* o digonal, se producen dos orbitales hibridados formando entre sí un ángulo de 180° debido a la repulsión mutua (*tabla I*). Esto hace que las moléculas que se formen sean lineales. Aparte de los

Tabla I – Distintas hibridaciones del átomo de carbono.

Configuración electrónica	Proceso de hibridación	Ejemplo
Estado fundamental C $\frac{\uparrow\downarrow}{1s}$ $\frac{\uparrow\downarrow}{2s}$ $\frac{\uparrow}{2p_x}$ $\frac{\uparrow}{2p_y}$ $\frac{}{2p_z}$		
Estado excitado C^* $\frac{\uparrow\downarrow}{1s}$ $\frac{\uparrow}{2s}$ $\frac{\uparrow}{2p_x}$ $\frac{\uparrow}{2p_y}$ $\frac{\uparrow}{2p_z}$		
Hibridación sp^3 C^* $\frac{\uparrow\downarrow}{1s}$ $\frac{\uparrow}{sp^3}$ $\frac{\uparrow}{sp^3}$ $\frac{\uparrow}{sp^3}$ $\frac{\uparrow}{sp^3}$	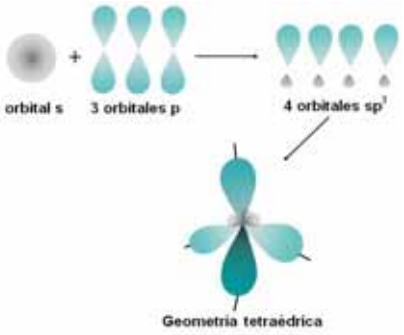	**Metano** 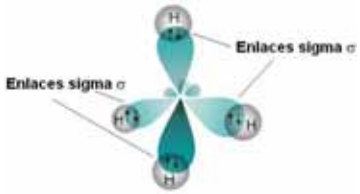
Hibridación sp^2 C^* $\frac{\uparrow\downarrow}{1s}$ $\frac{\uparrow}{sp^2}$ $\frac{\uparrow}{sp^2}$ $\frac{\uparrow}{sp^2}$ $\frac{\uparrow}{p}$	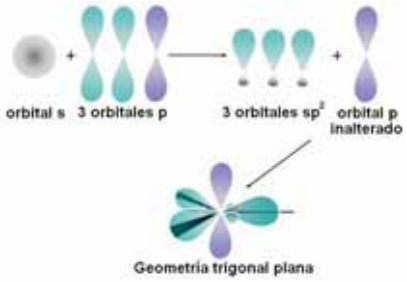	**Etileno** 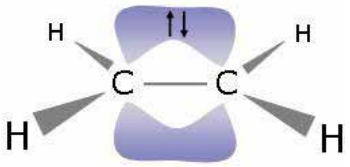 **Enlaces σ: líneas grises** **Enlaces π: regiones moradas**
Hibridación sp C^* $\frac{\uparrow\downarrow}{1s}$ $\frac{\uparrow}{sp}$ $\frac{\uparrow}{sp}$ $\frac{\uparrow}{p}$ $\frac{\uparrow}{p}$	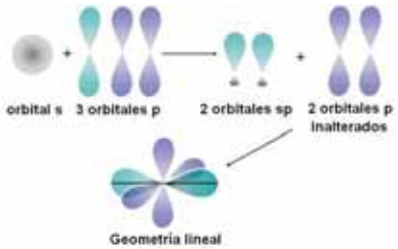	**Acetileno** 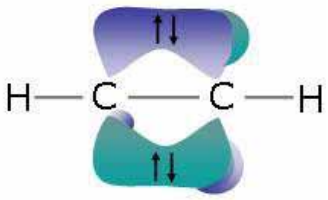 **Enlaces σ: líneas grises** **Enlaces π: regiones moradas y verdes**

orbitales hibridados también se tienen dos orbitales deslocalizados π que no entran en el proceso de hibridación. Ejemplos de hibridación *sp* los encontramos en la molécula de acetileno y en los carbinos. Conviene resaltar que el proceso de hibridación no se produce en átomos aislados, sino que surge de la interacción del átomo de carbono con otros átomos cercanos (bien de carbono o de otras especies, por ejemplo hidrógeno).

Formas alotrópicas

El átomo de carbono aislado posee una vida media muy corta, estabilizándose en una variedad de estructuras multiatómicas con diferentes configuraciones moleculares, denominadas formas alotrópicas. Esta diversidad en el ordenamiento espacial del carbono se halla íntimamente ligada a los tres tipos de hibridación posibles del átomo de carbono. Así, aunque compuestas únicamente de este elemento, las distintas formas alotrópicas del carbono presentan estructuras bien diferenciadas que obedecen a las diferencias en la ordenación espacial de los orbitales en los distintos tipos de hibridación. Como es bien conocido, las formas alotrópicas del carbono de mayor importancia tanto fundamental como aplicada son el diamante (hibridación sp^3) y el grafito (hibridación sp^2). Debido a sus diferentes estructuras físicas, así como a la diferente naturaleza de los enlaces provenientes de las distintas hibridaciones, las propiedades electrónicas y mecánicas de las diferentes formas alotrópicas varían mucho entre sí.

1.2 Grafito y grafeno

Tanto la estructura como las propiedades del grafito son una consecuencia directa de la hibridación sp^2 del átomo de carbono. El grafito presenta una estructura laminar en la cual cada una de las láminas es conocida como grafeno. Éste está compuesto por átomos de carbono formando una red hexagonal plana. El grafeno es un material puramente bidimensional que puede ser considerado como el constituyente básico de los materiales de carbono grafiticos (basados en la hibridación sp^2), desplegando una completa variedad dimensional, desde los fulerenos adimensionales hasta el grafito tridimensional, pasando por los nanotubos unidimensionales [6]. Debido a las excelentes propiedades que exhibe, el grafeno es considerado como un material muy prometedor en gran número de aplicaciones.

1.2.1 Estructura de los materiales grafíticos

Como se ha comentado en el apartado anterior, en la hibridación sp^2 del carbono se halla el origen de los diferentes materiales grafíticos. Cuando se produce esta hibridación, cada átomo de carbono se une a otros tres mediante fuertes enlaces covalentes (524 $kJ\ mol^{-1}$ [4]), denominados σ. Estos enlaces dan lugar a una red hexagonal plana de átomos de carbono con distancias entre primeros vecinos de 1.42 $\AA$. El orbital p no hibridado se superpone con los de los tres átomos vecinos, formándose una banda de orbitales ocupados π conocida como banda de valencia, así como una banda

de orbitales vacios π^*, denominada banda de conducción. Las propiedades eléctricas de los materiales grafíticos están en gran parte determinadas por los electrones π deslocalizados, los cuales poseen una gran movilidad en direcciones paralelas al plano. Debido a la ausencia de enlace químico en la dirección perpendicular al plano, las interacciones en esta dirección son muy débiles. A esta red plana de átomos de carbono, que constituye la unidad estructural básica de los materiales grafíticos, se la conoce como grafeno. Mediante el apilamiento de dos láminas de grafeno se obtiene grafeno bicapa, con una separación de $\sim 3.4\,\text{Å}$ entre capas. Esta separación es relativamente grande debido a que el acoplamiento entre las capas, que surge de la interacción de van der Waals entre los átomos de ambas [7], es comparativamente débil (7 $kJ\ mol^{-1}$ [4]). Aún así, la interacción entre las bandas π y π^* de ambas láminas confieren al grafeno bicapa unas características electrónicas claramente diferenciadas de las del grafeno. En el apilamiento de las dos láminas, los átomos de ambas no coinciden en las mismas posiciones, sino que generalmente las láminas se encuentran ligeramente desplazadas (o de manera equivalente, rotadas 60° con centro en uno de los átomos de carbono) entre sí, de modo que bajo el centro de cada uno de los hexágonos del grafeno superior se encuentra un átomo de carbono del inferior. Esto genera una asimetría entre dos posiciones diferenciadas de los átomos de carbono, puesto que únicamente la mitad de los átomos de una capa posee vecinos en la misma posición de la capa adyacente (posición α), mientras que el resto se encuentra sobre el centro de un hexágono (posición β) (ver *figura 1*). Dicha asimetría se manifiesta, por ejemplo, en las imágenes STM a resolución atómica de grafito, en las que por lo general solo los átomos en posiciones β resultan visibles, apareciendo en las imágenes una red triangular en vez de la red hexagonal que sería de esperar.

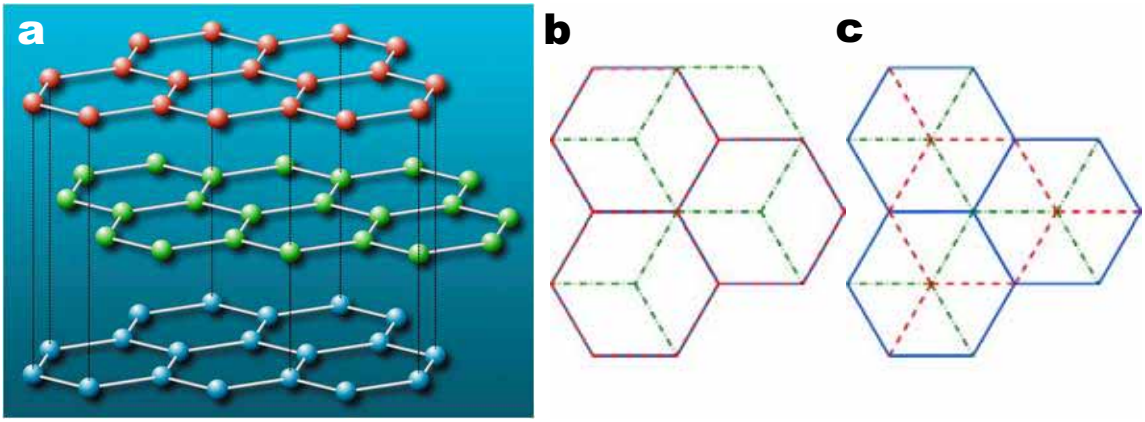

Figura 1 – Estructura del grafito: a-b) apilamiento de tipo Bernal ó *ABA* (*A*=rojo, azul); c) apilamiento *ABC* ó romboédrico.

Si se continúa el proceso de apilamiento, caben dos posibilidades para la posición que puede ocupar la tercera capa. Si etiquetamos las dos capas existentes como *A* y *B*, la nueva capa puede ser o bien de tipo *A*, obteniéndose una secuencia *ABA* (*figura 1 a-b*), o bien puede estar de nuevo desplazada (o, equivalentemente, rotada 60° respecto a una de las capas anteriores con centro en uno de los átomos que no presenta vecino en la otra capa) formando un nuevo tipo de capa (*C)*, obteniéndose así

una secuencia *ABC* (*figura 1 c*) (nótese que debido a la simetría de la red, una cuarta capa rotada un ángulo múltiplo de 60° sería equivalente a alguna de las capas ya existentes, de modo que no existe capa *D*). Estos dos tipos de secuencia dan origen a los apilamientos del grafito de tipo Bernal (*ABAB*), el más común y estable, y de tipo romboédrico (*ABCABC*). Las propiedades de las estructuras cristalinas obtenidas mediante el apilamiento sucesivo de grafenos dependen en gran medida del número de capas, pudiendo distinguirse hasta tres tipos distintos de materiales pseudo-bidimensionales con propiedades diferenciadas: grafeno, grafeno bicapa y grafeno multicapa [8,9]. De este modo, mientras que en el grafeno la estructura electrónica presenta bandas lineales y ausencia de un gap entre la banda de valencia y la de conducción, en el grafeno bicapa las bandas son parabólicas y resulta posible la apertura de un gap mediante la aplicación de un campo eléctrico externo [10]. Al aumentar el número de capas la estructura electrónica se complica de manera sucesiva, coexistiendo diferentes portadores de carga y dando lugar a la aparición de solapamientos finitos entre las bandas de conducción y valencia [11]. Cuando el apilamiento alcanza ~ 10 capas de grafenos, la inclusión de capas adicionales no modifica las propiedades de la estructura de un modo substancial. Es a partir de este momento cuando empezamos a hablar de grafito, es decir, de una estructura cristalina tridimensional compuesta de un apilamiento ordenado de planos de grafenos con una distancia interplanar de 3.35 $\mathring{A}$. Además de apilamientos de tipo Bernal y romboédrico, también se puede encontrar grafito en el que no es posible distinguir un orden de apilamiento entre planos adyacentes, conocido como grafito turbostrático. Este desorden disminuye de manera considerable la interacción entre capas, desembocando en un aumento de la distancia interplanar por encima de los 3.42 $\mathring{A}$ [12-14]. Esta débil interacción entre los planos hace que pueda ser considerado en cierta medida como un "*grafito bidimensional*" [13], compartiendo algunas de sus características con el grafeno.

1.2.2 Grafito

El grafito natural, un material abundante en diversas regiones del mundo, se ha venido empleando desde tiempos remotos, aunque hasta 1855 no fue identificado como una de las formas alotrópicas del carbono. Sin embargo, este grafito contiene numerosas imperfecciones e impurezas, por lo que, a pesar de su abundancia, para ciertas aplicaciones se hace necesario la producción de grafito de origen sintético de mayor cristalinidad. Existen diferentes maneras de producir grafito sintético, entre las que destacan la grafitización de carbón no grafítico, el depósito químico en fase vapor (CVD) de hidrocarburos a altas temperaturas y la cristalización de metales fundidos saturados con carbono (grafito *Kish*). Es posible obtener grafito de una gran perfección cristalina efectuando una pirólisis de hidrocarburos a elevadas temperaturas (>2000 *°C*), seguido de un tratamiento térmico de grafitización del carbono pirolítico resultante a temperaturas que superan los 2700 *°C*, y por lo general a presiones elevadas [4]. Al grafito así obtenido se le denomina grafito pirolítico altamente ordenado/orientado, conocido por sus siglas en inglés como HOPG (*Highly Ordered/Oriented Pyrolytic Graphite*). Este material es un agregado de monocristales de grafito de grandes tamaños (generalmente unas pocas micras a lo

largo del plano basal, y ~100 *nm* según la dirección c), y con una baja desviación angular de los cristales según el eje c (< 1°). Gracias a este elevado ordenamiento, el HOPG se suele emplear como monocromador de neutrones y de rayos X. Desde un punto de vista de la investigación, resulta también interesante el denominado grafito *Kish*, que se obtiene a partir de la cristalización de hierro fundido sobresaturado con carbono [15]. El grafito *Kish* posee una cristalinidad mayor que la del HOPG, aunque al presentarse en pequeños copos su uso está menos extendido que el de éste. Aún así, el grafito *Kish* se emplea con asiduidad para la obtención de grafenos a escala de laboratorio.

Debido a su peculiar estructura laminar y a las débiles interacciones que se producen entre los planos de grafeno, el grafito (así como los materiales grafíticos en general) posee un alto grado de anisotropía, por lo que algunas de sus propiedades varían considerablemente dependiendo de si éstas son medidas a lo largo del plano basal (direcciones *ab*) o en la dirección perpendicular a éste (dirección *c*) [7]. Atendiendo a su estructura electrónica, el grafito es un semimetal, con un gap nulo y una pequeña densidad de estados en el nivel de Fermi. De este modo, es un buen conductor eléctrico, gracias a la gran cantidad de electrones deslocalizados (electrones π) que existen entre las láminas. Estos electrones son libres para moverse a lo largo del plano basal pero no en la dirección perpendicular, debido a la relativamente elevada separación entre planos. Por esto, el grafito puede considerarse como un conductor a lo largo del plano basal (resistividad $2.5 - 5.0 \times 10^{-6}\ \Omega \cdot m$) mientras que en la dirección normal a éste la resistividad que presenta es típica de un material aislante ($3000 \times 10^{-6}\ \Omega \cdot m$) [4]. Las propiedades térmicas y acústicas también presentan un elevado grado de anisotropía, debido a que los fonones son capaces de propagarse muy rápido en las direcciones paralelas al plano basal gracias a los fuertes enlaces covalentes. Por el contrario, su velocidad en la dirección perpendicular al plano decrece significativamente. De este modo, en el plano ab el grafito puede considerarse como un buen conductor térmico ($\sim 390\ W/m \cdot K$ a $300\ K$), mientras que en la dirección c es considerado un buen aislante térmico($\sim 2\ W/m \cdot K$ a $300\ K$) [4].

El grafito se viene empleando en diversas aplicaciones prácticas desde hace varios siglos. Entre sus aplicaciones industriales destaca su empleo para la fabricación de electrodos, como material refractario y lubricante, así como moderador de neutrones en reactores nucleares.

1.2.3 Grafeno

El grafeno es una lámina monoatómica plana de átomos de carbono unidos mediante enlaces covalentes sp^2 (monocapa de grafito). Ha sido empleado durante las últimas décadas como modelo teórico de estudio de diversos materiales grafíticos, permitiendo explicar muchas de sus propiedades. A pesar de esto, hasta el año 2004 no se creía posible su existencia como entidad aislada, ya que se suponía que los cristales estrictamente bidimensionales eran termodinámicamente inestables. Esta inestabilidad sería debida a una contribución divergente de las fluctuaciones térmicas en redes cristalinas de baja dimensionalidad que teóricamente produciría desplazamientos atómicos

comparables a las distancias interatómicas a cualquier temperatura finita [16], dando lugar a la desintegración del cristal. Numerosas pruebas experimentales apoyaban esta hipótesis, entre ellas el hallazgo de que la temperatura de fusión de láminas delgadas decrece rápidamente al disminuir su espesor, lo que provoca que el filme se vuelva inestable para grosores correspondientes a aproximadamente una docena de monocapas [17,18]. Esto fuerza en general a los cristales bidimensionales a tomar una variedad de estructuras tridimensionales que les proporcionen estabilidad a costa de la pérdida de la bidimensionalidad. De esta manera, se suponía que el grafeno únicamente podía existir como constituyente básico de otros materiales grafíticos, aunque sin poseer una entidad real como objeto aislado. Sin embargo, en el año 2004 un grupo de científicos encabezados por A.K. Geim y K.S. Novoselov fueron capaces de obtener e identificar por vez primera láminas individuales de grafeno junto con otros cristales bidimensionales [11,19]. Partiendo de una pieza de HOPG, emplearon un procedimiento conocido como exfoliación micromecánica (*micromechanical cleavage*). Este método, que se basa en la relativa debilidad de la interacción entre las láminas de grafeno que conforman el grafito, consiste básicamente en la exfoliación repetida de la pieza de grafito empleando cinta adhesiva. Existen varias hipótesis para tratar de explicar la imprevista estabilidad de estas láminas aisladas. Por un lado, las láminas provienen de una estructura tridimensional previa, lo cual, unido a su pequeños tamaños laterales y a la fuerza de los enlaces covalentes entre los átomos de carbono, presumiblemente las hace resistentes a las fluctuaciones térmicas [8]. Por otro lado, las ondulaciones microscópicas que presentan las láminas podrían contribuir a su estabilidad, aparte de dar cuenta de algunas otras propiedades del grafeno [20].

Propiedades y aplicaciones del grafeno

Debido a las insólitas propiedades físicas que ostenta, se considera al grafeno como un material excepcional tanto desde el punto de vista de la investigación en física fundamental, como desde el punto de vista de sus aplicaciones prácticas. Atendiendo a su estructura electrónica, el grafeno es un caso especial de semimetal: posee un gap cero como los metales, con la peculiaridad de que la densidad de estados en el nivel de Fermi es nula [21], como ocurre en los semiconductores [22,23]. Es por esto por lo que también se le puede considerar como un semiconductor de banda prohibida (*gap*) nula. Además, su estructura electrónica de bandas presenta una dispersión lineal respecto al momento para bajas energías, semejante a la que proporciona la ecuación de Dirac para fermiones de masa nula. Esto convierte al grafeno monocapa en un sistema bidimensional de fermiones de Dirac de masa nula, algo de una importancia crucial a la hora de comprender sus inusuales propiedades electrónicas, como el efecto Hall cuántico (QHE) anómalo. Los electrones, en su movimiento a través del potencial periódico de la red cristalina del grafeno, pierden por completo su masa efectiva como consecuencia de la simetría hexagonal del cristal. De esta manera, los portadores de carga en el grafeno son cuasi-partículas sin masa que se mueven a una velocidad constante de $10^6\ m/s$ (es decir, unas 300 veces menor que la velocidad de la luz en el vacío), y cuyo comportamiento está regido por la ecuación

relativista de Dirac y no por la de Schrödinger. Se tiende así un inesperado puente entre dos disciplinas en principio alejadas, la física de la materia condensada y la teoría cuántica de campos (QFT, *Quantum Field Theory*), permitiendo comprobar la validez de diferentes efectos cuánticos predichos por esta última (paradoja de Klein, efecto Hall cuántico, etc.) mediante experimentos relativamente sencillos y de bajo coste concernientes a la medida de las propiedades electrónicas del grafeno. Los portadores de carga del grafeno poseen una gran movilidad intrínseca (puede llegar hasta los $2 \cdot 10^5\ cm^2\ V^{-1}s^{-1}$ a temperatura ambiente [24,25]) y se encuentran en una concentración muy elevada (10^{12} cm^{-2}). Esto implica que la resistividad intrínseca a temperatura ambiente es de tan solo $10^{-8}\Omega \cdot \mathrm{m}$ [26], valor que es incluso menor que el de la plata, el material conocido con una menor resistividad. La movilidad tan elevada que presentan los portadores de carga del grafeno, superando la de los actuales transistores de Si, asegura el transporte balístico a distancias sub-micrométricas incluso a temperatura ambiente. Debido a estas excepcionales propiedades electrónicas, se está trabajando en la implementación del grafeno en transistores de efecto de campo (FET) [11] con una velocidad de conmutación muy elevada (algunos prototipos ya han alcanzado los 100 GHz [27]), así como de transistores en los que el flujo de electrones es muy pequeño y está totalmente controlado (*single electron transistor*, SET) [28]. Por esto se postula al grafeno como un sustituto ideal del Si en la fabricación de circuitos integrados de altas prestaciones. Sin embargo, el hecho de que posea un gap nulo impide su aplicación de manera directa, por lo que resulta necesario procesar el grafeno de modo que se abra un gap. Entre otras tentativas, una ruta que puede proporcionar buenos resultados consiste en trabajar con estrechas cintas de grafeno (*graphene nanoribbons*, GNR), estructuras que se pueden considerar unidimensionales. Debido al confinamiento cuántico de los electrones que se produce en estas estructuras unidimensionales, los GNR presentan un gap que es lo suficientemente grande ($\geq 0.5\ eV$) como para permitir su aplicación en transistores que trabajen a temperatura ambiente [29].

Se sabe que la adsorción de moléculas sobre la superficie del grafeno da lugar a un dopaje del mismo, bien con electrones o huecos en función de la naturaleza del material adsorbido, y por tanto a pequeños cambios en su resistividad. Esto, unido a su elevada área superficial específica ($\sim$2600 $m^2 g^{-1}$ [30]), convierte al grafeno en un potencial candidato para la elaboración de sensores de gran sensibilidad (de gases [31], biosensores [32], etc.), pudiendo llegarse a niveles de detección de moléculas o átomos individuales [31]. La gran área superficial del grafeno y su gran conductividad lo postulan como posible sucesor del grafito en la fabricación de ánodos de baterías de ión litio [33]. La conductividad térmica a temperatura ambiente del grafeno es mayor que la de cualquier material conocido ($\sim$ 5000 $Wm^{-1}K^{-1}$ [34]), lo que lo convierte en un candidato ideal para la fabricación de disipadores térmicos y de materiales compuestos de gran conductividad térmica. Sus excepcionales propiedades mecánicas convierten al grafeno en el material más resistente conocido, con una resistencia a la tracción de 130 GPa y un elevado módulo de Young ($\sim$ 1.0 TPa [35]). Aprovechando

esto, se está intentando la elaboración de materiales compuestos de gran resistencia además de conductores de la electricidad gracias a la inclusión de grafeno [30].

Las propiedades ópticas del grafeno también le auguran un esperanzador futuro en un gran número de aplicaciones. Su transmitancia óptica T es muy elevada, $\sim 97.7\,\%$, e independiente de la longitud de onda en todo el rango visible [36,37], pudiendo ser expresada empleando únicamente la constante de estructura fina α sin que aparezca ningún parámetro característico del material:

$$T = \left(1 + \frac{\pi\alpha}{2}\right)^{-2} \approx 1 - \pi\alpha \approx 0.977$$

Esta elevada transmitancia óptica impide la observación visual directa mediante microscopía óptica de láminas de grafeno, por lo que para su identificación se necesita hacer uso de un efecto de interferencia cuando se encuentran soportadas sobre substratos de Si/SiO_2 del grosor adecuado. Sin embargo, gracias a ella y a su buena conductividad eléctrica, el grafeno se presenta como un candidato ideal para la fabricación de electrodos conductores transparentes, empleados por ejemplo en pantallas táctiles [38] y de cristal líquido [39,40], células fotovoltaicas orgánicas [41] y LEDs orgánicos [42]. A este respecto, el grafeno supera en términos de estabilidad química, flexibilidad y transparencia a los óxidos metálicos que se emplean en la actualidad (p.ej. ITO) [40]. Algunas de estas aplicaciones se encuentran ya en vías de implementación a nivel práctico [38], en lo que podría ser uno de los primeros usos a nivel industrial de este material.

El grafeno presenta además una gran transparencia a los haces de electrones, debido a su insignificante sección eficaz de dispersión electrónica. Esto los convierte en soportes ideales en TEM, dado que resultan prácticamente transparentes para esta técnica. De esta manera resulta posible observar átomos individuales adsorbidos [43].

Métodos de obtención de grafeno

Como ha ocurrido anteriormente con los fulerenos o los nanotubos de carbono, el aprovechamiento en casos prácticos de las excelentes propiedades de los grafenos se ha visto frenado por las dificultades en su obtención y procesamiento a gran escala. Como se indicó anteriormente, desde 2004 el grafeno se ha venido obteniendo a partir de piezas macroscópicas de grafito mediante exfoliación micromecánica (*figura 2*). El método se ha ido simplificando desde sus inicios, y en la actualidad se produce la exfoliación frotando directamente el grafito contra una superficie (generalmente *Si/SiO_2*) como si se escribiera sobre la misma [19,44]. Mediante este sencillo procedimiento resulta posible la obtención de láminas de grafeno monocapa de gran tamaño (hasta 0.2 *mm*) y de una calidad tanto estructural como electrónica excelente. El problema radica en que, por ser un proceso totalmente manual, la obtención del material es considerablemente laboriosa y de un rendimiento extremadamente bajo. Además, las láminas han de ser cuidadosamente localizadas con la

ayuda de un microscopio óptico entre una gran cantidad de pequeños copos de grafito que las enmascaran, un arduo proceso que puede llevar varias horas para la identificación de unas pocas láminas de grafeno. Por ello, en la actualidad se están desarrollando y refinando métodos alternativos para la preparación de grafeno con el objetivo de abaratar los costes de producción a la vez que se aumenta la cantidad de material obtenido. A este respecto, los métodos que en la actualidad resultan más prometedores son:

- Deposito químico en fase vapor (CVD) de hidrocarburos sobre metales de transición, como el níquel o el rutenio. Se expone un substrato metálico a hidrocarburos (generalmente metano), produciéndose una nucleación y crecimiento de una lámina de grafeno al descomponerse los hidrocarburos en la superficie metálica [45-47]. Mediante este método se sintetizan láminas monocapa de grafeno de una gran calidad estructural, aunque el hecho de involucrar altas temperaturas y bajas presiones lo convierte en un método muy costoso e instrumentalmente complejo. La presencia del substrato metálico imposibilita el empleo de los grafenos como componentes electrónicos sin una transferencia previa de éstos a un nuevo substrato aislante (o semiconductor) [45]. Por otro lado, permite la posibilidad de dopar las láminas mediante la sustitución de átomos introduciendo diferentes gases durante el crecimiento [48].
- Crecimiento epitaxial en superficies eléctricamente aislantes, principalmente el carburo de silicio, *SiC* [49-51]. Este método se basa en la sublimación térmica del silicio a temperaturas que pueden llegar a superar 1300 °C, a la vez que el carbono se reordena para formar una capa de grafeno. Se producen así láminas de una gran calidad estructural, aunque de nuevo la necesidad de trabajar en ultra alto vacio y la gran temperatura necesaria para producir la sublimación del silicio limitan enormemente su aplicación a gran escala. Sin embargo, recientes estudios realizados a presión atmosférica en *Ar* parecen indicar que es posible obtener láminas de una calidad estructural mejor incluso que la de las láminas obtenidas en vacío [52].
- Procesado químico de óxido de grafito, que implica la oxidación y posterior exfoliación de grafito en fase líquida, obteniéndose láminas de óxido de grafeno (grafeno fuertemente oxidado) que pueden ser reducidas para obtener dispersiones de grafeno [53,54]. La principal ventaja de este método es que se produce gran cantidad de material en medio acuoso, lo que facilita su procesado. El gran inconveniente de este método radica en la baja calidad estructural de las láminas obtenidas.
- Exfoliación de grafito prístino en determinados disolventes orgánicos [55,56] o surfactantes [57], obteniéndose láminas de grafeno de gran calidad, aunque sus tamaños laterales se restringen a unos pocos cientos de nanómetros. La ventaja de este método radica en que se evitan los procesos previos de oxidación y reducción, lo cual redunda en un

aumento en la calidad estructural de los grafenos obtenidos. Como contrapunto, la concentración de grafeno que se consigue es generalmente pequeña (~0.01 $mg\ ml^{-1}$), y las láminas obtenidas son sólo minoritariamente ($10 - 30\ \%$) monocapa, siendo el resto láminas de unas pocas capas [58].

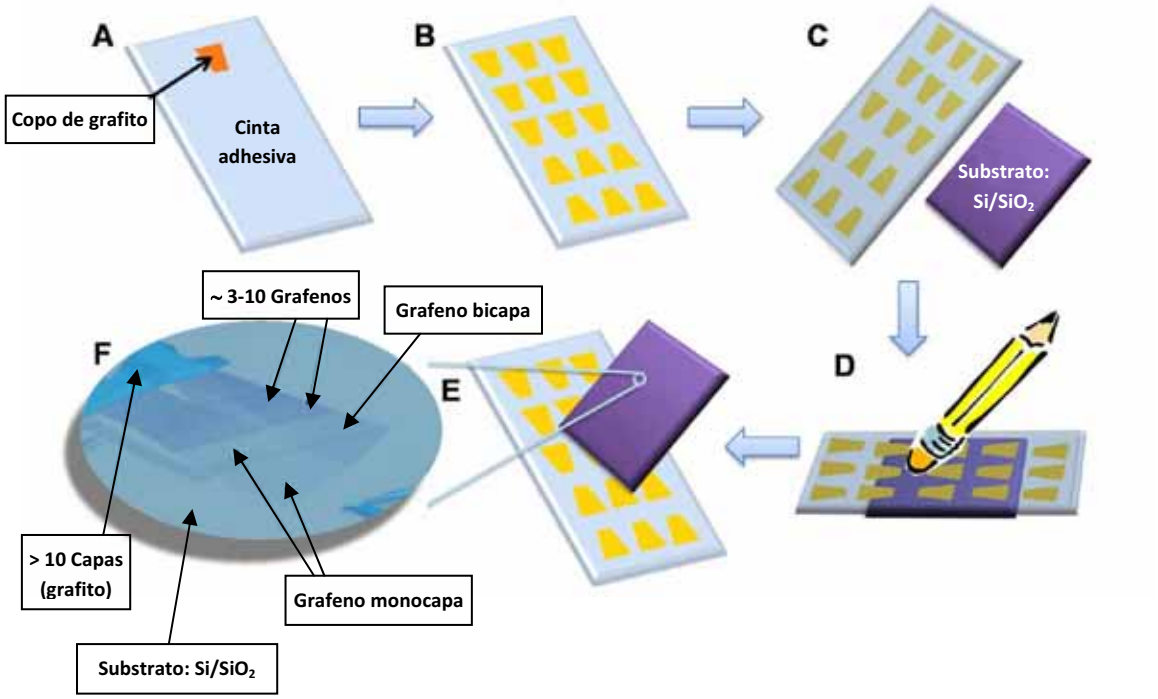

Figura 2 – Proceso de exfoliación micromecánica de grafito. **(A)** Un copo de grafito es adherido a cinta adhesiva. **(B)** Se exfolia el copo en repetidas ocasiones, obteniéndose varios copos más finos. **(C)** Se presionan los copos contra una superficie limpia de *Si/SiO₂* que actuará como substrato. **(D)** Se frota con suavidad la parte trasera de la cinta adhesiva, asegurándose así un contacto entre los copos y el substrato. **(E)** Se retira con cuidado la cinta, dejando láminas de grafenos sobre el substrato junto con una gran cantidad de material grafítico. **(F)** Cuando se encuentran sobre un substrato de *Si/SiO₂*, las láminas de grafeno se pueden identificar con la ayuda de un microscopio óptico gracias a un fenómeno de interferencia provocado por la diferencia de recorridos ópticos, permitiendo discriminar entre grafenos de diferentes capas. Adaptado con permiso de la información suplementaria de *Xu K., Cao P. and Heath J.R., Nano Lett. 9, 4446-4451 (2009)*. Copyright 2009 American Chemical Society.

Grafeno obtenido a partir de óxido de grafito

En lo que sigue nos centraremos en los grafenos obtenidos a partir de óxido de grafito, método que a día de hoy resulta prometedor con vistas a su producción y procesado a gran escala. Esto es debido a que se obtiene una gran cantidad de material estable en forma de dispersión acuosa u orgánica sin la necesidad de emplear surfactantes o estabilizadores, y con un bajo coste económico. El óxido de grafito fue preparado por vez primera hace aproximadamente 150 años por el químico B.C. Brodie [59] mediante un método que fue perfeccionado cerca de un siglo más tarde por W.S. Hummers y R.E. Offeman [60], y que involucra el empleo de sustancias fuertemente oxidantes ($KMnO_4$) en medio ácido (H_2SO_4). Tras el proceso de oxidación se obtiene un material que posee una estructura laminar constituida por capas apiladas de óxido de grafeno. Estas capas presentan una gran cantidad de funcionalidades de oxígeno, por lo que son altamente hidrófilas [53]. Los grupos oxigenados y las

moléculas de agua adsorbidas hacen aumentar de manera considerable la distancia entre láminas, con lo que la energía de interacción entre capas disminuye y el óxido de grafito resulta fácilmente exfoliable en medio acuoso (aunque algunos disolventes orgánicos polares también han demostrado ser efectivos [61]). Se obtienen así suspensiones coloidales de láminas monocapa de óxido de grafeno (GO, del inglés *graphene oxide*), estabilizadas gracias a la repulsión electrostática producida por la carga negativa que adquieren en dispersión debido a la ionización de los distintos grupos funcionales que presentan [54]. Para describir la estructura del GO se emplea a día de hoy el modelo de Lerf-Klinowski [62], basado en estudios mediante resonancia magnética nuclear (NMR). En él se describe al GO como un material no estequiométrico, formado por regiones aromáticas prístinas separadas entre sí mediante regiones alifáticas que contienen grupos hidroxilo y epoxi fijados en gran proporción sobre los planos basales,

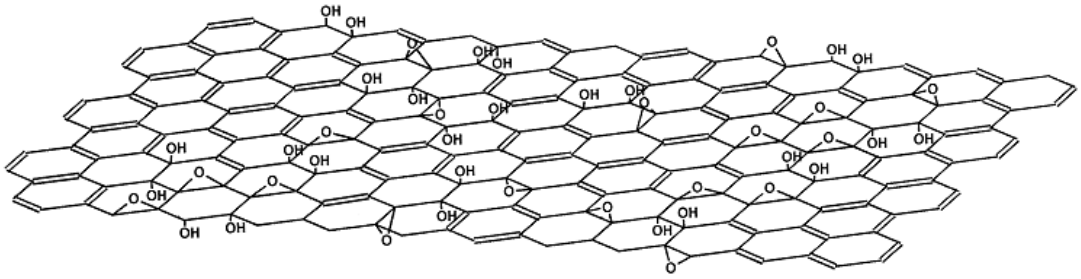

Figura 3 – Representación esquemática de la estructura de las láminas de GO. Los grupos hidroxilo y epoxy perturban la conjugación electrónica de la red grafítica mediante la formación de enlaces sp^3. Reproducido de la referencia [62], con permiso de Elsevier.

junto con una pequeña cantidad de grupos carbonilo y carboxilo que se hallan presentes en los bordes de las láminas [53,62] (ver *figura 3*). Debido a la presencia de todos estos grupos tanto el GO como el óxido de grafito son eléctricamente aislantes, lo que limita su aplicabilidad. Por ello, se necesitan tratamientos de reducción para poder obtener láminas conductoras. De los diferentes métodos existentes para efectuar la reducción controlada (reducción química [53,63], electroquímica [64] y térmica [39,65]) el más extendido emplea hidracina ($H_2N–NH_2$) como agente reductor [66,67]. Tras el proceso de reducción química, es posible efectuar un tratamiento térmico adicional entre 150-1100 *°C* para incrementar la eficiencia de la reducción y mejorar la calidad estructural de las láminas [68]. Sin embargo, debido a su gran toxicidad y peligrosidad, recientemente se han realizado estudios para sustituir la reducción con hidracina por otros procedimientos que involucren métodos o agentes reductores menos problemáticos [64,69-72]. Tras la reducción se incrementa enormemente la conductividad de las láminas, resultando ser hasta tres y cuatro órdenes de magnitud mayor que la original [73], presumiblemente como consecuencia de la restauración de la estructura grafítica original. Sin embargo, esta restauración no es completa y las funcionalidades oxigenadas introducidas en la fase de oxidación no son totalmente eliminadas de las láminas. De hecho, aunque la relación atómica *C/O* aumenta tras la reducción, desde valores de ~2 para el GO hasta valores de ~10 en el caso de reducción empleando hidracina [53], los valores relativamente bajos que se alcanzan indican que la presencia de

oxígeno continúa siendo significativa, lo cual repercute también en la baja calidad estructural de las láminas [74]. Por todo esto, los grafenos que se obtienen mediante este método distan mucho de ser las láminas perfectas que se obtienen por exfoliación mecánica [75], como queda patente en las imágenes obtenidas mediante microscopías de proximidad (*figura 4*). Para diferenciarse del grafeno prístino, a las láminas de grafeno obtenidas mediante exfoliación química de grafito se las conoce en la literatura mediante una serie de términos diferentes, entre los que destacan: grafeno químicamente modificado (CMG, *Chemically Modified Graphene*), óxido de grafeno reducido (rGO, *reduced Graphene Oxide*), óxido de grafeno químicamente reducido (CRGO, *Chemically Reduced Graphene Oxide*), grafeno químicamente derivado (CDG, *Chemically Derived Graphene*), grafeno químicamente convertido (CCG, *Chemically Converted Graphene*). En la mayoría de contextos estos términos se utilizan para referirse a las láminas provenientes de la reducción del GO, aunque CMG, CDG y CCG engloban un conjunto más amplio de materiales. En la presente Memoria se emplearán indistintamente varias de estas expresiones para referirse al óxido de grafeno químicamente reducido.

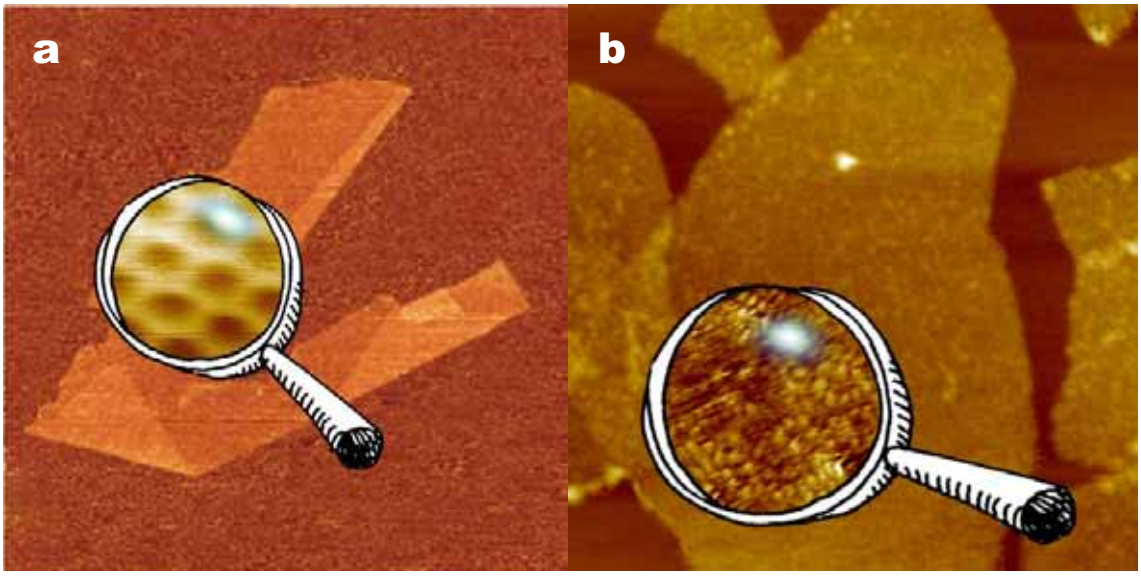

Figura 4 – Imágenes AFM (generales) y STM (ampliaciones) de láminas individuales de grafeno obtenido mediante exfoliación mecánica (a) y de óxido de grafeno reducido (b). (Imágenes de (a) adaptadas con permiso de referencia [19] (general) y de *Stolyarova E. et al., Procl. Natl. Acad. Sci. USA 104, 9209 (2007)* (ampliación), copyright (2005-2007) National Academy of Sciences, USA. Imágenes de (b) adaptadas de *Paredes J.I. et al., Langmuir 25, 5957 (2009)*, copyright 2009 American Chemical Society.

La menor calidad cristalina del CMG lleva aparejada una degradación en las propiedades del material en comparación con el grafeno prístino. Esta degradación presenta diferentes niveles dependiendo de la propiedad concreta (p. ej., la movilidad de los portadores de carga es entre dos y tres órdenes de magnitud menor [76], mientras que el módulo elástico se mantiene en un valor relativamente alto (0.25 *TPa* frente a 1 *TPa* para grafeno prístino [77]). Debido a esta degradación en sus propiedades, el CMG no resulta apto para cierto tipo de aplicaciones que requieren una gran cristalinidad y pureza de los grafenos (generalmente la elaboración de dispositivos electrónicos). Sin embargo, el CMG resulta muy útil cuando la cristalinidad de la red no constituye un factor tan decisivo.

Su facilidad de producción en masa y su procesabilidad convierten al CMG en un candidato idóneo para un gran número de aplicaciones. Así, puede ser empleado para preparar materiales compuestos conductores y de una gran resistencia mecánica [78,79], recubrimientos flexibles y conductores en pantallas táctiles [76], sensores moleculares de gases [80] ó soportes transparentes para TEM [81]. Con objeto de mejorar las propiedades de las láminas de CMG, son necesarios estudios adicionales para conocer de modo preciso la morfología y estructura de las láminas (tanto antes como después de la reducción), así como sus mecanismos de reacción, de modo que se puedan desarrollar procesos alternativos de producción que redunden en una mejora en la cristalinidad de las láminas.

1.2.4 Modificación superficial de materiales grafíticos. Oxidación

La modificación superficial controlada de materiales carbonosos presenta un considerable interés en gran número de disciplinas, como pueden ser la electroquímica, la bioquímica o la electrónica. De nuevo se vuelve a manifiestar la gran anisotropía de estos materiales, que en términos químicos se traduce en grandes diferencias en las reactividades químicas. Así, el plano basal del grafito (001) es químicamente muy inerte, con una energía superficial muy baja ($0.1\,Jm^{-2}$), debido a la pequeña densidad de estados cerca del nivel de Fermi. Por el contrario, la energía superficial es de unos $5\,Jm^{-2}$en los planos prismáticos (100) y (110) [4]. Estos planos prismáticos no solo existen en las terminaciones de los planos basales, sino también en defectos estructurales de la red grafítica como pueden ser vacantes o dislocaciones, de modo que es posible ajustar la reactividad de una superficie basal mediante la introducción controlada de defectos. La baja reactividad del plano basal prístino convierte al grafito puro en uno de los materiales más inertes químicamente hablando, resistente a la mayoría de ácidos y gases corrosivos. Sin embargo, la resistencia química del grafito es menor frente a los elementos de la columna *VI* de la tabla periódica, y en particular frente al oxígeno y los compuestos oxigenados [4]. Por ello, la oxidación constituye uno de los métodos más efectivos de modificación superficial de los materiales grafíticos. La oxidación del grafito en presencia de oxígeno molecular comienza por encima de $350-400$ ℃, temperaturas a las cuales a los carbonos en posiciones no basales se fija oxígeno, formándose funcionalidades oxigenadas que posteriormente pueden desorberse en forma de *CO* y CO_2. Por debajo de 700 ℃ la oxidación se produce exclusivamente en posiciones no basales (vacantes, dislocaciones, límites de grano, etc.), donde existen enlaces sp^2 no saturados o distorsionados que dan lugar al citado incremento de la reactividad [82]. Cuando la temperatura supera los $700-875$ ℃ (probablemente dependiendo del grado de cristalinidad del grafito), también las posiciones basales resultan oxidadas [82,83]. La oxidación térmica con oxígeno resulta ser un proceso altamente selectivo que da lugar a la formación de estructuras reconocibles, como pueden ser agujeros monocapa en la superficie, debido a la desorción de átomos de carbono como CO/CO_2 preferencialmente en defectos. La oxidación también conduce a la formación de diferentes grupos funcionales oxigenados, los cuales se unen en su mayoría a posiciones no basales [84]. La presencia de estas funcionalidades influye en las propiedades superficiales del material. Además del oxígeno

molecular, otros compuestos oxigenados resultan efectivos en la oxidación de materiales grafiticos. Entre ellos destacan el oxígeno atómico y el ozono, los cuales suelen ser mucho más reactivos que el oxígeno molecular, de manera que se pueden efectuar oxidaciones a menores temperaturas [82,83,85].

En el caso de grafitos muy perfectos, como el HOPG, resulta posible determinar los efectos de las oxidaciones/modificaciones en su estructura a escala atómica, al menos durante las etapas iniciales, empleando microscopías de proximidad. Esto es debido al alto grado de cristalinidad del material, que permite observar minúsculos cambios estructurales. De esta manera, es posible estudiar los distintos tipos de defectos puntuales que se introducen en el material por el tratamiento. Entre los defectos más comunes introducidos por las oxidaciones en materiales grafiticos destacan las vacantes atómicas y la implantación de distintos tipos de especies intersticiales. El conocimiento del tipo específico de defecto producido, así como de su evolución durante el proceso de oxidación, proporciona información sobre el modo en el que opera el tratamiento. De esta manera resulta posible identificar el tipo de ataque que se está produciendo y estudiar su dependencia con los parámetros de operación, pudiendo adecuar el tratamiento dependiendo de la aplicación concreta.

En materiales como el grafeno o el CMG, en los que cada átomo forma parte de la superficie, el estudio de la química superficial y la reactividad adquiere un papel fundamental. Es conocido que la reactividad del grafeno prístino frente a oxidaciones térmicas es mayor que la del HOPG [86]. Esta reactividad disminuye al aumentar el número de capas, de modo que en grafeno tricapa la reactividad es comparable a la del HOPG. Sin embargo, hasta la fecha no existen estudios sobre la reactividad del CMG y su comportamiento frente a atmosferas oxidantes, algo que resulta necesario conocer de cara a su implementación en aplicaciones prácticas.

2. Métodos de oxidación superficial

Se conocen diversos métodos de oxidación superficial de materiales grafíticos. Entre ellos destacan los plasmas por su posible importancia tecnológica y su flexibilidad a la hora de adecuar el tratamiento. La oxidación mediante tratamientos con ozono generado por radiación ultravioleta también resulta práctica, ya que se efectúa a presión ambiente y a temperaturas que por lo general se encuentran por debajo de los 100 ℃. También resulta interesante la oxidación empleando técnicas litográficas, entre las que destaca la litografía empleando microscopías de proximidad, con las que se logran oxidaciones extremadamente localizadas en la superficie.

2.1 Plasmas

2.1.1 Introducción a los plasmas

Por motivos históricos, los plasmas constituyen el conocido como “cuarto estado de la materia”, a pesar de que más del 99% de la materia visible en el universo se encuentre en forma de plasma [87]. Pese a su abundancia en el universo, el plasma no fue identificado hasta finales del siglo *XIX*

(1879) por el químico y físico inglés Sir William Crookes, quien, a la luz de sus investigaciones con descargas eléctricas en tubos de vacío, sugirió la existencia de un nuevo estado de la materia. Este nuevo estado no recibió el nombre de plasma hasta el año 1928 de manos de Irving Langmuir [88]. Su tardío descubrimiento se debe a las extraordinarias condiciones necesarias para su existencia, las cuales resultan incompatibles con la vida, y que convierten a la Tierra, demasiado densa y fría para la presencia de plasmas, en una isla de lo que denominamos "materia ordinaria".

La fuerza electromagnética es la causante de la existencia de una amplia variedad de estructuras, desde átomos y moléculas estables hasta redes cristalinas, y en general cualquiera de las estructuras, bien sea sólida, líquida o gaseosa, de la que nos hallamos rodeados en la naturaleza. La distinción básica entre los distintos estados de la materia radica en las diferentes energías de enlace que mantienen unidos sus constituyentes, resultando ser estables gracias a que esta energía de ligadura es mucho mayor que la energía térmica ambiental. De este modo, conforme la temperatura aumenta, estas estructuras comienzan a descomponerse de un modo escalonado: a una temperatura dada se produce una transición de fase de sólido a líquido, mientras que a temperaturas mayores la transición de fase se produce entre el estado líquido y el gaseoso. Por el contrario, la transición entre gas y gas ionizado no es una transición de fase, ya que se produce de manera gradual y no a una temperatura prefijada. En primer lugar se produce una disociación del gas molecular en gas atómico, el cual posteriormente resulta ionizado cuando la temperatura se eleva hasta valores en los que las colisiones entre átomos son suficientemente energéticas como para arrancar los electrones exteriores. Se produce así un conjunto de electrones libres (e^-) y de iones de carga positiva, siendo esta mezcla de iones positivos y electrones imbuidos en fuertes campos electromagnéticos lo que se conoce como plasma. Debido al hecho de que la descomposición térmica rompe las ligaduras interatómicas antes de que se produzca la ionización, la mayor parte de los plasmas terrestres comienzan siendo gases. De hecho, de una manera poco precisa los plasmas pueden ser definidos como gases ionizados en mayor o menor grado. En un plasma hay además fotones, iones negativos y especies neutras, tanto en el estado fundamental como en diferentes estados excitados. El hecho de que parte de las partículas que componen un plasma posean carga eléctrica, siendo por ello capaces tanto de crear como de interaccionar con campos electromagnéticos, unido a la libertad de movimiento de éstas (debido a la ausencia de enlaces químicos), confiere a los plasmas propiedades que no se observan en fluidos convencionales ni en sólidos, y que involucran movimientos colectivos de partículas de una gran complejidad.

En función de la densidad de partículas con carga y su energía electrónica media se puede hacer una clasificación de los distintos tipos de plasma existentes [89] (*figura 5*), cubriendo como se puede observar varios órdenes de magnitud tanto en densidades como en temperaturas. Atendiendo a su origen, podemos hablar de plasmas naturales, tanto espaciales/astrofísicos (núcleo solar, medio

intergaláctico, nebulosas...) como terrestres (rayos producidos en tormentas eléctricas, auroras, llamas...), y de plasmas de origen artificial (televisores, lámparas fluorescentes...). Los plasmas de origen artificial pueden ser generados por la acción de campos electromagnéticos muy intensos sobre algún gas, como ocurre en el interior de los tubos fluorescentes, o bien por la exposición del gas a temperaturas extremadamente altas, como es el caso de los reactores de fusión. Debido a su inherente reactividad química, el empleo de plasmas para la modificación superficial de materiales resulta muy prometedor.

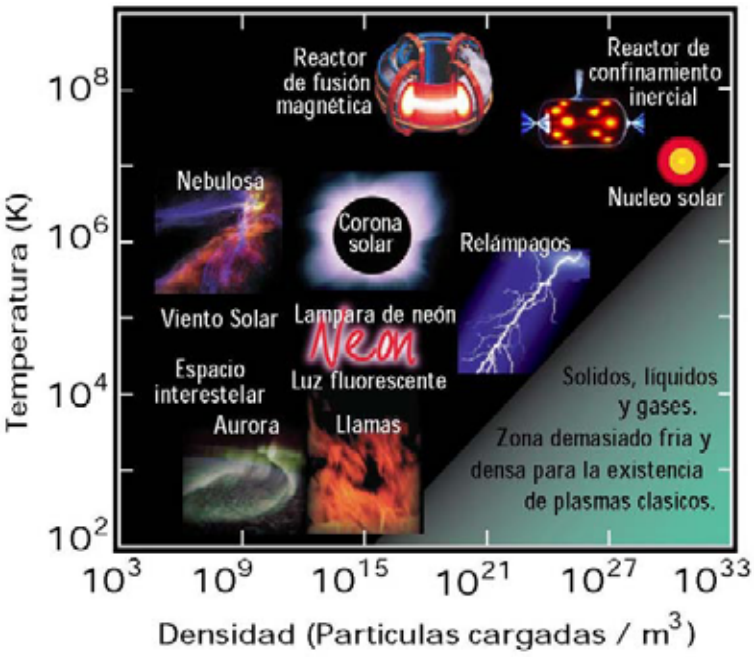

Figura 5 – Regiones de existencia de plasmas. *Copyright © 2010 Contemporary Physics Education Project (CPEP) – CPEPphysics.org.*

2.1.2 Modificación superficial con plasmas. Plasmas de oxígeno

Una vez que se produce la ionización del gas, los electrones libres toman energía del campo electromagnético, cediéndola mediante colisiones a las especies neutras presentes en el gas. De este modo se produce la formación de nuevas especies, incluyendo átomos, iones, radicales libres y especies metaestables, que por lo general son químicamente activas, por lo que a su vez pueden participar en reacciones formándose nuevas especies estables. Al estudio de estas reacciones se le denomina química de plasmas, y su principal interés se centra en los plasmas fríos y los arcos. Debido a que los electrones son, exceptuando los fotones, el componente más ligero de un plasma, las transferencias energéticas mediante colisión hacia los iones o las especies neutras son por lo general poco eficientes. Debido a esto, los electrones pueden adquirir energías medias algunos eV mayores que las de iones y especies neutras, equivalentes a decenas de miles de grados por encima de las temperaturas de éstas [90]. A su vez, la temperatura de los iones es mayor que la de las especies neutras, siendo por tanto el plasma un sistema en el cual las especies constituyentes no se encuentran por lo general en equilibrio térmico entre sí. Esto resulta común en plasmas levemente ionizados, como las descargas, donde los iones se encuentran prácticamente a temperatura ambiente. Atendiendo a si se ha alcanzado o no el equilibrio térmico entre las diferentes especies, podemos hablar de plasmas térmicos o no térmicos, respectivamente.

Los denominados plasmas fríos constituyen un tipo de plasma no térmico importante desde el punto de vista de las aplicaciones prácticas. En ellos el grado de ionización es muy bajo, y están caracterizados por unas energías electrónicas medias de $1 - 10\ eV$, y por unas densidades electrónicas de $10^8 - 10^{13}\ cm^{-3}$. La denominación de plasmas fríos se debe a que la temperatura de los iones y de las especies neutras es en la mayoría de las ocasiones solo ligeramente superior a la ambiental. Sin embargo, la temperatura de los electrones es dos o más órdenes de magnitud mayor, siendo ésta la causa de que en este tipo de plasmas se produzcan reacciones entre especies que de otra manera sólo se producirían a temperaturas más elevadas $(10^3 - 10^4\ K)$ [90].

Las especies reactivas presentes en el plasma interactúan con las superficies que se hallan expuestas al mismo. Dichas interacciones tienen lugar por medio de bombardeo de especies cargadas (sputtering), de reacciones químicas o bien por mecanismos asistidos por iones, obedeciendo la importancia relativa de cada uno de estos fenómenos en gran medida a la configuración concreta y los parámetros operativos del plasma. En el proceso de bombardeo, el material de la superficie es arrancado por un proceso puramente físico, provocado por la ruptura de enlaces en la superficie debido al impacto de iones energéticos. Este proceso de bombardeo carece generalmente de selectividad, produciéndose el ataque en puntos aleatorios de la superficie (aquellos en los que impactan los iones). En los procesos químicos, los átomos de la superficie del material reaccionan con las especies presentes en el plasma de acuerdo con los procesos de la química elemental. Este tipo de ataque suele ser selectivo, ya que es sensible a diferencias en los enlaces y a la composición química de las superficies. Así, en el caso del ataque del grafito por plasmas de oxígeno, las reacciones de tipo químico se producen preferentemente en las zonas en las que existen defectos más que en las posiciones basales perfectas. En los procesos asistidos por iones, el ataque químico se ve acelerado por un flujo de iones energéticos incidente sobre la superficie.

Existen diferentes maneras de ionizar un gas para la generación de un plasma frío, de las que a continuación se presentan brevemente las tres más comunes. Los llamados de descarga luminiscente necesitan de bajas presiones, y en ellos el plasma se genera por la aplicación de un campo electromagnético (generalmente de microondas o de radiofrecuencias). Los ataques que se producen en este tipo de plasmas son por lo general bastante uniformes y reproducibles. Los plasmas de corona consisten en la aplicación de un alto voltaje de baja frecuencia entre dos electrodos. Este tipo de plasmas presenta la ventaja de que permite la operación a presión atmosférica. Por último, se puede generar un plasma frío mediante una descarga de barrera dieléctrica (DBD). Este método se diferencia de la descarga de corona en que al menos uno de los electrodos ha de estar recubierto por una superficie dieléctrica, por lo que es necesario que la frecuencia del voltaje aplicado sea alta (*25-50 kHz*). La principal ventaja de este método frente a la descarga de corona es que proporciona una mayor uniformidad en el tratamiento.

Debido a la gran reactividad de los materiales grafíticos frente al oxígeno, los plasmas en los que el gas precursor es el oxígeno resultan de gran importancia. En este tipo de plasmas, las colisiones inelásticas entre electrones y las moléculas de oxígeno provocan una continua creación de especies químicamente reactivas, destacando el oxígeno atómico (O), iones de oxígeno molecular (O_2^+), así como diferentes estados excitados de O_2 y O. Bajo determinadas condiciones, estas especies son capaces de enlazarse a los átomos de carbono de la red grafítica, para posteriormente desorberse como CO_2 y CO.

2.1.3 Plasma generado mediante microondas (MW)

En un reactor de plasma de microondas (MW), el plasma es generado y mantenido por campos electromagnéticos de alta frecuencia (en el rango de las microondas). Se emplea para ello un magnetrón mediante el cual se genera radiación electromagnética de alta frecuencia (típicamente 2.45 *GHz*) [91]. Esta radiación es introducida mediante una guía de ondas en la cámara donde se genera el plasma, construida de material aislante (generalmente cuarzo ó alúmina). Este tipo de plasma permite mantener unas condiciones más adecuadas para efectuar ataques químicos que otros en los que la frecuencia empleada es menor (p.ej. plasmas generados mediante radiofrecuencias), debido a la mayor cantidad de especies reactivas que se generan y a que la frecuencia tan elevada impide en muchos casos que se produzca bombardeo de especies cargadas. Las principales especies reactivas que se producen en un plasma de oxígeno generado mediante microondas son neutras, principalmente el oxígeno atómico.

2.1.4 Plasma de descarga de barrera dieléctrica (DBD)

El plasma de barrera dieléctrica (DBD) fue documentado por vez primera en 1857 por Werner von Siemens, en un intento por generar ozono [92]. En un plasma DBD el plasma se genera al aplicar una descarga eléctrica a un gas contenido entre dos electrodos, de los que al menos uno está aislado eléctricamente del gas por la presencia de un material dieléctrico. Desde un punto de vista industrial, el plasma DBD presenta ciertas ventajas sobre otros tipos de plasma, siendo la más notable la posibilidad de operar a temperatura y presión ambiente. Esto abarata enormemente los costes, dado que se puede prescindir de los medios para efectuar vacío, y acelera la velocidad de procesado. Existen varios tipos de geometrías en las que se pueden disponer los electrodos, siendo las más comunes (y que se emplearán en el presente trabajo) las que se conocen bajo la denominación de descargas en volumen o volumétricas. En este tipo de geometría, los dos electrodos se encuentran separados por un espacio (*gap*) relleno del gas precursor. Es en este *gap* donde se genera el plasma, el cual consiste en una serie de microdescargas eléctricas producidas entre los dos electrodos. Debido a la presencia de la barrera dieléctrica entre los electrodos, se hace necesario el empleo de voltajes alternos de alta frecuencia para conseguir la generación de las descargas, dado que el dieléctrico impide el paso de corriente continua. La corriente de desplazamiento que puede atravesar el dieléctrico está determinada tanto por el valor de la constante dieléctrica y grosor del material empleado como por la variación temporal del voltaje aplicado. Para que se produzca transporte de corriente distinta de la capacitiva entre los electrodos, el

campo eléctrico ha de ser lo suficientemente intenso como para producir la ionización del gas, momento en el que se inician las microdescargas. El papel que juega el dieléctrico en un plasma DBD es doble. Por un lado es el encargado de extinguir las microdescargas debido a la carga que se acumula en su superficie, la cual genera un campo eléctrico local opuesto al que existe globalmente entre los electrodos. De esta manera, la duración de las microdescargas es solo del orden de unos pocos *ns* [93]. Esta corta duración de las microdescargas evita un calentamiento excesivo del gas (en aire el calentamiento suele ser menor de 10 °C [92]), de manera que la mayor parte de la energía de los electrones se emplea para excitar los átomos y moléculas del gas. Por otro lado, el dieléctrico distribuye las microdescargas de una manera más o menos homogénea por toda su superficie, lográndose tratamientos más uniformes que los logrados en otros tipos de descargas, como pueden ser las de corona.

2.2 Tratamientos con ozono generado por radiación ultravioleta (UVO)

El ozono (O_3) es una forma alotrópica del oxígeno que decae rápidamente a oxígeno diatómico (o molecular), O_2. El ozono se emplea comúnmente en limpieza de todo tipo de superficies de una manera rápida y efectiva (p.ej. material quirúrgico). El ozono es capaz de reaccionar con la superficie de los materiales grafíticos incluso a temperatura ambiente, al contrario de lo que ocurre con el oxígeno molecular.

El ozono se genera de forma natural en las capas bajas de la estratosfera por la interacción de moléculas de oxígeno con la radiación ultravioleta procedente del Sol. Una de las formas más comunes de producir ozono de manera artificial es mediante la disociación de oxígeno molecular con radiación ultravioleta generada por lámparas de *Hg* [94]. Al ozono producido de esta manera se le suele conocer por el acrónimo UVO (Ultravioleta/Ozono). La lámpara de Hg emite típicamente radiación ultravioleta en la que las longitudes de onda predominantes son 184.9 y 253.7 *nm*. Cuando el oxígeno molecular resulta irradiado por fotones de 184.9 *nm*, la molécula se disocia, produciéndose oxígeno atómico, *[O]*, que rápidamente se recombina para formar ozono (ver *reacciones i y ii*). Por su parte, la longitud de onda de 253.7 *nm* disocia el ozono formando oxígeno atómico [95] (ver *reacción iii*). Estas especies reactivas son las que permiten la oxidación y modificación de materiales grafíticos.

i) $O_2 + h\upsilon_1(\lambda = 184.9\ nm) \longrightarrow [O]$

ii) $[O] + O_2 \longrightarrow O_3$

iii) $O_3 + h\upsilon_2(\lambda = 253.7\ nm) \longrightarrow [O]$

2.3 Tratamientos térmicos en aire/oxígeno

La oxidación de materiales carbonosos mediante tratamiento térmico en aire/oxígeno es ampliamente usada para modificar sus superficies con vistas a diferentes aplicaciones. Se ha estudiado

la oxidación de grafito [83,96,97] como material modelo, lo que ha permitido conocer los mecanismos básicos del ataque (ver apartado 1.2.4 de este capítulo). Este tipo de oxidación ha demostrado ser altamente selectivo. En los últimos años se ha estudiado la oxidación de distintos tipos de grafeno prístino [86,98,99], pero no existen estudios de oxidaciones de rGO.

2.4 Litografía STM

La litografía STM se basa en el uso de la microscopía de efecto túnel (STM) para modificar/oxidar localmente la superficie de materiales con precisión nanométrica. Si bien de la microscopía STM y de la litografía STM se hablará con más detalle en el próximo apartado, relativo a las microscopias de proximidad, se ha incluido aquí la segunda debido a su condición de método de oxidación.

3. Microscopías de campo cercano o de proximidad (SPM)

3.1 Generalidades

Bajo la denominación de microscopías de campo cercano o de proximidad (SPM, del inglés *Scanning Probe Microscopy*), se encuentran agrupadas un amplio conjunto de técnicas de análisis superficial a nivel microscópico. Surgieron en el año 1981 como respuesta a las limitaciones en resolución que presenta la microscopía óptica. El primer miembro de la familia fue el microscopio de efecto túnel (STM, *Scanning Tunneling Microscope*)[100]. El STM fue el primer instrumento capaz de generar imágenes en espacio real de una superficie con resolución atómica. Desde su nacimiento, la familia de técnicas SPM se ha visto gradualmente ampliada mediante el desarrollo de nuevas variantes, impulsadas sobre todo tras la invención en 1986 del microscopio de fuerza atómica (AFM, *Atomic Force Microscope*) [101]. El elemento común a este tipo de microscopías es una punta extremadamente afilada que rastrea la superficie de la muestra a una distancia muy pequeña de ésta. A tales distancias (entre unos pocos ångström y unas decenas de nanómetro [102]) se establecen diferentes interacciones entre punta y muestra, permitiendo realizar un mapeado de distintas propiedades de la muestra a lo largo de su superficie al ser ésta barrida por la punta. La naturaleza de la interacción producida es específica para cada una de las diferentes variantes.

Componentes y funcionamiento de los microscopios de proximidad

Los diferentes tipos de microscopios de proximidad poseen una serie de elementos comunes. Uno de los elementos esenciales es la presencia de una sonda en la que se encuentra la punta. La interacción se produce entre el extremo de la punta y la superficie de la muestra próxima a ella. Para lograr una alta resolución, se hace necesario que la punta sea lo más afilada posible, de modo que la interacción esté muy localizada. Por ello se trabaja con puntas cuyos radios de curvatura están en el rango del nanómetro. Otro componente clave es el elemento encargado del movimiento relativo entre punta y muestra, denominado escáner. Por lo general, el escáner está formado por un conjunto de

elementos piezocerámicos cuya geometría proporciona un movimiento relativo entre punta y muestra en las tres direcciones espaciales mediante la aplicación de voltajes eléctricos. Este sistema permite el registro de la interacción punta-muestra punto a punto, una de las claves de la elevada resolución de estas microscopías. Para lograr resolución atómica, el escáner ha de ser extremadamente preciso en su movimiento (~1 *pm*). Debido a la pequeña separación entre punta y muestra a la que resulta necesario operar, se hace imprescindible el empleo de un sistema mecanizado capaz de acercar la punta a la muestra a distancias que puedan ser controladas por el escáner. A partir de ese momento, el escáner ya es capaz de ajustar por sí mismo la separación de acuerdo con los valores de operación previamente establecidos por el usuario para algún tipo de señal, conocida como *feedback* o realimentación (p.ej. la intensidad de la corriente túnel en STM o la deflexión del cantilever en AFM de contacto). El sistema de *feedback* es el encargado de comparar el valor instantáneo de la señal con el valor preestablecido por el usuario (conocido como *setpoint*) y modular la posición vertical del escáner para que la señal que se mide coincida con el valor preestablecido. Una vez que la punta se encuentra interaccionando con la muestra y se activa el sistema de realimentación, el escáner se encarga de rastrear la superficie de la muestra en un proceso conocido como barrido. Las variaciones verticales del escáner producidas durante el barrido para mantener la señal de medida en el valor preestablecido se usan para generar una imagen tridimensional de la superficie de la muestra, que en un principio representa su topografía. Cuando el sistema de *feedback* se encuentra activado, el microscopio trabaja en el modo conocido como señal constante, mientras que si se desactiva se entra en el modo de altura constante. En este segundo modo el escáner no se extiende/retrae verticalmente, por lo que la imagen se forma con las variaciones en la señal de interacción. Aunque en el modo de altura constante la adquisición de imágenes resulta más rápida (debido a que el escáner no se mueve verticalmente), solo puede ser utilizado en el estudio de superficies muy planas o en pequeñas áreas, para evitar la colisión entre la punta y la muestra. Debido a la alta resolución a la que se puede llegar a operar, se hace necesario algún procedimiento que permita aislar al sistema de vibraciones ambientales. Por lo general se opta por un diseño compacto y rígido del microscopio (encargado de filtrar las vibraciones de baja frecuencia), el cual a su vez se coloca sobre plataformas adecuadas (que filtran altas frecuencias). Por último, se requiere un sistema de adquisición y procesado de los datos.

Tipos de imágenes

En general, cada par de coordenadas (x, y) de una imagen SPM representa una posición sobre la superficie de la muestra. En el tipo más común de imágenes SPM, se pretende representar de manera más o menos fidedigna la topografía de la muestra. Para ello, la altura relativa de la muestra en cada punto (x, y) viene dada por el desplazamiento vertical del escáner necesario para mantener constante la señal de realimentación, conformando la coordenada z que se representa en la imagen. Estas imágenes se suelen denominar topográficas o de altura. Sin embargo, para que el desplazamiento vertical del escáner se corresponda con variaciones topográficas reales de la muestra, se ha de verificar

que ésta no se deforme por la interacción con la punta, y que la intensidad de la señal de realimentación solo dependa de la distancia entre punta y muestra. Esto no se cumple en todos los casos (p.ej. en STM la intensidad de la corriente túnel depende no solo de esta distancia, sino también de la densidad local de estados de la muestra), lo cual dificulta enormemente la interpretación de las imágenes de altura. Por otro lado, existe un tipo de imágenes en SPM en las que la tercera dimensión no representa una altura, sino el valor relativo de algún tipo de magnitud, y que no guarda necesariamente una correlación con la topografía. Un ejemplo lo constituyen las imágenes de fricción obtenidas en AFM en modo contacto, o las de fase en AFM tapping.

Influencia de la punta

La microscopía SPM se encuentra con una serie de dificultades durante el proceso de formación de imágenes que dan lugar a la formación de artefactos. Éstos son rasgos que aparecen en las imágenes pero que no se corresponden con la presencia de ningún tipo de atributo en la superficie de la muestra, sino que surgen debido al funcionamiento intrínseco de este tipo de microscopías. Los artefactos generalmente se encuentran en su mayor parte ligados a la morfología de la punta, al funcionamiento del escáner y en ocasiones al software de procesado. Los más importantes son los causados por el tamaño finito de la punta, que provoca no solo una disminución en la resolución sino también problemas de convolución entre la morfología de la muestra y de la propia punta. El caso extremo se presenta en aquellas situaciones en las que los rasgos de la muestra son significativamente más afilados que la propia punta, de modo que la imagen refleja en realidad la morfología de esta última (*figura 6*). El radio finito de la punta da también lugar a una disminución en el poder de resolución, lo que dificulta la estimación de tamaños laterales de diferentes estructuras en las superficies de las muestras (trincheras, pequeñas partículas, etc.). Otro problema que puede producirse y que se encuentra también relacionado con la punta es la existencia de "múltiples puntas". Esto suele ocurrir en puntas romas en las que no hay una única protuberancia que se encuentre significativamente más cerca de la muestra que el resto de la superficie de la punta. En estos casos, todas estas protuberancias actúan como punta de manera sucesiva en la formación de las

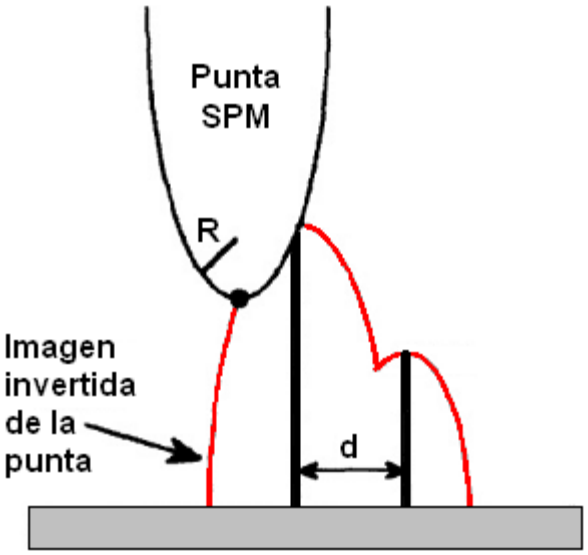

Figura 6 – Representación esquemática de los artefactos introducidos debido al radio finito R de la punta. Debido al efecto de convolución, la punta no es capaz de formar una imagen de los dos picos, sino que la imagen formada (rojo) refleja la morfología de la propia punta. El poder de resolución también se ve afectado negativamente. Adaptada con permiso de *Bustamante C. et al., Curr. Opin. Struct. Biol. 7, 709-716 (1997)*. Copyright Elsevier 1997.

imágenes, dando lugar a una repetición de manera artificial de algunos de los rasgos que hay en la superficie de la muestra en patrones fácilmente reconocibles. Por todo ello, conviene extremar las precauciones a la hora de interpretar y extraer datos de las imágenes SPM.

3.2 Tipos de microscopía SPM

3.2.1 Microscopía de efecto túnel

El efecto túnel es un fenómeno cuántico que permite a una partícula atravesar una barrera de potencial de energía mayor que la de la propia partícula, algo prohibido en mecánica clásica. En STM se hace uso de este efecto, ya que la señal que se mide es precisamente una corriente túnel. En este caso la sonda consiste en una punta metálica extremadamente afilada, generalmente de tungsteno (*W*) o de una aleación de *Pt/Ir* [103]. Punta y muestra se posicionan a una distancia inferior a 1 *nm*, a la vez que se establece una diferencia de potencial, V_b, generalmente entre unos pocos *mV* y unos pocos *V*. Esto hace que los electrones fluyan entre punta y muestra, atravesando mediante efecto túnel la barrera de energía potencial existente entre ambas. Para que esta corriente pueda fluir, la muestra ha de ser conductora, limitando el uso del STM a materiales metálicos o semiconductores (o a filmes atómicamente delgados de materiales aislantes [104]). La intensidad de la corriente túnel normalmente se halla entre unos pocos *nA* (para muestras bien conductoras) y unos pocos *pA* en el caso de muestras poco conductoras.

La dependencia de la corriente túnel con la distancia de separación entre punta y muestra puede ser calculada empleando la aproximación WKB (Wentzel–Kramers–Brillouin) para una barrera de potencial cuadrada de altura φ. La probabilidad de transmisión túnel para un electrón con energía E viene dada por el coeficiente de transmisión $|M|^2$, y según la aproximación WKB toma la forma:

$$|M|^2 \propto \exp\left(-2\int_0^s dx \sqrt{\frac{2m(\varphi-E)}{\hbar^2}}\right) = e^{-\frac{2s}{s_0}},$$

donde $s_0 = \sqrt{\frac{\hbar^2}{2m(\varphi-E)}}$, m es la masa del electrón y *s* es la distancia de separación entre punta-muestra.

El decaimiento exponencial de la corriente túnel con la distancia entre punta y muestra, garantiza que la mayor parte de la corriente túnel fluya a través de un único átomo de la punta, el cual se encuentra ligeramente más cercano a la muestra que el resto. De este modo, al emplear la corriente túnel como señal de realimentación se consigue una elevada resolución espacial tanto lateral (~ 0.1 Å) como vertical (~ 0.01 Å), permitiendo la visualización rutinaria de estructuras a nivel atómico [105].

Sin embargo, no solo la separación entre punta y muestra determina la magnitud de la corriente túnel, sino también la estructura electrónica de ambas. En una primera aproximación, se puede demostrar que la intensidad de la corriente túnel es proporcional a la densidad electrónica parcial local de la muestra, es decir, $I \propto \rho(r_0, E_F)$ [106]. Así, la variación espacial de $\rho(r_0, E_F)$ induce una

variación en la corriente túnel en STM. La densidad parcial representa los estados electrónicos de la muestra en la vecindad del nivel de Fermi (E_F), en un rango de energías determinado tanto por la magnitud como por la polaridad del voltaje, V_b. Esta densidad parcial, en contraposición a la densidad electrónica total, no representa necesariamente la topografía de la muestra. De este modo, las imágenes obtenidas son en general una combinación de efectos tanto topográficos como electrónicos. Esto resulta determinante en imágenes a escala atómica, aunque en imágenes de baja resolución se pueda considerar que la imagen obtenida representa de forma bastante precisa la topografía de la muestra. Por norma general, la punta se encuentra permanentemente conectada a tierra, por lo que el voltaje representa el potencial de la muestra respecto a tierra. De este modo, si V_b>0, los electrones fluirán desde la punta hacia los estados desocupados de más baja energía de la muestra (*Figura 7a*), siendo la imagen producida una representación de la distribución espacial de los mismos. En el caso de que sea V_b<0, los electrones fluirán hacia la punta desde los estados ocupados de más alta energía en la muestra (*Figura 7b*), que serán los que se vean representados en la imagen [107]. Aunque esta diferencia no presenta problemas en metales, por lo general en los materiales semiconductores existe una asimetría entre la parte superior de la banda de valencia y la inferior de la banda de conducción, de modo que las imágenes STM de semiconductores serán altamente dependientes de la polaridad del voltaje [108].

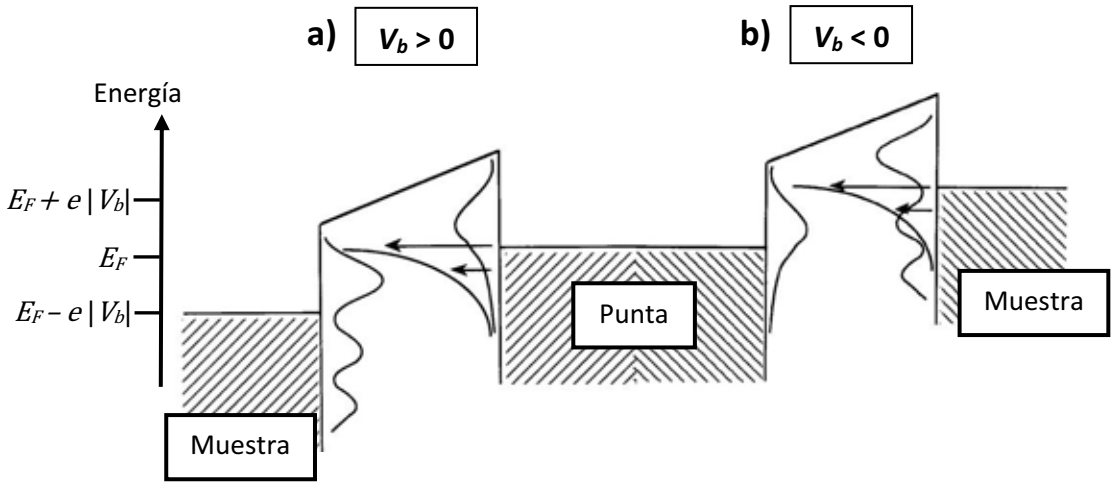

Figura 7 – Transferencia electrónica en microscopía de efecto túnel. (a) Cuando el voltaje de la muestra respecto a la punta es positivo (V_b > 0), los electrones fluyen desde los estados ocupados de la punta hacia los estados desocupados de la superficie de la muestra. (b) Al invertir la polaridad del voltaje (V_b < 0), el flujo de electrones se produce desde los estados ocupados de la superficie de la muestra hacia los estados desocupados de la punta.

Debido a que la imagen final obtenida mediante STM resulta de una combinación de efectos tanto topográficos como electrónicos, la interpretación de las imágenes se ve enormemente dificultada. Por lo general, se requiere de estudios adicionales (p.ej. simulaciones teóricas) para esclarecer el origen de los rasgos observados en las imágenes. Un ejemplo lo constituyen las vacantes atómicas en superficies grafíticas, que se visualizan como protuberancias mediante STM, a pesar de que

topográficamente sean esencialmente planas. Ello es debido a un aumento en la densidad local de estados electrónicos cerca del nivel de Fermi en los átomos que rodean dicha vacante. Resulta también interesante la influencia de los efectos electrónicos en el caso de las imágenes a escala atómica del plano basal del grafito prístinp. En éstas, a diferencia de la red hexagonal que cabría esperar en un principio (ver *figura 8a*), la interacción entre las capas provoca variaciones en la densidad local de estados electrónicos que en última instancia hacen que sólo resulten visibles la mitad de los átomos de la red (aquellos que no poseen un vecino inmediato en la capa inferior, ver *figura 8b-c*).

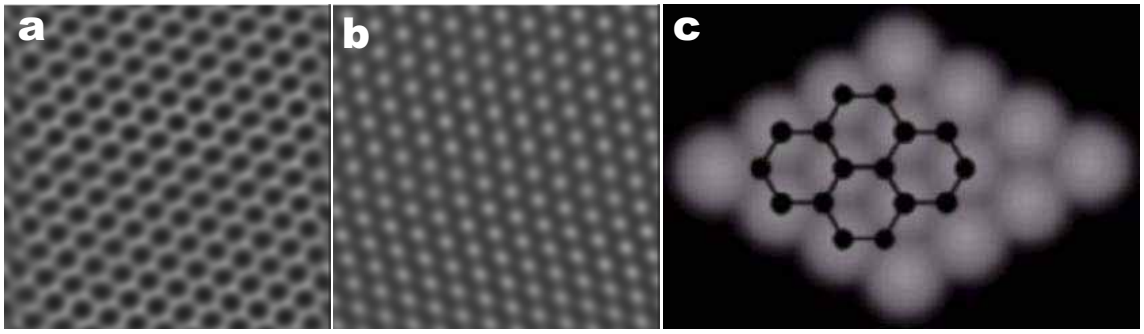

Figura 8 – Imágenes STM de grafito: a) esperada (red hexagonal, con los átomos de *C* en los vértices de los hexágonos); b) real (red triangular). c) Recreación: sólo se visualizan los átomos de *C* en posiciones β (sin vecinos en los planos adyacentes). (Tamaños de imágenes a y b: 3 nm x 3 nm)

3.2.2 Microscopía de fuerza atómica

A pesar de todas las ventajas que presenta y de su gran resolución, la microscopía STM tiene el inconveniente de que solo permite el estudio de materiales metálicos o semiconductores, puesto que en materiales no conductores resulta imposible mantener una corriente túnel. Para salvar las limitaciones inherentes a la técnica STM, se desarrolló la microscopía de fuerza atómica (AFM) [101], que se basa en la detección de las fuerzas de interacción que existen entre átomos y moléculas. Estas fuerzas, que pueden ser tanto de largo como de corto alcance, así como atractivas o repulsivas, existen en todos los materiales, por lo que el AFM es en principio aplicable a cualquier tipo de material. Además, mediante una elección adecuada del tipo de interacción que se mide, es posible trazar mapas superficiales de un gran número de propiedades, como por ejemplo fricción, adhesión, campos magnéticos (MFM), campos eléctricos (EFM) y conductividad (CAFM). Todo ello, unido a la posibilidad de operar en ambientes variados (ultra-alto vacío, aire, líquido) [109], dota al AFM de una gran flexibilidad, y permite su uso en diferentes disciplinas. Uno de los inconvenientes que presenta el AFM es que la resolución que se alcanza operando en condiciones normales ($\sim 1-2\,nm$ de resolución lateral) es bastante menor que la que se obtiene con STM. Esto es debido que la señal en AFM decae más lentamente con la distancia (ley de potencia) en comparación con el decaimiento en STM (exponencial). De este modo, mientras que en STM solo el ápice de la punta contribuye a la formación de la imagen, el área de interacción en AFM es considerablemente mayor [110]. A esto se une el mayor radio de curvatura que presentan en general las puntas empleadas en las distintas variantes de AFM.

Por otro lado, en las interacciones que se miden en AFM entra en juego la densidad electrónica total, de modo que las imágenes obtenidas en AFM representan la topografía de la muestra de un modo bastante más fiel que en el caso del STM.

Modos de operación en AFM

Para poder cuantificar y controlar la magnitud de las fuerzas de interacción que se establecen entre muestra y punta, esta última se coloca en el extremo de una palanca flexible, denominada cantilever. Las fuerzas generadas sobre la punta modifican el comportamiento del cantilever, lo que se traduce en variaciones en la deflexión, amplitud de oscilación, etc. del mismo. Existen varios métodos para detectar los cambios inducidos sobre el cantilever. En la variante más extendida, se hace incidir sobre el mismo un haz láser, cuyo reflejo llega hasta un detector fotoeléctrico segmentado. Los cambios en el voltaje producidos en éste permiten conocer en todo momento la magnitud de la deflexión del cantilever. La naturaleza e intensidad de las fuerzas ejercidas depende en gran medida de la separación entre punta y muestra, , pudiendo ser modelizadas empleando un potencial de tipo Lennard Jones (ver *figura 9*): – – . Este potencial, que describe la interacción entre pares de átomos o moléculas neutras, posee un primer término repulsivo que domina la interacción a distancias cortas y que es debido al principio de exclusión de Pauli. El segundo término de la interacción, que es atractivo y de largo alcance, surge de la fuerza de van der Waals. De este modo, la fuerza neta sobre el cantilever será atractiva cuando la separación entre punta y muestra sea relativamente grande y repulsiva para separaciones pequeñas.

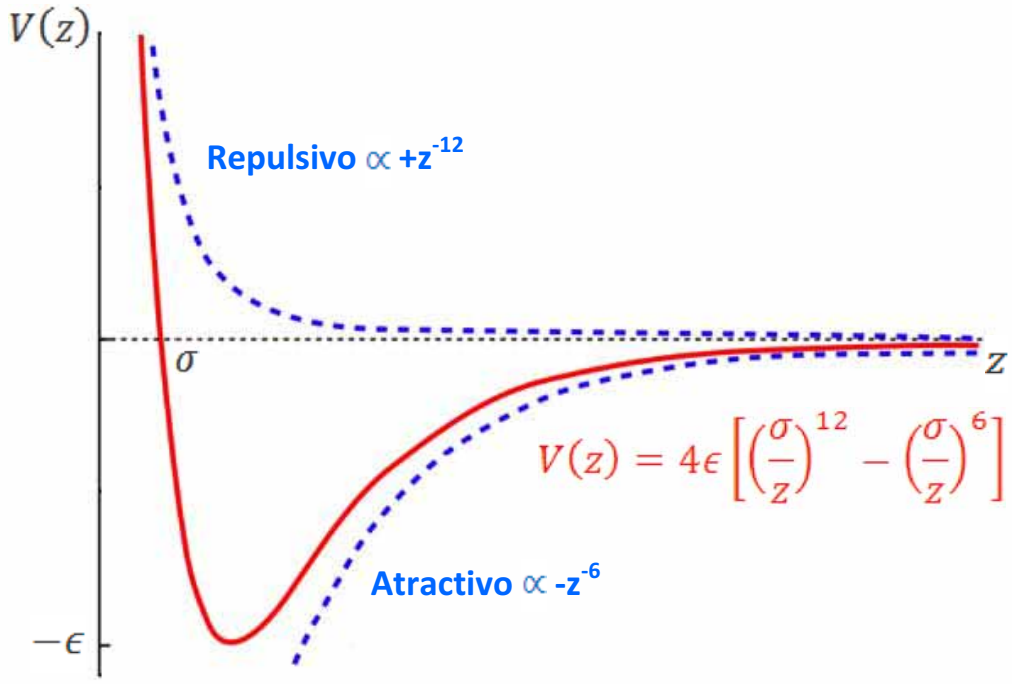

Figura 9 – Potencial de Lennard-Jones. Permite expresar las fuerzas intermoleculares entre punta y muestra en función de la separación entre ambas.

Teniendo en cuenta la dinámica del cantilever y el tipo de interacción que se establece entre punta y muestra, existen diferentes modos de operación del AFM, que se describen a continuación.

a) Modo estático (DC). AFM de contacto y microscopía de fuerza lateral (LFM)

En el modo estático, más comúnmente conocido como modo de contacto, el extremo de la punta se encuentra permanentemente en contacto físico (repulsión estérica) con la superficie de la muestra. Las fuerzas de interacción existentes entre ambas dan lugar a una deflexión vertical en el cantilever, cuya magnitud, regida por la ley de elasticidad de Hooke, depende tanto de la magnitud de la fuerza experimentada por la punta como de la constante de fuerza del cantilever [111]. Dependiendo de que se trabaje en el modo atractivo o repulsivo, la deflexión producida será negativa o positiva, respectivamente. Al desplazarse sobre la superficie de la muestra, los accidentes topográficos de la misma producen variaciones de esta deflexión. Generalmente, en AFM contacto se mantiene constante la fuerza de interacción punta-muestra durante la formación de la imagen, por lo cual se emplea la deflexión del cantilever como señal de feedback. De este modo, los ajustes de la posición vertical del escáner durante el barrido para mantener constante el valor de la deflexión darán lugar a la imagen topográfica de la superficie.

El hecho de que la punta se encuentre en permanente contacto con la muestra, unido al gran radio de curvatura de la primera, hace que el área de interacción entre ambas sea bastante elevada. Ello disminuye la resolución en el modo contacto e impide obtener resolución atómica verdadera (es decir, la visualización de rasgos individuales a escala atómica) [112]. Además, el contacto permanente entre punta y muestra convierte a esta variante del AFM en un método muy invasivo, haciendo que muestras delicadas resulten fácilmente dañadas y/o arrastradas por la punta. Dado que la deflexión del cantilever ha de ser significativamente mayor que las deformaciones producidas en la punta y la muestra, existen restricciones en el valor de la constante elástica, k, del cantilever en el modo AFM de contacto. Los valores de k oscilan por lo general entre $0.01 - 5\ N/m$ (las constantes de fuerza interatómicas/intermoleculares en sólidos se encuentran entre $10 - 100\ N/m$, llegando a ser tan pequeñas como $0.01\ N/m$ en muestras biológicas).

La microscopía de fuerza lateral (LFM, *Lateral Force Microscopy*) es una variante del modo AFM de contacto que identifica y traza diferencias en las fuerzas de fricción entre la punta y la superficie de la muestra, en base a la medida de la torsión lateral del cantilever. Las imágenes de fricción proporcionan información adicional de la muestra estudiada, pudiéndose observar heterogeneidades en la superficie originadas por diferencias de materiales, del grado de oxidación y/o funcionalización o cambios en la hidrofilicidad, y que no se manifiestan necesariamente en las imágenes de topografía.

b) Modos dinámicos (AC)

Para evitar los efectos invasivos del AFM de contacto surgieron los modos dinámicos, en los que no existe un contacto continuo entre punta y muestra. Esto se consigue acoplando el cantilever a un oscilador piezoeléctrico que se encuentra eléctricamente excitado a una frecuencia ligeramente menor (aunque en ocasiones puede ser mayor) que la frecuencia de resonancia libre del cantilever (frecuencia de resonancia cuando la punta no está interaccionando con la muestra), que por lo general se encuentra típicamente en el rango $10 - 500\,KHz$. La interacción de la punta con la muestra modifica las características de oscilación del cantilever (amplitud, fase y frecuencia de resonancia), que pueden ser empleadas para la formación de imágenes que proporcionan información sobre diversas propiedades de la muestra. Otra ventaja sobre el modo AFM de contacto estriba en el hecho de que el ruido en la medida de la deflexión del cantilever posee una componente que varía inversamente con la frecuencia, por lo que los modos dinámicos están menos sujetos al ruido que los modos cuasiestáticos, proporcionando por lo general una mayor resolución [113].

Existen dos métodos de operación diferenciados en el modo dinámico, caracterizados por la señal de realimentación que se emplea en cada uno de ellos. En el modo de modulación de amplitud (AM-AFM), también conocido como modo de contacto intermitente o *tapping*, se emplea la amplitud de la oscilación del cantilever como señal de realimentación. El modo de modulación de frecuencia (FM-AFM), o de no-contacto (NC-AFM), emplea la frecuencia de oscilación como señal de realimentación.

*b.1) AFM de contacto intermitente (*tapping*)*

En el modo *tapping*, se hace oscilar un cantilever rígido a una frecuencia cercana a su frecuencia natural de resonancia $(50 - 500\,KHz)$ y con una elevada amplitud $(100 - 200\,nm)$. Esta amplitud es mayor que la separación en el equilibrio entre punta y muestra, de modo que solo existe contacto entre ambas en el punto más bajo del recorrido oscilatorio. Con esto se consigue eliminar las fuerzas laterales, lo que redunda en un aumento de la resolución, así como minimizar las verticales, lo que reduce el daño sobre la muestra. Al ser un modo poco invasivo, se hace posible estudiar pequeños objetos levemente adheridos a sustratos (p.ej. moléculas o pequeñas partículas), algo que resulta tremendamente difícil en AFM de contacto. Por otro lado, las grandes amplitudes que se emplean en *tapping* evitan que la punta se quede adherida a la superficie de la muestra como ocurre en AFM de contacto [113].

La amplitud de oscilación del cantilever disminuye cuando la punta interacciona con la muestra, lo que provoca una pérdida de energía en el cantilever. Por lo general, en *tapping* se trabaja manteniendo la amplitud de oscilación del cantilever en un valor constante (menor que la amplitud libre). Durante el movimiento oscilatorio que describe el cantilever, la punta atraviesa regiones sometidas a fuerzas atractivas de largo alcance y otras sometidas a fuerzas repulsivas de corto alcance. El régimen de trabajo será atractivo o repulsivo dependiendo de la fuerza neta que actúa sobre la punta

en una oscilación completa [114]. Cuando las muestras son muy frágiles, se suele trabajar con amplitudes que sean tan próximas como sea posible a la amplitud que tendría el cantilever en el caso de una oscilación libre (es decir, con la punta alejada de la muestra). Con esto se consigue trabajar en el régimen atractivo, minimizando la fuerza de interacción entre punta y muestra.

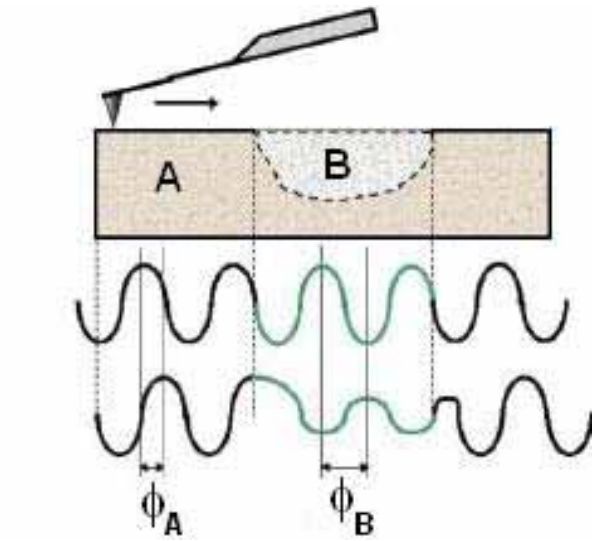

Figura 10 – Variaciones en el desfase entre la señal que hace oscilar al cantilever (curva superior) y la oscilación real del mismo (curva inferior) originadas por heterogeneidades locales en las características de la muestra.

La interacción punta-muestra provoca por lo general un desfase entre la señal periódica que alimenta al cantilever y la oscilación real de éste. Este desfase depende en gran medida de ciertas propiedades de la muestra, de modo que en superficies heterogéneas, bien porque estén compuestas de diferentes materiales o porque alguna de sus características varíe localmente, el contraste de las imágenes de fase refleja dicha heterogeneidad (*figura 10*). Así, las imágenes de fase permiten detectar, por lo general de manera cualitativa, variaciones en la composición química, adhesión, u otras propiedades de superficie de la muestra que no se manifiestan necesariamente en imágenes topográficas [114]. La detección de cambios en la fase es un elemento esencial en determinadas variantes del SPM, por ejemplo, en microscopía de fuerza magnética (MFM, *Magnetic Force Microscopy*) y de fuerza electrostática (EFM, *Electrostatic Force Microscopy*).

b.2) AFM de no contacto (FM-AFM/NC-AFM)

El modo FM-AFM/NC-AFM fue desarrollado con el objetivo de mejorar la sensibilidad del AFM *tapping* cuando se opera en vacío [115], hasta el punto de que permite alcanzar resolución atómica verdadera de manera rutinaria [116]. La denominación *"no contacto"* se debe a que la distancia entre punta y muestra es lo suficientemente elevada como para que solo se establezcan fuerzas atractivas. En este modo, se miden los cambios en la frecuencia de oscilación del cantilever, Δf, inducidos por la interacción punta-muestra que se requieren para mantener la amplitud de oscilación constante en todo momento. El valor de Δf se utiliza como señal de realimentación para la formación de imágenes topográficas. La amplitud típica de operación en este modo varía entre $0.25 - 40\, nm$ [117], valores considerablemente menores que los empleados en el modo *tapping*.

3.3 Espectroscopías SPM

Como ya se ha comentado, las diferentes técnicas SPM se basan en la detección de una señal derivada de una interacción extremadamente localizada entre la muestra y una punta afilada. Ello permite estudiar la interacción entre punta y muestra en puntos específicos de esta última, lo que se conoce con el nombre de espectroscopía SPM. Aunque existen diferentes variantes, aquí nos centraremos en las dos más comunes.

Espectroscopía de efecto túnel ó STS (Scanning Tunneling Spectroscopy)

La espectroscopía de efecto túnel (STS) permite obtener la información sobre la estructura electrónica de una superficie a partir de la dependencia de la corriente túnel con el voltaje aplicado. Habitualmente, se hace variar el voltaje mientras se mide la corriente túnel, obteniéndose curvas $I-V$, así como la conductancia frente al voltaje, $dI/dV-V$. Estas curvas proporcionan información sobre distintas propiedades electrónicas de la muestra, como el gap o la densidad de estados, con una gran resolución espacial.

Espectroscopía de fuerza (espectroscopía AFM)

La espectroscopía de fuerza utiliza el AFM para medir la magnitud de la interacción entre punta y muestra en función de la separación entre ambas, en lo que se conoce como curva de fuerza. Esta técnica permite detectar fuerzas en el rango de los *pN* (p.ej. enlaces atómicos o interacciones entre moléculas).

3.4 Nanomanipulación/nanofabricación mediante SPM

Un aspecto atractivo de las microscopías SPM es su capacidad para operar como una herramienta a nivel nanométrico/atómico [118], lo que resulta esencial en el campo de la nanotecnología. La nanomanipulación mediante SPM permite desde el posicionamiento controlado de átomos y moléculas individuales [119-121] hasta la alteración tanto física como química de una superficie a escala nanométrica [118,122]. Una ventaja de emplear SPM para realizar nanomanipulaciones es que el propio microscopio permite caracterizar posteriormente in situ el resultado a resolución atómica o nanométrica.

Litografía SPM ó SPL (Scanning Probe Lithography)

Entre las técnicas de manipulación mediante SPM destacan diferentes tipos de litografía, en los que se emplea la punta para "dibujar" sobre una superficie. Ello comporta una modificación de la propia superficie, bien física (mediante extracción o deposición de material) o química (p.ej. oxidación). Mediante programación previa del microscopio, es posible diseñar los patrones que se generan con precisión nanométrica. Un tipo de litografía que funciona bien con materiales carbonosos es la oxidación local anódica, mediante la que es posible oxidar localmente un material mediante la aplicación de una diferencia de potencial entre la punta y la muestra en atmósfera húmeda. Para ello se emplea un

microscopio STM (o AFM) en el que la punta actúa como cátodo mientras que el menisco de agua presente entre ésta y la superficie de la muestra actúa como electrolito. Se produce así una reacción entre los átomos de carbono y las moléculas de agua, que finalmente da lugar a la desorción de carbono en forma de *CO* y CO_2 [123]. Para que esta reacción electroquímica se produzca, se necesita trabajar con voltajes más elevados que los que se emplean habitualmente en STM ($\sim 1.4 - 3.0\,V$ dependiendo del material). A su vez, la corriente túnel también se incrementa para mantener la punta cerca de la superficie. Debido a la necesidad de trabajar en presencia del citado menisco, esta técnica es extremadamente sensible a las condiciones de humedad. Otro factor determinante en este tipo de procesos es la velocidad de la punta, facilitándose la oxidación a baja velocidad.

4. Espectroscopía Raman

En términos generales, el efecto Raman consiste en la dispersión inelástica de un fotón provocada por su interacción con la materia. Cuando se hace incidir radiación monocromática de frecuencia ν_0 sobre un material cualquiera, los fotones incidentes absorbidos excitan las moléculas del material llevándolas hasta un estado excitado virtual. Cuando el estado virtual decae, los fotones emitidos poseen en su mayoría la misma energía que la de los fotones absorbidos. Esto es lo que se conoce como dispersión elástica o de Rayleigh, y es la que se emplea, por ejemplo, en la obtención de los difractogramas de rayos X. Sin embargo una pequeña fracción de los fotones emitidos sufre un cambio de energía tras la dispersión (alrededor de uno de cada 10^6-10^8 fotones incidentes [124]), lo que se conoce como dispersión inelástica, emergiendo con una frecuencia ν_R distinta de la de los fotones incidentes (ν_0). Esto es lo que se conoce como efecto Raman en honor a su descubridor, el físico indio Sir C.V. Raman [125]. Existen dos tipos de dispersión Raman: en la conocida como dispersión Stokes, los fotones dispersados poseen una energía menor que la de los incidentes $\nu_R < \nu_0$, es decir, el material conserva parte de la energía del fotón incidente y acaba en un estado de mayor energía que el inicial. El caso en el que los fotones dispersados poseen una energía mayor ($\nu_R > \nu_0$), se conoce como dispersión anti-Stokes y se corresponde con una pérdida de energía del material. En ambos tipos de dispersión Raman, la energía de los fotones emergentes no es arbitraria, sino que ha de satisfacer la relación $\nu_R = \nu_0 \pm \nu_i$, siendo ν_i la frecuencia de alguno de los modos vibracionales o rotacionales del material con el que interacciona el fotón. En general, la dispersión Stokes prevalece sobre la anti-Stokes, debido a que en condiciones normales de temperatura la mayoría de las moléculas se encuentran en su estado fundamental. Aunque la diferencia entre las frecuencias inicial y final ha de corresponderse con la frecuencia ν_i de alguno de los modos normales de vibración del material dispersor, no todos los modos normales son activos en Raman debido a la existencia de una serie de reglas de selección impuestas por la mecánica cuántica. De esta manera, solo los modos de vibración que producen un cambio en la polarizabilidad son activos en Raman.

En esta espectroscopía se aprovecha el efecto Raman para inferir diferentes propiedades de un material, tanto químicas (como puede ser la presencia de diferentes compuestos químicos), como estructurales (por ejemplo, el grado de desorden cristalino en un material grafítico). Proporciona información de primera mano de las interacciones electrón-fonón, lo cual la hace ser muy sensible a la estructura cristalográfica y electrónica de la muestra. Aunque en principio es una técnica de caracterización no destructiva, en ocasiones la gran intensidad de la luz que se emplea (necesaria por el bajo porcentaje de dispersiones inelásticas) puede suponer un problema con algunos tipos de muestras. La profundidad del análisis se extiende solo unos pocos nanómetros, por lo que se la considera como una técnica de caracterización superficial. En un espectro Raman ordinario se representa la intensidad de fotones dispersados por la muestra en función del cambio en la frecuencia que han experimentado (normalmente se emplea el número de onda $\bar{\nu}$, en unidades de cm^{-1}). En general, en estos espectros se representa tan solo la parte correspondiente a las dispersiones Stokes, debido al hecho de que el espectro Raman es simétrico respecto a la banda de Rayleigh (aparecen las mismas bandas en la zona anti-Stokes que en la Stokes) y a la mayor prevalencia de las dispersiones Stokes frente a las anti-Stokes.

La espectroscopía Raman ha sido empleada con éxito en la investigación estructural de una gran cantidad de materiales carbonosos desde la década de 1970 [126], jugando un papel muy importante en la caracterización estructural e identificación de estos sólidos. Los espectros de los distintos materiales grafíticos muestran una serie de bandas características en el rango de 800 – 2000 cm^{-1}, conocido como espectro de primer orden. En el caso del grafito perfecto, el espectro Raman de primer orden sólo incluye una banda muy estrecha e intensa localizada en torno a 1580 cm^{-1}. A esta banda se la denomina banda *G* por su relación con el orden grafítico, y es debida al movimiento relativo de pares de átomos de carbono unidos mediante enlaces sp^2 a lo largo de la dirección del enlace [127], con lo que en realidad su existencia no requiere la presencia de anillos aromáticos, sólo la presencia de enlaces sp^2. A medida que el grafito va perdiendo su orden estructural (por ejemplo, por la introducción de defectos puntuales), comienzan a aparecer nuevas bandas en el espectro de primer orden debido a la relajación de las reglas de selección que estas imperfecciones provocan. En materiales que no se alejan excesivamente del grafito ideal (p.ej., grafito policristalino o con una pequeña densidad de defectos superficiales), la banda más apreciable en el espectro de primer orden, aparte de la *G*, es una banda localizada en torno a 1360 cm^{-1}, denominada *D*. Además, aparece una pequeña banda en torno a 1620 cm^{-1} [128], denominada banda *D'*, y que por lo general se presenta como un hombro en la vertiente de altas energías de la banda *G*. El origen de la banda *D* se atribuye normalmente a los movimientos radiales (conocidos como *radial breathing modes*) de los átomos de carbono en los anillos aromáticos [127], aunque la naturaleza exacta de esta banda es aún motivo de debate [129]. Las posiciones, anchuras e intensidades relativas de estas bandas, y más en particular de las bandas *D* y *G*, permiten identificar diferentes características del material en cuestión. Uno de los parámetros más empleados en muestras que se alejan relativamente poco del orden grafítico es la intensidad relativa de la banda *D*

respecto a la *G* (I_D/I_G), expresada como el cociente entre sus áreas. Esta intensidad crece con el desorden estructural en la red grafítica, sirviendo así como indicador del grado de desorden en materiales grafíticos [130] (ver *figura 11*). Sin embargo, llega un punto en el que el cociente I_D/I_G disminuye al seguir aumentando el desorden debido a la desaparición de los anillos aromáticos, lo que conlleva la disminución de la intensidad de la banda *D* [129] (nótese de nuevo que la presencia de la banda *G* no requiere de la existencia de dichos anillos). En el espectro de segundo orden (2300 – 3300 cm^{-1}), aparecen los sobretonos de las bandas del espectro de primer orden. El rasgo más característico en esta zona es una banda en torno a ~2700 cm^{-1}, llamada *2D* por ser el sobretono de la banda D [131]. Aunque las reglas de selección Raman prohíben la presencia de la banda *D* en materiales perfectamente grafíticos, la banda *2D* siempre se halla presente en los materiales reales. También se aprecia en la posición ~3250 cm^{-1} la banda *2D'*, el sobretono de la banda *D'* [129]. A medida que el grafito se aleja de su estructura ideal, las bandas de segundo orden comienzan a ensancharse y a perder intensidad, superponiéndose unas con otras hasta que resulta imposible su identificación individual (ver evolución en *figura 11*). Los espectros Raman de grafeno prístino presentan algunas diferencias respecto a los del grafito, siendo la más destacable la presencia de una banda *2D* muy intensa y estrecha. El estudio de esta banda permite la discriminación entre grafeno de una, dos, varias capas y grafito [131,132]. En láminas de grafeno provenientes de tratamientos químicos, la interpretación de los espectros Raman se complica. Aún así, su estudio aporta cierta información sobre la estructura de las láminas.

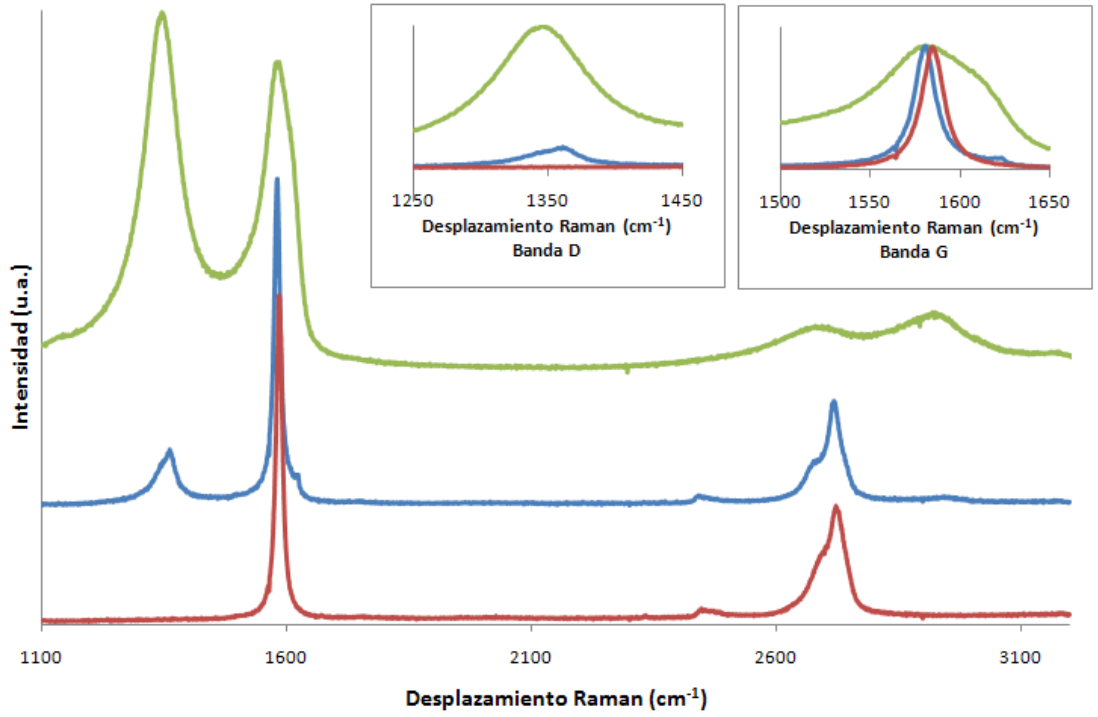

Figura 11 – Espectros Raman de grafito (rojo), grafito tratado en plasma DBD (azul) y óxido de grafeno reducido (verde). En los recuadros se muestran ampliaciones de las bandas *D* y *G*.

5. Espectroscopía fotoelectrónica de rayos X (XPS)

Existe todo un grupo de técnicas de caracterización que se basan en la interacción entre un haz de rayos X y los átomos de un material. Las distintas técnicas tienen su origen en los diferentes procesos que se suceden tras la interacción, entre ellos la emisión de fotoelectrones (XPS), emisión de electrones secundarios (espectroscopía Auger), rayos X emitidos por la muestra (XRF) ó rayos X absorbidos (EXAFS y XANES). La espectroscopía fotoelectrónica de rayos X (XPS) es una técnica cuantitativa de análisis superficial capaz de determinar la estequiometría, estado químico y la estructura electrónica de los elementos que existen en un material. Su funcionamiento se basa en el efecto fotoeléctrico, descubierto en 1887 por H. Hertz y descrito teóricamente por Einstein en 1905, y según el cual una superficie expuesta a radiación electromagnética de frecuencia superior a cierta frecuencia umbral (dependiente del material), absorberá los fotones incidentes emitiendo electrones. Para la obtención del espectro XPS, se hace incidir un haz monocromático de rayos X de energía conocida sobre la muestra en cuestión, de la que salen emitidos, por efecto fotoeléctrico, electrones con una amplia distribución de energías cinéticas. La energía cinética de cada uno de estos electrones se corresponde con la diferencia entre la energía de los fotones incidentes y la energía de ligadura del electrón expulsado (es decir, la energía que se ha necesitado para arrancar dichos electrones de la muestra), lo cual permite extraer información sobre el tipo de átomo al que se hallaba ligado dicho electrón. Debido a la baja energía que poseen estos electrones y a su fuerte interacción con la materia, solo aquellos que han sido emitidos suficientemente cerca de la superficie de la muestra escapan del material y pueden ser por tanto detectados, por lo cual el análisis solo proporciona información de la superficie del material (generalmente hasta unos 12 *nm* de profundidad). Mediante XPS se obtiene información no sólo de los elementos presentes en el material, sino que en ocasiones la técnica es lo suficientemente sensible como para discriminar el estado químico del átomo, debido a que la energía de enlace de un electrón en un determinado orbital varía ligeramente dependiendo del entorno de dicho átomo. Así, es posible obtener información sobre el estado de oxidación y el tipo de coordinación del átomo.

En el caso de materiales carbonosos, se analiza fundamentalmente la energía de ligadura de los electrones que ocupan el orbital *1s* del carbono (banda C_{1s}) y que tiene un valor de 284.6 *eV* en el caso de átomos de carbono en estructuras grafíticas perfectas. Del estudio de las componentes que conforman esta banda se deduce información sobre el estado de oxidación del material carbonoso, complementada con la información que proporciona la banda O_{1s}, correspondiente a energías del orbital *1s* del oxígeno. La relación del área entre diferentes bandas indica la proporción relativa de los distintos elementos.

6. Teoría del funcional de la densidad (DFT)

Por lo general, los estudios experimentales de superficies a resolución atómica mediante SPM, y en particular STM, resultan difíciles de interpretar. Las simulaciones teóricas proporcionan un nexo

entre las imágenes obtenidas por SPM y la topografía superficial y estructura electrónica de la muestra, permitiendo aclarar el origen de los rasgos observados en las imágenes. La teoría del funcional de la densidad (DFT, del inglés *Density Functional Theory*) es uno de los métodos más usados para cálculos *"ab initio"* de la estructura de átomos, moléculas, cristales y sus interacciones. Consiste en una formulación alternativa de la mecánica cuántica, empleada para investigar la estructura electrónica, generalmente en el estado fundamental, de sistemas de muchas partículas. En mecánica cuántica el ente fundamental con el que se trabaja es la función de onda, siendo la energía un funcional (una función que toma otra función como argumento) de dicha función de onda. En la teoría del funcional de la densidad, el objeto básico es la densidad electrónica, siendo la energía un funcional de ella. Se cumple además que la energía será mínima para la densidad real del sistema. La ventaja de esta formulación reside en el hecho de que es mucho más sencillo trabajar con densidades electrónicas que con funciones de onda (solo se requieren 3 variables frente a las 3N de la función de onda para sistemas de N partículas). En 1964, Hohenberg y Kohn demostraron que es posible calcular todo observable de un sistema electrónico a partir de la densidad electrónica [133], lo que significa que la densidad electrónica y la función de onda contienen en principio la misma información.

7. Referencias y notas

1 Anders E. and Grevesse N., "*Abundances of the elements: Meteoritic and solar*," Geochim. Cosmochim. Acta **53**, 197-214 (1989).

2 McDonough W.F. and Sun S.s., "*The composition of the Earth*," Chem. Geol. **120**, 223-253 (1995).

3 Frieden E., "*The Chemical Elements of Life*," Sci. Am. **227**, 52-60 (1972).

4 Pierson H.O., *"Handbook of carbon, graphite, diamond and fullerenes: properties, processing and applications,"* Noyes Publications (1993).

5 Dresselhaus M.S., Dresselhaus G. and Eklund P.C., *"Science of Fullerenes and Carbon Nanotubes,"* Academic Press (1996).

6 Rao C.N.R., Biswas K., Subrahmanyam K.S. and Govindaraj A., "*Graphene, the new nanocarbon*," J. Mater. Chem. **19**, 2457-2469 (2009).

7 Chung D.D.L., "*Review graphite*," J. Mater. Sci. **37**, 1475-1489 (2002).

8 Geim A.K. and Novoselov K.S., "*The rise of graphene*," Nat. Mater. **6**, 183-191 (2007).

9 Terrones M., Botello-Méndez A.R., Campos-Delgado J., López-Urías F., Vega-Cantú Y.I., Rodríguez-Macías F.J., Elías A.L., Muñoz-Sandoval E., Cano-Márquez A.G., Charlier J.-C. and Terrones H., "*Graphene and graphite nanoribbons: Morphology, properties, synthesis, defects and applications*," Nano Today **5**, 351-372 (2010).

10 Castro E.V., Peres N., Santos J.L.d., Guinea F. and Neto A.C., "*Bilayer graphene: gap tunability and edge properties*," J. Phys. Conf. Ser. **129**, 012002 (2008).

11 Novoselov K.S., Geim A.K., Morozov S.V., Jiang D., Zhang Y., Dubonos S.V., Grigorieva I.V. and Firsov A.A., "*Electric Field Effect in Atomically Thin Carbon Films*," Science **306**, 666-669 (2004).

12 Dresselhaus M.S., Dresselhaus G., Sugihara K., Spain I.L. and Goldberg H.A., *"Graphite Fibers and Filaments,"* Springer Verlag (1988).

13 Pimenta M.A., Dresselhaus G., Dresselhaus M.S., Cancado L.G., Jorio A. and Saito R., "*Studying disorder in graphite-based systems by Raman spectroscopy*," Phys. Chem. Chem. Phys. **9**, 1276-1291 (2007).

14 Li Z.Q., Lu C.J., Xia Z.P., Zhou Y. and Luo Z., "*X-ray diffraction patterns of graphite and turbostratic carbon*," Carbon **45**, 1686-1695 (2007).

15 Liu S. and Loper Jr C.R., "*The formation of kish graphite*," Carbon **29**, 547-555 (1991).

16 Mermin N.D., "*Crystalline order in two dimensions*," Phys. Rev. **176**, 250-254 (1968).

17 Venables J.A., Spiller G.D.T. and Hanbucken M., "*Nucleation and growth of thin films*," Rep. Prog. Phys. **47**, 399-459 (1984).

18 Evans J.W., Thiel P.A. and Bartelt M.C., "*Morphological evolution during epitaxial thin film growth: Formation of 2D islands and 3D mounds*," Surf. Sci. Rep. **61**, 1-128 (2006).

19 Novoselov K.S., Jiang D., Schedin F., Booth T.J., Khotkevich V.V., Morozov S.V. and Geim A.K., "*Two-dimensional atomic crystals*," Procl. Natl. Acad. Sci. USA **102**, 10451-10453 (2005).

20 Meyer J.C., Geim A.K., Katsnelson M.I., Novoselov K.S., Booth T.J. and Roth S., "*The structure of suspended graphene sheets*," Nature **446**, 60-63 (2007).

21 Los semimetales se caracterizan por la ausencia de un gap entre las bandas de conducción y valencia, así como por poseer una baja (aunque no necesariamente nula) densidad de estados en el nivel de Fermi en comparación con los metales.

22 Wallace P.R., "*The Band Theory of Graphite*," Phys. Rev. **71**, 622-634 (1947).

23 Neto A.H.C., Guinea F., Peres N.M.R., Novoselov K.S. and Geim A.K., "*The electronic properties of graphene*," Rev. Mod. Phys. **81**, 109-162 (2009).

24 Morozov S.V., Novoselov K.S., Katsnelson M.I., Schedin F., Elias D.C., Jaszczak J.A. and Geim A.K., "*Giant Intrinsic Carrier Mobilities in Graphene and Its Bilayer*," Phys. Rev. Lett. **100**, 016602 (2008).

25 Chen J.-H., Jang C., Xiao S., Ishigami M. and Fuhrer M.S., "*Intrinsic and extrinsic performance limits of graphene devices on SiO_2*," Nat. Nanotechnol. **3**, 206-209 (2008).

26 La conductividad laminar (sheet conductivity) de un material bidimensional viene dado por la expresión σ=enμ, mediante la cual se obtiene una resistividad laminar de 31 Ω/sq para el grafeno. A partir de este valor se puede calcular la resistividad haciendo uso del grosor de una lámina de grafeno (0.335 nm).

27 Lin Y.-M., Dimitrakopoulos C., Jenkins K.A., Farmer D.B., Chiu H.-Y., Grill A. and Avouris P., "*100-GHz Transistors from Wafer-Scale Epitaxial Graphene*," Science **327**, 662 (2010).

28 Stampfer C., Schurtenberger E., Molitor F., Güttinger J., Ihn T. and Ensslin K., "*Tunable Graphene Single Electron Transistor*," Nano Lett. **8**, 2378-2383 (2008).

29 Han M.Y., Ozyilmaz B., Zhang Y.B. and Kim P., "*Energy band-gap engineering of graphene nanoribbons*," Phys. Rev. Lett. **98**, 206805 (2007).

30 Stankovich S., Dikin D.A., Dommett G.H.B., Kohlhaas K.M., Zimney E.J., Stach E.A., Piner R.D., Nguyen S.T. and Ruoff R.S., "*Graphene-based composite materials*," Nature **442**, 282-286 (2006).

31 Schedin F., Geim A.K., Morozov S.V., Hill E.W., Blake P., Katsnelson M.I. and Novoselov K.S., "*Detection of individual gas molecules adsorbed on graphene*," Nat. Mater. **6**, 652-655 (2007).

32 Shan C., Yang H., Song J., Han D., Ivaska A. and Niu L., "*Direct Electrochemistry of Glucose Oxidase and Biosensing for Glucose Based on Graphene*," Anal. Chem. **81**, 2378-2382 (2009).

33 Yoo E., Kim J., Hosono E., Zhou H.-s., Kudo T. and Honma I., "*Large Reversible Li Storage of Graphene Nanosheet Families for Use in Rechargeable Lithium Ion Batteries*," Nano Lett. **8**, 2277-2282 (2008).

34 Balandin A.A., Ghosh S., Bao W., Calizo I., Teweldebrhan D., Miao F. and Lau C.N., "*Superior Thermal Conductivity of Single-Layer Graphene*," Nano Lett. **8**, 902-907 (2008).

35 Lee C., Wei X., Kysar J.W. and Hone J., "*Measurement of the Elastic Properties and Intrinsic Strength of Monolayer Graphene*," Science **321**, 385-388 (2008).

36 Kuzmenko A.B., van Heumen E., Carbone F. and van der Marel D., "*Universal Optical Conductance of Graphite*," Phys. Rev. Lett. **100**, 117401 (2008).

37 Nair R.R., Blake P., Grigorenko A.N., Novoselov K.S., Booth T.J., Stauber T., Peres N.M.R. and Geim A.K., "*Fine Structure Constant Defines Visual Transparency of Graphene*," Science **320**, 1308 (2008).

38 Bae S., Kim H., Lee Y., Xu X., Park J.-S., Zheng Y., Balakrishnan J., Lei T., Ri Kim H., Song Y.I., Kim Y.-J., Kim K.S., Ozyilmaz B., Ahn J.-H., Hong B.H. and Iijima S., "*Roll-to-roll production of 30-inch graphene films for transparent electrodes*," Nat. Nanotechnol. **5**, 574-578 (2010).

39 Schniepp H.C., Li J.-L., McAllister M.J., Sai H., Herrera-Alonso M., Adamson D.H., Prud'homme R.K., Car R., Saville D.A. and Aksay I.A., "*Functionalized Single Graphene Sheets Derived from Splitting Graphite Oxide*," J. Phys. Chem. B **110**, 8535-8539 (2006).

40 Blake P., Brimicombe P.D., Nair R.R., Booth T.J., Jiang D., Schedin F., Ponomarenko L.A., Morozov S.V., Gleeson H.F., Hill E.W., Geim A.K. and Novoselov K.S., "*Graphene-Based Liquid Crystal Device*," Nano Lett. **8**, 1704-1708 (2008).

41 Wang X., Zhi L. and Mullen K., "*Transparent, Conductive Graphene Electrodes for Dye-Sensitized Solar Cells*," Nano Lett. **8**, 323-327 (2007).

42 Matyba P., Yamaguchi H., Eda G., Chhowalla M., Edman L. and Robinson N.D., "*Graphene and Mobile Ions: The Key to All-Plastic, Solution-Processed Light-Emitting Devices*," ACS Nano **4**, 637-642 (2010).

43 Meyer J.C., Girit C.O., Crommie M.F. and Zettl A., "*Imaging and dynamics of light atoms and molecules on graphene*," Nature **454**, 319-322 (2008).

44 Geim A.K. and MacDonald A.H., "*Graphene: Exploring carbon flatland*," Phys. Today **60**, 35-41 (2007).

45 Kim K.S., Zhao Y., Jang H., Lee S.Y., Kim J.M., Kim K.S., Ahn J.-H., Kim P., Choi J.-Y. and Hong B.H., "*Large-scale pattern growth of graphene films for stretchable transparent electrodes*," Nature **457**, 706-710 (2009).

46 Reina A., Jia X.T., Ho J., Nezich D., Son H.B., Bulovic V., Dresselhaus M.S. and Kong J., "*Large Area, Few-Layer Graphene Films on Arbitrary Substrates by Chemical Vapor Deposition*," Nano Lett. **9**, 30-35 (2009).

47 Sutter P.W., Flege J.-I. and Sutter E.A., "*Epitaxial graphene on ruthenium*," Nat. Mater. **7**, 406-411 (2008).

48 Wei D.C., Liu Y.Q., Wang Y., Zhang H.L., Huang L.P. and Yu G., "*Synthesis of N-Doped Graphene by Chemical Vapor Deposition and Its Electrical Properties*," Nano Lett. **9**, 1752-1758 (2009).

49 Berger C., Song Z., Li T., Li X., Ogbazghi A.Y., Feng R., Dai Z., Marchenkov A.N., Conrad E.H., First P.N. and de Heer W.A., "*Ultrathin Epitaxial Graphite: 2D Electron Gas Properties and a Route toward Graphene-based Nanoelectronics*," J. Phys. Chem. B **108**, 19912-19916 (2004).

50 de Heer W.A., Berger C., Wu X., First P.N., Conrad E.H., Li X., Li T., Sprinkle M., Hass J., Sadowski M.L., Potemski M. and Martinez G., "*Epitaxial graphene*," Solid State Commun. **143**, 92-100 (2007).

51 Ohta T., Bostwick A., Seyller T., Horn K. and Rotenberg E., "*Controlling the electronic structure of bilayer graphene*," Science **313**, 951-954 (2006).

52 Emtsev K.V., Bostwick A., Horn K., Jobst J., Kellogg G.L., Ley L., McChesney J.L., Ohta T., Reshanov S.A., Rohrl J., Rotenberg E., Schmid A.K., Waldmann D., Weber H.B. and Seyller T., "*Towards wafer-size graphene layers by atmospheric pressure graphitization of silicon carbide*," Nat. Mater. **8**, 203-207 (2009).

53 Stankovich S., Piner R.D., Chen X., Wu N., Nguyen S.T. and Ruoff R.S., "*Stable aqueous dispersions of graphitic nanoplatelets via the reduction of exfoliated graphite oxide in the presence of poly(sodium 4-styrenesulfonate)*," J. Mater. Chem. **16**, 155-158 (2006).

54 Li D., Muller M.B., Gilje S., Kaner R.B. and Wallace G.G., "*Processable aqueous dispersions of graphene nanosheets*," Nat. Nanotechnol. **3**, 101-105 (2008).

55 Bourlinos A.B., Georgakilas V., Zboril R., Steriotis T.A. and Athanasios K. Stubos, "*Liquid-Phase Exfoliation of Graphite Towards Solubilized Graphenes*," Small **5**, 1841-1845 (2009).

56 Hernandez Y., Nicolosi V., Lotya M., Blighe F.M., Sun Z.Y., De S., McGovern I.T., Holland B., Byrne M., Gun'ko Y.K., Boland J.J., Niraj P., Duesberg G., Krishnamurthy S., Goodhue R., Hutchison J., Scardaci V., Ferrari A.C. and Coleman J.N., "*High-yield production of graphene by liquid-phase exfoliation of graphite*," Nat. Nanotechnol. **3**, 563-568 (2008).

57 De S., King P.J., Lotya M., O'Neill A., Doherty E.M., Hernandez Y., Duesberg G.S. and Coleman J.N., "*Flexible, Transparent, Conducting Films of Randomly Stacked Graphene from Surfactant-Stabilized, Oxide-Free Graphene Dispersions*," Small **6**, 458-464 (2010).

58 Coleman J.N., "*Liquid-Phase Exfoliation of Nanotubes and Graphene*," Adv. Funct. Mater. **19**, 3680-3695 (2009).

59 Brodie B.C., "*On the Atomic Weight of Graphite*," Phil. Trans. R. Soc. London **149**, 249-259 (1859).

60 Hummers W.S. and Offeman R.E., "*Preparation of Graphitic Oxide*," J. Am. Chem. Soc. **80**, 1339-1339 (1958).

61 Paredes J.I., Villar-Rodil S., Martinez-Alonso A. and Tascon J.M.D., "*Graphene Oxide Dispersions in Organic Solvents*," Langmuir **24**, 10560-10564 (2008).

62 He H., Klinowski J., Forster M. and Lerf A., "*A new structural model for graphite oxide*," Chem. Phys. Lett. **287**, 53-56 (1998).

63 Si Y. and Samulski E.T., "*Synthesis of Water Soluble Graphene*," Nano Lett. **8**, 1679-1682 (2008).

64 Guo H.-L., Wang X.-F., Qian Q.-Y., Wang F.-B. and Xia X.-H., "*A Green Approach to the Synthesis of Graphene Nanosheets*," ACS Nano **3**, 2653-2659 (2009).

65 McAllister M.J., Li J.-L., Adamson D.H., Schniepp H.C., Abdala A.A., Liu J., Herrera-Alonso M., Milius D.L., Car R., Prud'homme R.K. and Aksay I.A., "*Single Sheet Functionalized Graphene by Oxidation and Thermal Expansion of Graphite*," Chem. Mat. **19**, 4396-4404 (2007).

66 Stankovich S., Dikin D.A., Piner R.D., Kohlhaas K.A., Kleinhammes A., Jia Y., Wu Y., Nguyen S.T. and Ruoff R.S., "*Synthesis of graphene-based nanosheets via chemical reduction of exfoliated graphite oxide*," Carbon **45**, 1558-1565 (2007).

67 Tung V.C., Allen M.J., Yang Y. and Kaner R.B., "*High-throughput solution processing of large-scale graphene*," Nat. Nanotechnol. **4**, 25-29 (2009).

68 Gao X., Jang J. and Nagase S., "*Hydrazine and Thermal Reduction of Graphene Oxide: Reaction Mechanisms, Product Structures, and Reaction Design*," J. Phys. Chem. C **114**, 832-842 (2010).

69 Zhang J., Yang H., Shen G., Cheng P., Zhang J., Guo S., Yang H., Shen G., Cheng P., Zhang J. and Guo S., "*Reduction of graphene oxide via L-ascorbic acid*," Chem. Commun. **46**, 1112-1114 (2010).

70 Fernández-Merino M.J., Guardia L., Paredes J.I., Villar-Rodil S., Solís-Fernández P., Martínez-Alonso A. and Tascón J.M.D., "*Vitamin C Is an Ideal Substitute for Hydrazine in the Reduction of Graphene Oxide Suspensions*," J. Phys. Chem. C **114**, 6426-6432 (2010).

71 Zhu C., Guo S., Fang Y. and Dong S., "*Reducing Sugar: New Functional Molecules for the Green Synthesis of Graphene Nanosheets*," ACS Nano **4**, 2429-2437 (2010).

72 Salas E.C., Sun Z., Lüttge A. and Tour J.M., "*Reduction of Graphene Oxide via Bacterial Respiration*," ACS Nano **4**, 4852-4856 (2010).

73 Gómez-Navarro C., Weitz R.T., Bittner A.M., Scolari M., Mews A., Burghard M. and Kern K., "*Electronic Transport Properties of Individual Chemically Reduced Graphene Oxide Sheets*," Nano Lett. **7**, 3499-3503 (2007).

74 Mattevi C., Eda G., Agnoli S., Miller S., Mkhoyan K.A., Celik O., Mostrogiovanni D., Granozzi G., Garfunkel E. and Chhowalla M., "*Evolution of Electrical, Chemical, and Structural Properties of Transparent and Conducting Chemically Derived Graphene Thin Films*," Adv. Funct. Mater. **19**, 2577-2583 (2009).

75 Dreyer D.R., Park S., Bielawski C.W. and Ruoff R.S., "*The chemistry of graphene oxide*," Chem. Soc. Rev. **39**, 228-240 (2010).

76 Eda G., Fanchini G. and Chhowalla M., "*Large-area ultrathin films of reduced graphene oxide as a transparent and flexible electronic material*," Nat. Nanotechnol. **3**, 270-274 (2008).

77 Gómez-Navarro C., Burghard M. and Kern K., "*Elastic Properties of Chemically Derived Single Graphene Sheets*," Nano Lett. **8**, 2045-2049 (2008).

78 Villar-Rodil S., Paredes J.I., Martinez-Alonso A. and Tascon J.M.D., "*Preparation of graphene dispersions and graphene-polymer composites in organic media*," J. Mater. Chem. **19**, 3591-3593 (2009).

79 Kim H., Abdala A.A. and Macosko C.W., "*Graphene/Polymer Nanocomposites*," Macromolecules **43**, 6515-6530 (2010).

80 Robinson J.T., Perkins F.K., Snow E.S., Wei Z. and Sheehan P.E., "*Reduced Graphene Oxide Molecular Sensors*," Nano Lett. **8**, 3137-3140 (2008).

81 Wilson N.R., Pandey P.A., Beanland R., Young R.J., Kinloch I.A., Gong L., Liu Z., Suenaga K., Rourke J.P., York S.J. and Sloan J., "*Graphene Oxide: Structural Analysis and Application as a Highly Transparent Support for Electron Microscopy*," ACS Nano **3**, 2547-2556 (2009).

82 Chang H. and Bard A.J., "*Scanning Tunneling Microscopy Studies of Carbon-Oxygen Reactions on Highly Oriented Pyrolytic Graphite* " J. Am. Chem. Soc. **113**, 5588-5596 (1991).

83 Hahn J.R., "*Kinetic study of graphite oxidation along two lattice directions*," Carbon **43**, 1506-1511 (2005).

84 Boehm H.P., "*Surface oxides on carbon and their analysis: a critical assessment*," Carbon **40**, 145-149 (2002).

85 Hahn J.R., Kang H., Lee S.M. and Lee Y.H., "*Mechanistic Study of Defect-Induced Oxidation of Graphite*," J. Phys. Chem. B **103**, 9944-9951 (1999).

86 Liu L., Ryu S., Tomasik M.R., Stolyarova E., Jung N., Hybertsen M.S., Steigerwald M.L., Brus L.E. and Flynn G.W., "*Graphene Oxidation: Thickness-Dependent Etching and Strong Chemical Doping*," Nano Lett. **8**, 1965-1970 (2008).

87 Gurnett D.A. and Bhattacharjee A., *"Introduction to Plasma Physics,"* Cambridge University Press (2005).

88 Langmuir I., "*Oscillations in Ionized Gases*," Procl. Natl. Acad. Sci. USA **14**, 627-637 (1928).

89 Lieberman M.A. and Lichtenberg A., *"Principles of Plasma Discharges and Materials Processing,"* John Wiley and Sons (1994).

90 Flamm D.L. and Manos D.M. (eds), *Plasma Etching: An Introduction*. (Academic Press, San Diego, 1989).

91 Conrads H. and Schmidt M., "*Plasma generation and plasma sources*," Plasma Sources Sci. Technol. **9**, 441-454 (2000).

92 Kogelschatz U.S., "*Dielectric-barrier discharges: Their history, discharge physics, and industrial applications*," Plasma Chem. Plasma Process. **23**, 1-46 (2003).

93 Bogaerts A., Neyts E., Gijbels R. and van der Mullen J., "*Gas discharge plasmas and their applications*," Spectrochim. Acta B **57**, 609-658 (2002).

94 Dohan J.M. and Masschelein W.J., "*The Photochemical Generation of Ozone : Present State-of-the-Art*," Ozone-Sci. Eng. **9**, 315 - 334 (1987).

95 Bradley R.H. and Mathieson I., "*Chemical Interactions of Ultraviolet Light with Wool Fiber Surfaces*," J. Colloid Interface Sci. **194**, 338-343 (1997).

96 Lee S.M., Lee Y.H., Hwang Y.G., Hahn J.R. and Kang H., "*Defect-Induced oxidation of graphite*," Phys. Rev. Lett. **82**, 217-220 (1999).

97 Paredes J.I., Martinez-Alonso A. and Tascon J.M.D., "*Comparative study of the air and oxygen plasma oxidation of highly oriented pyrolytic graphite: a scanning tunneling and atomic force microscopy investigation*," Carbon **38**, 1183-1197 (2000).

98 Osváth Z., Nemes-Incze P., Tapasztó L., Horváth Z.E. and Biró L.P., "*Thermal oxidation of few-layer graphite plates: An SPM study*," Phys. Status Solidi A **205**, 1419-1423 (2008).

99 Starodub E., Bartelt N.C. and McCarty K.F., "*Oxidation of Graphene on Metals*," J. Phys. Chem. C **114**, 5134-5140 (2010).

100 Binnig G., Rohrer H., Gerber C. and Weibel E., "*Surface studies by scanning tunneling microscopy*," Phys. Rev. Lett. **49**, 57-61 (1982).

101 Binnig G., Quate C.F. and Gerber C., "*Atomic force microscope*," Phys. Rev. Lett. **56**, 930-933 (1986).

102 Paredes J.I., Martinez-Alonso A. and Tascon J.M.D., "*Application of scanning tunneling and atomic force microscopies to the characterization of microporous and mesoporous materials*," Microporous Mesoporous Mat. **65**, 93-126 (2003).

103 Generalmente las puntas de W se suelen emplear cuando se trabaja en ultra-alto vacío, dado que son propensas a oxidarse fácilmente en aire, mientras que las de Pt/Ir se utilizan en condiciones ambientales.

104 Simic-Milosevic V., Heyde M., Nilius N., König T., Rust H.P., Sterrer M., Risse T., Freund H.J., Giordano L. and Pacchioni G., "*Au Dimers on Thin MgO (001) Films: Flat and Charged or Upright and Neutral?*," J. Am. Chem. Soc. **130**, 7814-7815 (2008).

105 Buchner F., "Fundamentals", in *STM Investigation of Molecular Architectures of Porphyrinoids on a Ag(111) Surface* (Springer Berlin Heidelberg, 2010), pp. 5-15.

106 Tersoff J. and Hamann D.R., "*Theory of the Scanning Tunneling Microscope*," Phys. Rev. B **31**, 805-813 (1985).

107 Magonov S.N. and Whangbo M.H., "*Interpreting STM and AFM Images*," Adv. Mater. **6**, 355-371 (1994).

108 Feenstra R.M., Stroscio J.A., Tersoff J. and Fein A.P., "*Atom-selective imaging of the GaAs(110) surface*," Phys. Rev. Lett. **58**, 1192-1195 (1987).

109 Midgley P.A. and Durkan C., "*The frontiers of microscopy*," Mater. Today **11**, 8-11 (2008).

110 Voitchovsky K., Kuna J.J., Contera S.A., Tosatti E. and Stellacci F., "*Direct mapping of the solid-liquid adhesion energy with subnanometre resolution*," Nat. Nanotechnol. **5**, 401-405 (2010).

111 Cappella B. and Dietler G., "*Force-distance curves by atomic force microscopy*," Surf. Sci. Rep. **34**, 1-104 (1999).

112 Hölscher H., Schwarz U.D., Zwörner O. and Wiesendanger R., "*Consequences of the stick-slip movement for the scanning force microscopy imaging of graphite*," Phys. Rev. B **57**, 2477-2481 (1998).

113 Giessibl F.J., "*AFM's path to atomic resolution*," Mater. Today **May 2005**, 32-41 (2005).

114 García R. and Pérez R., "*Dynamic atomic force microscopy methods*," Surf. Sci. Rep. **47**, 197-301 (2002).

115 Albrecht T.R., Grutter P., Horne D. and Rugar D., "*Frequency modulation detection using high-Q cantilevers for enhanced force microscope sensitivity*," J. Appl. Phys. **69**, 668-673 (1991).

116 Giessibl F.J., "*Atomic Resolution of the Silicon (111)-(7x7) Surface by Atomic Force Microscopy*," Science **267**, 68-71 (1995).

117 Giessibl F.J., "*Advances in atomic force microscopy*," Rev. Mod. Phys. **75**, 949-983 (2003).

118 Ringger M., Hidber H.R., Schlögl R., Oelhafen P. and Güntherodt H.-J., "*Nanometer lithography with the scanning tunneling microscope*," Appl. Phys. Lett. **46**, 832-834 (1985).

119 Eigler D.M. and Schweizer E.K., "*Positioning single atoms with a scanning tunnelling microscope*," Nature **344**, 524-526 (1990).

120 Crommie M.F., Lutz C.P. and Eigler D.M., "*Confinement of Electrons to Quantum Corrals on a Metal Surface*," Science **262**, 218-220 (1993).

121 Schull G., Frederiksen T., Arnau A., Sanchez-Portal D. and Berndt R., "*Atomic-scale engineering of electrodes for single-molecule contacts*," Nat. Nanotechnol. **6**, 23-27 (2011).

122 Wouters D. and Schubert U.S., "*Nanolithography and Nanochemistry: Probe-Related Patterning Techniques and Chemical Modification for Nanometer-Sized Devices*," Angew. Chem. Int. Ed. **43**, 2480-2495 (2004).

123 Biró L.P. and Lambin P., "*Nanopatterning of graphene with crystallographic orientation control*," Carbon **48**, 2677-2689 (2010).

124 Letokhov V.S., "*Raman spectroscopy*," Opt. Laser Technol. **10**, 129-137 (1978).

125 Raman C.V. and Krishnan K.S., "*A new type of secondary radiation*," Nature **121**, 501-502 (1928).

126 Tuinstra F. and Koenig J.L., "*Raman Spectrum of Graphite*," J. Chem. Phys. **53**, 1126-1130 (1970).

127 Ferrari A.C. and Robertson J., "*Interpretation of Raman spectra of disordered and amorphous carbon*," Phys. Rev. B **61**, 14095-14107 (2000).

128 Nemanich R.J. and Solin S.A., "*First- and second-order Raman scattering from finite-size crystals of graphite*," Phys. Rev. B **20**, 392-401 (1979).

129 Ferrari A.C., "*Raman spectroscopy of graphene and graphite: Disorder, electron-phonon coupling, doping and nonadiabatic effects*," Solid State Commun. **143**, 47-57 (2007).

130 Cuesta A., Dhamelincourt P., Laureyns J., Martinez-Alonso A. and Tascon J.M.D., "*Raman microprobe studies on carbon materials*," Carbon **32**, 1523-1532 (1994).

131 Ferrari A.C., Meyer J.C., Scardaci V., Casiraghi C., Lazzeri M., Mauri F., Piscanec S., Jiang D., Novoselov K.S., Roth S. and Geim A.K., "*Raman spectrum of graphene and graphene layers*," Phys. Rev. Lett. **97**, 187401 (2006).

132 Gupta A., Chen G., Joshi P., Tadigadapa S. and Eklund, "*Raman Scattering from High-Frequency Phonons in Supported n-Graphene Layer Films*," Nano Lett. **6**, 2667-2673 (2006).

133 Hohenberg P. and Kohn W., "*Inhomogeneous electron gas*," Phys. Rev. **136**, B864-B871 (1964).

Objetivos y planteamiento de la memoria 2

1. Objetivos

Resulta evidente la importancia tecnológica de los materiales carbonosos de estructura grafítica. El interés en estos materiales se ha incrementado en las últimas dos décadas debido al descubrimiento de distintos tipos de materiales nanoestructurados de carbono: fulerenos, nanotubos y grafeno. Este último es un candidato excepcionalmente prometedor con vistas a un gran número de aplicaciones prácticas en electrónica, sensores, materiales compuestos, almacenamiento de energía, etc.

La estructura y química superficiales de estos materiales pueden influir de manera considerable en sus propiedades, de modo que resulta esencial disponer de métodos eficientes que permitan controlar estas características a escalas nanométrica/atómica. Uno de los métodos más eficaces de modificación superficial de materiales grafíticos es la oxidación. Ello se debe a que la superficie de estos materiales, aunque en general muy inerte en términos químicos, es relativamente vulnerable al ataque con agentes oxidantes. Así, el desarrollo de nuevos métodos de oxidación y el estudio detallado de sus efectos adquiere gran importancia. Entre los diferentes tipos de oxidación conocidos destacan, por su flexibilidad e importancia industrial, los efectuados mediante plasmas. También resulta interesante, de cara a sus aplicaciones tecnológicas, el desarrollo de métodos controlados de oxidación local.

Las microscopías de proximidad constituyen una poderosa herramienta de análisis superficial a escala atómica y nanométrica. Por ello resultan esenciales para conocer y comprender los efectos que la oxidación provoca en las superficies de materiales grafíticos, permitiendo seguir la evolución de los tratamientos a escala atómica desde los instantes iniciales.

Conforme a lo anteriormente expuesto, en el presente trabajo se plantea como objetivo general el *estudio de los efectos a escalas atómica y nanométrica de diferentes tipos de oxidación sobre la superficie de materiales grafíticos, en particular de grafito y grafeno.* Como objetivos específicos, se plantean los siguientes:

- Estudiar y comprender la modificación a escalas nanométrica y atómica de grafito mediante oxidación por plasma de descarga de barrera dieléctrica y ozono generado por radiación ultravioleta, dos métodos de oxidación poco empleados en el campo de los materiales carbonosos.
- Establecer los mecanismos básicos de ataque de materiales grafíticos mediante los dos tipos de oxidación mencionados en el punto anterior.
- Estudiar las características morfológicas/estructurales a escalas nanométrica y atómica de grafeno químicamente modificado obtenido a partir de óxido de grafito.
- Determinar el comportamiento del grafeno químicamente modificado frente a atmósferas oxidantes.

- Desarrollar un método controlado de oxidación local de grafeno químicamente modificado.

2. Organización de la memoria

Tras la introducción (capítulo 1) y el presente capítulo, en el capítulo 3 se describe de manera breve tanto los materiales empleados como los diferentes métodos experimentales usados.

En el capítulo 4 se exponen los resultados obtenidos, así como su discusión. Estos resultados se recogen como un compendio de artículos, publicados o enviados a revistas revisadas por pares y englobadas dentro de áreas relacionadas con la temática de la presente memoria. En la tabla siguiente se incluyen los índices de calidad de las revistas en las que se han publicado los artículos, así como la posición de cada una de ellas en relación al número total de revistas del área correspondiente.

Tabla 1 – Índices de calidad (2009) de las revistas en las que se han publicado los artículos recogidos en la presente memoria.

Revista	Índice de impacto	Puesto/nº de revistas total	Área
Carbon	4.504	22/212	Materials Science, Multidisciplinary
Journal of Colloid and Interface Science	3.019	38/121	Chemistry, Physical
Journal of Physical Chemistry C	4.224	24/212	Materials Science, Multidisciplinary
Langmuir	3.898	27/212	Materials Science, Multidisciplinary

Fuente: Journal Citation Reports (2009), www.isiknowledge.com

El capítulo 4 se divide en tres bloques, cada uno de ellos precedido de un resumen en el que se recogen los objetivos, los resultados más relevantes y las conclusiones de los artículos correspondientes:

- Oxidación de HOPG mediante plasma de descarga de barrera dieléctrica y ozono generado mediante radiación ultravioleta.
- Caracterización mediante microscopías de proximidad de grafenos preparados a partir de óxido de grafito.
- Comportamiento frente a oxidación en fase gas de grafeno preparado a partir de óxido de grafito.

La Memoria concluye con un breve capítulo de conclusiones generales (capítulo 5) y un anexo en el que se incluye una lista de publicaciones complementarias y de contribuciones a congresos.

3 Materiales y métodos

1. Materiales

A continuación se describen los materiales objeto de estudio del presente trabajo:

- Grafito pirolítico altamente orientado (HOPG) de grado ZYH (desviación angular del eje c $\approx 3.5°$), producido por Advanced Ceramics Corporation (EE.UU). Antes de cada tratamiento, se procedió a la exfoliación de la cara superior de la pieza a tratar, con el fin de trabajar con una superficie limpia.
- Óxido de grafeno (GO), preparado a partir de grafito natural en polvo (Fluka 50870). Para ello se oxidó el grafito mediante el método de Hummers [1], exfoliándose posteriormente en medio acuoso el óxido de grafito resultante para dar lugar a láminas monocapa de GO en dispersión acuosa.
- Óxido de grafeno reducido químicamente (CMG/rGO), obtenido mediante la reducción de GO con monohidrato de hidracina a $95\,℃$ [2]. Antes del tratamiento de reducción, se ajustó el pH de la dispersión a ~ 10 mediante la adición de una pequeña cantidad de amoniaco, lo que favorece la estabilidad coloidal de las láminas de CMG en base a repulsiones electrostáticas.

Se prepararon filmes delgados (también denominados papeles) de GO y CMG mediante filtración en vacío de las dispersiones correspondientes a través de membranas de alúmina Anodisc (Whatman) con un tamaño de poro de $0.2\,\mu m$ y un diámetro de 47 mm. Típicamente se filtraban volúmenes de 250 ml de dispersión a concentraciones de $\sim 0.1\,mg/ml$.

2. Métodos de oxidación superficial

Los métodos de oxidación empleados pueden ser clasificados en dos tipos diferenciados: (1) oxidaciones de carácter global, en las que la superficie del material resulta completamente expuesta al agente oxidante (plasmas, UVO y oxidación térmica en aire), y (2) oxidación de carácter local (litografía STM), en la que la oxidación se restringe a una pequeña región de la superficie de la muestra.

- *Plasma generado mediante microondas (MW):* El equipo utilizado para efectuar los tratamientos de plasma MW fue un modelo 200-G de Technics Plasma GmbH (Alemania), en el cual el plasma es generado en una pequeña cavidad cilíndrica de unos 24 y 22 cm de diámetro y altura, respectivamente, mediante un campo electromagnético de MW (2.45 GHz) que a su vez es generado por un magnetrón. Los tratamientos se llevaron a cabo a presiones de 1 Pa, empleando oxígeno de una pureza 99.9990 % como gas precursor y a diferentes potencias y tiempo, que se indican en los lugares correspondientes.
- *Plasma generado mediante descarga de barrera dieléctrica (DBD):* Los tratamientos en plasma DBD se efectuaron en un equipo de descarga en volumen, modelo VB-A4 (Arcotec GmbH, Alemania). Éste consta de un electrodo inferior plano y conectado a

tierra, que sirve de soporte para las muestras a tratar, y de un electrodo superior cilíndrico conectado a una fuente sinusoidal de alto voltaje. El electrodo inferior es móvil, de modo que se consigue minimizar el efecto memoria de este tipo de plasmas, causante de que las microdescargas se produzcan siempre en los mismos puntos. Mediante la elección de la velocidad del electrodo inferior y el número de pases bajo el electrodo superior, se puede establecer el tiempo de tratamiento deseado, pudiendo ser tan pequeño como unos pocos ms. Además de la velocidad, también se pueden variar la potencia, el tamaño del gap (distancia entre los electrodos) y el tipo de gas precursor. En el presente trabajo, se emplearon velocidades del electrodo de 1.33 m/s, mientras que la potencia y el gap se fijaron a 200 W y 2.4 mm respectivamente. Como gas precursor se utilizó la atmósfera de la cámara (aire).

- *Ozono generado por radiación ultravioleta (UVO):* El aparato empleado para efectuar los tratamientos de UVO fue un modelo 42 de Jelight Company Inc. (USA). En éste, la muestra se coloca en una cámara ventilada en la que existe una lámpara de mercurio de baja presión. Esta irradia la cámara con radiación ultravioleta, en la que las longitudes de onda principales son, por orden de intensidad, 253.7 y 184.9 nm. En presencia del oxígeno molecular del aire presente en la cámara, la radiación genera distintas especies reactivas, principalmente ozono y, en menor cantidad, oxígeno atómico. La potencia de la radiación de 253.7 nm es de $28\ mW\ cm^{-2}$. La muestra puede ser colocada a diferentes distancias de la lámpara. La temperatura dentro de la cámara se incrementa con el tiempo de tratamiento, estabilizándose a ~ 65 y 95 ℃, respectivamente, para las distancias mayores y menores que se emplearon (39.5 mm y 7.35 mm).

- *Oxidación térmica en aire:* Se llevó a cabo en un horno horizontal de cuarzo, con un diámetro interior de 20 mm. La temperatura en el interior del horno se midió con un termopar de Pt/Rh colocado cerca de la muestra. Primeramente se calentó la muestra en un flujo de Ar $(100\ ml\ min^{-1})$ a 20 ℃$\ min^{-1}$ hasta la temperatura de oxidación deseada (indicada en cada caso en concreto), momento en el cual el flujo de Ar se reemplaza por uno de aire sintético $(50\ ml\ min^{-1})$.

- *Litografía STM:* Para llevar a cabo la litografías STM, se empleó el mismo equipo que el usado para la obtención de imágenes (ver apartado siguiente). La única diferencia con el modo de obtención de imágenes es la necesidad de trabajar a voltajes más elevados. En el caso concreto del CMG, los voltajes empleados para oxidar mediante litografía STM fueron de $\sim 1400 - 1800\ mV$. Para compensar el alejamiento de la punta que se produce debido a estos valores relativamente altos de voltaje, se trabajó con corrientes más elevadas $(1.45\ nA)$ que las habitualmente empleadas para la obtención de imágenes.

3. Métodos de caracterización

La principal herramienta de caracterización la constituyeron las microscopías STM y AFM, que fueron complementadas con espectroscopía Raman y XPS. En algunos casos, la interpretación de las imágenes STM se apoyó en simulaciones teóricas basadas en DFT.

Microscopías de proximidad: Se empleó un equipo Nanoscope IIIa Multimode, de Veeco Instruments (Santa Bárbara, CA). Este aparato permite la operación tanto en STM como en diferentes variantes de AFM. Para STM se emplearon puntas de Pt/Ir (80/20), de Veeco Instruments, preparadas mecánicamente, trabajando en el modo de corriente constante. Los parámetros túnel típicos usados en STM estándar fueron 1 nA de corriente y 100 mV de voltaje, excepto en los casos en los que se expliciten otros valores. Para estudiar muestras poco conductoras se empleó un convertidor de baja corriente que permite trabajar a corrientes de $\sim 1\ pA$. En AFM de contacto, se emplearon cantilevers triangulares de Si_3N_4 con puntas piramidales integradas (radios de curvatura nominales de 20 – 60 nm y constantes de fuerza nominales $0.06 - 0.58\ N\ m^{-1}$), y se trabajó en el modo de deflexión constante del cantilever (fuerza constante). Para la captura de imágenes de fuerza lateral (o fricción), se fijó el ángulo de barrido a 90°, de modo que la dirección de barrido fuese perpendicular al eje principal del cantilever. Para AFM *tapping* se emplearon cantilevers rectangulares de silicio con constantes de fuerza nominales de $\sim 40\ N\ m^{-1}$ y frecuencias de resonancia típicas entre 200 y 300 KHz. Para el estudio de GO y del CMG, las láminas se depositaron sobre diferentes substratos (principalmente HOPG, aunque también mica y Si/SiO_2), calentando el substrato a temperaturas de $\sim 50 - 60$ ℃ antes de depositar sobre el mismo una gota de la dispersión correspondiente. Con este método es posible obtener diferentes densidades de material depositado.

Espectroscopía Raman: Se utilizó un espectrómetro HR 800 Jobin Yvon Horiba, empleando como fuente de excitación la raya verde (λ = 532 nm) de un láser de Argón (CDPS532M de Jobin Yvon Horiba). La potencia de salida y la potencia incidente sobre la muestra fueron, respectivamente, de 100 mW y 20 mW. Se empleó una rendija de 200 µm de anchura, con la polarización de la luz siempre perpendicular al plano de incidencia. Los espectros se obtuvieron en aire y a temperatura ambiente en el rango espectral $900 - 3200\ cm^{-1}$.

Espectroscopía XPS: Se utilizó un espectrómetro *SPECS* provisto de un analizador *PHOIBOS 100 MCD*, utilizando radiación Al K_α (1486.6 eV) a una potencia de 100 W y a una presión inferior a $1.2 \cdot 10^{-7}\ Pa$. Las medidas se efectuaron con el analizador perpendicular al plano de la muestra en el modo de energía de paso constante. Para muestras no conductoras (papel de óxido de grafeno), el efecto de carga superficial observado fue corregido mediante un cañón de electrones operando a 0.4 eV y 0.10 mA. Para la obtención de los espectros generales se realizaron 10 acumulaciones en el rango 0 - 1250 eV, con un paso de energía en el analizador de 50 eV y una velocidad de $1\ eV\ canal^{-1}s^{-1}$. La composición atómica superficial se determinó a partir de las áreas de los picos correspondientes a los

elementos encontrados tras efectuar una sustracción tipo Shirley de la señal de fondo (background*)*. En el cálculo se incluyeron correcciones por la transmisión del analizador y de los factores de sensibilidad atómica para cada elemento.

Espectroscopía de absorción ultravioleta-visible (UV-vis): La concentración de las dispersiones de GO y CMG se determinó empleando espectroscopía de absorción UV-vis (espectrofotómetro Helios α de Thermo Spectronic). Para ello, se comparó la absorbancia a 231 nm (GO) ó 268 nm (CMG) de la muestra problema con la de dispersiones de referencia que presentaban concentraciones conocidas.

Análisis termogravimétricos: Se empleó una termobalanza SDT Q600 (TA Instruments) con crisoles de *Pt*, trabajando con flujos de $100\ ml\ min^{-1}$ de *Ar* o de aire sintético (dependiendo del caso). La velocidad de calentamiento fue de $10\ ℃\ min^{-1}$.

Teoría del funcional de la densidad (DFT): Para los cálculos teóricos basados en DFT, se empleó el código DACAPO, que implementa el método de supercelda y usa conjuntos de ondas planas como bases. Los resultados de los cálculos permitieron simular imágenes STM de estructuras hipotéticas, que posteriormente fueron comparadas con las imágenes STM obtenidas experimentalmente. Dicha comparación proporcionó información valiosa sobre la naturaleza de las estructuras observadas por STM.

4. Referencias

1 Hummers W.S. and Offeman R.E., "*Preparation of Graphitic Oxide*," J. Am. Chem. Soc. **80**, 1339-1339 (1958).

2 Li D., Muller M.B., Gilje S., Kaner R.B. and Wallace G.G., "*Processable aqueous dispersions of graphene nanosheets*," Nat. Nanotechnol. **3**, 101-105 (2008).

Resúmenes y Artículos 4

4.1 Oxidación de HOPG

Artículo I

Publicado en la revista Journal of Colloid and Interface Science: "*A comparison between physically and chemically driven etching in the oxidation of graphite surfaces*"

Artículo II

Publicado en la revista Carbon: "*New atomic-scale features in graphite surfaces treated in a dielectric barrier discharge plasma*"

Artículo III

Publicado en la revista Journal of Physical Chemistry C: "*A combined experimental and theoretical investigation of atomic-acale defects produced on graphite surfaces by dielectric barrier discharge plasma treatment*"

Para estudiar a escala atómica la oxidación de materiales carbonosos, el grafito resulta un material de partida muy adecuado. Por una parte sirve como material de referencia para posteriores estudios de materiales estructuralmente más complejos y de mayor transcendencia tecnológica (p.ej. fibras, nanofibras y nanotubos de carbono), debido a que presenta una estructura ordenada y perfectamente reconocible, que ha sido estudiada en profundidad y en la cual resulta fácil identificar pequeños cambios introducidos por el tratamiento. Por otra, gracias a su estructura plana y al gran tamaño de las piezas con las que se trabaja, es un material ideal para su estudio mediante microscopías de proximidad. Además, puesto que en futuros trabajos el grafito será empleado como substrato de los materiales que se desean oxidar (en particular láminas de grafeno), conocer los efectos que tiene la oxidación sobre él permitirá discernir entre efectos de la oxidación del substrato y del propio material soportado. Es por ello que esta primera parte del trabajo se centra en el estudio de la oxidación de grafito pirolítico altamente orientado (HOPG) mediante dos técnicas muy poco empleadas hasta el momento en la oxidación de materiales carbonosos. En este estudio se ha encontrado un tipo de defecto a escala atómica que no había sido documentado con anterioridad y del que se ha efectuado un estudio en detalle para desentrañar su origen y naturaleza.

a) DBD frente a UVO

Los métodos de oxidación que se han estudiado, plasma de descarga de barrera dieléctrica (DBD) y tratamientos en ozono generado por radiación ultravioleta (UVO), resultan, a priori,

complementarios en cierto sentido. Así, se espera que las oxidaciones en ambos estén regidas por mecanismos radicalmente distintos, lo cual desembocará en diferencias notables en la evolución del proceso de oxidación y en los rasgos formados en la superficie del grafito. El estudio en paralelo de los efectos a escalas atómica/nanométrica de estos dos tipos particulares de oxidación permite poner de relieve los dos mecanismos básicos subyacentes en las oxidaciones de materiales carbonosos, y que en última instancia resultan responsables de los cambios morfológicos y estructurales producidos durante la oxidación. Como veremos, mientras que la oxidación en DBD está regida por fenómenos puramente físicos, la oxidación en UVO lo está por fenómenos químicos, presentando cada una de ellas características enormemente diferenciadas que condicionan de manera decisiva la evolución del proceso de oxidación.

a.1) DBD

El seguimiento de la evolución de las superficies de HOPG oxidadas se efectuó mediante microscopía de efecto túnel (STM), que permite un estudio a resolución atómica en condiciones ambientales. Tras los primeros instantes de oxidación en DBD se observan en la superficie del HOPG, mediante STM, una serie de zonas circulares de unos pocos centenares de micras en las que la estructura grafítica ha resultado alterada. Cada una de estas zonas, causadas por el impacto de uno de los filamentos característicos del plasma generado mediante DBD, está constituida por una miríada de rasgos a escala atómica. Las densidades de estos rasgos se incrementan desde los bordes hacia el centro de las zonas, donde la densidad es tan elevada que no resulta posible la visualización individual de los rasgos y solo se observa una superficie rugosa y homogénea. Los rasgos observados son, mayoritariamente, protuberancias y depresiones, y tanto su apariencia como los estudios efectuados para determinar su naturaleza apuntan, como se verá más adelante, que están asociados a la presencia de vacantes de carbono y clusters intersticiales de oxígeno, respectivamente. También se observan pequeñas elevaciones asociadas a la presencia de átomos intersticiales de C/Ar bajo el grafeno superficial. El aumento del tiempo de tratamiento sólo provoca una mayor cantidad de impactos de filamento, lo cual redunda en un aumento en la densidad de los rasgos observados hasta que finalmente las zonas en las que el grafito ha resultado alterado llegan a cubrir toda la superficie. A estas alturas del tratamiento, la concentración de defectos es tan elevada en la totalidad de la superficie que resulta imposible identificar los rasgos de manera individual, mostrándose la superficie dominada por una morfología rugosa similar a la observada en las zonas centrales de los impactos de filamentos en los estadios iniciales de la oxidación. Un ulterior incremento en el tiempo de tratamiento solo consigue aumentar la rugosidad superficial observada. Esta evolución del tratamiento, en la que se produce un aumento en la densidad de los rasgos producidos pero la apariencia de éstos permanece inalterada, sugiere una escasa selectividad de la oxidación en DBD. Todo esto, junto con la presencia de especies implantadas (defectos intersticiales), es claro indicio de que el ataque se produce por un bombardeo contra la superficie del grafito de los iones y especies cargadas que se generan en el plasma y que son

acelerados contra el HOPG a causa del intenso campo eléctrico generado entre los electrodos. De este modo, la oxidación en DBD está regida por mecanismos físicos (bombardeo), cuya característica principal es la ausencia de selectividad.

a.2) UVO

Durante los instantes iniciales de la oxidación mediante UVO, los rasgos a escala atómica observables mediante STM en las superficies oxidadas se atribuyen, por sus características y apariencia, a vacantes atómicas en la red grafítica. A diferencia de lo que ocurre en la oxidación por plasma de DBD, no se observan indicios de la presencia de ningún tipo de especie implantada bajo el grafeno superficial. Esto era de esperar, puesto que en la oxidación por UVO no existe un mecanismo que produzca una aceleración de iones o especies cargadas en la cámara de tratamiento (no existen campos electromagnéticos externos). Por ello, el proceso que lleva a la formación de estas vacantes ha de ser radicalmente distinto del involucrado en la formación de vacantes en la oxidación mediante DBD, donde se producían debido al bombardeo de especies energéticas. Las especies químicamente reactivas producidas por la irradiación ultravioleta (principalmente oxígeno atómico, ozono y oxígeno molecular excitado) se quimisorben en la superficie del grafito, debilitando los enlaces entre átomos de carbono y finalmente rompiéndolos tras la formación de una molécula de CO/CO_2 que deja tras de sí una vacante en la red. Así, la evolución temporal de la oxidación es radicalmente distinta de la seguida por las muestras oxidadas en DBD, puesto que la selectividad química jugará un papel predominante. Las observaciones experimentales corroboran esta diferencia, puesto que en vez de un aumento en la densidad de vacantes ahora se observa su crecimiento, formando agujeros monocapa de forma aproximadamente circular. Estos agujeros no presentan un tamaño uniforme, lo cual es una clara indicación de que se siguen creando nuevas vacantes/agujeros continuamente durante todo el proceso de oxidación. Cuando las oxidaciones son lo suficientemente largas, los agujeros comienzan a combinarse entre sí, dejando atrás un intrincado patrón de terrazas de grafito esencialmente planas, debido a que las zonas de los grafenos inferiores que quedan expuestas por los agujeros también comienzan a oxidarse formando nuevos agujeros. La presencia y evolución de estos agujeros, así como de otras formaciones (p.ej. trincheras producidas a partir de bordes de grano), delatan el elevado grado de selectividad de este tipo de oxidación, un rasgo inequívoco de ataques regidos por mecanismos químicos. La selectividad observada está provocada por la gran movilidad sobre la superficie de las especies oxigenadas una vez adsorbidas sobre el plano basal perfecto y su diferente reactividad con defectos y con sitios perfectos de plano basal. Esta selectividad proporciona la posibilidad de controlar de manera muy precisa las modificaciones efectuadas en la muestra (p.ej. el tamaño de los agujeros).

a.3) Ataque físico frente a ataque químico

Los estudios efectuados dan cuenta de las diferencias existentes en los cambios, tanto estructurales como químicos, introducidos en la superficie del grafito mediante oxidaciones regidas por

procesos físicos (plasma DBD) y químicos (UVO). En el primer tipo, la oxidación avanza mediante la acumulación progresiva de defectos a escala atómica en posiciones totalmente arbitrarias. Esto incrementa la reactividad superficial del grafito, lo cual puede ser explotado con vistas a diferentes aplicaciones (p.ej. anclar partículas de catalizador). Por el contrario, las oxidaciones regidas por procesos químicos son sensibles a la reactividad de la superficie, lo que provoca la característica formación de agujeros y trincheras. Un ejemplo de la utilidad de este tipo de ataque puede ser la introducción de agujeros del tamaño deseado en la superficie del HOPG, empleándolos como "corrales" para mantener confinado algún tipo de molécula o nanocluster, mientras que la reactividad del HOPG se mantiene baja gracias a que la superficie en su conjunto permanece esencialmente inalterada. Conocer estas diferencias puede permitir adecuar los tratamientos en función de los requerimientos específicos del uso final.

b) Depresiones en DBD

Si bien el resto de los defectos encontrados tras los tratamientos son bastante comunes en otros tipos de oxidaciones, y sus características se encuentran documentadas en la literatura existente, las depresiones halladas por STM tras las oxidaciones en plasma DBD constituyen un tipo de defecto que nunca antes había sido observado en grafito o cualquier otro material carbonoso. Es por ello que se efectuaron estudios adicionales, tanto teóricos como experimentales, encaminados a aclarar su origen y naturaleza.

En primer lugar, se descartó que las depresiones observadas en las imágenes STM se correspondiesen con accidentes topográficos reales (es decir, zonas combadas y/o agujeros en la superficie del HOPG); los hechos más esclarecedores al respecto fueron la ausencia de bordes definidos (como los que se encuentran en agujeros formados en el grafeno superficial) y la dependencia de la profundidad aparente de la depresión con los parámetros túnel empleados en la captura de la imagen. De este modo, las depresiones observadas han de estar asociadas a una variación (en concreto una disminución) en la densidad local de estados electrónicos (LDOS) cerca del nivel de Fermi. Esta es una situación similar a la que se da en el caso de las vacantes atómicas, en las que la protuberancia observada por STM es debida a un incremento en la LDOS de los átomos de carbono adyacentes a la vacante.

Los tratamientos térmicos en atmósfera inerte efectuados a piezas de grafito oxidado con DBD confirmaron el origen de las protuberancias como vacantes atómicas. Además, debido a la desaparición de éstas a las temperaturas empleadas, estos tratamientos proporcionaron muestras libres de vacantes pero en las que todavía permanecen las depresiones gracias a la menor movilidad que mostraron. Así, fue posible realizar un estudio del comportamiento de las depresiones frente a la oxidación térmica, que mostraron una baja reactividad en comparación con el caso de las vacantes. Esta baja reactividad es totalmente consistente con la idea de las depresiones como zonas de relativamente baja LDOS, en

contraposición con el caso de las vacantes, en las que la reactividad se ve incrementada por el aumento de la LDOS.

Debido al carácter puramente físico del ataque en este tipo de plasma, los defectos que se espera observar son vacantes así como defectos intersticiales. El estudio mediante XPS muestra que durante los instantes iniciales de la oxidación únicamente se introduce oxígeno en la superficie en cantidades apreciables, y sólo después de un cierto tiempo aparece también nitrógeno, aunque en menores cantidades. El hecho de que éstos sean los únicos elementos encontrados y que las depresiones no se observen tras oxidación térmica o mediante otros tipos de plasma que no conllevan ataque físico apunta a especies intersticiales como origen de las depresiones, en concreto especies oxigenadas debido su presencia desde los momentos iniciales de la oxidación. Debido a la elevada electronegatividad del oxígeno, es de esperar que su presencia intersticial se vea acompañada de una disminución de la LDOS en el grafeno superficial del grafito. Esto se ve confirmado por las simulaciones efectuadas con átomos de oxígeno atrapados intersticialmente bajo el grafeno superior, a la vez que se reproduce el comportamiento observado experimentalmente (p.ej. dependencia de la profundidad con los parámetros túnel). De este modo, todas las evidencias apuntan a que la aparición de depresiones en las imágenes STM es debida a la presencia de clusters intersticiales de oxígeno.

Journal of Colloid and Interface Science 344 (2010) 451–459

Contents lists available at ScienceDirect

Journal of Colloid and Interface Science

www.elsevier.com/locate/jcis

A comparison between physically and chemically driven etching in the oxidation of graphite surfaces

P. Solís-Fernández, J.I. Paredes *, A. Cosío, A. Martínez-Alonso, J.M.D. Tascón

Instituto Nacional del Carbón, CSIC, Apartado 73, 33080 Oviedo, Spain

ARTICLE INFO

Article history:
Received 25 June 2009
Accepted 12 January 2010
Available online 18 January 2010

Keywords:
Graphite
Oxidation
Plasma
Etching
Scanning tunneling microscopy

ABSTRACT

The etching of graphite surfaces by two different types of oxidative treatments, namely dielectric barrier discharge (DBD) air plasma and ultraviolet-generated ozone (UVO), has been investigated and compared by means of scanning tunneling microscopy (STM), Raman spectroscopy and X-ray photoelectron spectroscopy (XPS). Although the attack is initiated in both cases with the formation of individual, isolated atomic-scale defects (in particular, atomic vacancies), its subsequent evolution indicated that different mechanisms drive the surface modification in the two types of treatment, which greatly differ in etching selectivity. Thus, physical processes (i.e., ion bombardment) dominate the attack by DBD air plasma, which are not present in the case of UVO oxidation. The effects of the different etching mechanisms on the graphite surface structure, as visualized by STM down to the atomic scale, are discussed and found to be consistent with the Raman spectroscopy and XPS data. This type of information can be relevant when selecting the most appropriate type of surface modification of carbon materials for specific purposes.

1. Introduction

The surface modification of carbonaceous materials is of great interest for their use in a wide range of applications, e.g. as catalyst supports [1], biomedical materials [2], or first-wall materials in nuclear reactors [3]. Depending on the specific use the carbon material will be given, different surface characteristics (for example, nanostructure or chemical composition) must be tuned to different levels in order to modulate such properties as adhesion [4,5], wettability [6], or adsorption [7]. This implies that several different methods for the controlled modification of carbon surfaces must be available, as well as an in-depth understanding of their effects on carbon surfaces at the microscopic level. As a particularly relevant type of surface modification of carbon materials, we concentrate here on oxidation. Oxidation of carbon materials is a topic of scientific and technological relevance [6,8–13], and can be carried out through a variety of approaches. Thus, carbon surfaces can be oxidized via high temperature treatment under air or molecular oxygen [9,14], through oxygen ion bombardment [15–18], by exposure to oxygen-containing plasmas [10,11,19,20] or ozone [21,22], or by wet chemical and electrochemical means [23].

In general terms, two main mechanisms are responsible for the structural and morphological changes induced on carbon surfaces by the different types of oxidation, namely chemical and physical attack. Chemical attack is based on the combination of surface carbon atoms with the chemically active species from the oxidative medium, e.g. atomic oxygen in hyperthermal beams or in oxygen plasmas [11,24] or molecular oxygen in high temperature air oxidation [8,9], forming functional groups that can eventually desorb as CO or CO_2. Physical attack proceeds through the collision of energetic charged species, such as O^+ or O_2^+ ions, onto the carbon surface, leading to the creation of structural damage and/or ion implantation. Physical attack obviously holds in the case of modification via oxygen ion bombardment, but also for some types of plasmas [10,25,26]. Thus, the relative contribution of each mechanism, or even the prevalence of one over the other, will be determined by the specific type of oxidation.

Although the oxidation methods mentioned above are widely employed to modify and manipulate the surface of carbon materials, in many cases their effects on the carbonaceous structure at the microscopic level have not been well established. More specifically, a comparison of the effects of chemical and physical attack on the nanometric and atomic-scale structure of carbon surfaces has never been reported. To provide insight into these questions, here we investigate and compare the modification of the surface of graphite, taken as a model carbon material, by two very different types of oxidation treatments, namely dielectric barrier discharge (DBD)-generated air plasma oxidation and ultraviolet-generated ozone (UVO) oxidation. Very little information is available in the literature on the oxidation of carbon materials, and particularly of graphite, by DBD plasma [27–30], even though it presents some

* Corresponding author. Fax: +34 985 29 76 62.
E-mail address: paredes@incar.csic.es (J.I. Paredes).

0021-9797/$ - see front matter © 2010 Elsevier Inc. All rights reserved.
doi:10.1016/j.jcis.2010.01.018

practical advantages over other types of plasmas (e.g., no need of working under vacuum). Likewise, UVO oxidation has been shown to be a convenient method to control such characteristics as the electrical conductivity in carbon nanotubes [21,22], but again, microscopic knowledge about the etching process is currently missing. In this work, we employ scanning tunneling microscopy (STM) to obtain information, down to the atomic scale, about the etching of graphite surfaces by both types of oxidation treatment. Raman and X-ray photoelectron spectroscopies are used to provide complementary insights on the effects of these oxidative treatments on carbon surface chemistry.

2. Experimental

For the present study, ZYH grade HOPG from Advanced Ceramics Corporation (USA) was employed. The typical size of the graphite pieces was $\sim 10 \times 10 \times 1.5$ mm^3. Before each treatment, the HOPG samples were cleaved in air with adhesive tape to obtain fresh, pristine surfaces. DBD-generated air plasma treatments were carried out in a laboratory-scale volume type unit (Arcotec VB-A4, Arcotec GmbH, Germany) working at atmospheric pressure. This plasma treatment unit basically consists of two metallic electrodes, one of them covered with a layer of dielectric material, connected to a high voltage alternating current. The plasma is created in the air gap existing between the two electrodes and comprises a large number of tiny plasma filaments generated at random locations, each one incorporating a rapid succession of discrete microdischarges [31]. The main advantage of this type of plasma is that it allows operation at atmospheric pressure, in contrast to more conventional plasma systems, which can only operate at low pressure, facilitating the implementation of industrial-scale devices. Typical treatment times with the DBD plasma apparatus used here range from several milliseconds to a few seconds. The plasma was generated at a total power of 200 W with a separation between the two electrodes of 2.4 mm. The power per unit area was ~ 6 W cm^{-2}. For the UVO treatments, an UVO cleaner model 42 from Jelight (USA) was employed. This equipment consists of a stainless steel treatment chamber ($\sim 170 \times 165 \times 40$ mm^3) with a low pressure mercury vapor grid lamp placed on the top. The lamp provides ultraviolet (UV) radiation mainly at wavelengths of 253.7 and 184.9 nm. The power per unit area delivered by the 253.7 nm wavelength radiation, which is the most intense, was 0.28 W cm^{-2}. Freshly cleaved HOPG samples were placed in the treatment chamber at a distance of 7.4 mm from the UV lamp and subjected to different exposure times, which typically ranged between 5 and 60 min.

Characterization of DBD air plasma-treated and UVO-treated HOPG samples was mainly carried out by STM, but complemented by Raman and X-ray photoelectron spectroscopies. The STM measurements were accomplished in air at room temperature with a Nanoscope IIIa Multimode apparatus, from Veeco Instruments (USA), working in the constant current mode (variable height) and employing mechanically prepared Pt/Ir (80/20) tips (Veeco Instruments). The tips were made by simply cutting Pt/Ir wire with a clean cutter. The quality of the tips was first checked by imaging the surface of pristine, untreated graphite. Only those tips that yielded high quality images, both on the micrometer and atomic scales, were selected for the oxidation studies. Nanometer-scale images were recorded with tunneling parameters of 1 nA (tunneling current) and 100 mV (bias voltage), whereas tunneling currents as high as 6 nA and bias voltages as low as 5 mV were employed for atomic-scale imaging. Raman spectra were collected on an HR 800 LabRam instrument, from Jobin-Yvon (France), with a laser excitation wavelength of 532 nm. X-ray photoelectron spectroscopy (XPS) was carried out with a SAGE HR 100 spectrometer, from SPECS (Germany), using a Mg Kα X-ray source and working at a base pressure of $\sim 10^{-10}$ mbar and an operating pressure of 10^{-9} mbar or slightly below. Relative atomic concentrations were determined with atomic sensitivity factors given by Wagner et al. [32] after Shirley background subtraction and peak area integration.

3. Results and discussion

It is the aim of the present work to compare the modifications induced on the nanometric- and atomic-scale structure of graphite surfaces by DBD air plasma and UVO oxidations. Performing very short treatments is most suitable to this end, as the early stages of modification usually bear the footprint of the individual events of the process, so isolated atomic-scale defects can in principle be visualized by a high resolution technique such as STM [11]. In the case of the DBD air plasma, the shortest possible treatments were ~ 9 ms long. STM imaging of HOPG surfaces subjected to such a treatment revealed that a significant fraction of the surface remains completely unaltered, whereas only some localized areas showed evidence of plasma-induced attack. With the aid of an optical microscope coupled to the STM instrument that helped to select specific locations for inspection by the latter technique, it was determined that these areas display approximately a round shape with a diameter of about 400 μm, and can be attributed to the effect of one of the filaments that make up the plasma. Within the filament-struck areas, the HOPG surface displayed an atomically rough morphology, where isolated atomic-scale defects could not be discerned (see below). Rather, the whole surface within these areas became uniformly modified and intact graphitic areas, however small, could not be observed. Nevertheless, we could ascertain the presence of a transition region about several tens of micrometers wide between the filament-struck areas and the unaltered, pristine HOPG areas surrounding them where isolated atomic-scale defects were noticed. This is illustrated in Fig. 1. At some point when moving from a pristine, unaltered HOPG area towards a given filament-struck area, a low density of defects on an otherwise intact graphite background emerges (Fig. 1a). These defects are just between one and several nm large and are seen either as protrusions (bright spots with an apparent height of $\sim$0.2–0.3 nm, blue arrow in Fig. 1a) or as depressions (dark spots, white arrow in Fig. 1a). Furthermore, as we move closer to the filament-struck area, the density of defects steadily increases (Fig. 1b and c) up to the point where the defects are no longer individually resolved and the atomically rough, highly uniform morphology referred to above arises (Fig. 1d). The existence of such transition region can be explained by a decrease in the plasma density as we move from the center of the filament toward its border. The results of Fig. 1 suggest that the appearance of the created defects does not change significantly as DBD plasma attack progresses, but just an increase in their density is observed instead, implying that the attack proceeds simply through creation of individual atomic-scale defects at random locations on the graphite surface.

We now compare the progression of the attack on graphite by DBD air plasma with that by UVO oxidation. In the latter case, a completely different evolution was observed, as noticed in the STM images of Fig. 2. Exposure times of 5 min were required to observe by STM the first changes on the HOPG surface, whereas shorter treatments did not usually lead to any noticeable modifications. These first changes involve the emergence of a number of small protrusions (bright spots of $\sim$0.2–0.3 nm of apparent height) between one and a few nm in lateral size, the rest of the surface retaining the structure of pristine graphite (Fig. 2a). As opposed to the case of DBD air plasma, these protrusions are the only type of atomic-scale defect developed upon UVO oxidation, i.e. no depressions are created. When the UVO treatment

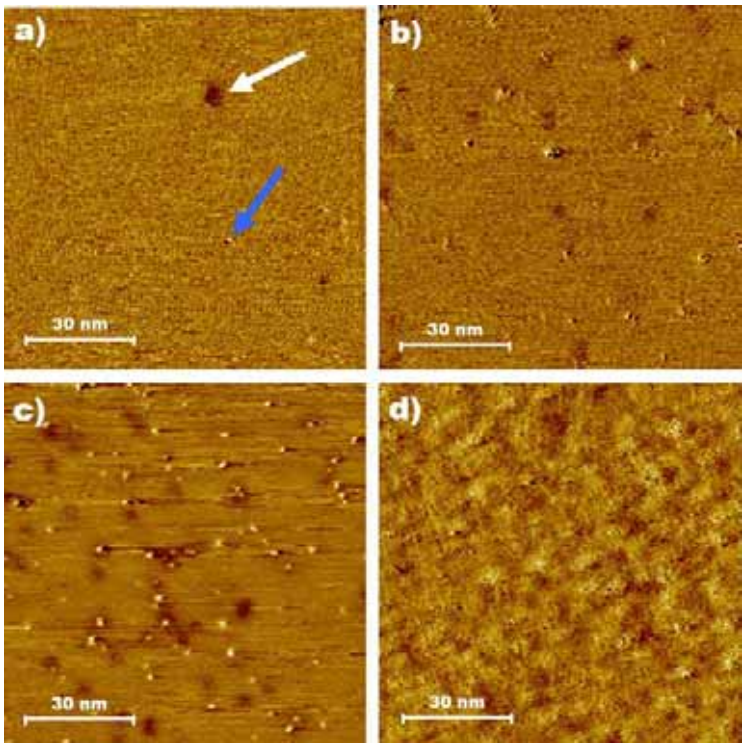

Fig. 1. STM images evidencing the modification of a graphite surface subjected to DBD air plasma. Isolated atomic-scale defects with increasing concentration are noticed in (a) through (c). When the defect density reaches a certain point, the defects are no longer individually resolved and a uniformly rough morphology appears, as in (d).

time is increased to 20 min, some monolayer-deep pits of nanometric dimensions appear on the surface, which coexist with the atomic-scale defects (Fig. 2b). We note that such pits are distinctly different to the depressions described for the DBD air plasma-treated samples: the former display atomically sharp edges and depths of ~0.35 nm, i.e. they actually correspond to monolayer-deep pits. By contrast, the DBD plasma-induced depressions possess very smooth edges and depths of ~0.1–0.2 nm, which suggests that they are not actual pits and must therefore be attributed to another type of feature. This point will be discussed in more detail below. As the UVO treatment time is further increased, larger numbers of pits are observed and the diameter of the largest ones increases (e.g., Fig. 2c for a 30 min treatment), which indicates that new pits are being created and the pits previously created are continuously growing. For sufficiently long treatments (e.g., 60 min, Fig. 2d), the pits merge, leaving behind remnants of the topmost graphene layer and exposing the underlying layers to oxidation, which also start developing pits. Thus, in the case of UVO oxidation, a layer-by-layer removal of the surface graphenes is evident (see line profile as an inset to Fig. 2d), which is not the case for DBD air plasma oxidation. Although the UVO oxidations reported in Fig. 2 were made at a fixed separation between the HOPG substrate and the UV lamp (7.4 mm), we also performed experiments at different separations. As the distance to the lamp is increased, it is reasonable to assume that the sample surface will be exposed to lower concentrations of ozone. The STM images (not shown) indicated that in such case the etching behavior was the same as that documented in Fig. 2, but only the etching rate became noticeably slower, consistent with the expected lower ozone concentration for larger graphite-UV lamp separations.

As mentioned previously, there are in principle two main mechanisms that can be contributing to the structural modifications observed on the graphite surface upon oxidation: physical and chemical attack. The former consists of a bombardment of ions onto the sample surface. Provided that the kinetic energy of the impinging ions is high enough, carbon atoms can be sputtered from the graphite surface, creating atomic vacancies, and/or the ion species can be implanted below the topmost graphene layers [10,11,25]. Physical attack is a non-selective process, which means that the ion-induced defects are generated with equal or very similar probability on all types of surface sites, e.g. on perfect sites of basal planes as well as on sites that display beforehand some kind of defect [26]. Thus, the attack basically progresses via creation of increasing numbers of atomic-scale defects on random locations, without large-sized localized features being developed. Chemical attack, by contrast, is based on the combination of surface carbon atoms with chemically reactive species (oxygenated species). During this process, a significant etching of the graphite surface can take place, as the oxygen-containing functional groups that generally form may eventually desorb as CO or CO_2. Chemical attack can be, and usually is, a highly selective process in that etching progresses much faster at defect sites (vacancies, step edges, grain boundaries, etc.) compared to perfect sites due to the presence of carbon atoms with dangling bonds readily available for combination with the oxygenated species. This selectivity leads to the development of localized features on the graphite surface, such as pits or trenches, thus constituting a clear signature of chemical attack.

Taking into account the previous considerations, it becomes immediately apparent that UVO oxidation of graphite is driven by chemical attack, whereas DBD air plasma oxidation should be

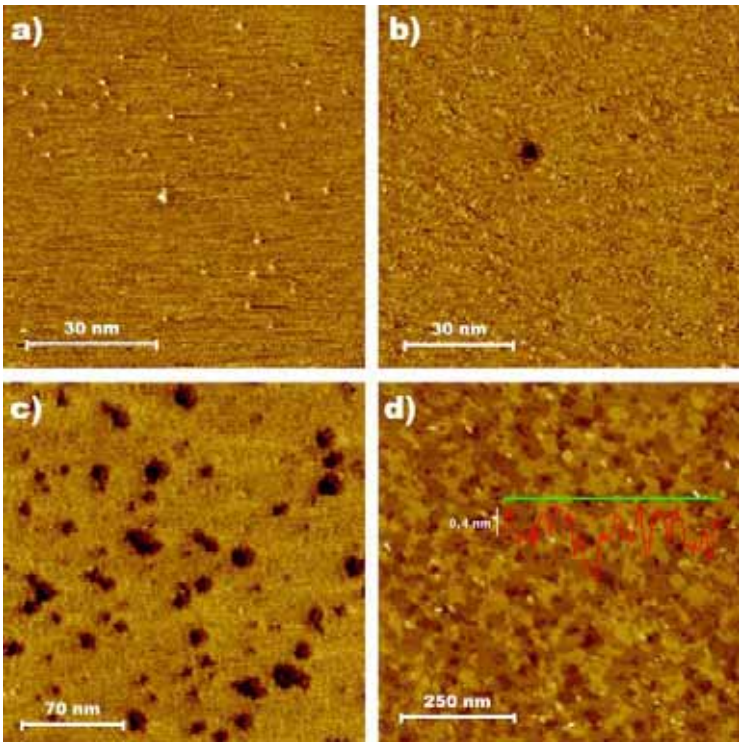

Fig. 2. STM images of graphite surfaces subjected UVO oxidation for different periods of time: 5 (a), 20 (b), 30 (c) and 60 min (d). The line profile shown as an inset to (d) reveals height differences of ~0.35 nm, corresponding to the height of one graphene, which highlights the layer-by-layer nature of the etching.

dominated by physical processes. In the former case, the development of pits of growing size (Fig. 2) indicates that removal of carbon atoms is taking place preferentially at defect sites, such as graphene edges. Another sign of selective etching, and therefore of chemically-driven attack, in the UVO-treated samples is the formation of trenches (Fig. 3), which can be attributed to the presence of grain boundaries in the HOPG mosaic crystal [33].

By contrast, no signs of localized etching were ever observed on HOPG samples exposed to DBD air plasma, i.e. no pits, trenches or other features indicative of selective removal of carbon atoms develop upon DBD air plasma oxidation. This is mostly evidenced from the nanometer-scale STM images of graphite surfaces subjected to the DBD plasma for increasingly longer times, as illustrated in Fig. 4 for samples treated for 71 (a), 213 (b) and 1064 (c) ms. For such relatively long treatments, and in contrast with the short treatments described above (e.g., 9 ms, Fig. 1), the whole HOPG surface becomes uniformly modified and pristine, unaltered graphitic sections are no longer noticed. We note from Fig. 4 that the most significant change observed upon long DBD air plasma treatments is the emergence of an increasingly rougher morphology (see representative line profiles in Fig. 4 obtained along the marked white lines in the images), without localized features characteristic of selective attack being developed. This strongly suggests that, in the case of DBD air plasma, the attack is dominated by non-selective, physical processes (i.e., ion bombardment). Such conclusion would also be consistent with the results reported in Fig. 1, which pointed to the idea that the rough morphologies induced by this type of plasma are mainly the consequence of a simple accumulation of atomic-scale defects generated at random locations on the graphite surface. The development of uniform rough morphologies is known to be a typical effect of ion bombardment [34]. It has been shown that physical attack (ion bombardment) in plasma oxidation can be substantial in certain types of plasmas, where ions attain enough kinetic energy to create permanent defects on graphite as a result of their acceleration by the electromagnetic fields of the plasma [25]. Although a diagnosis of the DBD plasma has not been reported, the observations of the present work are strong indication that ion bombardment, and thus physical processes, are the dominant mechanism in the attack of graphite by this type of plasma.

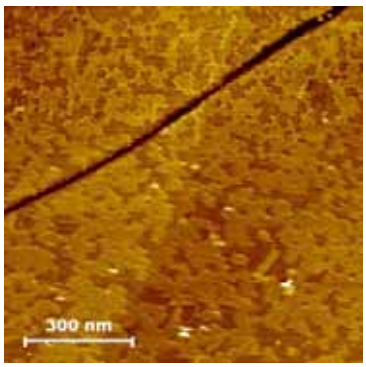

Fig. 3. STM image of a typical trench developed on the graphite surface upon UVO oxidation for 60 min.

Fig. 5 shows detailed atomic resolution images of the different types of defects that were observed: protrusions (a) and depressions (b) in the case of DBD air plasma oxidation, and only

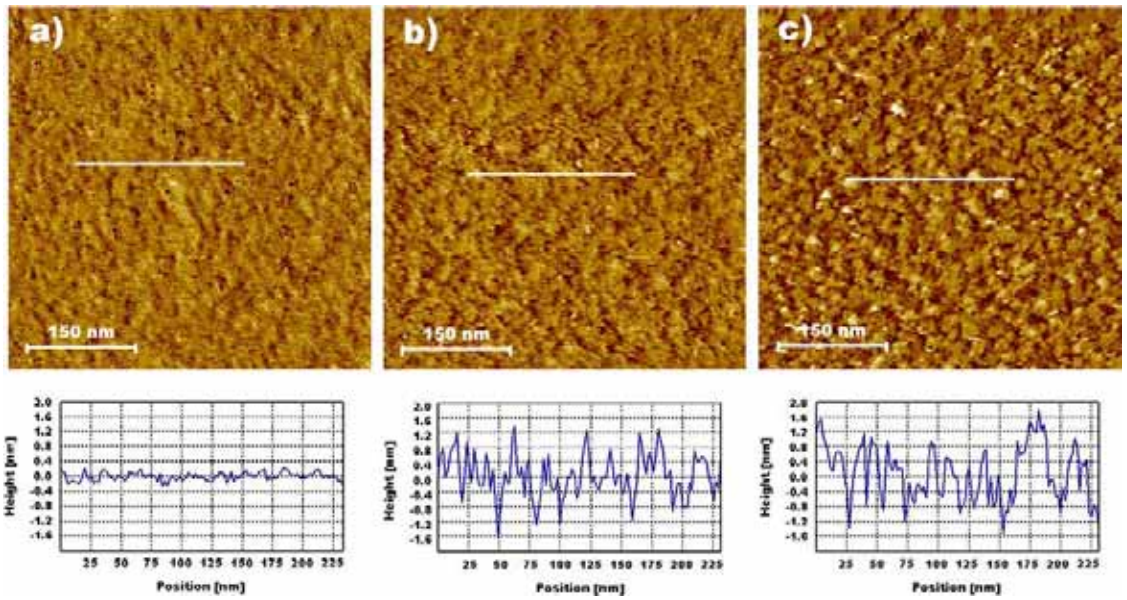

Fig. 4. Nanometer-scale STM images of graphite surfaces subjected to DBD air plasma treatment for 71 (a), 213 (b) and 1064 ms (c).

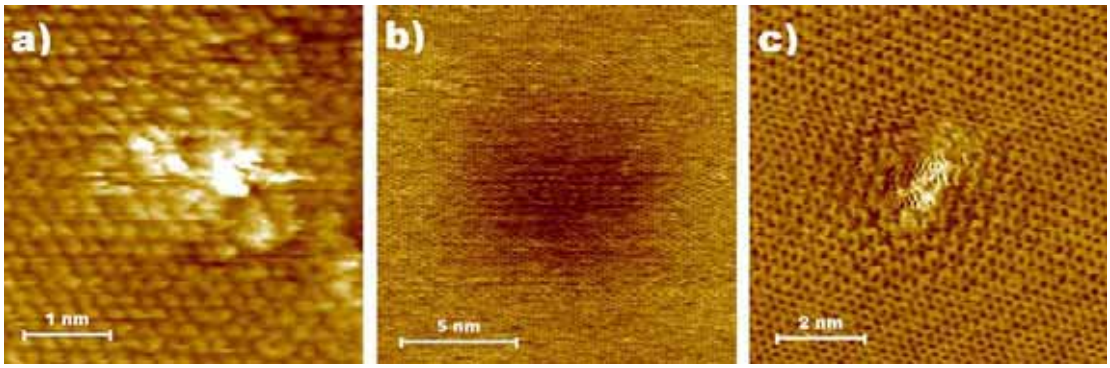

Fig. 5. Atomic-scale STM images of the individual defects induced by DBD air plasma (a, b) and UVO (c) treatment on the graphite surface.

protrusions (c) in the case of UVO oxidation. For both types of treatment, the characteristics of the protrusions, i.e. lateral size between one and a few nm, height ~0.2–0.3 nm and distorted local atomic-scale structure, strongly suggest that they correspond to mono- and multi-atomic vacancies on the HOPG surface. It is well known that atomic vacancies on graphite induce an enhancement of the density of electronic states near the Fermi level in the region surrounding the vacancy and are thus visualized by STM as apparent protrusions [35]. The protrusion size can be as small as ~1 nm for monoatomic vacancies and up to a few nm for multiatomic vacancies [11,36]. Although we attribute the protrusions of both the DBD air plasma-treated and UVO-oxidized HOPG to atomic vacancies, their formation must have proceeded through different mechanisms in the two cases, as the dominant etching processes are also different. Since DBD air plasma treatment seems to be governed by physical effects, sputtering of surface carbon atoms induced by ion bombardment should be responsible for the creation of the atomic vacancies in this case. As a matter of fact, ion bombardment has been reported to generate atomic vacancies, among other types of defect, on the graphite surface [35,37]. We also note that the atomic-scale pattern of graphite in Fig. 5a far away from the defect is triangular, which is the expected structure in the STM images of graphite, whereas the pattern in Fig. 5c is of honeycomb type. It has been well reported in the literature that the former type is predominantly found over the latter, in agreement with our own observations. However, the reason why the honeycomb structure is sometimes found has not yet been outright clarified. It has been suggested that it might arise as a result of a slight displacement of the uppermost graphene layer relative to the layers underneath [38], but a conclusive explanation has not been given so far. We also observe a lattice distortion in the area immediately surrounding the protrusion in Fig. 5c, which can be identified as a $(\sqrt{3} \times \sqrt{3})R30^\circ$ superstructure. This is a well-known type of distortion of electronic origin that is occasionally observed by STM near defects on graphitic surfaces [11].

Concerning UVO oxidation, it is not likely that the initial atomic vacancies (Fig. 2a), which subsequently develop into nanometer-sized pits (Fig. 2b and c), were created by ion bombardment in

an overall etching process that is dominated by chemical attack. This is because no external electromagnetic fields that could accelerate any charged species are created inside the UVO treatment chamber, and the thermal energy (~0.03 eV) is much smaller than the threshold energy required for the creation of a carbon vacancy or any other type of stable defect [15]. Instead, we propose an etching mechanism that would be similar to that reported for the oxidation of graphite by microwave-generated plasma [11]: the chemically reactive O and O_3 species, and also possibly excited O_2 species, produced by UV irradiation of O_2 molecules become chemisorbed onto the graphite basal surface, leading to a weakening and a subsequent finite probability of destruction of the C—C bonds adjacent to the chemisorbed species, eventually causing the formation of a gaseous oxidation product, such as CO. Thus, the release of a carbon atom from the graphite surface in the form of a CO molecule would leave behind an atomic vacancy, explaining the formation of this type of defect on the UVO-treated samples (Fig. 2a). The ensuing etching selectivity and development of localized features (pits, trenches; see Figs. 2 and 3) can be explained if we assume that the chemisorbed O or O_3 species can diffuse over the graphite surface, which would lead to one of the two following possible scenarios: either (1) the chemisorbed species desorbs as CO at some point of its random path across a pristine area of the graphite surface, generating an atomic vacancy, or (2) during its random diffusion the chemisorbed species meets a vacancy site previously created, where it becomes more strongly chemisorbed as a result of the presence of dangling bonds/increased electronic density, forming an oxygen functional group that eventually desorbs as CO/CO_2, thereby expanding the original vacancy, first into multiatomic vacancies and then into nanometer-sized pits (or through widening of grain boundaries). Such mechanism provides the basis for the selectivity observed in the etching of the graphite surface upon UVO oxidation (Figs. 2 and 3), and is in marked contrast with the complete lack of selectivity observed for DBD air plasma oxidation (Figs. 1 and 4), dominated by ion bombardment.

Ion bombardment not only induces sputtering of carbon atoms from the graphite surface, but also leads to implantation of the impinging species, as well as of a fraction of the sputtered carbon atoms, below the surface graphene [39]. It has been shown that Ar, C or Cs atoms implanted on graphite usually lead to the appearance of recognizable features in the STM images, in the form of protruding dome-like structures a few nm in lateral size with unperturbed atomic-scale pattern and atomically smooth edges [15,37,40]. We have occasionally observed such type of protruding feature in the STM images of DBD air plasma-treated graphite (images not shown), which we attribute to implanted Ar or C atoms, but never in the STM images of samples oxidized by UVO, consistent with a lack of ion bombardment in the latter case. Furthermore, the depressions observed for DBD air plasma-oxidized HOPG share many characteristics with the STM features induced by implanted Ar or C atoms, i.e. rounded, dome-like shape, unperturbed atomic-scale pattern and atomically smooth edge, which suggests that they also correspond to some implanted species. To the best of our knowledge, no general rule has been reported in the literature that can tell us which types of implanted species will lead to a depression or to a protruding structure. In the case of implanted Ar, C or Cs, their protruding appearance by STM was attributed to an upward deformation of the surface graphene due to the presence of the interstitial atom and/or to an increase of the local density of electronic states near the Fermi level for the surface graphene as a result of charge donation from the implanted species [15,37,40]. Along the same lines, the depression can be tentatively ascribed to an area of reduced local density of states near the Fermi level due to charge donation from the surface graphene to the implanted species. This implies that the latter should possess a charge-accepting or electronegative character, and a likely candidate in this regard would be an oxygen species [30]. As will be shown below, only oxygen is introduced on the graphite surface in significant amounts upon DBD air plasma treatment. Thus, a reasonable mechanism for the etching of graphite by this type of plasma would involve the bombardment of plasma-generated oxygen ions, such as O^+, having a twofold effect: (1) ejection of carbon atoms from the graphite surface with the consequential creation of atomic vacancies, which are detected as protrusions in the STM images, and (2) implantation of the impinging oxygen species below the surface graphene, which are visualized by STM as depressions.

To further illustrate the basic differences in the etching mechanism between the two types of treatment, we show in Fig. 6 typical atomic-scale images of HOPG surfaces following extended exposure to the DBD air plasma (71 ms, a) and UVO (60 min, b). In Fig. 6a, we see atomic-sized spots, indicating that atomic resolution was indeed achieved, but the spots are not arranged into the triangular pattern characteristic of pristine graphite and atomic-scale periodicity is apparently absent. Thus, we can conclude that no graphitic, ordered areas of significant dimensions remain on the HOPG surface upon extended DBD air plasma treatments. In the case of UVO oxidation, because etching occurs preferentially at defect sites, a considerable fraction of the graphite surface remains essentially unaltered, and distorted structures in the atomic-scale STM images are mostly observed at, or close to, the etch pit edges (Fig. 6b). In consequence, structures with graphitic order are retained to a much greater extent on the HOPG surface upon UVO oxidation compared to oxidation by DBD air plasma.

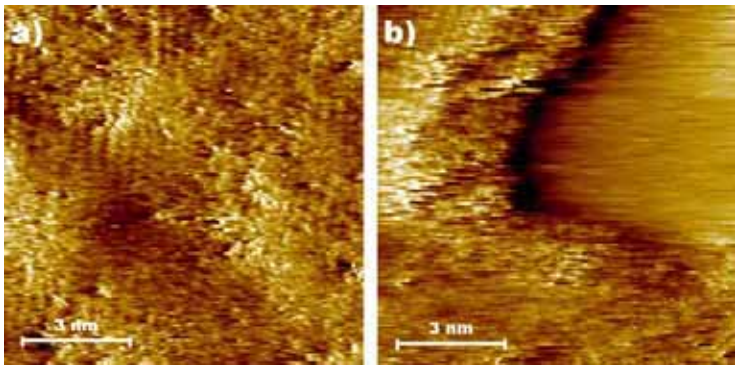

Fig. 6. Atomic-scale STM images of graphite surfaces following extended exposure to DBD air plasma (71 ms, a) and UVO (60 min, b).

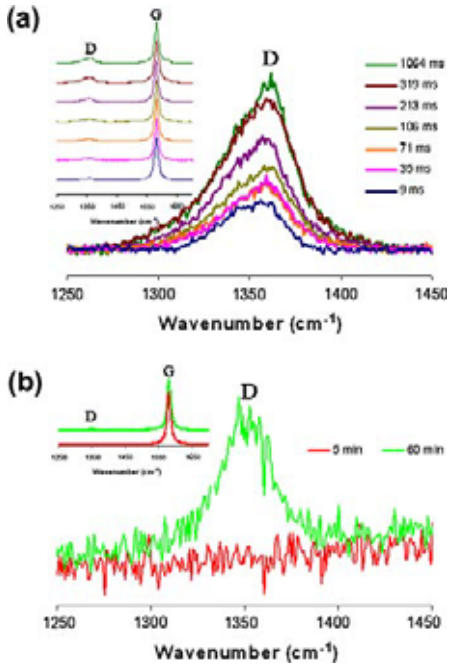

Fig. 7. Raman D band measured for graphite surfaces subjected to DBD air plasma (a) and UVO (b) for different periods of time. The insets to (a) and (b) show Raman spectra covering both the D and G bands. To allow a direct comparison between samples modified by a given type of treatment for different times, their G band has been normalized to the same height.

The substantial differences in surface structure revealed by a local probe such as STM between DBD air plasma- and UVO-oxidized graphite were also evidenced by global probes of surface structure (Raman spectroscopy) and chemistry (XPS). The inset of Fig. 7a shows representative Raman spectra for HOPG samples treated by DBD air plasma for several different periods. For short treatments (i.e., up to 35 ms), the modification of the graphite surface by the plasma was not uniform, as mentioned previously. In these cases, the Raman spectra were recorded by focusing the laser within filament-struck areas. On the other hand, for long plasma treatments the HOPG surface is knocked by a sufficiently large number of filaments, so that the modification is essentially uniform. The Raman spectrum of all the plasma-treated samples is dominated by the well-known G band, located at $\sim$1580 cm^{-1}. A weak band at $\sim$1360 cm^{-1} (the D band) is also observed, its relative intensity increasing with plasma treatment time. The D band is absent from pristine, defect-free graphite and its appearance is related to the presence of structural disorder in graphitic materials, in such a way that the integrated intensity ratio for the D and G bands (I_D/I_G) increases with the amount of disorder [41]. We see from Fig. 7a that the intensity of the D band steadily increases with the DBD plasma treatment time, which indicates the progressive introduction of defects on the graphite surface. In any case, however, the creation of structural disorder is quite limited, as the I_D/I_G ratio remains relatively small even for the longest treatment (i.e. 1064 ms, $I_D/I_G \sim 0.28$). The introduction of structural disorder was also evidenced for the UVO-oxidized samples, although to a much smaller extent (Fig. 7b). No appreciable D band could be detected for an UVO treatment time of 5 min, which only generated isolated atomic vacancies on the HOPG surface (Fig. 2a), whereas long treatments (e.g., 60 min, Fig. 2d) only led to faint D bands (see inset of Fig. 7b) with I_D/I_G ratios as small as 0.04. Thus, UVO oxidation can only introduce a tiny amount of structural disorder on graphite.

From the Raman spectroscopy results, we can make several observations. First, the small I_D/I_G ratios measured for DBD air plasma- and UVO-treated HOPG are probably related to a large degree to the fact that modification only affects the few uppermost graphene layers of the sample in both cases, while at least several tens of graphene layers are typically probed by this technique [33]. Consequently, most of the sampled volume in the Raman experiments documented here corresponds to unmodified, defect-free graphite, which does not contribute to the D band. Second, the differences reported between the Raman spectra of DBD air plasma- and UVO-oxidized graphite are consistent with the STM observations. Atomic-scale STM imaging indicated that graphitic order was essentially preserved on a significant fraction of the HOPG surface following UVO treatments of any length, structural disorder being mainly associated with the edges of pits and trenches (Fig. 6b). By contrast, structural disorder was ubiquitous on graphite surfaces treated by DBD air plasma (Fig. 6a). Accordingly, more intense D bands should be expected in the Raman spectra of samples exposed to DBD air plasma compared to samples oxidized by UVO, in agreement with the experimental results (Fig. 7).

We anticipate that more oxygen functionalities can be introduced on HOPG surfaces exposed to DBD air plasma in relation to surfaces oxidized by UVO. This is because we expect oxygen functional groups to be mainly located at defects, much more abundant in the former, where carbon atoms with dangling bonds, and therefore susceptible to bind to oxygen, are present [11]. We also note that, according to the previous discussion, oxygen may be additionally present as interstitial species below the surface graphene due to ion bombardment in the case of DBD air plasma, a mechanism that is not possible for UVO oxidation. Consistent with these expectations, the XPS results indicated that more oxygen could be introduced through DBD air plasma treatment compared to UVO oxidation (Table 1). For DBD air plasma oxidation, the atomic percentage of oxygen steadily increases with treatment time up to a value of $\sim$7%, attained after exposures of 213 ms, which apparently cannot be raised further with longer treatments (e.g., 319 or 1064 ms). A small amount of nitrogen (below 1%) is also introduced, but only after extended treatment (213 ms and longer times). By contrast, the atomic percentage of oxygen on HOPG surfaces following UVO oxidations is much smaller, reaching only 1.5% for the longest treatments (60 min). Fig. 8 shows the high resolution C1s (a), O1s (b) and N1s (c) spectra for the sample with the most extensive chemical modification (i.e. the sample treated by DBD plasma for 213 ms). The C1s spectrum (Fig. 8a) was fitted

Table 1
Atomic percentages of C, O and N determined by XPS for graphite samples exposed to DBD air plasma and UVO for different periods of time.

	DBD air plasma							UVO	
	9 ms	35 ms	71 ms	106 ms	213 ms	319 ms	1064 ms	5 min	60 min
C	98.8	98.7	96.3	95.2	92.0	93.6	93.1	99.4	98.5
O	1.2	1.3	3.7	4.8	7.1	5.7	6.2	0.6	1.5
N	–	–	–	–	0.9	0.7	0.7	–	–

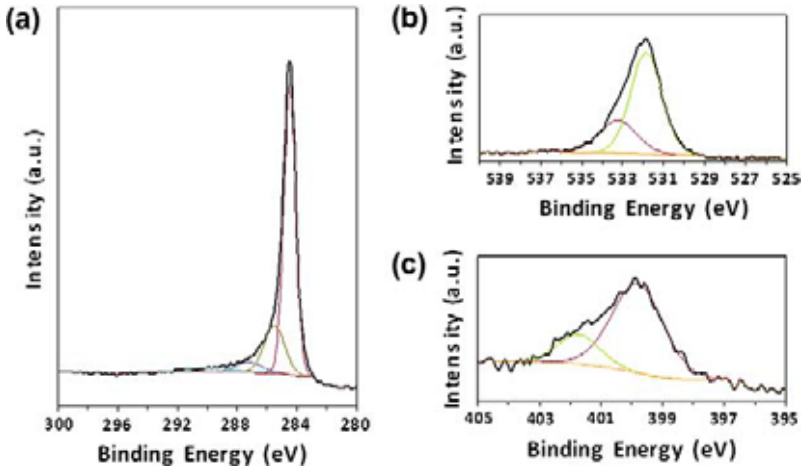

Fig. 8. High-resolution C1s (a), O1s (b) and N1s (c) X-ray photoelectron spectra of a graphite surface subjected to DBD air plasma treatment for 213 ms.

to four components, located at 284.5 (graphitic C=C species), 285.5 (C—C bonding in defected regions, C—O and C—N species), 287.2 (C=O species) and 289.9 eV ($\pi \rightarrow \pi^*$ shake-up satellite) [33]. We note from Fig. 8a that the contribution from the 285.5 and 287.2 eV components is not very significant, in agreement with the relatively limited amount of oxygen and nitrogen introduced on this sample surface (~7% O and ~1% N, Table 1). The O1s spectrum (Fig. 8b) was fitted to two components: 531.9 (C—O—C/C—OH groups and adsorbed O_2/H_2O) and 533.3 eV (O=C—O groups and adsorbed O_2/H_2O). Finally, the N1s spectrum (Fig. 8c) could be fitted to components at 399.8 (amide, amine and pyrrolic nitrogen groups) and 401.7 eV (quaternary nitrogen).

Taken together, the STM, Raman spectroscopy and XPS results consistently show evidence of the differences in structural and chemical characteristics induced by physically driven (DBD air plasma) and chemically driven (UVO) attack in the oxidation of graphite surfaces. Understanding such differences could be useful when choosing the most adequate type of surface modification for specific purposes. Thus, DBD air plasma treatment would be preferred over UVO oxidation when a significant and uniform increase in surface reactivity is required, for instance if the carbon surface is to be used as a support for catalyst particles, where the uniformity of the particle dispersion is often a critical issue [5,42]. On the other hand, oxidation by UVO would be the treatment of choice if corrals (i.e., the etch pits) are needed to confine molecules that are subsequently studied by scanning probe microscopy techniques [43], while surface reactivity is kept relatively low.

4. Conclusions

STM, Raman spectroscopy and XPS have revealed significant differences in the surface structure and chemistry of graphite as a result of oxidation treatments by DBD air plasma and UVO. Different mechanisms are thought to dominate the etching process in the two cases. For DBD air plasma treatment, etching was deduced to be non-selective and to proceed mainly via physical processes (i.e., ion bombardment), in such a way that the attack basically progresses by a simple accumulation of atomic-scale defects (vacancy and interstitial defects) generated at random locations on the graphite surface. By contrast, etching by UVO is much more selective and takes place via creation of atomic vacancies at a limited number of surface locations, which subsequently expand into nanometer-sized pits, a process attributed to the combination of surface carbon atoms with chemically reactive O and O_3. As a result, the graphite surfaces can exhibit significant structural differences depending on the type of treatment they were subjected to: atomic-scale disorder can be ubiquitously produced with DBD air plasma, whereas a large fraction of the sample surface retains a clearly graphitic character upon UVO treatments, structural disorder being mainly located at or near the pit edges. The amount of oxygen that can be introduced on the graphite surface by these two treatments was clearly related to such structural characteristics. Lower oxygen contents were measured by XPS on UVO-oxidized samples compared to samples treated by DBD air plasma, which can be explained by the presence of a significant fraction of unaltered, graphitic areas on the former, where oxygen functional groups are not thought to be present.

Acknowledgments

Funding of this work by the Spanish MEC through project CTQ2005-09105-C04-02 and by CSIC (I3 project 200680I198) is gratefully acknowledged. P.S.-F. also acknowledges CSIC for an I3P pre-doctoral contract.

References

[1] E. Auer, A. Freund, J. Pietsch, T. Tacke, Appl. Catal. Gen. 173 (1998) 259.
[2] Z. Xu, P. Hu, S. Wang, X. Wang, Appl. Surf. Sci. 254 (2008) 1915.
[3] J. Roth, E. Tsitrone, A. Loarte, Nucl. Instrum. Meth. B 258 (2007) 253.
[4] Y. Kusano, H. Mortensen, B. Stenum, S. Goutianos, S. Mitra, A. Ghanbari-Siahkali, P. Kingshott, B.F. Sorensen, H. Bindslev, Int. J. Adhes. Adhes. 27 (2007) 402.
[5] D.-Q. Yang, E. Sacher, Chem. Mater. 18 (2006) 1811.
[6] U. Cvelbar, B. Markoli, I. Poberaj, A. Zalar, L. Kosec, S. Spaic, Appl. Surf. Sci. 253 (2006) 1861.
[7] S. Kwon, R. Vidic, E. Borguet, Carbon 40 (2002) 2351.
[8] H. Chang, A.J. Bard, J. Am. Chem. Soc. 113 (1991) 5588.
[9] S.M. Lee, Y.H. Lee, Y.G. Hwang, J.R. Hahn, H. Kang, Phys. Rev. Lett. 82 (1999) 217.
[10] J.I. Paredes, A. Martinez-Alonso, J.M.D. Tascon, J. Mater. Chem. 10 (2000) 1575.
[11] J.I. Paredes, A. Martinez-Alonso, J.M.D. Tascon, Langmuir 18 (2002) 4314.
[12] E. Vietzke, T. Tanabe, V. Philipps, M. Erdweg, K. Flaskamp, J. Nucl. Mater. 145–147 (1987) 425.
[13] F. Stevens, L.A. Kolodny, J. Thomas, P. Beebe, J. Phys. Chem. B 102 (1998) 10799.
[14] J.R. Hahn, H. Kang, J. Vac. Sci. Technol. A 17 (1999) 1606.
[15] D. Marton, H. Bu, K.J. Boyd, S.S. Todorov, A.H. Albayati, J.W. Rabalais, Surf. Sci. 326 (1995) L489.
[16] B. An, S. Fukuyama, K. Yokogawa, M. Yoshimura, Jpn. J. Appl. Phys. 39 (2000) 3732.
[17] J.C.M. López, M.C.G. Passeggi Jr, J. Ferrón, Surf. Sci. 602 (2008) 671.

[18] J.R. Hahn, H. Kang, Surf. Sci. 358 (1996) 165.
[19] J.I. Paredes, A. Martinez-Alonso, J.M.D. Tascon, Carbon 40 (2002) 1101.
[20] B.L. Rousseau, Appl. Phys. A 77 (2003) 591.
[21] J.M. Simmons, B.M. Nichols, S.E. Baker, M.S. Marcus, O.M. Castellini, C.S. Lee, R.J. Hamers, M.A. Eriksson, J. Phys. Chem. B 110 (2006) 7113.
[22] S. Agrawal, M.S. Raghuveer, H. Li, G. Ramanath, Appl. Phys. Lett. 90 (2007) 193104.
[23] J.M. Peng, J.-B. Donnet, T.K. Wang, S. Rebouillat (Eds.), Carbon Fibers, Dekker, New York, 1998 (Chapter 3).
[24] K.T. Nicholson, T.K. Minton, S.J. Sibener, J. Phys. Chem. B 109 (2005) 8476.
[25] H.-X. You, N.M.D. Brown, K.F. Al-Assadi, Surf. Sci. 284 (1993) 263.
[26] M.A. Lieberman, A. Lichtenberg, Principles of Plasma Discharges and Materials Processing, John Wiley and Sons, New York, 1994 (Chapter 9).
[27] T.I.T. Okpalugo, P. Papakonstantinou, H. Murphy, J. Mclaughlin, N.M.D. Brown, Carbon 43 (2005) 2951.
[28] D. Lee, S.H. Hong, W.-T. Ju, K.-H. Paek, Surf. Coat. Technol. 200 (2005) 2277.
[29] S. Kodama, H. Sekiguchi, Thin Solid Films 506–507 (2006) 327.
[30] P. Solís-Fernández, J.I. Paredes, M.J. López, I. Cabria, J.A. Alonso, A. Martínez-Alonso, J.M.D. Tascón, J. Phys. Chem. C 113 (2009) 18719.
[31] A. Chirokov, A. Gutsol, A. Fridman, K.D. Sieber, J.M. Grace, K.S. Robinson, Plasma Sources Sci. Technol. 13 (2004) 623.
[32] C.D. Wagner, L.E. Davis, M.V. Zeller, J.A. Taylor, R.H. Raymond, L.H. Gale, Surf. Interface Anal. 3 (1981) 211.
[33] J.I. Paredes, A. Martinez-Alonso, J.M.D. Tascon, Langmuir 23 (2007) 8932.
[34] S. Habenicht, Phys. Rev. B 63 (2001) 125419.
[35] J.R. Hahn, H. Kang, S. Song, I.C. Jeon, Phys. Rev. B 53 (1996) 1725.
[36] J.R. Hahn, H. Kang, Phys. Rev. B 60 (1999) 6007.
[37] J. Kibsgaard, J.V. Lauritsen, E. Laegsgaard, B.S. Clausen, H. Topsoe, F. Besenbacher, J. Am. Chem. Soc. 128 (2006) 13950.
[38] J.I. Paredes, A. Martinez-Alonso, J.M.D. Tascon, Carbon 39 (2001) 476.
[39] A.V. Krasheninnikov, F. Banhart, Nat. Mater. 6 (2007) 723.
[40] J.R. Hahn, H. Kang, J. Phys. Chem. B 106 (2002) 7445.
[41] A.C. Ferrari, J. Robertson, Phys. Rev. B 61 (2000) 14095.
[42] L.L. Wang, X.C. Ma, Y. Qi, P. Jiang, J.F. Jia, Q.K. Xue, J. Jiao, X.H. Bao, Ultramicroscopy 105 (2005) 1.
[43] H. Hovel, T. Becker, A. Bettac, B. Reihl, M. Tschudy, E.J. Williams, J. Appl. Phys. 81 (1997) 154.

New atomic-scale features in graphite surfaces treated in a dielectric barrier discharge plasma

*Pablo Solís-Fernández, Juan I. Paredes, Amelia Martínez-Alonso, Juan M.D. Tascón**

Instituto Nacional del Carbón, CSIC, Apartado 73, 33080 Oviedo, Spain

ARTICLE INFO

Article history:
Received 17 March 2008
Accepted 16 May 2008
Available online 3 June 2008

ABSTRACT

The effects of an air plasma generated by a dielectric barrier discharge (DBD) on highly oriented pyrolytic graphite (HOPG) have been investigated through scanning tunneling microscopy (STM), Raman and XPS spectroscopies. Three main types of nanometer/atomic scale features were identified by STM: (i) small bumps, attributed to surface atomic vacancies; (ii) smooth bumps, attributed to interstitial Ar or C atoms; and (iii) depressions not previously reported for graphite, and tentatively attributed to interstitial oxygen species. The evolution of the STM features suggests that the surface modification of HOPG by an air DBD plasma is dominated by physical processes (ion bombardment).

Plasmas are promising media for the surface modification and functionalization of highly ordered (and therefore, little reactive) carbonaceous solids such as graphites. Information on the mechanism of graphite attack by some low-pressure plasmas is readily available [1]. However, this is not the case with a dielectric barrier discharge (DBD) plasma, which only in the last few years has been employed for surface treatment and that offers some possible advantages for practical uses (e.g., no need of working under vacuum). Very rare examples exist on the use of DBD plasma as a surface treatment medium for carbons [2–5], rather it has been applied to other materials, such as polymers [6–8]. Central to the understanding of the modification of carbonaceous solids by plasmas is the investigation of the individual events (down to the nanometric/atomic scale) that drive the etching process [1]. In this work, we have used scanning tunneling microscopy (STM) to investigate for the first time the individual events that drive the DBD plasma attack of highly oriented pyrolytic graphite (HOPG). It is expected that the use of HOPG as a model carbon material will shed some light on the general features of DBD plasma-carbon interactions, and will therefore provide guidelines for the treatment of less "ideal" solid carbons.

HOPG (ZYH grade) was cut into pieces of approximate dimensions $10 \times 10 \times 1.5$ mm^3. The HOPG pieces were exposed to an air plasma generated in a DBD at atmospheric pressure and room temperature in a plasma processor (Arcotec VB A4). The typical operational parameters (200 W power, 9 ms treatment time) were adjusted so as to produce minimum sample modification focusing on the individual effects (down to the atomic level) brought about by DBD plasma exposure on the graphite surface. To study the effect of treatment time, longer exposures (up to 70 ms) were also employed. The plasma-treated samples were characterized by STM in a Nanoscope IIIa Multimode apparatus (Veeco Instruments) operating in air at room temperature in the constant current mode with tunneling parameters of 100 mV (bias voltage) and 1.0 nA (tunneling current). Mechanically prepared Pt/Ir (80/20) tips were employed. Additional characterization was carried out by means of Raman spectroscopy (Horiba Jobin-Yvon LabRam instrument, with a laser excitation wavelength of 532 nm) and X-ray photoelectron spectroscopy (XPS; SAGE HR 100 spectrometer from SPECS, using a Mg Kα X-ray source).

Let us first focus on the types of features revealed by STM at the nanometric/atomic level on the surface of DBD plasma-treated HOPG. Fig. 1a shows a general, nanometer scale STM image that reveals the individual effects of this plasma on the HOPG surface. Two main types of feature have developed upon plasma exposure: protrusions or bumps (bright features) and depressions (dark features), where the former can be further divided into two sub-types, as described below. All these features can be attributed to different types of atomic-scale defects formed by the plasma treatment on the graphite lattice, namely:

(a) Small bumps 1–7 nm in diameter and ~0.2–0.3 nm high, mostly rounded in shape and with distorted atomic-scale structure (Fig. 1b). In principle, these features can be attributed to the presence of atomic vacancies on the HOPG surface, either single-atom (~1 nm wide, Fig. 1b) or multi-atom (>1 nm), induced by plasma

* *Corresponding author:* Fax: +34 985 297662.
E-mail address: tascon@incar.csic.es (J.M.D. Tascón).
0008-6223/$ - see front matter
doi:10.1016/j.carbon.2008.05.021

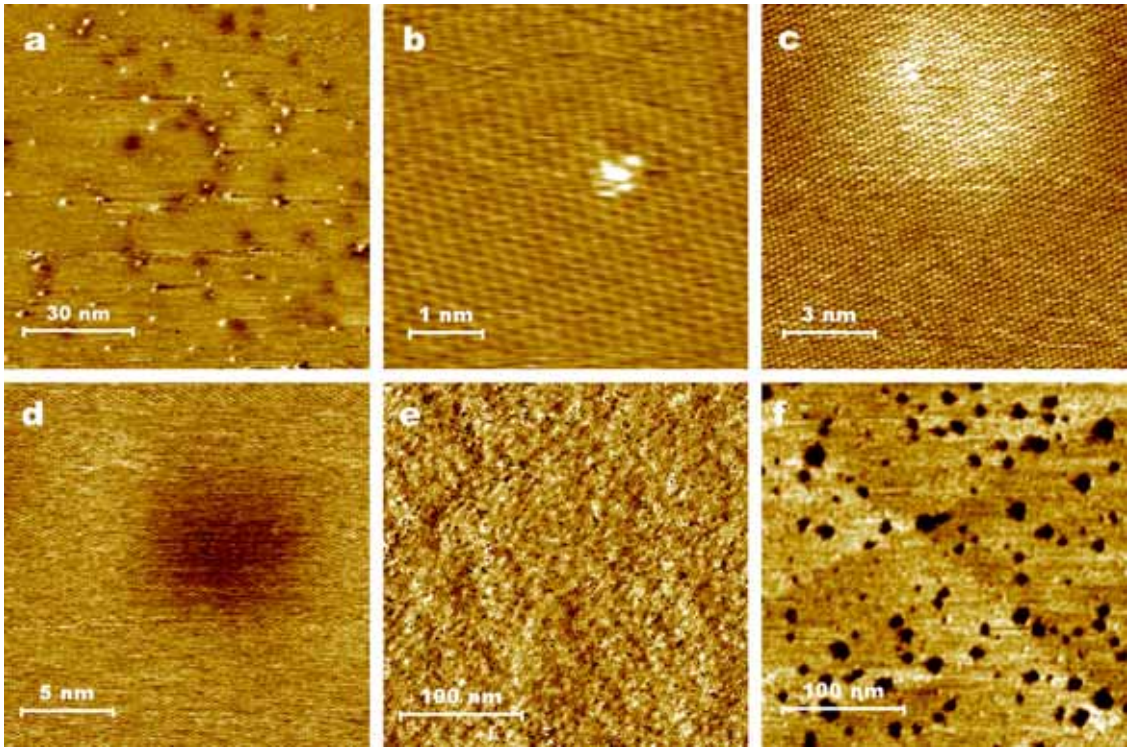

Fig. 1 – (a) General, nanometer scale STM image of HOPG revealing the individual effects of DBD plasma used, (b) Atomic resolution image of a small bump attributed to a single-atom vacancy, (c) Atomic scale image of a smooth bump ascribed to interstitial Ar or C atoms, (d) Atomic scale image of a circular depression attributed to interstitial oxygen species, (e) Typical nanometer scale STM image of the HOPG surface after extended treatment in DBD plasma and (f) Typical nanometer scale STM image of the HOPG surface exposed to UV-generated ozone.

attack. Atomic vacancies in graphite display an essentially flat topography, but induce an increase in the density of electronic states near the Fermi level in the carbon atoms around them, which is reflected in the STM images as an apparent protrusion [9,10]. Similar bumps have been found in HOPG samples modified by exposure to more conventional types of plasmas, e.g., oxygen microwave plasma, and attributed to atomic vacancies, as they develop into nanometer-sized pits with extended plasma treatment [1,11].

(b) Smooth bumps of very low height (<0.1 nm) and an extended diameter (~6 nm) (Fig. 1c), where the structure and periodicity of pristine graphite as seen by STM (i.e., a triangular pattern with ~0.25 nm periodicity) is maintained throughout the bump. Features with such characteristics have been previously attributed to interstitial Ar or C atoms [12]. Let us remember here that the concentration of Ar in ambient air is close to 1%, i.e. higher than that of, for instance, CO_2. Unlike the features described in (a), the origin of these smooth bumps would be principally topographic (rather than electronic). This type of defect was very rare in comparison with the other types.

(c) Smooth circular depressions, 5–7 nm in diameter and only ~0.2 nm deep, where the structure and periodicity of pristine graphite is preserved (Fig. 1d). To the best of our knowledge, this kind of feature has never been reported for HOPG or any other carbon material. The depressions cannot be attributed to pits on the HOPG surface, as their depth is significantly smaller than that of monolayer-deep pits (~0.34 nm). Furthermore, the edge of the depressions is not defined at all, since the apparent height smoothly decreases when moving from outside of the depression towards its center. This is in marked contrast with the extremely sharp edges characteristic of monolayer-deep pits in graphite [13]. These observations lead us to conclude that the depressions seen in the STM images do not have a topographical origin, but an electronic one, comparable to imaging of the atomic vacancies as bumps. The fact that the structure and periodicity of the pristine graphite lattice is preserved within the depression, similar to the case of bumps attributed to interstitial atoms in graphite [10,12], suggests that the depressions could also be produced by interstitial species. Thus, we tentatively attribute the depressions to the presence of interstitial oxygen species located between the two outermost graphenes in the sample. The electronegative character of oxygen would induce a phenomenon opposite to that in (a), whereby a decrease in the density of electronic states near the Fermi level of the carbon atoms in the uppermost graphene is imaged in

STM as an apparent depression, although the surface topography would remain mostly flat.

The observation and interpretation of features (b) and (c) requires the DBD plasma attack to be driven, at least in part, by physical processes (i.e., ion bombardment). In this regard, when comparing HOPG samples exposed to the DBD plasma for different periods of time, we have observed that the defects imaged by STM did not evolve with treatment time (i.e., the bumps and depressions did not grow in size, nor changed their appearance), and only an increase of their densities with increasing time of exposure could be observed. This strongly suggests that the phenomena involved in their formation are physical in nature, which is supported by the close similarity of the findings from this work to the effects, for example, of sputtering with low-energy ions, whereby insertion of different species and vacancy creation has been said to occur [9,12]. Unlike this, a typical chemical attack such as that produced by oxygen microwave plasma, ozone or thermal treatment with molecular oxygen would be more selective and would progress to create pits and trenches in the HOPG surface at long exposure times [13,14]; however, we have never observed such features in the case of DBD plasma treatment. This is exemplified in Fig. 1e, which depicts a typical general image of an HOPG surface after a long (70 ms) DBD plasma treatment. In this case, the surface structure is characterized by an extremely uniform, smoothly rough topography without large scale features, such as pits or trenches, suggesting a non-selective attack. By contrast, ozone-treated HOPG surfaces (Fig. 1f) are characterized by the development of 0.3–1.0 nm deep pits, indicative of selective chemical attack. These facts lead us to conclude that the etching involved in the interaction of air DBD plasma with the HOPG surface is mainly physical, rather than chemical, in nature. As mentioned above, this would be different to the case of oxygen microwave plasma, where the attack is chemical in nature [1], but would be relatively similar to radiofrequency-generated plasmas [15–17].

The Raman spectrum of an air DBD plasma-treated graphite surface in an area with a density of defects similar to that

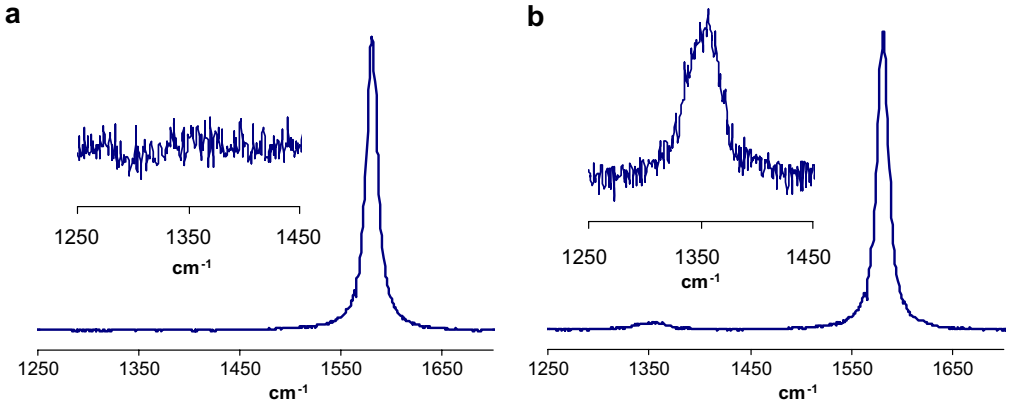

Fig. 2 – Raman spectra of pristine, untreated HOPG (a) and HOPG treated in the DBD plasma with a density of features similar to that in Fig. 1a (b). The insets show an enlargement of the D-band regions. To facilitate comparisons between both spectra, their G band has been normalized to the same height for clarity.

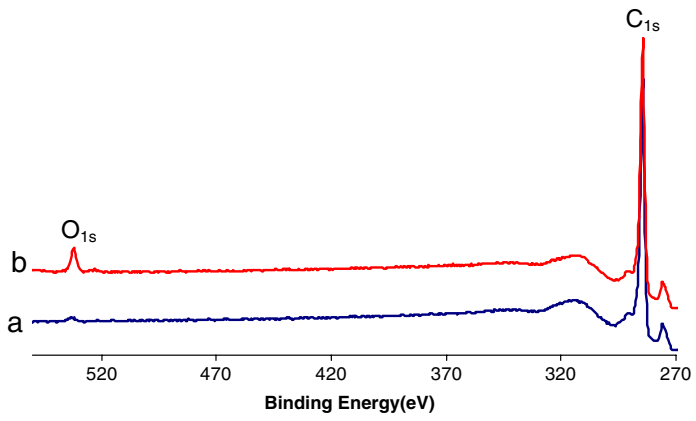

Fig. 3 – X-ray photoelectron spectra of pristine, untreated HOPG (a) and HOPG treated in the DBD plasma (b). To allow comparison, the spectra have been normalized to the same height of the C 1s peak and they have been offset for clarity.

seen in Fig. 1a indicates the introduction of structural damage to the carbon lattice (development of the D band at ~1360 cm^{-1}, Fig. 2). The integrated intensity ratio of the D and G bands increased from 0 (spectrum a) to 0.042 (spectrum b). This should be mostly attributed to the presence of atomic vacancies, as the structural distortion introduced in the carbon lattice by interstitial species would be expected to be comparatively smaller. Concerning the surface chemistry of the DBD plasma-treated HOPG samples, the XPS data (Fig. 3) revealed the introduction of only oxygen after the treatment; the O_{1s} to C_{1s} atomic ratio increased from 0.006 (untreated, spectrum a) to 0.038 (70 ms treatment, spectrum b). This result supports the idea that if the depressions seen in the STM images are to be attributed to interstitial species, these should be oxygen species. On the other hand, the absence of N_{1s} band at 400 eV in the spectra of Fig. 3 allows one to rule out a possible ascription of both the smooth bumps with very small height and the depressions to interstitial nitrogen species (a weak N_{1s} band could be observed to appear only after very aggressive DBD plasma treatments at much longer exposure times).

To summarize our findings, modification by air DBD plasma of the HOPG surface generates three different types of nanometric/atomic scale defects with different apparent heights, which we tentatively attribute to atomic vacancies, interstitial oxygen species and other types of interstitial atoms. The features thought to be due to interstitial oxygen species (smooth depressions) have not been previously reported on HOPG, and thus constitute a novel type of atomic-scale feature of carbon materials revealed by STM. The etching induced by DBD plasma was interpreted to be mainly physical, which would explain why the formation of interstitial species below the topmost graphene seems to be favored in this type of treatment.

Acknowledgements

P.S.-F. acknowledges receipt of an I3P pre-doctoral Contract from CSIC. Funding of this work by the Spanish MEC through projects CTQ2005-09105-CO4-02 and VEM2004-08576 is gratefully acknowledged. Financial support from CSIC (I3 Project No. 200680I198) is also acknowledged.

REFERENCES

[1] Paredes JI, Martínez-Alonso A, Tascón JMD. Early stages of plasma oxidation of graphite: nanoscale physicochemical changes as detected by scanning probe microscopies. Langmuir 2002;18(11):4314–23.

[2] Okpalugo TIT, Papakonstantinou P, Murphy H, Mclaughlin J, Brown NMD. Oxidative functionalization of carbon nanotubes in atmospheric pressure filamentary dielectric barrier discharge (APDBD). Carbon 2005;43(14):2951–9.

[3] Lee D, Hong SH, Paek KH, Ju WT. Adsorbability enhancement of activated carbon by dielectric barrier discharge plasma treatment. Surf Coat Technol 2005;200(7):2277–82.

[4] Kodama S, Sekiguchi H. Estimation of point of zero charge for activated carbon treated with atmospheric pressure non-thermal oxygen plasmas. Thin Solid Films 2006;506:327–30.

[5] Kusano Y, Mortensen H, Stenum B, Goutianos S, Mitra S, Ghanbari-Siahkali A, et al. Atmospheric pressure plasma treatment of glassy carbon for adhesion improvement. Int J Adhesion Adhesives 2007;27(5):402–8.

[6] Liu CZ, Brown NMD, Meenan BJ. Dielectric barrier discharge (DBD) processing of PMMA surface: optimization of operational parameters. Surf Coat Technol 2006;201(6):2341–50.

[7] Borcia G, Brown NMD. Hydrophobic coatings on selected polymers in an atmospheric pressure dielectric barrier discharge. J Phys D: Appl Phys 2007;40(7):1927–36.

[8] Morent R, De Geyter N, Leys C, Gengembre L, Payen E. Study of the ageing behaviour of polymer films treated with a dielectric barrier discharge in air, helium and argon at medium pressure. Surf Coat Technol 2007;201(18):7847–54.

[9] Hahn JR, Kang H. Vacancy and interstitial defects at graphite surfaces: Scanning tunneling microscopic study of the structure, electronic property, and yield for ion-induced defect creation. Phys Rev 1999;B60(8):6007–17.

[10] Kibsgaard J, Lauritsen JV, Lægsgaard E, Clausen BS, Topsøe H, Besenbacher F. Cluster-support interactions and morphology of MoS_2 nanoclusters in a graphite-supported hydrotreating model catalyst. J Am Chem Soc 2006;128:13950–8.

[11] Paredes JI, Martínez-Alonso A, Tascón JMD. Characterization of microporosity and mesoporosity in carbonaceous materials by scanning tunneling microscopy. Langmuir 2001;17(2):474–80.

[12] Marton D, Bu H, Boyd KJ, Todorov SS, Albayati AH, Rabalais JW. On the defect structure due to low-energy ion-bombardment of graphite. Surf Sci 1995;326(3):L489–93.

[13] Paredes JI, Martínez-Alonso A, Tascón JMD. Comparative study of the air and oxygen plasma oxidation of graphite: a scanning tunneling and atomic force microscopy investigation. Carbon 2000;38(8):1183–97.

[14] Paredes JI, Martínez-Alonso A, Tascón JMD. Atomic force microscopy investigation of the surface modification of highly oriented pyrolytic graphite by oxygen plasma. J Mater Chem 2000;10(7):1585–91.

[15] You HX, Brown NMD, Al-Assadi KF. An exploratory study by scanning tunneling microscopy of the surface modification of highly oriented pyrolytic graphite using an argon radio-frequency plasma discharge. J Mater Sci Lett 1992;11(24):1671–4.

[16] You H-X, Brown NMD, Al-Assadi KF. Radio-frequency (RF) plasma etching of graphite with oxygen: a scanning tunneling microscope study. Surf Sci 1993;284(3):263–72.

[17] You HX, Brown NMD, Al-Assadi KF, Meenan BJ. Surface characterization of highly oriented pyrolytic graphite modified by oxygen radio-frequency plasmas. J Mater Sci Lett 1993;12(4):201–4.

J. Phys. Chem. C **2009,** *113,* 18719–18729 **18719**

A Combined Experimental and Theoretical Investigation of Atomic-Scale Defects Produced on Graphite Surfaces by Dielectric Barrier Discharge Plasma Treatment

P. Solís-Fernández,[†] J. I. Paredes,*[,†] M. J. López,[‡] I. Cabria,[‡] J. A. Alonso,[‡] A. Martínez-Alonso,[†] and J. M. D. Tascón[†]

Instituto Nacional del Carbón, CSIC, Apartado 73, 33080 Oviedo, Spain, and Departamento de Física Teórica, Atómica y Óptica, Universidad de Valladolid, 47011 Valladolid, Spain

Received: March 5, 2009; Revised Manuscript Received: July 29, 2009

The characteristics and nature of atomic-scale defects produced on graphite surfaces by dielectric barrier discharge (DBD) plasma oxidation have been investigated, both experimentally and theoretically. Two main types of defect visualized by scanning tunneling microscopy (STM) were studied: protrusions ∼1−5 nm in diameter and smooth circular depressions 5−7 nm wide, the latter constituting a novel type of defect on carbon surfaces that was only very recently reported for the first time. STM and atomic force microscopy (AFM) experiments indicated that both the protrusions and the depressions are not associated to topographical features on the graphite surface and that their observation by STM should be related to electronic effects. The thermal behavior of the protrusions, which could only be removed at a temperature of ∼900 °C, as well as their reactivity toward molecular oxygen, allowed their identification as multiatomic vacancies. In comparison, the depressions displayed a higher thermal stability (they could be eliminated only at ∼1200 °C) and a lower reactivity toward oxidation. Density functional theory (DFT) calculations suggested that the depressions are associated with two-dimensional clusters of interstitial oxygen formed by the agglomeration of migrating oxygen atoms. Such clusters induce a lowering in the local density of electronic states on the graphite surface and are therefore detected as a depression by STM. Taken as a whole, the findings reported here provide a consistent picture of the basic mechanism underlying the modification of graphitic surfaces by this type of plasma, which is driven by physical processes (i.e., ion bombardment).

1. Introduction

The surface properties of carbon materials and their modification are highly relevant in many applications. These include first-wall materials for nuclear reactors,[1−4] re-entry shields of spacecraft,[5] biomedical materials,[6−9] anodes for fuel cells[10,11] and Li-ion batteries,[12] or catalyst supports.[13,14] Among the existing methods for the surface modification of carbon materials (e.g., bombardment with high[15] and low[16,17] energy ions, high temperature oxidation,[18] or wet chemical and electrochemical oxidation[19]), surface modification by plasmas is particularly attractive owing to a number of advantageous features: it is a nonpolluting, potentially scalable process, the modification is strictly restricted to the surface of the material without affecting its bulk properties, the treatments are relatively easy to control, and different chemical species can be readily obtained just by changing a few processing parameters.[20] In particular, plasma oxidation (i.e., plasma treatment under oxygen-containing gases) is widely employed to control such properties as adhesion, molecular adsorption, wettabilitty, or surface porosity.[21−26]

As with any other type of surface modification of a material, attaining an in-depth knowledge of the basic processes that lead to the surface modification of carbon materials by plasmas is not only important from the viewpoint of applications but also from a fundamental science perspective. This typically involves unraveling the individual events that drive the process and modify the surface at the nanometer/atomic scale on a model carbon material such as graphite.[27] The modified morphological, structural, and/or chemical properties of the final carbon surface will usually be the result of the combination of a very large number of such events.[28]

As part of an ongoing research effort in this direction, we are interested in the surface modification of graphite by means of dielectric barrier discharge (DBD)-generated plasma. In previous work, the nanometer/atomic-scale effects of other types of plasmas, mostly microwave (MW)-excited oxygen plasmas, on graphite as a model carbon material have been thoroughly investigated, and the basic events that drive the etching process in such plasmas are now relatively well understood.[27,28] However, this is not the case with oxidation of carbon surfaces by DBD plasmas. DBD-generated plasmas present some particular advantages in relation to the more common low-pressure MW and radiofrequency plasmas, the main one being the possibility of operating at atmospheric pressure. This is a very attractive feature, since it significantly facilitates the implementation of DBD systems to industrial-scale applications. Previous studies have addressed the main morphological and chemical changes experienced by both carbonaceous (carbon nanotubes) and polymeric materials following DBD plasma oxidation,[29−31] but knowledge about the DBD plasma attack from a fundamental science perspective, e.g. how etching proceeds on the atomic level and the types of defect that are generated, is currently very limited.

We have recently reported on the modification of graphite surfaces through DBD air plasma treatment.[32] Scanning tunneling microscopy (STM) imaging revealed that two main types of atomic-scale defect were created, one of which (visualized

* Corresponding author. Telephone: (+34) 985 11 90 90. Fax: (+34) 985 29 76 62. E-mail: paredes@incar.csic.es.
[†] Instituto Nacional del Carbón.
[‡] Universidad de Valladolid.

10.1021/jp9020323 CCC: $40.75
Published on Web 10/05/2009

as an apparent depression) had never been documented for carbon materials. Given the novelty of these defects, and given that their characteristics and nature, especially for the new type of defect, are not known, a more in-depth study of the system is required to unveil the nature of these defects. To this end, here we investigate the characteristics of these atomic-scale defects through additional STM measurements and atomic force microscopy (AFM), as well as through examination of their thermal annealing and oxidation behavior. Furthermore, in an effort to elucidate the nature of the defects, we perform density functional theory (DFT) calculations to simulate the STM images of the modified surface and relate the results of such calculations to the information provided by the experiments. From the insight provided by this combined study, we give a compelling picture of the nature and atomistic structure of the observed defects.

2. Experimental and Computational Details

The graphite employed in this study was grade ZYH highly oriented pyrolytic graphite (HOPG), acquired from Advanced Ceramics Corporation (Cleveland, OH). HOPG pieces with dimensions $\sim 10 \times 10 \times 1.5$ mm^3 were typically employed. Just before each treatment, the sample surface was cleaved in air using adhesive tape to obtain a fresh, pristine graphite surface. DBD air plasma treatments were carried out in a laboratory-scale, volume type unit (VB-A4, from Arcotec GmbH, Germany).[33] This device allows the generation of plasmas under atmospheric pressure conditions by means of a discharge between two electrodes, one of which is covered by a layer of a dielectric ceramic material acting as an electrically insulating barrier. In the configuration used for the present study, the lower electrode was planar and electrically grounded, serving also as a support for the samples to be treated. The upper electrode consisted of one cylinder covered by ceramic material lying parallel to the lower electrode and connected to a high voltage sinusoidal power source. During the treatments, the lower electrode, and therefore the sample, was moved at a controllable speed (1.33 m s^{-1}), passing underneath the fixed upper electrode a given, user-selectable number of times. From the lower electrode speed, upper electrode diameter, and number of times that the former was passed underneath the latter, the exposure time of the sample to the plasma can be derived. For the present work, exposure times of graphite to the DBD plasma ranged between $\sim$9 ms, which are the shortest possible treatments in our plasma system, and $\sim$1000 ms. As will be shown below, such treatment times are sufficient to lead to extensive modifications of the graphite surface.

In the most common DBD geometry, which was the one employed here and is known as the volume discharge (VD) geometry, the gap between the electrodes is filled with the precursor gas of the plasma (air in our case). For the present studies, this gap was set to $\sim$2.4 mm, which is a typical value for this DBD plasma system. Changing the gap around such a value within certain limits did not have very significant effects on the results. The plasma power used was typically 200 W. Again in this case, qualitatively similar results were obtained when this parameter was changed. For VD geometries, the generated plasmas are typically composed of a large number of tiny cylindrical microdischarges (a few hundred micrometers in diameter) bridging the gap between the two electrodes. Such microdischarges are continuously produced and possess very short lifetimes (around tens of nanoseconds).[34] Although the microdischarges initially strike random locations of the sample surface, charge accumulation on spots previously struck by a microdischarge gives rise to the so-called memory effect, by which subsequent microdischarges will strike the same spots on the sample surface.[34,35] The groups of microdischarges striking the same location on the sample surface are called filaments, which are visible to the naked eye. As discussed in the following section, this feature must be taken into account when analyzing the effects of this type of plasma on the graphite surface.

The plasma-treated samples were investigated mostly by STM under ambient conditions with a Nanoscope IIIa Multimode apparatus (Veeco Instruments, Santa Barbara, CA) using mechanically prepared Pt/Ir (80/20) tips. Images were collected in the constant current mode (variable height). Unless otherwise specified, the tunneling parameters employed for the recording of nanometer scale images were 1 nA (tunneling current) and 100 mV (bias voltage). For atomic resolution imaging, tunneling currents as high as 6 nA and bias voltages as low as 5 mV were used. Further characterization of the samples was carried out by atomic force microscopy (AFM) and Raman spectroscopy. AFM was carried out in the contact mode of operation with the Nanoscope IIIa Multimode instrument. Microfabricated triangular Si_3N_4 cantilevers with a nominal spring constant of 0.06 N m^{-1} were employed. Height (topography) and lateral force (friction) images were recorded simultaneously with the fast scan direction perpendicular to the main axis of the cantilever.

Raman spectra were collected in the range from 1200 to 1900 cm^{-1} on a Jobin-Yvon Horiba HR 800 spectrometer (Villeneuve d'Asq, France) with a laser excitation wavelength of 532 nm. As some of the most relevant plasma-treated samples were spatially heterogeneous on scales of several tens of micrometers, the ability to record images by STM/AFM and obtain Raman spectra at specific surface locations turned out to be crucial. This was possible through the use of optical microscopes coupled to either the STM/AFM equipment and the Raman spectrometer. Features characteristic of the graphite surface, such as step edges, large enough to be visible under the optical microscope, were used as reference marks that helped to locate specific areas for the STM/AFM and Raman measurements.

Theoretical calculations were carried out within the framework of the DFT using the DACAPO code.[36] The code implements the supercell method and uses plane waves basis sets. Vanderbilt ultrasoft pseudopotentials[37,38] were used to represent the effect of the ionic cores on the valence electrons, and the generalized gradient approximation (GGA-PW91)[39] was used for the exchange-correlation functional. The surface of graphite was represented through a slab formed by three graphene layers with ABA stacking placed at the experimental interlayer distance of graphite (0.334 nm). The calculated equilibrium C−C bond distance in the graphene layer of 0.1424 nm was used to fix the **a** and **b** cell parameters and, therefore, the size of the supercells in the x and y directions. The cell size in the z direction was taken large enough (2 nm) to minimize the interaction between slabs in different supercells. For most of the calculations, each graphene layer of the supercell contained (8×8) unit cells of graphene with two carbon atoms each. An energy cutoff of 350 eV for the plane waves and a [2,2,1] Monkhorst-Pack k-point sampling guarantees an accuracy better than 50 meV in the calculated binding energies. The simulated STM images derived from the DFT calculations were obtained as topographs of constant local density of electronic states.

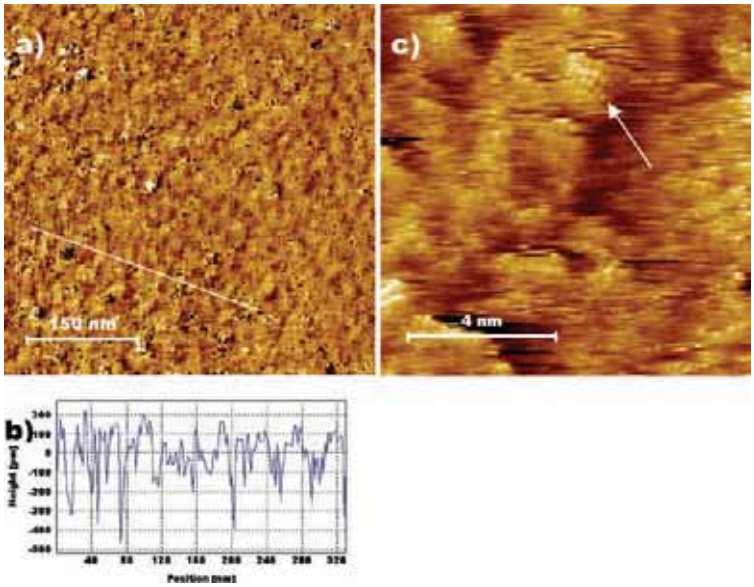

Figure 1. (a) General, nanometer-scale STM image of HOPG treated for 211 ms by DBD air plasma. (b) Height profile along the white line marked in part a. (c) Atomic-scale STM image of the same sample showing a generally disordered surface with some locally ordered areas (white arrow).

3. Results and Discussion

3.1. General Aspects of DBD Air Plasma Modification of Graphite. As mentioned in the previous section, the plasma generated with the DBD system used in the present work is indeed made up of a number of discrete plasma filaments a few hundred micrometers in diameter, which strike random locations of the sample surface. Only within these filaments is a plasma actually generated. At a given point on the HOPG surface, the structural and chemical modifications produced by the DBD plasma treatment will be the cumulative result of the several different plasma filaments that have struck that particular point. This means that a uniform modification of the sample surface will only be achieved when the plasma treatment time is large enough so that every point on the HOPG surface has been statistically struck by approximately the same (large) number of plasma filaments. On the other hand, if the plasma treatment time can be made short enough, most of the HOPG surface will not be struck by any filament and only some locations will be modified by the effect of just one filament. We are mainly interested in studying the individual atomic-scale defects created on the HOPG surface upon DBD plasma exposure. For this purpose, short plasma treatments are best suited, as these obviously lead to much lower numbers of individual events modifying the graphite surface and, therefore, to samples where isolated defects are more likely to be observable by a high resolution technique such as STM.

Before focusing on the short treatments, it is instructive to consider the general effects of longer plasma treatments on the HOPG surface. In this case, the surface becomes extensively modified on the atomic scale, so individual signs of the plasma attack are obscured by the cumulative effect of many events which occurred at the same point on the surface. From the exhaustive observation by STM of HOPG samples exposed to the plasma for different periods of time, it was determined that uniform, extensive modification of the graphite surface could be achieved for treatment times longer than about 70 ms. Treatments shorter than ∼35 ms yielded graphite surfaces where some areas were left completely unmodified (only pristine graphite was observed by STM) and others were altered by the plasma filaments. Figure 1 shows a typical nanometer-scale STM image (a), a line profile (b) taken along the direction indicated by the white line in part a and an atomic-scale image (c) of a graphite sample exposed to the DBD plasma for 211 ms (i.e., a long treatment). The surface becomes homogeneously roughened on the atomic scale, as compared to the atomic flatness of pristine HOPG, and height variations are typically in the subnanometer range (Figure 1b), indicating that although atomic roughness is developed, the HOPG surface is still extremely flat. On the atomic scale (Figure 1c), the graphite surface appears highly disorganized, atomic-sized features exhibiting some degree of periodicity are rather scarce (e.g., white arrow in Figure 1c), and individual, isolated defects cannot be identified. Apart from this atomic scale roughness, no distinctive localized features, such as pits or trenches, were observed to develop on the graphite surface upon long DBD air plasma treatments, which was attributed to the fact that attack under this type of plasma is dominated by nonselective physical processes (i.e., ion bombardment).[32] This behavior is markedly different to that observed on HOPG following other types of oxidation, including oxidation in molecular oxygen, atomic oxygen, and MW oxygen plasma,[18,27,28,40,41] which are driven by selective chemical processes and lead to the generation of localized pits and trenches.

The previous observations suggest that a significant application of DBD air plasma treatment of carbon materials, such as carbon fibers and nanotubes, could be in the field of composite materials. For this application, a good interfacial interaction between the carbon material and the matrix (typically, a polymer) is required. As the surface of carbon materials is usually rather inert, surface treatments need to be carried out to introduce chemical groups (e.g., oxygen groups) that allow enhanced interaction with the matrix. Ideally, the treatment should be exclusively superficial, i.e., the bulk of the material should not be affected, and uniform, so that interfacial tensions are well distributed across the carbon surface. Such requirements are apparently met by DBD air plasma treatment.

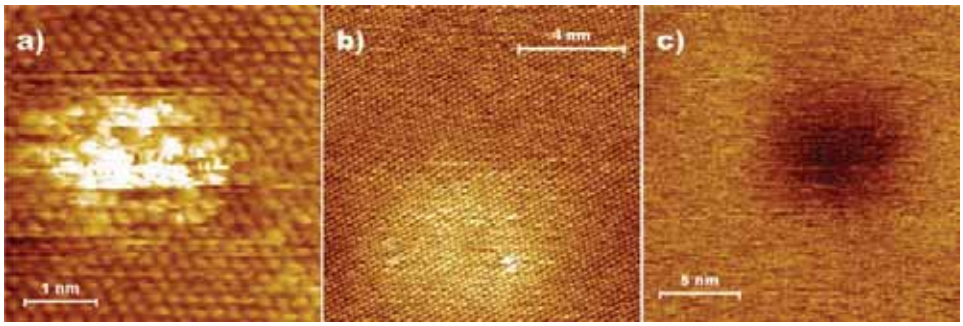

Figure 2. STM images of the different atomic-scale features found in the DBD air plasma-treated HOPG samples: 1−5 nm large protrusions (a); smooth circular bumps ∼6 nm wide (b); smooth circular depressions ∼5−7 nm wide (c).

To investigate the individual modifications produced by the DBD plasma treatment on the HOPG surface, the latter was submitted to very short plasma treatments (9 ms). In this case, isolated atomic-scale features were observed.[32] The features can be divided into three types: protrusions 1−5 nm in diameter and ∼0.2−0.3 nm high with distorted atomic-scale structure (Figure 2a); smooth circular bumps of very low height (<0.1 nm) and relatively large diameter (∼6 nm) that exhibit the same atomic-scale structure (triangular pattern) and periodicity (∼0.25 nm) as that of pristine graphite (Figure 2b); smooth circular depressions (Figure 2c), which were typically ∼0.1−0.2 nm deep (under tunneling parameters of 100 mV and 1 nA; see below) and also preserved the structure and periodicity of pristine graphite. The smooth bumps were only very occasionally found in the images, the protrusions and smooth depressions being clearly dominant. However, the spatial distribution of these defects over the graphite surface was not uniform. Indeed, STM imaging revealed that the HOPG surface has remained completely unaltered in many areas, whereas only some specific regions appeared modified. These modified regions displayed approximately circular shapes, with diameters of about 400 μm, and each of them was most probably the result of the modification produced by just one plasma filament. Within the filament-struck areas, even at the lowest possible plasma power, the morphology observed by STM was very similar to that obtained following longer plasma treatments (Figure 1), where it was not possible to clearly visualize the individual effects of the attack. However, between the heavily modified circular areas and the pristine, unmodified areas surrounding them, there were rim regions many tens of micrometers wide that displayed a smooth, gradual transition from the perfect graphitic structure to the extensively modified one. It was over such rim regions where the isolated defects could be observed.

By means of the optical microscope coupled to the STM apparatus, it was possible to locate several distinctive features typically produced when fresh HOPG surfaces are prepared by mechanical cleavage. These features served as a spatial reference to position the STM tip onto specific locations of the HOPG surface, which in turn allowed the sequential recording of a series of images at several different points, from the unaltered, defect-free areas to the heavily modified, filament-struck areas, but most especially across the rim regions. This is illustrated in the series of STM images presented in Figure 3, obtained at different points along an imaginary line that started on the unmodified area (a), crossed the rim region of a given filament-struck area (b−d), and finished within the extensively modified, filament-struck area (e). As expected, the unmodified area (Figure 3a) appears atomically flat and featureless. By contrast, the isolated defects (protrusions and depressions; white and black arrow, respectively, in Figure 3b) were observed in the rim region, and their density increased as the STM tip was moved closer to the filament struck-area (Figure 3 b→c→d). The appearance of such defects was not dependent on their surface density, i.e., when moving across the rim region toward the filament-struck area only larger numbers of the same types of defect were observed without additional features arising. When the filament-struck area proper was reached, the defect density was so high that they could no longer be individually resolved and an atomically rough, continuous surface morphology similar to that obtained for long treatments was noticed (Figure 3e). This observation strongly suggests that such morphology is basically the result of a simple accumulation of the mentioned defects, which in turn would be in agreement with a physically driven etching mechanism (i.e., ion bombardment). It was also noticed that the protrusions and depressions appeared intermingled throughout the rim region: no areas exhibiting only one defect type were ever encountered; rather, comparable numbers of both defect types were always seen. The presence of defects in the rim region and within the filament-struck area correlated with the intensity of the (defect-related) D band of graphite in the corresponding Raman spectra. Figure 3f shows in detail the D band of the Raman spectra (spectral region 1250−1450 cm^{-1}) recorded at locations equivalent to those illustrated in the images a through e of the same figure. The corresponding general spectra (1250−1700 cm^{-1}), which include both the D and G bands of graphite, are given in the inset to Figure 3f. No detectable D band is observed on either the unmodified area (Figure 3a) or the sites of the rim region with very low defect density (up to several hundred defects per square micrometer, e.g., Figure 3b). By contrast, a finite D band is already measured at points with defect densities around 1000 μm^{-2} (e.g., Figure 3c). Then, the integrated intensity ratio of the D and G bands increases with the defect density as spectra are recorded closer to, and within, the filament-struck area (e.g., Figure 3d,e). This result implies that at least one of the defect types seen in the STM images is related to localized structural disorder on the graphite lattice.

3.2. Characteristics of the Atomic-Scale Defects. Regarding the nature of the atomic-scale defects generated upon the DBD air plasma treatments, the protrusions with distorted structure (Figure 2a) can in principle be attributed to atomic vacancies on the graphite surface, as their characteristics match those previously reported for such a type of defect, created either through chemical attack, e.g., in a MW oxygen plasma,[27] or via physical sputtering with an ion beam.[17,42] Atomic vacancies in graphite are known to enhance the local density of electronic states (LDOS) near the Fermi level in the carbon atoms surrounding the vacancy and are thus reflected as apparent

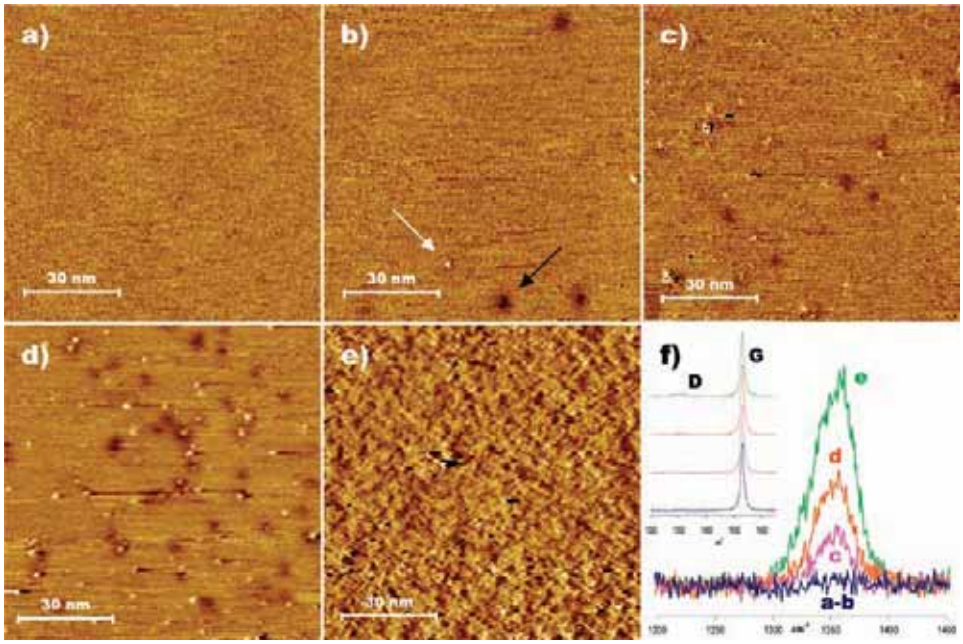

Figure 3. (a−e) Series of STM images of an HOPG sample treated by DBD air plasma for 9 ms recorded along an imaginary line that started at an unmodified area (a), crossed the rim region of a filament-struck area (b−d), and finished within the extensively modified filament-struck area (e). Along the image series, an increasing defect density is clearly noticed. (f) Raman spectra in the 1200−1450 cm^{-1} region showing the intensity of the D band at different positions, equivalent to those of images (a−e). The spectra were normalized to the G band intensity. The D band intensity (or more specifically, the D/G integrated intensity ratio) correlates with the defect density. The inset presents wider range Raman spectra (1250−1700 cm^{-1}) evidencing both the D and G bands.

protrusions (bright spots) in the STM images, although the actual topography of the defect is essentially flat.[17,27,42] The smallest protrusions (∼1 nm) would be ascribed to single-atom vacancies, whereas protrusions larger than 1 nm would correspond to multiatom vacancies.[27] As will be shown below, the additional experiments with the DBD plasma-treated samples support the assignment of the protrusions to atomic vacancies. Features with the same characteristics as those of the smooth circular bumps (Figure 2b) have also been reported for some other types of surface modification of graphite and are attributed to interstitial C or Ar atoms.[42,43] By contrast, the smooth depressions (Figure 2c) have only been observed under the DBD plasma-treatment,[32] and their nature has not been investigated until now. Gaining insight into the nature of these defects requires investigation of their characteristics.

First of all, we note that the apparent depth of the depressions (∼0.1−.2 nm), as measured under standard tunneling parameters (100 mV bias voltage, 1 nA tunneling current), was clearly smaller than that of monolayer-deep pits in graphite (∼0.34 nm). Moreover, it was observed that the apparent depth could be modified by changing the tunneling parameters. Figure 4 shows STM images and corresponding line profiles of the same depression recorded under different tunneling parameters: 100 mV, 1 nA (a); 25 mV, 10 nA (b); 10 mV, 25 nA (c). The apparent depth of the depression [∼0.08 (a), 0.17 (b), and 0.25 (c) nm] increased as the STM electrical resistance was decreased, as opposed to the case of mono- or multilayer deep pits in graphite, whose depth remains unaltered (results not shown). Such modulation of the depression depth was observed to be reversible, as the depth value measured under a given set of tunneling parameters (e.g., 100 mV and 1 nA) was recovered after imaging under different sets of parameters. In addition, the edge of the depressions was ill-defined on the atomic scale (e.g., Figure 2c and height profiles in Figure 4): the height variation when moving from outside the depressions toward their interior was only very gradual, in marked contrast to the atomically sharp edges that are typically observed for mono- or multilayer deep pits on the graphite surface.[18,28,44] Such observations strongly suggest that the smooth depressions, similarly to vacancy-induced protrusions, are not real topographical features (i.e., pits) but must have an essentially electronic origin instead, which is known to be the other source of image contrast in STM.[45]

Contact mode AFM observations also supported the previous conclusion. Typical height and lateral force images recorded simultaneously on areas with defect densities similar to those observed in Figure 3d are presented in Figure 5a and 5b, respectively. The contrast observed in the lateral force image (Figure 5b) indicates that the defects generated following the DBD plasma treatment are indeed detectable by AFM (no contrast is observed in the height and lateral force images of pristine, untreated HOPG). However, the corresponding height image (Figure 5a) is essentially flat and featureless, implying that the DBD-induced defects are not associated with topographical variations. Consequently, their observation by STM (Figures 2 and 3) must be related mainly to electronic effects.[27] If the depressions are ascribed to electronic effects, we have to conclude that they correspond to surface areas where the LDOS near the Fermi level is reduced in comparison to the pristine, defect-free HOPG surface, just as the vacancy-induced protrusions correspond to areas of increased LDOS near the Fermi level.[17,27,42]

Further insight into the characteristics of the reported defects was gained by investigating their thermal behavior. To this end, DBD plasma-exposed HOPG samples were subjected to heat treatment (annealing) at different temperatures. The heat treat-

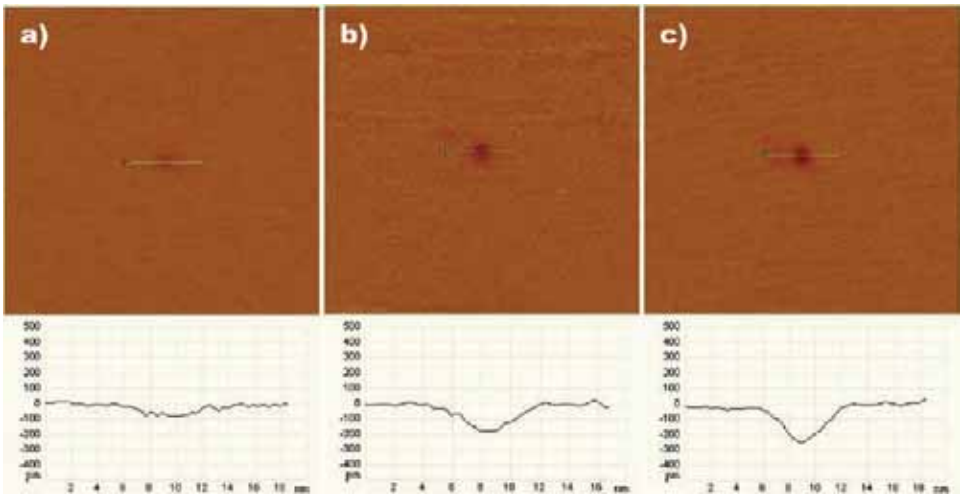

Figure 4. STM images along with their correspondent height profiles of the same isolated depression recorded under different conditions of tunneling current (I) and bias voltage (V_{bias}). (a) $I = 1$ nA, $V_{bias} = 100$ mV; apparent depth of the depression: 0.08 nm. (b) $I = 10$ nA, $V_{bias} = 25$ mV, apparent depth: 0.17 nm. (c) $I = 25$ nA, $V_{bias} = 10$ mV, apparent depth: 0.25 nm. Lateral size for the three images: 75 nm.

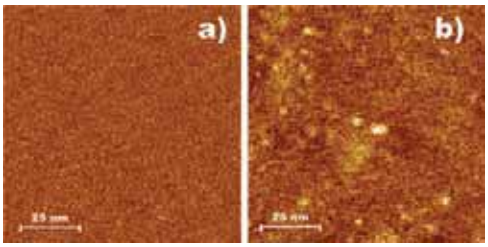

Figure 5. Typical height (a) and lateral force (b) images simultaneously recorded by AFM in the contact mode on areas of DBD air plasma-treated HOPG with defect densities similar to those of Figure 3d.

ments were performed under flowing Ar atmosphere at the desired temperature for 60 min. It was observed that annealing at 300 and 600 °C did not have any appreciable effect on both the protrusions and the depressions. However, annealing at 900 °C led to the removal of the protrusions, yielding graphite surfaces exclusively decorated with depressions. This is illustrated in Figure 6, which shows the same DBD plasma-treated sample before (a) and after (b) heat treatment at 900 °C. The protrusions, which appear highly intermingled with the depressions in the as-treated samples (Figure 6a), are completely absent from the samples annealed at 900 °C (Figure 6b). Finally, at a temperature of 1200 °C both types of defect were removed from the HOPG surface (images not shown).

To assist in the interpretation of this result, the thermal behavior of the DBD-induced defects was compared with that of the atomic-scale defects produced on the graphite surface through MW oxygen plasma treatment. Previous work has shown that controlled exposure of HOPG surfaces to MW oxygen plasma leads to the generation of single- and multiatom vacancies as the only type of atomic-scale defect.[27,28] Thus, as observed by STM, the basal surface of graphite treated with MW oxygen plasma under controlled conditions appears decorated with protrusions one to several nanometers large that display distorted atomic-scale structure.[27] Annealing experiments on MW oxygen plasma-treated samples decorated mostly with multivacancies indicated that removal of this defect type was only achieved when the heat treatment temperature was 900 °C (images not shown), i.e., the same temperature as that needed for the removal of the protrusions in the DBD plasma-exposed samples. We interpret that the atomic vacancies become highly mobile at 900 °C and diffuse over the graphite surface until they are annihilated at step edges. The fact that the protrusions created with the DBD plasma are removed at the same temperature (900 °C) as the MW plasma-generated atomic vacancies supports the idea that the former are also atomic vacancies.

As discussed above, the protrusions and depressions imaged by STM on the surface of DBD plasma-treated HOPG are interpreted as a modulation of the LDOS near the Fermi level at specific surface sites. This modulation should have an influence on the reactivity of the related defects toward electronegative molecules such as O_2. Surface sites with increased LDOS near the Fermi level (e.g., the vacancy-induced protrusions) should exhibit an enhanced reactivity toward O_2 compared to pristine sites of the graphite basal plane, since more electrons are readily available at this site for the oxygen molecule.[46,47] On the contrary, surface sites with reduced LDOS near the Fermi level (i.e., the depressions) should possess a low reactivity, as fewer electrons are available for the electronegative molecule. To corroborate this point, DBD plasma-treated samples, with and without annealing at 900 °C, were subjected to thermal oxidation in air at 550 °C. It is well-known that carbon atoms from perfect sites of basal planes do not react with O_2 at this temperature, and oxidation only takes place at surface defects (e.g., atomic vacancies or step edges), leading to the development of etch pits in the case of atomic vacancies.[18,44,46] Therefore, it can be anticipated that oxidation of DBD plasma-treated graphite surfaces under such conditions will exclusively take place at the protrusions, the depressions remaining unaffected due to their low reactivity (decreased LDOS).

Figure 6c corresponds to a DBD plasma-treated HOPG sample that was subjected to thermal oxidation at 550 °C for 10 min. Before the thermal oxidation, the sample displayed both protrusions and depressions. After the oxidation, some etch pits 7−10 nm wide (e.g., black arrows in Figure 6c) were seen together with the ∼6 nm large depressions (e.g., white arrows). By contrast, when thermal oxidation was carried out on a DBD plasma-treated sample that only possessed depressions (the protrusions were previously removed by annealing at 900 °C),

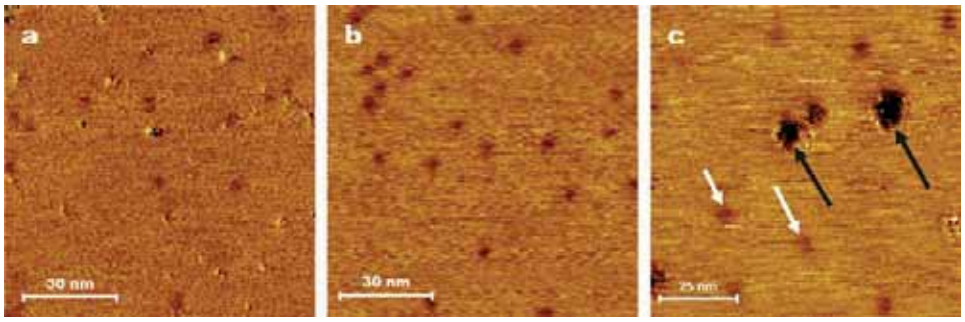

Figure 6. (a, b) STM images of the same DBD air plasma-treated HOPG sample before (a) and after (b) heat treatment under Ar at 900 °C for 1 h. Following heat treatment, only depressions are retained on the graphite surface. (c) STM image of a DBD air plasma-treated HOPG sample that was subjected to thermal oxidation in air at 550 °C for 10 min. Before thermal oxidation, only protrusions and depressions were observed. After thermal oxidation, the depressions were still present (e.g., white arrows), whereas the protrusions tended to disappear and etch pits were seen to develop (e.g., black arrows).

no etch pits were observed to develop and the depressions did not experience any apparent change (images not shown). Such results imply that only the protrusions (atomic vacancies) are etched by O_2 under such conditions and therefore support the idea that the depressions are sites of comparatively low reactivity. Figure 6c also highlights a fundamental difference between chemical and physical attack: the development of pits at localized sites of the graphite surface is a clear signature of selective, chemically driven etching, as expected from a thermal oxidation process. By contrast, no pitting was ever induced on DBD air plasma-treated graphite, indicating that chemical attack should not be the dominant etching mechanism.

From the results presented beforehand, it can be concluded that DBD air plasma modification of graphite proceeds through the creation of two types of atomic-scale defect, which are visualized by STM as protrusions and depressions. The atomic-scale structure, thermal behavior and reactivity toward O_2 of the protrusions strongly suggest that they correspond to atomic vacancies. This kind of defect has been well documented in previous STM studies of modified graphite.[17,27,42,48] On the other hand, the nature of the depressions is less obvious. The evidence obtained here indicates that they are sites of reduced LDOS near the Fermi level, are not associated to any topographical feature on the graphite surface, and possess a relatively high thermal stability and a comparatively low reactivity toward oxidation. Although such type of STM feature has not been reported for graphite or any other carbon material following any kind of surface treatment other than DBD air plasma, features with similar characteristics have been previously observed by STM on the surface of MoS_2 and attributed to substitutional acceptor metal impurities present in natural samples of this material.[49] In our previous report, we tentatively attributed the depressions to the presence of interstitial oxygen species.[32]

As mentioned above, the modification of HOPG by the DBD air plasma treatment must be mainly a physically driven process, which means that ion bombardment should play a prominent role in the creation of the reported atomic-scale defects. It is well-known that ion bombardment induces two main types of point defects on graphitic structures, namely, atomic vacancies through displacement of lattice carbon atoms by the impinging ions, and interstitials via ion implantation between the topmost graphene layers.[42,50−52] The large number of atomic vacancies produced by the DBD plasma treatment constitutes compelling indication that ion bombardment is indeed taking place in such a plasma. Accordingly, implantation of bombarding species should also be expected. In this regard, the comparatively scarce, smooth circular bumps of very low height reported here (Figure 2b) exhibit a close similarity to the features reported previously for Ar^+-bombarded graphite, which were attributed to interstitially implanted Ar atoms.[42,43] We therefore ascribe such features to Ar atoms (present in ambient air at a concentration of ∼1%) implanted between the topmost graphene layers of HOPG. Thus, it is reasonable to conclude that the depressions could also be due to some species implanted below the surface graphene. Taking into account that X-ray photoelectron spectroscopy (XPS) measurements of most of the DBD air plasma-treated samples only showed evidence of the introduction of oxygen on the graphite surface (nitrogen was only introduced in very small amounts after very long treatment times), we infer that the depressions should be associated to interstitial oxygen species implanted just below the surface graphene and interacting with it. As oxygen is electronegative, it would act as an electron acceptor, removing electronic charge from its neighboring carbon atoms. The possibility that the oxygen species responsible for the depressions could be located on the graphite surface (as opposed to below the surface) seems unlikely, since it would be very difficult, if not impossible, to image them by STM under the conditions employed in the present work. Furthermore, oxygen species adsorbed on the graphite surface should also be expected after, for example, MW oxygen plasma treatment or hyperthermal atomic oxygen exposure, but in these cases depressions were never observed.[27,28,53]

The presence of oxygen species interacting with the graphene basal plane, as opposed to interacting with the graphene edges, is reminiscent of the situation found for graphite oxide and graphene oxide. Graphite and graphene oxide are heavily oxygenated derivatives of graphite and graphene produced through aggressive oxidation of the latter, and their basal planes are thought to be decorated with large amounts of oxygen functionalities.[54] It has been recently shown by STM that graphene oxide sheets deposited onto HOPG display reduced LDOS near the Fermi level compared to the bare HOPG surface.[55] Although in the case of graphene oxide the density of oxygen species grafted onto the basal plane is expected to be exceedingly large, thus preventing the STM visualization of individual oxygen sites surrounded by pristine graphene, this result suggests that the oxygen species interacting with the graphene basal plane are responsible for the reduction in the LDOS, which in turn supports the idea that the depressions reported by STM in the present work are associated to oxygen species.

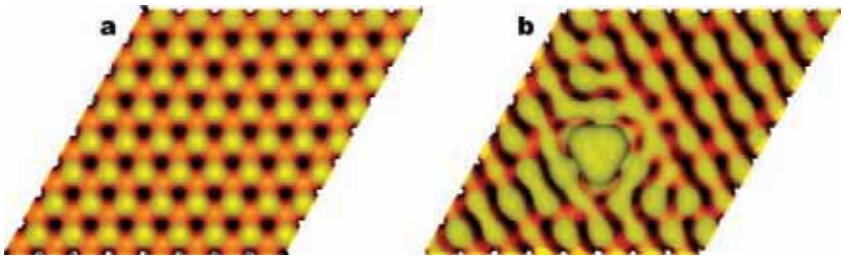

Figure 7. (a) Calculated STM image of the free surface of pristine graphite. The bright (yellow) and clear (orange) spots correspond to carbon atoms in β and α positions, respectively; the dark spot is coincident with the center of the hexagonal honeycomb lattice. (b) STM image of a single carbon vacancy in α position on the graphite surface; a similar result is obtained for a vacancy in β position. The triangular protrusion arises from the three dangling bonds around the vacant site.

While the electronic effects of electronegative species implanted in graphite had never been visualized at high resolution, those of electropositive species (e.g., alkali metals) have been previously studied to some extent, mainly in connection with their promoting role in carbon oxidation.[56] Specifically, Hahn and Kang have suggested that Cs implanted below the surface graphene promotes the oxidation of HOPG by O_2 through electronic charge transfer from the Cs atom to the surface carbon atoms surrounding it.[56] This charge donation increases the LDOS of the graphite surface and hence its surface reactivity toward O_2. In the present case of DBD air plasma-treated graphite, a similar mechanism, but with opposite effects, should be applicable: the electronegativity of oxygen would induce electronic charge transfer from the surface carbon atoms, decreasing the LDOS at the graphite surface and thus the local reactivity toward O_2. The fact that the reported depressions were not etched by oxidation at 550 °C would be consistent with this conclusion.

3.3. Insight from DFT-Based Calculations. To gain insight and help to interpret the experimental STM images reported above, DFT calculations of several defect structures on the graphite surface as well as below the surface were performed. The aim was to identify possible types of defect that give rise to the observed STM features, in particular the smooth depressions. First of all, we note that the DFT methodology employed here reproduces correctly the triangular pattern characteristic of the atomic-scale STM images of pristine graphite surfaces (Figure 7a). Furthermore, in agreement with previous theoretical calculations for graphite and graphene,[57−59] a single-atom vacancy leads to the appearance of a small protrusion in the simulated STM image, as illustrated in Figure 7b. The dangling bonds associated to the vacancy are responsible for an increase in the LDOS near the Fermi level, which is in turn reflected as a protrusion in the STM image. Concerning the reported smooth depressions, the experimental evidence suggests that they could originate from oxygen species interstitially implanted just below the surface graphene. However, from the theoretical point of view it is not known how the STM images of graphite are modified by the presence of interstitial oxygen. To shed some light on this question, different DFT calculations were carried out. In principle, given the highly electronegative nature of oxygen atoms, it could be conceived that the adsorption of an oxygen atom on top of the surface graphene (rather than below it) would remove electrons from the Fermi level (the calculated Mulliken charge of adsorbed atomic oxygen is $-0.29\ e$), thus leading to a depression in the STM image. Nevertheless, the calculated STM image clearly displayed a very small but prominent protrusion at the oxygen adsorption site (image not shown). The reason for such effect is that some hybridized electronic states from oxygen and the graphite surface lay at the Fermi level. Similar to previous calculations,[60,61] adsorption of oxygen atoms on top of the surface graphene was seen to take place preferentially in the epoxy configuration, i.e., above a C−C bond of the surface. Although the binding energy is quite substantial (1.72 eV), it is most likely that the oxygen atoms become desorbed as a result of the strong forces exerted by the probing STM tip, particularly under ambient conditions,[45] implying that this type of defect cannot be visualized in the STM images.

Interstitial oxygen located just below the surface graphene attaches also in epoxy configuration either above a C−C bond of the first subsurface graphene or below a C−C bond of the surface graphene with binding energies of 0.47 and 0.45 eV, respectively. The former configuration cannot be traced through STM, since the corresponding simulated image does not exhibit any special feature and is virtually identical to that of pristine graphite shown in Figure 7a. By contrast, the latter configuration leads to a slightly distorted atomic-scale pattern at the site of the oxygen atom (Figure 8a). Interestingly, the results of the DFT calculations show that the individual interstitial oxygen atoms tend to agglomerate, forming two-dimensional (not three-dimensional; see below) clusters of interstitial oxygen. We have found that the interstitial oxygen atoms become more stable when they cluster together by attaching to alternate C−C bonds (attachment to adjacent C−C bonds is not favorable): the binding energy per oxygen atom was seen to increase as the cluster size increases. The binding energy per atom of a 12-oxygen-atom cluster is about twice as much as that of a single interstitial oxygen atom. At the same time, a depression develops in the simulated STM images. Figure 8b,c,d shows the simulated STM images for clusters of 2, 3, and 12 interstitial oxygen atoms, respectively, attached (from below) to alternate C−C bonds of the surface graphene. The structure of the 12-oxygen-atom cluster is presented in Figure 9. Due to the presence of the interstitial oxygen cluster, there is a lowering in the LDOS at the Fermi level on the surface graphene, which is in turn visualized as a depression ∼0.15−0.17 nm deep in the simulated STM image. Therefore, these results provide indication that the depressions observed in the experimental STM images reflect the presence of stable two-dimensional clusters of interstitial oxygen formed by the agglomeration of individual interstitial oxygen atoms.

We note that the lateral size of the largest calculated STM depression (∼0.9 nm for the 12-oxygen-atom cluster, Figure 8d) is smaller than that typically reported in the experimental STM images (5−7 nm) due to limitations in the supercell size that can be used in the calculations. The ($8 \times 8 \times 3$) slab that we have used contains 384 carbon atoms and is computationally very demanding. Using larger slabs would be extremely expensive. Consequently, our calculations are not informative about the preferred size of the interstitial oxygen clusters.

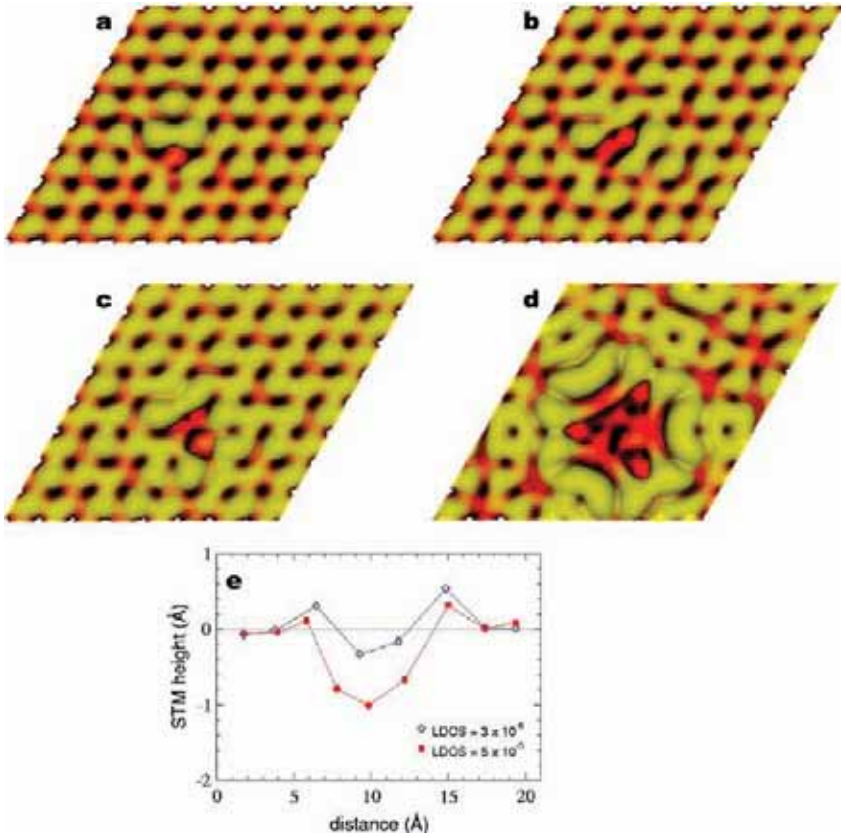

Figure 8. Calculated STM images of the graphite surface with different numbers [one (a), 2 (b), 3 (c), and 12 (d)] of oxygen atoms interstitially located just below the surface graphene and bonded to C−C atoms in epoxy configuration. In b, c, and d the oxygen atoms are attached to alternate C−C bonds of the surface graphene. (e) STM height profiles along a horizontal line going through the center of the depression shown in d for two values of the LDOS: 3×10^{-6} eV^{-1} $Å^{-3}$ (diamonds) and 5×10^{-5} eV^{-1} $Å^{-3}$ (circles). The plotted values are averaged over the lateral size of the individual atoms. Larger values of the LDOS exhibit deeper height profiles, in agreement with the experimentally recorded profiles for increasing tunneling current (see Figure 4).

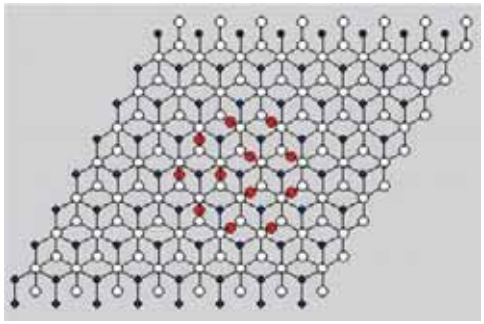

Figure 9. Top view of the structure of a cluster of 12 interstitial oxygen atoms located just below the surface graphene. The carbon atoms of the surface layer are depicted in white and those of the first subsurface layer in black; the oxygen atoms are represented in red.

Nevertheless, the actual size of the depressions observed in the experiments is most probably due to kinetic rather than to stability effects. From the growth pattern of the oxygen clusters found in the theoretical calculations (i.e., the oxygen atoms are attached to alternate C−C bonds of the surface graphene) one can estimate that the experimental depressions 5−7 nm wide would correspond to a cluster with a few to several hundred oxygen atoms. The difference in size between the observed and the calculated defects gives rise also to some differences in the corresponding STM images: the experimental STM images of the depressions exhibit a rounded shape (Figure 2c) whereas the calculated ones (Figure 8d) are somewhat faceted. Assuming that the actual, large clusters grow out of oxygen atoms coming from random directions, one would reasonably expect that the calculations would yield more rounded shapes for large clusters, in agreement with the experimental observations. What is important to note is that only this type of structure (i.e., oxygen clusters) leads to a depression in the simulated STM images. Other reasonable types of defect did not yield depressions in the calculations.

Figure 8e shows simulated STM height profiles along a line parallel to the surface going across the depression caused by the intercalated 12-oxygen-atom cluster. The points in the profiles are extracted from the calculated STM isosurfaces (appropriately averaged over the lateral size of the individual atoms to better mimic the lateral atomic resolution of the experiment) for two different values of the LDOS: 3×10^{-6} eV^{-1} $Å^{-3}$ and 5×10^{-5} eV^{-1} $Å^{-3}$. The apparent depth of the depression (we recall that it is not a topographical but an electronic feature) increases with increasing values of the LDOS. This behavior correlates with the experimental observation reported in Figure 4 that the apparent depth of the depressions increases with the tunneling current used to record the STM images. As it is well-known, higher tunneling currents map out isosurfaces of higher values of the LDOS. Therefore, the

experimental height profiles (Figure 4) can be explained from the behavior induced by the interstitial oxygen clusters in the isosurfaces of LDOS.

It is worth noticing that the growth of interstitial oxygen clusters in three- dimensions, i.e., the formation of clusters consisting of two or more layers of oxygen atoms, can be ruled out on the basis of both theoretical calculations and experimental evidence. (i) Clusters of two or more layers of oxygen atoms intercalated between two graphenes are energetically unfavorable as compared with a single interstitial layer. (ii) A three-dimensional interstitial cluster should lead to a topographical protrusion on the graphite surface. Even if such clusters were visualized as depressions by STM, because the electronic effects could still dominate over topography, the associated topographical protrusions should be clearly apparent in the AFM height images. The fact that no protrusions were detected in the AFM height images (Figure 5a) is strong indication that three-dimensional clusters do not form.

The two types of atomic-scale defect investigated here, protrusions and depressions, were visualized in most cases as individual entities (Figure 3b and 3c), and therefore we have treated them as separate defects. However, one can notice that as the density of defects increases (when approaching the region of a given filament-struck area) some protrusions appear next to depressions (Figure 3d). In our view, the vacancies (observed as protrusions) could act as nucleation centers for the interstitial oxygen clusters (observed as depressions), so that the individual oxygen atoms would agglomerate next to a vacancy site. This effect is only observed when the density of defects is moderate. For low densities of defects, interstitial oxygen atoms will agglomerate and form clusters before having the occasion of meeting a vacancy.

Another point worth discussing is that of the relatively high thermal stability of the depressions. As shown above, the depressions are stable at 900 °C and only disappear following heat treatment at 1200 °C. This seems to be consistent with the idea of the depressions as large clusters of oxygen atoms, rather than individual oxygen atoms or very small clusters, which would be expected to possess a high mobility and therefore disappear at much lower annealing temperatures. The findings reported here can also shed light into different, but related, phenomena observed on graphite. For instance, thermal desorption studies of O^+-bombarded graphite revealed the presence of sites where the implanted oxygen became strongly bound and could only be removed upon annealing at temperatures around 1200 °C,[62] i.e., a similar temperature to that required for the removal of the depressions in the present work. In view of the present experimental and theoretical results, such sites could be attributed to large clusters of interstitial oxygen.

4. Conclusions

The characteristics and nature of the defects produced on graphite surfaces by DBD-generated air plasma treatment and the processes that drive such modifications have been elucidated through combined STM/AFM experiments and DFT calculations. The recorded STM images provided indication that DBD plasma attack is dominated by physical processes (i.e., ion bombardment). Through controlled treatments, it was possible to isolate the individual effects of this type of plasma on the graphite surface, which consisted in the generation of two types of atomic scale defect: 1−5 nm wide protrusions and smooth circular depressions ∼5−7 nm in diameter. AFM observations and detailed inspection of defect characteristics indicated that both types of defect were of electronic, rather than topographic, origin. The protrusions could be removed by annealing the plasma-treated samples at 900 °C and were etched into monolayer-deep pits via air oxidation at 550 °C. These features were consistent with the protrusions being atomic vacancies. On the other hand, elucidating the nature of the depressions was more difficult, since they constitute a new type of defect that has been only recently and exclusively observed on DBD-treated graphite surfaces. The depressions possessed a higher thermal stability and a lower reactivity toward oxidation compared to those of the protrusions. DFT calculations suggest that they are the electronic signature of two-dimensional interstitial oxygen clusters located just below the surface graphene. Thus, the general picture that emerges from all these results is that DBD air plasma modification of graphitic surfaces proceeds mostly through bombardment of oxygen ions, which has a 2-fold effect: (1) sputtering of surface carbon atoms, leading to the creation of atomic vacancies on the graphite surface, and (2) implantation of the impinging oxygen ions below the surface graphene, which subsequently migrate and agglomerate, forming large clusters of interstitial oxygen.

Acknowledgment. P.S.-F. acknowledges receipt of an I3P predoctoral contract from CSIC. I.C. acknowledges support from MEC-FSE through the Ramón y Cajal Program. Financial support from the Spanish MEC through projects CTQ2005-09105-C04-02, MAT2005-06544-C03-01, and MAT2008-06483-C03-01, and from the Junta de Castilla y León through projects VA017A08 and GR23, is gratefully acknowledged.

References and Notes

(1) Koizlik, K.; Linke, J.; Nickel, H. *J. Nucl. Mater.* **1991**, *179−181*, 1100–1103.
(2) Pierson, H. O.; Mullendore, A. W. *Thin Solid Films* **1979**, *63*, 257–261.
(3) Roth, J.; Tsitrone, E.; Loarte, A. *Nucl. Instrum. Methods Phys. Res., Sect. B:* **2007**, *258*, 253–263.
(4) Moormann, R.; Hinssen, H. K.; Krussenberg, A. K.; Stauch, B.; Wu, C. H. *J. Nucl. Mater.* **1994**, *212−215*, 1178–1182.
(5) Liedtke, V.; Olivares, I. H.; Langer, M.; Haruvy, Y. F. *J. Eur. Ceram. Soc.* **2007**, *27*, 1493–1502.
(6) Xu, Z.; Hu, P.; Wang, S.; Wang, X. *Appl. Surf. Sci.* **2008**, *254*, 1915–1918.
(7) Bystrzejewski, M.; Huczko, A.; Lange, H. *Sens. Actuators, B* **2005**, *109*, 81–85.
(8) Bokros, J. C. *Carbon* **1977**, *15*, 355–371.
(9) Yin, Y.; Hang, L.; Xu, J.; McKenzie, D. R.; Bilek, M. M. M. *Thin Solid Films* **2008**, *516*, 5157–5161.
(10) Kjeang, E.; McKechnie, J.; Sinton, D.; Djilali, N. *J. Power Sources* **2007**, *168*, 379–390.
(11) Hackett, G. A.; Zondlo, J. W.; Svensson, R. *J. Power Sources* **2007**, *168*, 111–118.
(12) Zaghib, K.; Striebel, K.; Guerfi, A.; Shim, J.; Armand, M.; Gauthier, M. *Electrochim. Acta* **2004**, *50*, 263–270.
(13) Li, W.; Han, C.; Liu, W.; Zhang, M.; Tao, K. *Catal. Today* **2007**, *125*, 278–281.
(14) Auer, E.; Freund, A.; Pietsch, J.; Tacke, T. *Appl. Catal. A: Gen.* **1998**, *173*, 259–271.
(15) Ogiso, H.; Mizutani, W.; Nakano, S.; Tokumoto, H.; Yamanaka, K. *Appl. Phys. A: Mater. Sci. Process.* **1998**, *66*, S1155−S1158.
(16) Matlis, S.; Vered, R.; Lempert, G. D.; Marom, G.; Lifshitz, Y. *Compos. Sci. Technol.* **1993**, *48*, 301–305.
(17) Hahn, J. R.; Kang, H.; Song, S.; Jeon, I. C. *Phys. Rev. B* **1996**, *53*, R1725–R1728.
(18) Chang, H.; Bard, A. J. *J. Am. Chem. Soc.* **1991**, *113*, 5588–5596.
(19) Peng, J. M.; Donnet, J.-B.; Wang, T. K.; Rebouillat, S. *Carbon Fibers*; Dekker: New York, 1998; Ch. 3.
(20) Felten, A.; Bittencourt, C.; Pireaux, J. J.; Van Lier, G.; Charlier, J. C. *J. Appl. Phys.* **2005**, *98*, 074308.
(21) Kwon, S.; Vidic, R.; Borguet, E. *Carbon* **2002**, *40*, 2351–2358.
(22) Yang, D. Q.; Sacher, E. *Chem. Mater.* **2006**, *18*, 1811–1816.
(23) Han, S. S.; Kim, H. S.; Han, K. S.; Lee, J. Y.; Lee, H. M.; Kang, J. K.; Woo, S. I.; van Duin, A. C. T.; Goddard, W. A. *Appl. Phys. Lett.* **2005**, *87*, 213113.

(24) Rawat, D. S.; Taylor, N.; Talapatra, S.; Dhali, S. K.; Ajayan, P. M.; Migone, A. D. *Phys. Rev. B* **2006**, *74*, 113403.
(25) Korovchenko, P.; Renken, A.; Kiwi-Minsker, L. *Catal. Today* **2005**, *102*−*103*, 133–141.
(26) Tang, S.; Lu, N.; Wang, J. K.; Ryu, S. K.; Choi, H. S. *J. Phys. Chem. C* **2007**, *111*, 1820–1829.
(27) Paredes, J. I.; Martinez-Alonso, A.; Tascon, J. M. D. *Langmuir* **2002**, *18*, 4314–4323.
(28) Paredes, J. I.; Martinez-Alonso, A.; Tascon, J. M. D. *Langmuir* **2007**, *23*, 8932–8943.
(29) Okpalugo, T. I. T.; Papakonstantinou, P.; Murphy, H.; Mclaughlin, J.; Brown, N. M. D. *Carbon* **2005**, *43*, 2951–2959.
(30) De Geyter, N.; Morent, R.; Leys, C.; Gengembre, L.; Payen, E. *Surf. Coat. Technol.* **2007**, *201*, 7066–7075.
(31) Liu, C.; Brown, N. M. D.; Meenan, B. J. *Surf. Coat. Technol.* **2006**, *201*, 2341–2350.
(32) Solís-Fernández, P.; Paredes, J. I.; Martinez-Alonso, A.; Tascon, J. M. D. *Carbon* **2008**, *46*, 1364–1367.
(33) Gibalov, V. I.; Pietsch, G. J. *J. Phys. D: Appl. Phys.* **2000**, *33*, 2618–2636.
(34) Chirokov, A.; Gutsol, A.; Fridman, A.; Sieber, K. D.; Grace, J. M.; Robinson, K. S. *Plasma Sources Sci. Technol.* **2004**, *13*, 623–635.
(35) Eliasson, B.; Hirth, M.; Kogelschatz, U. *J. Phys. D: Appl. Phys.* **1987**, *20*, 1421–1437.
(36) Hammer, B.; Hansen, L. B.; Nørskov, J. K. *Phys. Rev. B* **1999**, *59*, 7413.
(37) Vanderbilt, D. *Phys. Rev. B* **1990**, *41*, 7892.
(38) Laasonen, K.; Pasquarello, A.; Car, R.; Lee, C.; Vanderbilt, D. *Phys. Rev. B* **1993**, *47*, 10142.
(39) Perdew, J. P.; Chevary, J. A.; Vosko, S. H.; Jackson, K. A.; Pederson, M. R.; Singh, D. J.; Fiolhais, C. *Phys. Rev. B* **1992**, *46*, 6671.
(40) Nicholson, K. T.; Minton, T. K.; Sibener, S. J. *J. Phys. Chem. B* **2005**, *109*, 8476–8480.
(41) Paredes, J. I.; Martinez-Alonso, A.; Tascon, J. M. D. *J. Mater. Chem.* **2000**, *10*, 1585–1591.
(42) Kibsgaard, J.; Lauritsen, J. V.; Laegsgaard, E.; Clausen, B. S.; Topsoe, H.; Besenbacher, F. *J. Am. Chem. Soc.* **2006**, *128*, 13950–13958.
(43) Marton, D.; Bu, H.; Boyd, K. J.; Todorov, S. S.; Albayati, A. H.; Rabalais, J. W. *Surf. Sci.* **1995**, *326*, L489–L493.
(44) Paredes, J. I.; Martinez-Alonso, A.; Tascon, J. M. D. *Carbon* **2000**, *38*, 1183–1197.
(45) Magonov, S. N.; Whangbo, M.-H. *Surface Analysis with STM and AFM*; VCH: Weinheim, 1996.
(46) Hahn, J. R.; Kang, H. *J. Vac. Sci. Technol. A* **1999**, *17*, 1606–1609.
(47) Carlsson, J. M.; Scheffler, M. *Phys. Rev. Lett.* **2006**, *96*, 046806.
(48) Marton, D.; Boyd, K. J.; Lytle, T.; Rabalais, J. W. *Phys. Rev. B* **1993**, *48*, 6757–6766.
(49) Wang, J. F.; Rose, K. C.; Lieber, C. M. *J. Phys. Chem. B* **1999**, *103*, 8405–8409.
(50) Hahn, J. R.; Kang, H. *Surf. Sci.* **1996**, *358*, 165–169.
(51) Banhart, F. *Rep. Prog. Phys.* **1999**, *62*, 1181–1221.
(52) Krasheninnikov, A. V.; Banhart, F. *Nat. Mater.* **2007**, *6*, 723–733.
(53) Kinoshita, H.; Umeno, M.; Tagawa, M.; Ohmae, N. *Surf. Sci.* **1999**, *440*, 49–59.
(54) Stankovich, S.; Dikin, D. A.; Dommett, G. H. B.; Kohlhaas, K. M.; Zimney, E. J.; Stach, E. A.; Piner, R. D.; Nguyen, S. T.; Ruoff, R. S. *Nature* **2006**, *442*, 282–286.
(55) Pandey, D.; Reifenberger, R.; Piner, R. *Surf. Sci.* **2008**, *602*, 1607–1613.
(56) Hahn, J. R.; Kang, H. *J. Phys. Chem. B* **2002**, *106*, 7445–7448.
(57) Hjort, M.; Stafstrom, S. *Phys. Rev. B* **2000**, *61*, 14089–14094.
(58) Krasheninnikov, A. V.; Elesin, V. F. *Surf. Sci.* **2000**, *454*−*456*, 519–524.
(59) Amara, H.; Latil, S.; Meunier, V.; Lambin, P.; Charlier, J. C. *Phys. Rev. B* **2007**, *76*, 115423.
(60) Lamoen, D.; Persson, B. N. J. *J. Chem. Phys.* **1998**, *108*, 3332–3341.
(61) Incze, A.; Pasturel, A.; Chatillon, C. *Surf. Sci.* **2003**, *537*, 55–63.
(62) Refke, A.; Philipps, V.; Vietzke, E. *J. Nucl. Mater.* **1997**, *250*, 13–22.

JP9020323

4.2 Caracterización de grafenos provenientes de óxido de grafito

Artículo IV

Publicado en la revista Langmuir: "*Atomic force and scanning tunneling microscopy imaging of graphene nanosheets derived from graphite oxide*"

Artículo V

Publicado en la revista Carbon: "*Determining the thickness of chemically modified graphenes by scanning probe microscopy*"

Como ya se ha comentado en la introducción, la preparación de grafeno por métodos químicos a partir de óxido de grafito constituye una ruta realmente prometedora para la obtención de este material. Por un lado, es un método que resulta fácilmente escalable, permitiendo la obtención de una gran cantidad de material a costes bajos. Además, el producto es obtenido en forma de dispersión acuosa u orgánica, lo cual facilita su manipulación. Por el contrario, las láminas de grafeno obtenidas por este método distan mucho de ser perfectas. Esto es debido a que el proceso de reducción no es capaz de eliminar de forma completa las funcionalidades oxigenadas que, junto a una considerable cantidad de defectos estructurales, fueron introducidas por la oxidación. Por ello resulta necesario un estudio en profundidad de las características y estructura de las láminas obtenidas por este método, tanto antes (GO) como después (rGO) del proceso de reducción. En esta segunda parte del trabajo nos centramos en el estudio de las láminas de GO y rGO empleando principalmente microscopías de proximidad. Para la preparación de GO se empleó el método de Hummers ya comentado en el apartado de materiales y métodos, mientras que la reducción química para obtener rGO se llevó a cabo con monohidrato de hidracina.

Caracterización global de las láminas

Diversas técnicas de caracterización global dan cuenta de los efectos del proceso de reducción. La observación más significativa es una importante disminución en la cantidad de funcionalidades oxigenadas (el cociente atómico O/C pasa de 0.43 a 0.16 al reducir), principalmente de los grupos más lábiles (como indica la fuerte pérdida de masa a unos 200 °C observada en el análisis termogravimétrico del GO, y que no aparece en el caso del rGO). En los espectros Raman es llamativo que, tras la reducción, el cociente de intensidades de las bandas D y G (I_D/I_G) que se obtiene sea sólo ligeramente inferior al que se obtiene antes de reducir (0.13 para el material de partida, 1.46 al oxidar, 1.43 al reducir). Esto se interpreta como una disminución del grado de amorfización durante el proceso de

reducción, lo que en carbones esencialmente grafíticos como éste se sabe que produce un aumento en el cociente I_D/I_G, que se contrarresta con la disminución asociada con la restauración de la aromaticidad de la red. El proceso de reducción incrementa de manera drástica la conductividad de las láminas, lo cual es un claro indicio de la restauración de la red grafítica. Mientras que no fue posible medir la conductividad antes de la reducción (por ser muy pequeña), para los papeles de rGO se obtuvieron valores de conductividad entre 4160–9960 S m^{-1} dependiendo del grado de reducción.

Caracterización local de láminas individuales – microscopías SPM

Para su caracterización a nivel microscópico, las láminas de GO y rGO fueron depositadas sobre un substrato (generalmente HOPG). Las imágenes de topografía en el modo tapping atractivo muestran la presencia de las láminas recubriendo el sustrato, aunque no se aprecian cambios significativos en la morfología de las láminas tras el proceso de reducción, a pesar de que al menos una disminución de la altura sería esperable para el rGO. Así, tanto para el GO como para el rGO, las láminas presentan alturas aparentes bastante uniformes, que se corresponden con la altura de láminas individuales (~0.9–1.2 nm respecto al sustrato), y tamaños laterales que abarcan desde unos cientos de nm hasta una micra. Por otro lado, se sabe que el régimen atractivo del modo tapping es sensible a diferencias químicas, dando lugar a contraste en imágenes de fase. En nuestro caso, las diferencias en la cantidad de los grupos funcionales oxigenados hidrófilos presentes en la superficie de las láminas permiten discriminar entre GO y rGO. De este modo, utilizando como referencia común el sustrato de HOPG, se observa que, mientras que el GO aparece con un contraste diferente al del HOPG, el contraste de fase entre rGO y substrato es esencialmente inexistente. Esto parece una clara indicación de que tras el proceso de reducción la hidrofilicidad de las láminas se ha visto reducida a valores comparables a los del HOPG, lo que es consistente con la eliminación de gran parte de los grupos funcionales oxigenados.

El estudio mediante STM de las láminas de GO antes de la reducción presenta algunas complicaciones derivadas de la baja conductividad de éstas. Como consecuencia de ello, no resulta posible la obtención de imágenes con parámetros túnel estándar (~1 nA, ~100 mV), puesto que la punta arrastra a las láminas al no ser éstas capaces de mantener una corriente de tal magnitud. Así, para poder visualizar las láminas de GO por STM se hace necesario trabajar en el modo de baja corriente (~1 pA) a voltajes relativamente altos (~2000 mV). Estos parámetros túnel implican que la punta está barriendo sobre la superficie a distancias relativamente grandes, lo cual dificulta la formación de las imágenes, que en general presentan mucho ruido. Además, se encontraron importantes inconsistencias en las mediciones de altura de las láminas, llegándose incluso al caso extremo de observar en ocasiones una inversión de contraste. En estos casos, las láminas parecen incrustadas en el substrato, aunque sólo resulta ser un efecto del proceso de formación de las imágenes en STM provocado por las grandes diferencias de conductividad entre substrato y lámina. Tras la reducción, el aumento en la conductividad hace posible la visualización de las láminas de rGO empleando parámetros túnel estándar. Los tamaños

laterales y las formas de las láminas observadas son totalmente consistentes con las observaciones en AFM en modo tapping. El problema surge con los grosores aparentes observados, que son ostensiblemente menores: ~0.4–0.6 nm, frente a los ~0.9–1.2 nm obtenidos en modo tapping. Esta discrepancia, junto con la ausencia de una disminución del grosor aparente tras la reducción evidenciada en tapping, nos llevó a plantearnos la necesidad de un estudio detallado del procedimiento empleado para medir de manera precisa grosores de objetos extremadamente delgados.

Morfología a escala nanométrica. A esta escala, las imágenes de tapping muestran, tanto para el GO como para el rGO, la superficie de las láminas conformada por una morfología globular, cuyos rasgos presentan tamaños laterales de 5–10 nm. La rugosidad superficial disminuye ligeramente tras la reducción, siendo aproximadamente 0.11 nm para el GO y 0.09 nm para el rGO. El estudio mediante STM del rGO muestra la misma estructura globular observada en AFM aunque con mayor detalle. El hecho de que exista tan poca diferencia entre las imágenes de tapping y de STM indica que el tipo de estructura observado es básicamente de origen topográfico y no electrónico, y probablemente está asociado con una distorsión en la red del grafeno debido a la presencia de una gran cantidad de defectos estructurales.

Morfología a escala atómica. Debido a la elevada separación existente entre la punta y la superficie de la muestra en STM de baja corriente, con las consiguientes perturbaciones que ello conlleva, el estudio del GO a escala atómica resulta totalmente impracticable. Una vez efectuada la reducción, las imágenes STM a resolución atómica de las láminas de rGO constituyen una evidencia directa del grado de desorden estructural que presentan. En contraste con las imágenes de HOPG prístino, es de destacar la ausencia de orden o periodicidad de largo alcance a escala atómica, existiendo sólo pequeñas zonas aisladas de unos pocos nanómetros en las que sí se aprecia orden. Todo este desorden, que ya se podía anticipar a la vista de los espectros Raman, es debido a la presencia de funcionalidades de oxígeno y defectos estructurales creados durante los procesos de oxidación/reducción.

Medición de pequeños grosores mediante SPM

Como ya se ha indicado, las inconsistencias que se presentaron durante el estudio de los grosores de estas láminas sacaron a la luz la problemática existente en la medición precisa del grosor de láminas extremadamente delgadas mediante microscopías de proximidad. Por lo general, las medidas de grosor se efectúan midiendo la altura aparente de la lámina respecto al sustrato, con lo que estas mediciones se encuentran condicionadas por las diferencias en la interacción entre la sonda SPM y los distintos materiales. Estas diferencias son causantes de la introducción de artefactos en las imágenes debido a la naturaleza del mecanismo de medición en SPM, que interpreta una diferencia real en la interacción como una diferencia aparente de altura. Aunque la magnitud de esta diferencia artificial de altura no presenta un gran problema en la mayoría de las situaciones, en el caso de láminas

atómicamente delgadas estos artefactos pueden llegar a distorsionar completamente el grosor medido de las mismas, al ser del mismo orden de magnitud. Esto resulta especialmente importante en el caso de láminas de grafeno, por ser uno de los materiales más finos que existen. Por ello, se hizo un estudio de la medida del grosor de GO y rGO empleando diferentes sustratos y técnicas SPM, tratando de determinar la magnitud de esta incertidumbre y los mejores métodos para evitarla. Aún así, los resultados obtenidos pueden generalizarse a la medida de grosores de láminas delgadas de cualquier material, proporcionando una serie de recomendaciones y de procedimientos a evitar.

En general, las observaciones realizadas se pueden resumir en los siguientes puntos:

1. Al efectuar la medida (altura aparente) entre lámina y sustrato, el grosor obtenido depende tanto del sustrato empleado como del modo SPM utilizado.
2. Por el contrario, cuando las medidas de grosor se efectúan a partir de alturas aparentes entre láminas, los valores obtenidos son bastante uniformes y no dependen ni del substrato ni de la técnica SPM empleados. De este modo, al medir grosores en zonas de láminas superpuestas o plegadas sobre sí mismas se obtienen valores de ~0.9–1.1 nm y ~0.5–0.7 nm para el GO y el rGO, respectivamente.

Un claro ejemplo de esto se puede ver en la *figura 1*, en la que se muestran perfiles de altura en imágenes de láminas de rGO soportadas sobre HOPG y obtenidas mediante diferentes técnicas. Como se aprecia en la figura, los grosores medidos respecto al HOPG son claramente dependientes de la técnica empleada, mientras que los grosores en solapamientos son relativamente constantes. De esta manera, el procedimiento tradicional de medir la altura aparente de las láminas respecto al substrato proporciona valores ficticios de grosor de lámina y debe evitarse en la medida de lo posible. Sin embargo, esto no siempre resulta posible, ya que la densidad de láminas puede no ser lo suficientemente elevada, como ocurre por ejemplo en el caso de grafenos obtenidos mediante exfoliación mecánica.

En el modo tapping resulta posible hacer una estimación del error cometido en la medida del grosor al medir entre lámina y substrato. En la *figura 2* se puede observar la amplitud de oscilación del cantilever en el modo tapping en función del desplazamiento del *piezo*, tomada con la punta sobre el HOPG y sobre el GO. Se aprecia cómo la amplitud decrece más rápidamente al extenderse el *piezo* sobre el GO que sobre el HOPG. Esto provoca una sobreestimación de la altura de la lámina de GO al medir respecto al HOPG, puesto que una extensión del *piezo* significa una disminución en la distancia entre cantilever y muestra. De este modo, cuanto más cerca se trabaje de la amplitud libre la diferencia en el desplazamiento del *piezo* entre el GO y el HOPG es menor, lo que se traduce en que la sobreestimación ΔZ de la medida de la altura sea menor. Esto justifica la elección del régimen atractivo para hacer medidas más precisas, puesto que en éste las amplitudes de *setpoint* A_P con las que se trabaja son más

cercanas a la amplitud libre. Esta estimación en el error cometido en la medida resulta útil en el caso de que no sea posible la medición del grosor entre láminas.

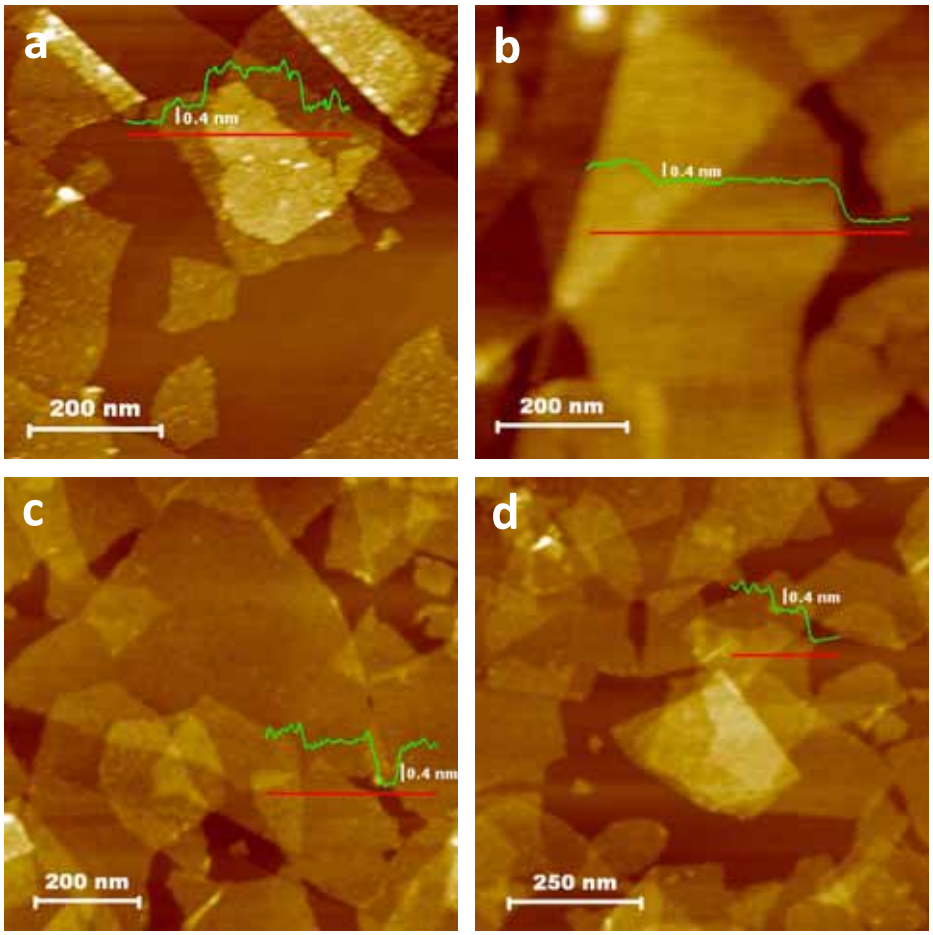

Figura 1 – Imágenes de rGO soportado sobre HOPG tomadas con STM (a), AFM contacto (b), y AFM tapping en modo atractivo (c) y repulsivo (d). Los perfiles incluidos permiten estimar los grosores de las láminas respecto al substrato y respecto a otras láminas sobre las que se superponen.

En el caso de las imágenes STM el comportamiento observado es completamente diferente al de AFM, ya que el grosor medido respecto al substrato resulta ser menor que el medido entre láminas. Esto es probablemente debido a la menor conductividad de las láminas respecto a la del substrato (HOPG), que provoca que la punta barra la superficie a menor altura sobre las láminas para tratar de mantener la misma corriente túnel que sobre el HOPG. De este modo el grosor de los grafenos se está subestimando cuando se mide respecto al substrato, llegando, en algunos casos límite de baja conductividad, a observarse las imágenes de contraste invertido anteriormente comentadas (esto solo resulta posible en el caso de baja corriente, en el que la punta está muy alejada de la superficie de la muestra). Para sortear este defecto de la técnica, también en el caso de STM resulta preferible realizar las medidas en solapamientos de grafenos. De hecho, los valores obtenidos en solapamientos son solo ligeramente mayores que los medidos con las diferentes técnicas de AFM.

Como conclusión, se puede afirmar que los grosores reales de las láminas son de ~0.9–1.1 nm para el GO, mientras que tras la reducción el grosor disminuye de manera considerable hasta ~0.5–0.7 nm. A pesar de esta disminución en el grosor, no se llega al valor del grafeno prístino (0.34 nm), algo esperable debido a la considerable cantidad de oxígeno que continúa existiendo en las láminas tras la reducción.

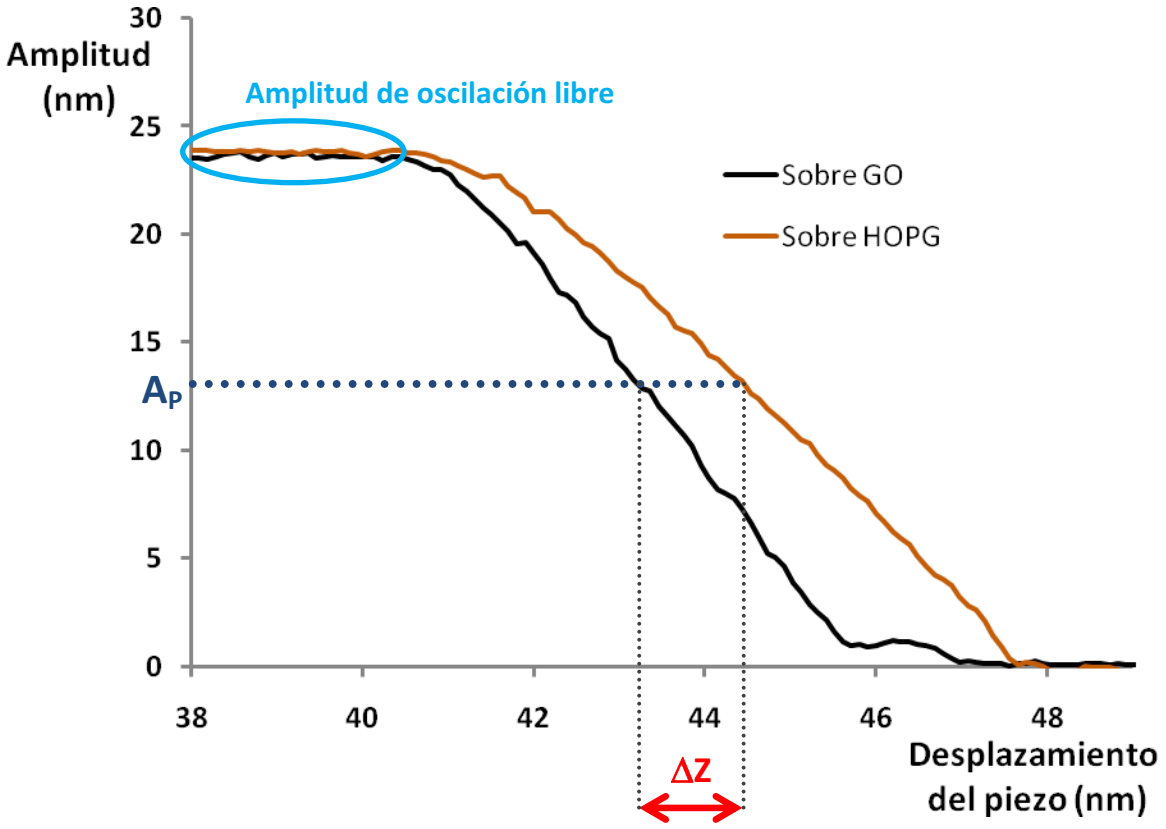

Figura 2 – Amplitud de oscilación del cantilever en modo tapping en función del desplazamiento del *piezo* (distancia punta-muestra) sobre el HOPG y sobre el GO. Cuanto más cerca se encuentre la amplitud de *setpoint* A_P de la amplitud libre, menor será la sobreestimación ΔZ que haremos de la altura. Es por esto que resulta conveniente trabajar en el modo atractivo siempre que sea posible.

Langmuir
Article
pubs.acs.org/Langmuir

Atomic Force and Scanning Tunneling Microscopy Imaging of Graphene Nanosheets Derived from Graphite Oxide

J. I. Paredes,* S. Villar-Rodil, P. Solís-Fernández, A. Martínez-Alonso, and J. M. D. Tascón

Instituto Nacional del Carbón, CSIC, Apartado 73, 33080 Oviedo, Spain

Received December 22, 2008. Revised Manuscript Received February 11, 2009

Graphene nanosheets produced in the form of stable aqueous dispersions by chemical reduction of graphene oxide and deposited onto graphite substrates have been investigated by atomic force and scanning tunneling microscopy (AFM/STM). The chemically reduced graphene oxide nanosheets were hardly distinguishable from their unreduced counterparts in the topographic AFM images. However, they could be readily discriminated through phase imaging in the attractive regime of tapping-mode AFM, probably because of differences in hydrophilicity arising from their distinct oxygen contents. The chemically reduced nanosheets displayed a smoothly undulated, globular morphology on the nanometer scale, with typical vertical variations in the subnanometer range and lateral feature sizes of ∼5−10 nm. Such morphology was attributed to be the result of significant structural disorder in the carbon skeleton, which originates during the strong oxidation that leads to graphene oxide and remains after chemical reduction. Direct evidence of structural disorder was provided by atomic-scale STM imaging, which revealed an absence of long-range periodicity in the graphene nanosheets. Only structured domains a few nanometers large were observed instead. Likewise, the nanosheet edges appeared atomically rough and ill-defined, though smooth on the nanometer scale. The unreduced graphene oxide nanosheets could only be imaged by STM at very low tunneling currents (∼1 pA), being visualized in some cases with inverted contrast relative to the graphite substrate, a result that was attributed to their extremely low conductivity. Complementary characterization of the unreduced and chemically reduced nanosheets was carried out by thermogravimetric analysis as well as UV−visible absorption and X-ray photoelectron and Raman spectroscopies. In particular, the somewhat puzzling Raman results were interpreted to be the result of an amorphous character of the graphene oxide material.

1. Introduction

Interest in graphene in the fields of condensed matter physics and materials science has been rapidly growing over the past few years as a result of its first successful isolation[1,2] and the subsequent discovery of new and unusual fundamental physical properties, which mainly originate from its two-dimensional nature.[3−8] In parallel with these developments from the basic science perspective, many applications have been proposed and are currently being explored for graphene and some of its chemically modified forms (most notably, those derived from graphite oxide), including their use in nanoelectronic devices,[1,9−12] electrically conductive and mechanically reinforced composite materials,[13,14] gas sensors,[15,16] supercapacitors,[17] Li-ion batteries,[18] or drug delivery.[19]

Chemically modified graphene derived from graphite oxide is particularly attractive for materials science applications, as it can be conveniently processed in liquid phase in bulk quantities, thus facilitating the preparation of, e.g., ultrathin films,[11,12,16,20] paper-like materials,[21−23] or composites.[13,14,24] More specifically, due to the hydrophilicity and ionizability of many of its oxygen-containing functional groups, graphite oxide can be readily exfoliated in water to yield stable dispersions of single-layer sheets (graphene oxide sheets).[13,25,26] These dispersions constitute a strategic starting point

*Corresponding author. Telephone number: (+34) 985 11 90 90. Fax number: (+34) 985 29 76 62. E-mail address: paredes@incar.csic.es

(1) Novoselov, K. S.; Geim, A. K.; Morozov, S. V.; Jiang, D.; Zhang, Y.; Dubonos, S. V.; Grigorieva, I. V.; Firsov, A. A. *Science* **2004**, *306*, 666–669.
(2) Novoselov, K. S.; Jiang, D.; Schedin, F.; Booth, T. J.; Khotkevich, V. V.; Morozov, S. V.; Geim, A. K. *Proc. Natl. Acad. Sci. U.S.A.* **2005**, *102*, 10451–10453.
(3) Geim, A. K.; Novoselov, K. S. *Nat. Mater.* **2007**, *6*, 183–191.
(4) Fasolino, A.; Los, J. H.; Katsnelson, M. I. *Nat. Mater.* **2007**, *6*, 858–861.
(5) Miao, F.; Wijeratne, S.; Zhang, Y.; Coskun, U. C.; Bao, W.; Lau, C. N. *Science* **2008**, *317*, 1530–1533.
(6) Chen, J.-H.; Jang, C.; Adam, S.; Fuhrer, M. S.; Williams, E. D.; Ishigami, M. *Nat. Phys.* **2008**, *4*, 377–381.
(7) Li, Z. Q.; Henriksen, E. A.; Jiang, Z.; Hao, Z.; Martin, M. C.; Kim, P.; Stormer, H. L.; Basov, D. N. *Nat. Phys.* **2008**, *4*, 532–535.
(8) Martin, J.; Akerman, N.; Ulbricht, G.; Lohmann, T.; Smet, J. H.; von Klitzing, K.; Yacoby, A. *Nat. Phys.* **2008**, *4*, 144–148.
(9) Gilje, S.; Han, S.; Wang, M.; Wang, K. L.; Kaner, R. B. *Nano Lett.* **2007**, *7*, 3394–3398.
(10) Li, X.; Wang, X.; Zhang, L.; Lee, S.; Dai, H. *Science* **2008**, *319*, 1229–1232.
(11) Eda, G.; Fanchini, G.; Chhowalla, M. *Nat. Nanotechnol.* **2008**, *3*, 270–274.
(12) Wang, X.; Zhi, L.; Müllen, K. *Nano Lett.* **2008**, *8*, 323–327.
(13) Stankovich, S.; Dikin, D. A.; Dommett, G. H. B.; Kohlhaas, K. M.; Zimney, E. J.; Stach, E. A.; Piner, R. D.; Nguyen, S. T.; Ruoff, R. S. *Nature (London)* **2006**, *442*, 282–286.
(14) Ramanathan, T.; Abdala, A. A.; Stankovich, S.; Dikin, D. A.; Herrera-Alonso, M.; Piner, R. D.; Adamson, D. H.; Schniepp, H. C.; Chen, X.; Ruoff, R. S.; Nguyen, S. T.; Aksay, I. A.; Prud′homme, R. K.; Brinson, L. C. *Nat. Nanotechnol.* **2008**, *3*, 327–331.
(15) Schedin, F.; Geim, A. K.; Morozov, S. V.; Hill, E. W.; Blake, P.; Katsnelson, M. I.; Novoselov, K. S. *Nat. Mater.* **2007**, *6*, 652–655.
(16) Robinson, J. T.; Perkins, F. K.; Snow, E. S.; Wei, Z.; Sheehan, P. E. *Nano Lett.* **2008**, *8*, 3137–3140.
(17) Stoller, M. D.; Park, S.; Zhu, Y.; An, J.; Ruoff, R. S. *Nano Lett.* **2008**, *8*, 3498–3502.
(18) Yoo, E. J.; Kim, J.; Hosono, E.; Zhou, H.; Kudo, T.; Honma, I. *Nano Lett.* **2008**, *8*, 2277–2282.
(19) Liu, Z.; Robinson, J. T.; Sun, X.; Dai, H. *J. Am. Chem. Soc.* **2008**, *130*, 10876–10877.
(20) Becerril, H. A.; Mao, J.; Liu, Z.; Stoltenberg, R. M.; Bao, Z.; Chen, Y. *ACS Nano* **2008**, *2*, 463–470.
(21) Dikin, D. A.; Stankovich, S.; Zimney, E. J.; Piner, R. D.; Dommett, G. H. B.; Evmenenko, G.; Nguyen, S. T.; Ruoff, R. S. *Nature (London)* **2007**, *448*, 457–460.
(22) Chen, H.; Müller, M. B.; Gilmore, K. J.; Wallace, G. G.; Li, D. *Adv. Mater.* **2008**, *20*, 3557–3561.
(23) Xu, Y.; Bai, H.; Lu, G.; Li, C.; Shi, G. *J. Am. Chem. Soc.* **2008**, *130*, 5856–5857.
(24) Verdejo, R.; Barroso-Bujans, F.; Rodriguez-Perez, M. A.; de Saja, J. A.; Lopez-Manchado, M. A. *J. Mater. Chem.* **2008**, *18*, 2221–2226.
(25) Stankovich, S.; Dikin, D. A.; Piner, R. D.; Colas, K. A.; Kleinhammes, A.; Jia, Y.; Wu, Y.; Nguyen, S. T.; Ruoff, R. S. *Carbon* **2007**, *45*, 1558–1565.
(26) Li, D.; Müller, M. B.; Gilje, S.; Kaner, R. B.; Wallace, G. G. *Nat. Nanotechnol.* **2008**, *3*, 101–105.

for the large-scale production of graphene, which is typically achieved by chemical or thermal reduction.[9,11−13,16,18,20,23,25−30] For instance, it has very recently been reported that aqueous dispersions of electrically conductive graphene nanosheets exhibiting long-term stability can be prepared via chemical reduction of the nonconductive graphene oxide dispersions without the aid of surfactants or any other stabilizers.[26] However, it has also been recognized that such chemically derived graphene differs significantly from its pristine, defect-free counterpart, which is usually produced by micromechanical cleavage of bulk graphite.[1−3] In particular, chemically reduced graphene oxide is thought to contain, apart from residual oxygen functionalities, a significant amount of structural disorder inherited from the oxidative transformation of graphite to graphite oxide,[11,25,27,28] even though direct microscopic information in this respect has so far not been documented. Thus, for the further advancement of materials based on this chemically modified form of graphene, an in-depth knowledge of its local nanometer- and atomic-scale structure would be highly desirable.

Here, we report the use of atomic force and scanning tunneling microscopies (AFM/STM) to probe the local characteristics (nanometer-scale morphology and atomic-scale structure) of graphene nanosheets produced as stable aqueous dispersions by chemical reduction of the corresponding graphene oxide dispersions. To date, AFM has been employed for the most part to examine only general features (i.e., sheet thickness and lateral dimensions) of pristine or chemically modified graphene sheets,[2,10,11,13,25,29] and much less frequently to image its detailed nanoscale morphology,[31,32] which has not been undertaken for the specific case of chemically reduced graphene oxide. Detailed AFM images of the so-called functionalized graphene sheets (FGSs) have been previously reported,[31] but these constitute a different type of chemically modified graphene from that documented here. FGSs are prepared through rapid thermal expansion at 1050 °C of graphite oxide, whereas the graphene nanosheets studied here are produced by chemical reaction with a reducing agent (hydrazine) at low temperature. Therefore, structural and chemical differences could be expected between both types of graphene. Likewise, atomic-scale STM studies of graphene are rather scarce, and, again, these concern only pristine samples prepared by micromechanical cleavage,[32−34] epitaxial growth,[35,36] or STM lithography,[37] but not samples prepared by chemical reduction of graphene oxide. This is, to the best of our knowledge, the first report that provides direct structural information down to the atomic scale for such type of graphene.

2. Experimental Section

The graphene nanosheets investigated in this work were produced in the form of stable dispersions in water following the procedure recently reported by Li et al.,[26] which consists of three steps: (1) synthesis of graphite oxide from pristine graphite powder, (2) exfoliation and dispersion in water of the graphite oxide product as single-layer sheets (graphene oxide sheets), and (3) conversion of the graphene oxide sheets back to graphene by controlled chemical reduction. Graphite oxide was prepared from natural graphite powder (Fluka 50870) via the Hummers method using $NaNO_3$, H_2SO_4, and $KMnO_4$.[38,39] The oxidized material was purified by washing with 10% HCl solution, repeatedly rinsing with copious amounts of Milli-Q water, and filtering through standard filter paper with a Büchner funnel, after which a thick graphite oxide slurry was obtained. To make dispersions in water, either the graphite oxide slurry was directly used or, alternatively, a dried graphite oxide powder was employed. The latter was prepared by drying the slurry under vacuum (80 °C, 3 h), peeling the resulting ∼0.5 mm thick film off the filter paper, and gently grinding it with a mortar and pestle. In a typical exfoliation process, a small amount of the graphite oxide slurry or dried powder was added to a given volume of water and sonicated in an ultrasound bath cleaner (JP Selecta Ultrasons system, 40 kHz) for 1 h. Then, the sonicated dispersion was centrifuged (Eppendorf 5424 microcentrifuge) at 20238*g* for 20 min to remove unexfoliated graphite oxide particles, and the supernatant, which was the final graphene oxide dispersion, was collected. Subsequent characterization of the dispersions by different techniques did not yield significant differences between those derived from the slurry and from the dried powder. Chemical reduction of the dispersed graphene oxide sheets was carried out by reaction with hydrazine monohydrate after adjusting the pH of the dispersion to ∼10 with ammonia to promote the colloidal stability of the sheets through electrostatic repulsion. As such stability also critically depends on the amount of reducing agent employed in relation to the mass of graphene oxide present in the dispersion,[26] it was necessary to work with graphene oxide dispersions of known concentration, for which UV−visible (UV−vis) absorption spectroscopy was employed. A calibration curve relating absorbance at 231 nm (see below for the choice of such wavelength) and graphene oxide concentration was obtained by measuring the absorbance for different dispersions of known concentration (prepared by sonication of the dried powder). Reduction was typically accomplished for graphene oxide dispersions with a concentration of 0.1 mg mL^{-1}, using 2 μL of 25% ammonia solution and 0.1 μL of hydrazine monohydrate for each mL of graphene oxide dispersion, which has been reported as the optimal ratio for reduction.[26] The reaction was carried out in a water bath at 95 °C for 1 h.

A general characterization of the graphene oxide material before and after chemical reduction, in dispersed state or processed into solid films (depending on the technique used), was performed by UV−vis absorption spectroscopy, thermogravimetric analysis (TGA), X-ray photoelectron spectroscopy (XPS) and Raman spectroscopy. The films were prepared either in the form of substrate-supported ultrathin coatings or as free-standing paper-like materials. In the former case, the dispersion was cast dropwise onto a preheated (∼60−70 °C) flat metallic disk until a uniform dark film covering the whole substrate was visible to the naked eye. Unreduced and chemically reduced graphene oxide paper was produced, as reported elsewhere,[21,22] by filtering the corresponding aqueous dispersion through an Anodisc membrane filter 47 mm in diameter and 0.2 μm of pore size (Whatman). UV−vis absorption spectra of the dispersions were recorded with a double-beam Heλios α spectrophotometer, from Thermo Spectronic. TGA of the free-standing paper was

(27) Gómez-Navarro, C.; Weitz, R. T.; Bittner, A. M.; Scolari, M.; Mews, A.; Burghard, M.; Kern, K. *Nano Lett*. **2007**, *7*, 3499–3503.
(28) Wang, G.; Yang, J.; Park, J.; Gou, X.; Wang, B.; Liu, H.; Yao, J. *J. Phys. Chem. C* **2008**, *112*, 8192–8195.
(29) Si, Y.; Samulski, E. T. *Nano Lett*. **2008**, *8*, 1679–1682.
(30) Park, S.; An, J.; Piner, R. D.; Jung, I.; Yang, D.; Velamakanni, A.; Nguyen, S. T.; Ruoff, R. S. *Chem. Mater*. **2008**, *20*, 6592–6594.
(31) Schniepp, H. C.; Li, J.-L.; McAllister, M. J.; Sai, H.; Herrera-Alonso, M.; Adamson, D. H.; Prud′homme, R. K.; Car, R.; Saville, D. A.; Aksay, I. A. *J. Phys. Chem. B* **2006**, *110*, 8535–8539.
(32) Ishigami, M.; Chen, J. H.; Cullen, W. G.; Fuhrer, M. S.; Williams, E. D. *Nano Lett*. **2007**, *7*, 1643–1648.
(33) Stolyarova, E.; Rim, K. T.; Ryu, S.; Maultzsch, J.; Kim, P.; Brus, L. E.; Heinz, T. F.; Hybertsen, M. S.; Flynn, G. W. *Proc. Natl. Acad. Sci. U.S.A*. **2007**, *104*, 9209–9212.
(34) Stolyarova, E.; Stolyarov, D.; Liu, L.; Rim, K. T.; Zhang, Y.; Han, M.; Hybersten, M.; Kim, P.; Flynn, G. *J. Phys. Chem. C* **2008**, *112*, 6681–6688.
(35) Rutter, G. M.; Crain, J. N.; Guisinger, N. P.; Li, T.; First, P. N.; Stroscio, J. A. *Science* **2007**, *317*, 219–222.
(36) Mallet, P.; Varchon, F.; Naud, C.; Magaud, L.; Berger, C.; Veuillen, J.-Y. *Phys. Rev. B* **2007**, *76*, 041403.
(37) Tapasztó, L.; Dobrik, G.; Lambin, P.; Biró, L. P. *Nat. Nanotechnol*. **2008**, *3*, 397–401.
(38) Hummers, W.; Offeman, R. *J. Am. Chem. Soc*. **1958**, *80*, 1339.
(39) Paredes, J. I.; Villar-Rodil, S.; Martínez-Alonso, A.; Tascón, J. M. D. *Langmuir* **2008**, *24*, 10560–10564.

accomplished by means of an SDT Q600 thermobalance (TA Instruments) under Ar gas flow (100 mL min^{-1}) at a heating rate of 10 °C min^{-1}, using Pt crucibles. For XPS measurement of the paper samples, a SPECS system working under 10^{-7} Pa with a monochromatic Al Kα X-ray source (100 W) was employed. The surface charging effect observed for the nonconductive, unreduced graphene oxide sample was corrected by the use of an electron flood gun operating at 0.4 eV and 0.10 mA.[39] Surface composition (atomic %) of the samples was determined from the survey spectra by considering the integrated intensities of the main XPS peaks of the elements that were found. Raman measurements were made with a Horiba Jobin-Yvon LabRam instrument at a laser excitation wavelength of 532 nm.

For the AFM and STM investigations, the unreduced and chemically reduced graphene oxide aqueous dispersions were drop-cast onto freshly cleaved, atomically flat highly oriented pyrolytic graphite (HOPG) substrates (ZYH grade, from Advanced Ceramics Corporation) and then allowed to dry in air at room temperature. The dispersions were also deposited onto freshly cleaved mica (grade V-1, Electron Microscopy Sciences), and the nanosheets displayed (by AFM) a similar appearance to that of the sheets deposited onto HOPG. However, as mica is electrically nonconductive, it cannot be employed for STM studies. For this reason, in the present work HOPG was the substrate of choice, and all the presented results were obtained on this material. AFM and STM were carried out under ambient conditions (relative humidity ~40%, temperature ~22−24 °C) with a Nanoscope IIIa Multimode apparatus (Veeco Instruments). AFM was performed in the tapping mode of operation using rectangular silicon cantilevers with spring constant of ~40 N m^{-1} and typical resonance frequencies between 250 and 300 kHz. Imaging was accomplished in the attractive regime of tip−sample interaction,[40,41] recording height (topography) and phase images simultaneously. STM measurements were performed in the constant current mode (variable height) with mechanically prepared Pt/Ir (80/20) tips. To allow operation with tunneling currents down to the pA regime, a low-current converter was coupled to the Nanoscope IIIa system. Unless otherwise stated, the STM images presented here are height images.

3. Results and Discussion

3.1. Global Characterization of Graphene Dispersions and Thin Films. Figure 1 (inset) shows a digital picture of 0.1 mg mL^{-1} graphene oxide dispersion in water (left), together with its chemically reduced counterpart (right). The yellow-brown color characteristic of the unreduced dispersion changes to black following reduction, suggesting that deoxygenation of the graphene nanosheets has effectively come about.[13,26] The picture was taken 5 months after preparation of both dispersions, and none of them shows any visible sign of precipitation, which indicates that both the unreduced and reduced dispersions possess long-term stability. Additional evidence for reduction is presented in the UV−vis spectra of Figure 1. In agreement with previous reports,[26,39] the spectrum obtained for the unreduced graphene oxide dispersion (orange plot) exhibits a maximum at 231 nm (attributed to $\pi \rightarrow \pi^*$ transitions of aromatic C−C bonds) and a shoulder at ~300 nm (ascribed to $n \rightarrow \pi^*$ transitions of C=O bonds). After reduction (black plot), the maximum redshifts to about 270 nm, and a significant increase in absorbance is noticed for the whole range of wavelengths larger than 231 nm. Both effects are indication that electronic conjugation has been restored, at least to some extent, within the carbon framework of the graphene nanosheets.[26,42]

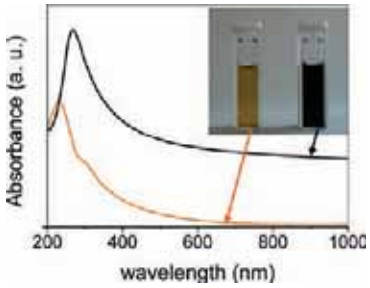

Figure 1. UV−vis spectra for unreduced (orange) and chemically reduced (black) graphene oxide dispersions in water. Inset: digital picture of the unreduced (left) and reduced (right) aqueous dispersions.

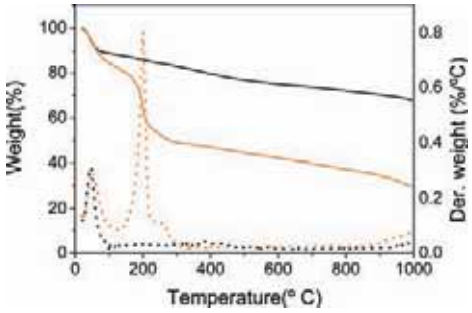

Figure 2. TG (solid curves) and DTG (dotted curves) plots for unreduced (orange) and chemically reduced (black) graphene oxide material.

Further proof of the chemical transformations induced by reduction was obtained by TGA and XPS measurements. Figure 2 shows the thermogravimetric (TG) and differential thermogravimetric (DTG) plots for the unreduced graphene oxide material (full and dotted orange curves, respectively) and the reduced material (solid and dotted black curves, respectively). For the unreduced material, the main mass loss (~30%) occurs around 200 °C, and is attributed to the decomposition of labile oxygen functional groups.[25,39] The mass loss at temperatures below 100 °C (~15%) can be ascribed to the removal of adsorbed water, whereas the steady loss observed for temperatures above 300 °C and up to 1000 °C, which amounts to ~20%, is assigned to the release of more stable oxygen functionalities.[39] Following reduction, the sharp mass loss around 200 °C is no longer observed, suggesting that the labile oxygen functional groups in graphene oxide are largely removed by reaction with hydrazine. On the other hand, a slow, steady mass loss (~20%) over the whole temperature range above 100 °C is retained after reduction, which implies that the more stable oxygen functionalities are not eliminated from graphene by the chemical reduction. The reduced material also displays a significant mass loss (~10%) below 100 °C due to water desorption. The presence of oxygen on both samples was directly evidenced by XPS. Figure 3 presents high-resolution core-level C 1s spectra for the unreduced graphene oxide material (a) and its reduced counterpart (b). For the unreduced material, a complex band showing two maxima ~2 eV apart can be noticed. This band was fitted to three components, located at 284.6 (graphitic C=C species),

(40) James, P. J.; Antognozzi, M.; Tamayo, J.; McMaster, T. J.; Newton, J. M.; Miles, M. J. *Langmuir* **2001**, *17*, 349–360.
(41) Paredes, J. I.; Villar-Rodil, S.; Tamargo-Martínez, K.; Martínez-Alonso, A.; Tascón, J. M. D. *Langmuir* **2006**, *22*, 4728–4733.
(42) Skoog, D. A.; Holler, F. J.; Nieman. T. A. *Principles of Instrumental Analysis*; Hartcourt Brace & Company: Philadelphia, PA, 1998; Chapter 13.

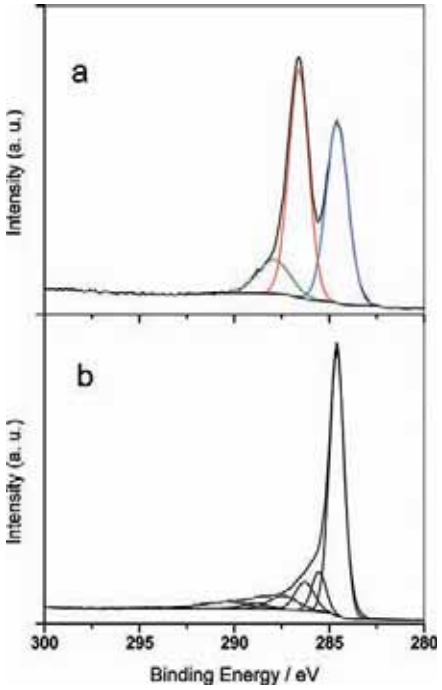

Figure 3. High-resolution C 1s XPS spectra for unreduced (a) and chemically reduced (b) graphene oxide material.

286.6 (C−O species), and 287.9 eV (C═O species), as reported previously.[39] It has been suggested that defect (sp^3) C−C species give rise to a component very close to 286.6 eV,[43,44] so in the present case it is very likely that the 286.6 eV component also bears a contribution from these species. After reduction, the relative contribution of the components associated with oxygenated and sp^3 carbon species was seen to decrease very significantly (Figure 3b, see also Table 1), which agrees with previous reports from the literature.[11,25,26,30,31] In this case, the C 1s band was fitted to six components, located at 284.6 (graphitic C═C species), 285.5 (localized alternant hydrocarbon),[43] 286.3 (C−O, C−N[45] and sp^3 carbon species), 287.4 (C═O and $\pi\rightarrow\pi^*$ shake up peak of band centered at 285.5 eV), 288.8 (COOH), and 290.0 eV ($\pi\rightarrow\pi^*$ shake up peak of band centered at 284.6 eV). Deoxygenation of the graphene nanosheets by the chemical reduction process was also evidenced from the O/C atomic ratios derived from the XPS survey spectra (not shown), which yielded values of 0.43 for the unreduced graphene oxide material and 0.16 for the reduced material. The residual oxygen functionalities retained following reduction would still render the nanosheets somewhat hydrophilic, imparting them with colloidal stability in water,[26] and also explaining the significant amount of water that this material is able to adsorb (see TG results, Figure 2).

Raman spectroscopy was employed to obtain global structural information, as opposed to the local structural information that would be provided by atomic-scale STM, for the unreduced and chemically reduced samples. The results of the Raman measurements are presented in Figure 4, which shows first- and second-order spectra. For comparison purposes, the spectrum of the pristine graphite powder used to prepare the chemically modified graphenes is included in Figure 4a. The first-order spectrum of this pristine graphite is characterized by a strong band at ~1580 cm^{-1} (G band) and a very weak band at ~1340 cm^{-1} (D band). The latter is induced by structural disorder, in such a way that the integrated intensity ratio of the D and G bands (I_D/I_G) increases with the amount of disorder for graphitic materials, vanishing for completely defect-free graphite.[46] The second-order (two-photon) spectrum of the starting graphite sample is dominated by a strong band at ~2690 cm^{-1} (2D band) and a weak band at ~3240 cm^{-1}. The 2D band is the overtone (second harmonic) of the D band, whereas the band at ~3240 cm^{-1} corresponds to the overtone of a band located at ~1620 cm^{-1} (D′ band) in the first-order spectrum,[47] which, in the present case, is seen as a weak shoulder on the high wavenumber side of the G band in Figure 4a. Similar to the case of the D band, the D′ band is not present in defect-free graphite, and its relative intensity increases with graphitic disorder. Raman spectra of the chemically modified graphenes [Figure 4b (unreduced material) and c (reduced material)] were recorded for the thin solid film samples (both substrate-supported coating and free-standing paper; see Experimental Section) as well as for the liquid samples (aqueous dispersions), without significant differences being detected between the spectra for the different preparations of the same material. As noticed from the spectrum of the unreduced graphene oxide material in Figure 4b, the I_D/I_G ratio increases dramatically in comparison with that of the starting graphite material (from 0.13 to 1.46), implying that the oxidation process has introduced a considerable amount of structural disorder in the graphene lattice. The same conclusion can be drawn when the second-order spectrum is inspected. First, the 2D band is seen to broaden and decrease in relative intensity compared to the G band, an effect that has been related to the presence of defects in graphitic materials.[47] Second, a band appears at ~2920 cm^{-1}, partly obscuring the 2D band. This new band results from the combination of the two modes that give rise to the first-order D and G bands, and is caused by lattice disorder.[47] When the Raman spectrum of the chemically reduced material (Figure, 4c) is compared with that of the unreduced sample (Figure 4b), subtle, rather than drastic, changes are observed. Even though the I_D/I_G ratio remains essentially constant (1.43 vs 1.46 before reduction), the shape of the first-order spectrum has been altered to some extent. The G band of the chemically reduced material is somewhat asymmetric, displaying an intense shoulder on its high wavenumber side, which is not evident on the G band of the unreduced material. This shoulder could in principle correspond to the D′ band located at ~1620 cm^{-1} previously discussed. Regarding the second-order spectrum, the 2D band appears more intense and defined in relation to the band at ~2920 cm^{-1} after chemical reduction (compare Figure 4c with b). Similar changes upon chemical reduction of graphene oxide have been recently documented by other groups,[23,25,27,30] even with an increased I_D/I_G ratio following reduction reported in one case.[25] This result is quite unexpected and apparently contradicts the idea that, after chemical reduction and subsequent restoration of the aromaticity on the graphene lattice, a significantly reduced D band might be anticipated. Stankovich et al. interpret such a result by assuming that reduction increases the number of aromatic domains of smaller overall size in graphene, which would lead to an enhancement of the I_D/I_G ratio.[25] However, if

(43) Yang, D.-Q.; Rochette, J.-F.; Sacher, E. *Langmuir* **2005**, *21*, 8539–8545.
(44) Yang, D.-Q.; Sacher, E. *Langmuir* **2006**, *22*, 860–862.
(45) Wang, Q.; Kaliaguine, S.; Ait-Kadi, A. *J. Appl. Polym. Sci.* **1993**, *48*, 121–148.
(46) Ferrari, A. C.; Robertson, J. *Phys. Rev. B* **2000**, *61*, 14095–14107.
(47) Chieu, T. C.; Dresselhaus, M. S.; Endo, M. *Phys. Rev. B* **1982**, *26*, 5867–5877.

Table 1. Assignment of Carbon Species and Their Relative Weight for Unreduced and Chemically Reduced Graphene Oxide As Obtained by Fitting High-Resolution Core-Level C1s XPS Spectra

Unreduced Graphene Oxide						
binding energy (eV)	284.6		286.6	287.9		
assignment	C=C		C−O sp^3 C−C	C=O		
% area	41.25		47.49	11.26		
Reduced Graphene Oxide						
binding energy (eV)	284.6	285.5	286.3	287.4	288.8	290.0
assignment	C=C	localized hydrocarb.	C−O C-N sp^3 C−C	C=O $\pi\rightarrow\pi^*$	COOH	$\pi\rightarrow\pi^*$
% area	66.48	9.51	9.18	6.72	2.53	5.58

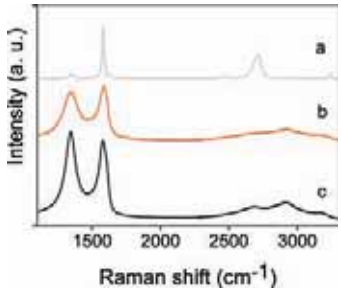

Figure 4. Raman spectra for pristine natural graphite powder (a), unreduced graphene oxide film (b), and chemically reduced graphene oxide film (c).

this interpretation was correct, a decrease in the 2D band relative to the band at ∼2920 cm^{-1} should be likely expected after reduction,[47] which was not observed either in the present work (Figure 4) or in previous ones.[30] We believe that the apparent contradiction can be solved by assuming that the carbon lattice in graphene oxide has developed some degree of amorphous character due to the oxidation process itself. Previous work with disordered and amorphous carbon materials has shown that, rather than increasing, the I_D/I_G ratio decreases upon amorphization of highly defected, but essentially graphitic, carbons, the effect being attributed to a large distortion of the 6-fold aromatic rings.[46] In such a case, the I_D/I_G ratio cannot be used as a measure of structural disorder and, accordingly, comparisons between materials of amorphous and graphitic character are no longer valid. Taking into account that the basal plane in graphene oxide is heavily decorated with oxygen functionalities such as epoxides and hydroxyls,[13,25,48] a significant distortion of the aromatic rings, and consequently a certain amorphous character, should be expected for this unreduced material. On the other hand, when the graphene oxide sheet is deoxygenated by the chemical reduction process, the distortion of the 6-fold rings is removed, and the carbon lattice returns to an essentially graphitic, but highly defected, state. Thus, an increase in the I_D/I_G ratio upon chemical reduction would even be possible.[25] We note that a similar amorphization phenomenon has been recently invoked to interpret Raman spectroscopy and atomic-scale STM results of plasma-oxidized graphite.[49]

3.2. Local Characterization of Individual Graphene Nanosheets. Figure 5 shows general height (a,c) and phase (b,d) tapping-mode AFM images of unreduced (a,b) and chemically reduced (c,d) graphene oxide nanosheets deposited onto HOPG, as obtained in the attractive regime of tip−sample interaction. Typical line profiles taken along the marked red lines are also presented superimposed onto each image. Tapping-mode AFM imaging was performed in the attractive regime with a 2-fold purpose: first, to avoid any disturbance to the nanosheets by the AFM tip, as this regime has been proven to be extremely gentle in comparison not only with contact-mode AFM but also with the repulsive regime of tapping mode;[41,50] second, to probe chemical differences between the unreduced and the reduced graphene oxide nanosheets. It has been previously shown that phase imaging in the attractive regime of tapping mode is able to locally detect the presence of hydrophilic oxygen groups on carbon surfaces,[51−53] so a discrimination between the unreduced and reduced nanosheets based on phase images would, in principle, be possible. As the height images and corresponding line profiles show, there are no noticeable morphological differences between the unreduced (Figure 5a) and chemically reduced (Figure 5c) nanosheets at this magnification. In both cases, sheets of uniform height relative to the HOPG substrate (∼1.0−1.2 nm) and lateral dimensions ranging from a few hundred nanometers to about 1 μm are observed. In accordance with previous reports,[13,25,26] these objects are interpreted to be single-layer sheets. By contrast, significant differences between both samples were observed in the phase images. Since both the unreduced and reduced nanosheets were deposited onto freshly cleaved HOPG, this substrate served as a common reference against which the phase values of the sheets could be compared.[53] For the unreduced sheets (Figure 5b), the measured phase was clearly different (∼2−3° higher; see line profile) to that of the unoxidized, pristine HOPG surface, whereas the phase of the chemically reduced sheets was essentially the same as that of the substrate (Figure 5d). For carbon surfaces, a phase shift upward of this magnitude relative to the pristine HOPG substrate can be interpreted as a signature of the presence of hydrophilic oxygen functionalities,[51−53] so its observation on the unreduced graphene oxide material constitutes local evidence of the strong oxidation of the sheets. Detailed inspection of the phase image in Figure 5b reveals that, while all the sheets display a generally increased phase relative to that of the HOPG background, there exist some local variations in the actual phase values from sheet to sheet or even within an individual sheet. This can be seen, for instance, when comparing the two sheets identified by black and white arrows in Figure 5a,b. The sheet

(48) Szabo, T.; Berkesi, O.; Forgo, P.; Josepovits, K.; Sanakis, Y.; Petridis, D.; Dekany, I. *Chem. Mater.* **2006**, *18*, 2740–2749.
(49) Paredes, J. I.; Martínez-Alonso, A.; Tascón, J. M. D. *Langmuir* **2007**, *23*, 8932–8943.
(50) San Paulo, A.; García, R. *Biophys. J.* **2000**, *78*, 1599–1605.
(51) Paredes, J. I.; Martínez-Alonso, A.; Tascón, J. M. D. *Langmuir* **2002**, *18*, 4314–4323.
(52) Paredes, J. I.; Martínez-Alonso, A.; Tascón, J. M. D. *Chem. Commun.* **2002**, 1790–1791.
(53) Paredes, J. I.; Martínez-Alonso, A.; Tascón, J. M. D. *Langmuir* **2003**, *19*, 7665–7668.

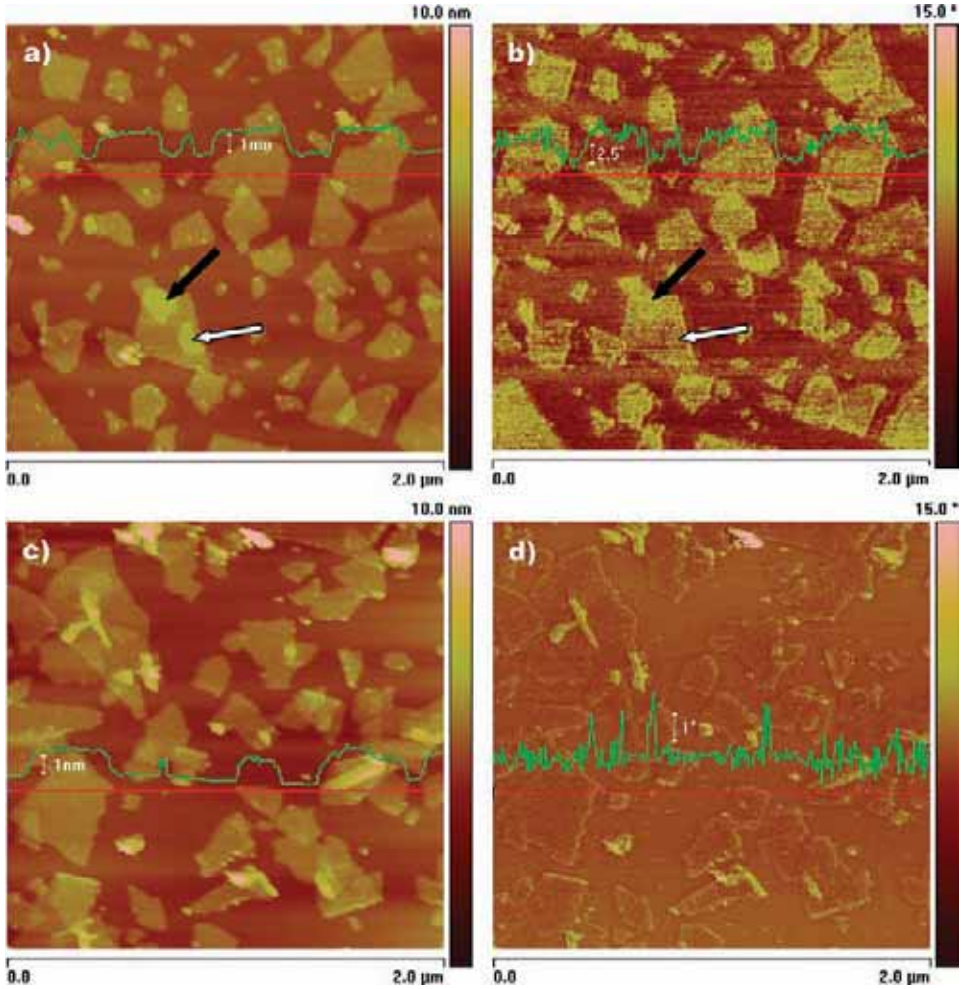

Figure 5. Height (a,c) and corresponding phase (b,d) tapping-mode AFM images of unreduced (a,b) and chemically reduced (c,d) graphene oxide nanosheets deposited from aqueous dispersions onto freshly cleaved HOPG. The images were recorded in the attractive regime of tip−sample interaction. Superimposed onto each image is a line profile taken along the marked red line.

denoted by the black arrow exhibits a higher phase than that of the sheet marked by the white arrow. Such observations suggest that different graphene oxide sheets could be oxidized to somewhat different extents and that single sheets may exhibit areas with different levels of oxidation on the nanometer scale. On the other hand, the fact that the chemically reduced graphene oxide sheets present very similar phase values to that of the HOPG substrate (Figure 5d) suggests that reduction has decreased the hydrophilicity of the sheets to a level closer (although most probably not identical) to that of the HOPG surface. This result could be certainly expected, as it has been shown that a dried dispersion of chemically reduced graphene oxide cannot be redispersed in water (i.e., it is hydrophobic), whereas redispersion is possible for the dried, unreduced graphene oxide material.[21,26]

Figure 6 shows tapping mode AFM images of individual sheets in more detail (a,b) and of the nanometer-scale morphology of the sheets at high magnification (c,d), together with typical line profiles (e,f) for the unreduced (a,c,e) and chemically reduced (b,d,f) graphene oxide nanosheets. The line profile in Figure 6e (f) was taken along the white line marked in Figure 6c (d). In general terms, the unreduced sheets as well as their chemically reduced counterparts display a rather smooth appearance (Figure 6a,b), both in terms of *z*-scale roughness (see below) and sheet perimeter. In particular, we note that no significant spikes or crevices are observed along the sheet perimeter. On the nanometer scale, the sheets display a uniform globular or bumpy morphology with feature sizes ranging typically between 5 and 10 nm (Figure 6c,d). Although such morphology is common to the unreduced and chemically reduced graphene oxide sheets, subtle differences between both samples regarding *z*-scale roughness become evident when their respective images, line profiles, and root-mean-square (rms) values are compared, the roughness being slightly larger for the unreduced sheets (rms values of 0.108 nm vs 0.095 nm for the unreduced and reduced nanosheets, respectively). In any case, even for the relatively rough unreduced graphene oxide sheets, the measured height variations are always in the subnanometer range (see Figure 6e,f), indicating that the sheets are essentially flat objects. We tentatively interpret the slightly rough morphology of the sheets as a consequence of the structural disorder induced by oxidation (see Raman spectroscopy results) and maybe also of the presence of the oxygen functionalities themselves, which are probably not evenly distributed across the

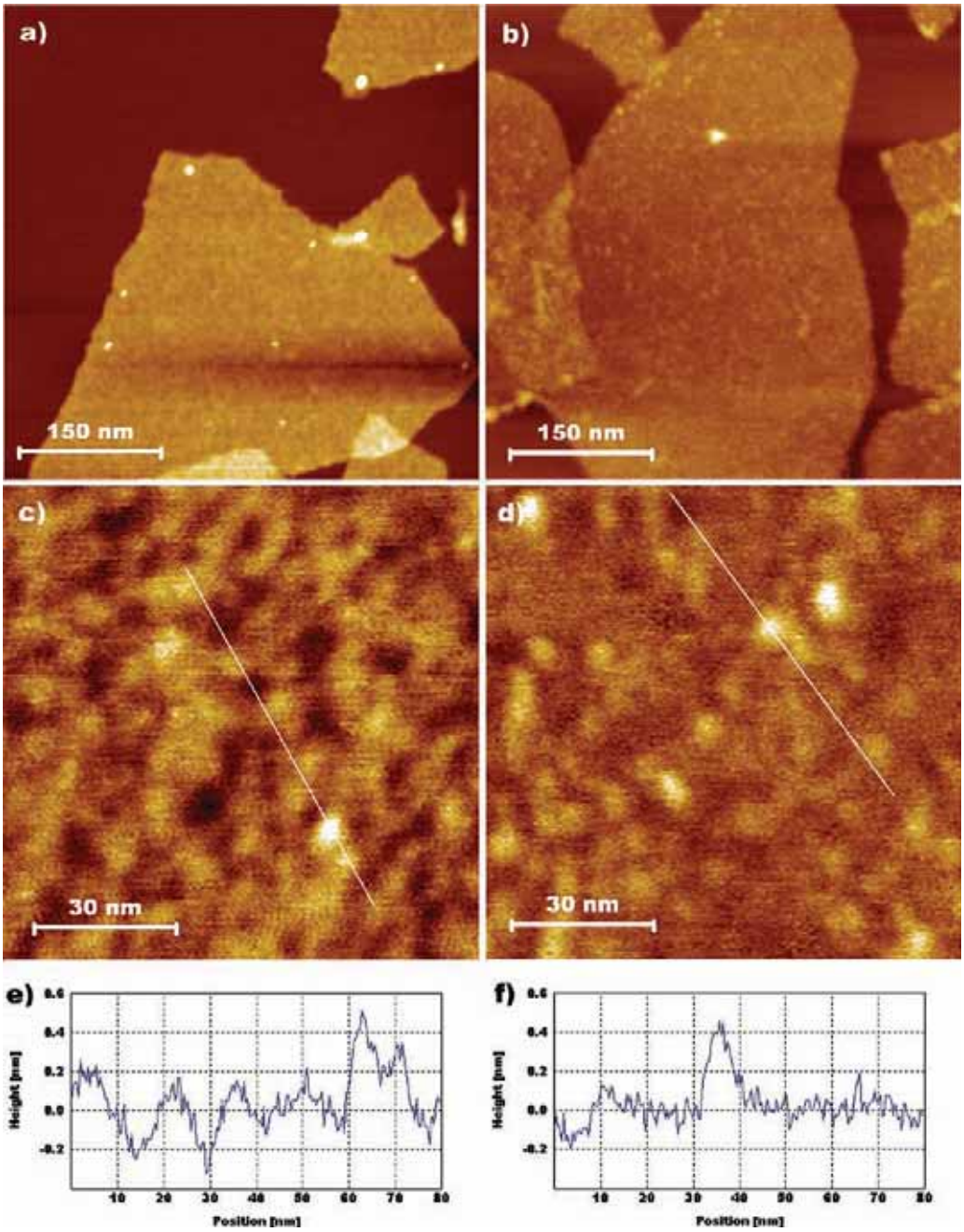

Figure 6. Detailed tapping mode AFM height images (a−d) and line profiles (e,f) for unreduced (a,c,e) and chemically reduced (b,d,f) graphene oxide nanosheets deposited from aqueous dispersions onto freshly cleaved HOPG. The line profiles in e and f were taken from the white lines marked in c and d, respectively.

graphene surface.[27] As the amount of oxygen functional groups on the graphene surface is considerably diminished following chemical reduction (see XPS data), the possible roughness induced by such groups should be accordingly smaller in the chemically reduced sheets, which would explain the reported differences between the unreduced and the reduced samples in Figure 6c,d. We note that the sheets investigated here were deposited onto atomically flat surfaces (mainly HOPG, but also mica), so a contribution of the substrates to the observed topography of the sheets can be ruled out. This is different to many AFM studies of graphene, which use the technologically relevant (but atomically rough) SiO_2/Si substrate. In such case, even pristine, defect-free graphene exhibits some degree of roughness, and this has been attributed to the fact that the graphene sheet partially conforms to the corrugation of the underlying substrate.[32,33] We also note that the chemically reduced graphene oxide nanosheets appear to be structurally different to the FGSs reported elsewhere, which were also deposited onto atomically flat HOPG and studied by AFM.[31] The latter type of graphene was seen to display a significant

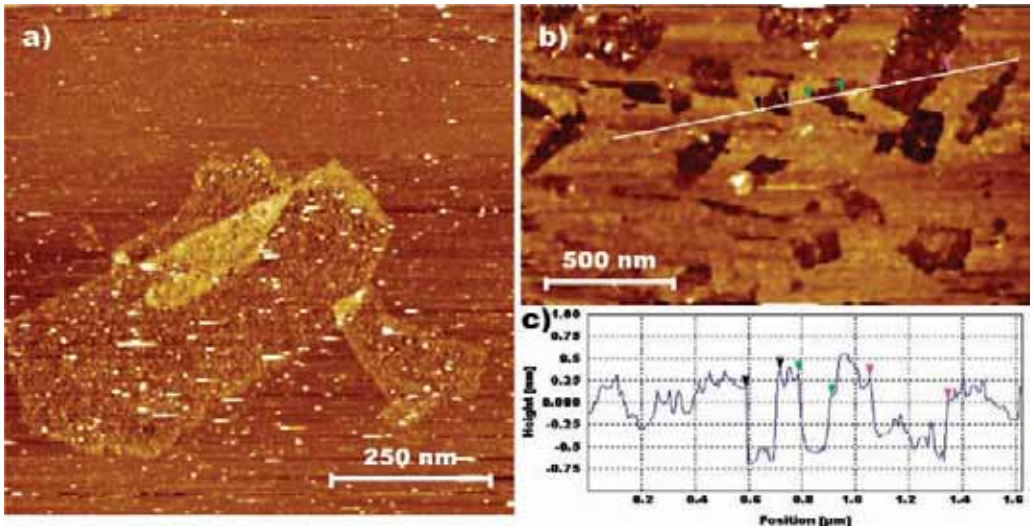

Figure 7. STM images of unreduced graphene oxide nanosheets deposited from an aqueous dispersion onto HOPG and visualized with normal (a) and inverted (b) contrast. Tunneling parameters: $I = 0.5$ pA, $V = -2000$ mV (a); $I = 1$ pA, $V = 2000$ mV (b). (c) Line profile taken along the white line marked in panel b.

number of wrinkles, attributed to line defects in the carbon lattice. As such type of feature was never observed in our chemically reduced nanosheets, we interpret that the wrinkles are the result of structural modifications during the high-temperature (1050 °C) treatment to which the FGSs are subjected.

Next, we discuss the results of the STM measurements. As could be anticipated because of their electrically nonconductive nature, it was not possible to image the unreduced graphene oxide nanosheets under tunneling conditions typically employed to study graphitic surfaces, i.e., using tunneling currents in the nanoampere and sub-nanoampere regime and bias voltages from a few tens to several hundreds of millivolts. Most probably, tunneling currents of such magnitude cannot flow through the unreduced nanosheets, with the consequence that they are swept away by the STM tip, and only the conductive HOPG substrate is visualized, as was indeed the case. An alternative explanation could be that the large number of functional groups on the graphene oxide sheets does not allow the latter to come close enough to the HOPG substrate, so as to induce a significant van der Waals interaction between the nanosheet and substrate. Thus, if such interaction is too weak, the anisotropic electric field of the STM tip could sweep away the nanosheet. Indeed, this effect reportedly made the observation of functionalized carbon nanotubes very difficult.[54] In any case, the sheets became visible when the STM was operated under very low tunneling currents (~1 pA or below) and large bias voltages (~2000 mV). This is exemplified in Figure 7a, which shows features (sheets) whose lateral dimensions are consistent with those observed in the AFM images of the same sample (Figure 5a). It should also be noted that, in some cases, depending on the tip used, the unreduced nanosheets were visualized with inverted contrast relative to the HOPG substrate. Figure 7b shows an example of this type of image, which is characterized by the presence of a considerable number of dark features. Taking into account that the density, size and shape of such features is coincident with those of the graphene oxide nanosheets seen by AFM (Figure 5a) and that the features were not observed on pristine HOPG onto which no dispersion was deposited, we conclude that they correspond to the nanosheets, which are imaged with inverted contrast relative to the HOPG substrate. As illustrated in the line profile of Figure 7c, which was taken along the white line marked in Figure 7b, the sheets are visualized with an apparent depth of ~0.5−1.0 nm below the HOPG surface. It is well-known that both topography and electronic structure contribute to the image contrast in STM, which is due to the fact that the measured tunneling current over a given surface depends not only on the tip−sample separation but also on the local density of electronic states near the Fermi level of the sample surface.[55] Thus, for a very poorly conductive area of the surface (the graphene oxide sheets in the present case), the density of electronic states near the Fermi level is much smaller than that for a highly conductive region (the HOPG substrate), giving rise to lower tunneling currents over the former. Alternatively, a lower tunneling current over the graphene oxide nanosheets could arise from a larger separation (and thus a lower tunneling probability) between the nanosheet and the HOPG substrate owing to the presence of a very large number of oxygen functionalities on the former. If one or both effects are large enough, as it appears to be here in some cases, they can completely counterbalance the topographical contribution to the tunneling current, resulting in the sheets being imaged with inverted contrast. However, these appear to be necessary but not sufficient conditions for the emergence of inverted contrast, as the latter is only observed with some specific tips. Thus, the characteristics of the STM tips also play a key role in the appearance of inverted contrast. Inverted contrast arising from electronic effects has been well documented in the STM literature of substrate-supported molecules and particles.[56−58] In this

(54) Kónya, Z.; Vesselenyi, I.; Niesz, K.; Kukovecz, A.; Demortier, A.; Fonseca, A.; Delhalle, J.; Mekhalif, Z.; Nagy, J. B.; Koós, A. A.; Osváth, Z.; Kocsonya, A.; Biró, L. P.; Kiricsi, I. *Chem. Phys. Lett.* **2002**, *360*, 429–435.

(55) Magonov, S. N.; Whangbo, M.-H. *Surface Analysis with STM and AFM*; VCH: Weinheim, Germany, 1996.

(56) Guo, Q.; Yin, J.; Palmer, R. E.; Bampos, N.; Sanders, J. K. M. *Chem. Phys. Lett.* **2005**, *402*, 121–125.

(57) MacLeod, J. M.; Miwa, R. H.; Srivastava, G. P.; Malean, A. B. *Surf. Sci.* **2005**, *576*, 116–122.

(58) Kim, D. H.; Shapir, E.; Jeong, H.; Porath, D.; Yi, J. *Phys. Rev. B* **2006**, *73*, 235416.

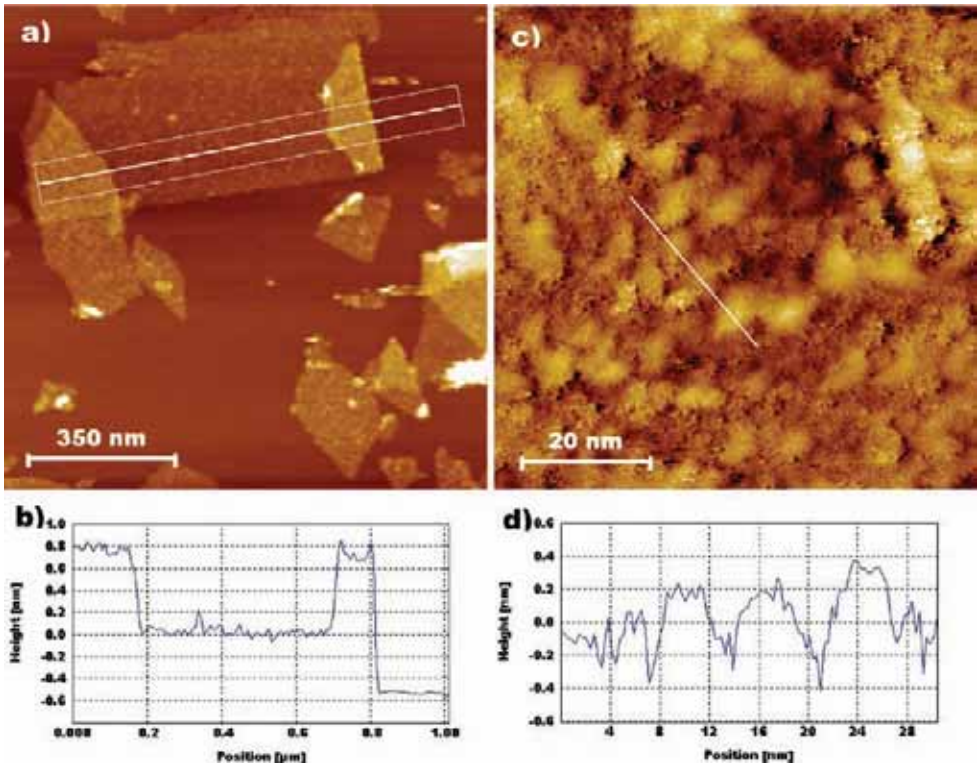

Figure 8. Nanometer-scale STM images (a,c) and line profiles (b,d) of chemically reduced graphene oxide nanosheets deposited onto HOPG from their dispersion in water. The line profile in panel b represents the average obtained within the marked rectangle in panel a, whereas that in d was taken along the white line marked in c. Tunneling parameters: $I = 0.5$ nA, $V = 100$ mV (a); $I = 0.5$ nA, $V = 500$ mV (c).

respect, we note that a similar effect to that observed here (contrast reversal depending on the tip used) has been reported for the STM imaging of purple membranes on HOPG and attributed to differences in the local geometry of the STM tips.[59]

Following chemical reduction, STM images of the nanosheets could be routinely achieved even at relatively high tunnelling currents (up to several nanoamperes) and low bias voltages (down to several millivolts) without inverted contrast, implying that the reduced nanosheets have become electrically conductive, as expected. Figure 8a shows a general STM image that spans several nanosheets, their size and shape being consistent with those observed in the AFM images of the same sample (Figure 5c). As measured by STM and exemplified in the averaged multiple profile of Figure 8b, virtually all the nanosheets were ~0.6−0.8 nm high (relative to the HOPG substrate), while the overlapping areas of two or more nanosheets or the folded regions of a single sheet exhibited heights that were integer multiples of this value. Such value is noticeably smaller than that obtained by AFM for the same sample (1.0−1.2 nm). In the case of AFM, it has been speculated that several factors, rather than just the actual sheet thickness, have an influence on the measured height of graphene or chemically modified graphene over a given substrate, in particular the different interaction of the AFM tip with the graphene sheet and with the substrate.[1,31,60,61] Regarding STM, it is also very likely that the tip interacts differently with the defective, chemically modified graphene nanosheets and with the pristine HOPG surface as a result of differences in their electronic structure. Indeed, a dramatic example in this respect was the inverted contrast observed for the unreduced graphene oxide nanosheets (Figure 7a). Although these nanosheets become electrically conductive after chemical reduction, their conductivity has been shown to lag significantly behind that of pristine, defect-free graphene,[27] implying a somewhat different electronic structure to that of the latter. Furthermore, the tunneling geometry is more complex over the nanosheet than it is over the bare HOPG substrate.[62,63] All these effects could contribute to the apparent height (relative to the supporting substrate) measured by STM for the chemically reduced nanosheets. Likewise, taking into account that the nature of the tip−sample interaction used for imaging is very different in AFM and STM, it is not surprising that the two techniques lead to different values of sheet height relative to the HOPG substrate as a result of the mentioned contributions to the measured height. The main question raised in connection with these observations is that of the accurate measurement of the actual nanosheet thickness. Since in principle this cannot be done by measuring the nanosheet height relative to the supporting substrate because of the potential spurious contributions discussed above, it should be made by measuring the nanosheet height relative to another nanosheet (e.g., using two overlapping sheets), so that the possible influence of the tip interacting with objects of different nature is removed. With tapping mode

(59) García, R.; Tamayo, J. *Langmuir* **1995**, *11*, 2109–2114.
(60) Gupta, A.; Chen, G.; Joshi, P.; Tadigadapa, S.; Eklund, P. C. *Nano Lett.* **2006**, *6*, 2667–2673.
(61) Nemes-Incze, P.; Osváth, Z.; Kamarás, K.; Biró, L. P. *Carbon* **2008**, *46*, 1435–1442.
(62) Biró, L. P.; Gyulai, J.; Lambin, Ph.; Nagy, J. B.; Lazarescu, S.; Mark, G. I.; Fonseca, A.; Surján, P. R.; Szekeres, Zs.; Thiry, P. A.; Lucas, A. A. *Carbon* **1998**, *36*, 689–696.
(63) Mark, G. I.; Biró, L. P.; Gyulai, J.; Thiry, P. A.; Lucas, A. A.; Lambin, P. *Phys. Rev. B* **2000**, *62*, 2797–2805.

AFM, this measurement should be ideally carried out in the attractive regime, rather than in the repulsive one, as only the former is minimally invasive.[41] In the repulsive regime, sample deformation, which could affect the measured heights, cannot be ruled out, and the deformation could be different for the overlapping and nonoverlapping areas of two nanosheets. When we measure (in the attractive regime) the height of the overlapping area between two sheets relative to the nonoverlapping area, we obtain a value of ~1.0 nm for the unreduced graphene oxide nanosheets and ~0.6 nm for their chemically reduced counterparts. These values should in principle correspond to the actual thickness of the sheets, and are reasonable in that the reduced sheets turn out to be thinner than the unreduced ones, as expected due to the removal of a large majority of the oxygen functional groups. In line with the reasoning made in the case of AFM, the actual thickness of chemically reduced nanosheets should also be determined with STM by measuring the height of an overlapping area or folded region relative to the nonoverlapping area or nonfolded region of a nanosheet. Such height turned out to be ~0.7 nm, which is very close to that obtained independently by AFM (~0.6 nm), thus reinforcing the idea that 0.6−0.7 nm is the actual thickness of the chemically reduced graphene oxide nanosheets.

Figure 8c shows the detailed nanometer-scale morphology of the chemically reduced graphene oxide nanosheets as imaged by STM. A line profile displaying the typical height variations across the nanosheets is also presented (Figure 8d). In comparing this and other STM images of similar magnification with their AFM counterparts (e.g., Figure 8c vs 6d), we see that there is a good agreement between the general morphology visualized by the two techniques (both unveil the same type of globular/bumpy feature), although finer structural detail is provided by STM (for instance, concerning the shape of the bumps). This higher resolving power on the nanoscale is probably due to the fact that the tips used for STM are somewhat sharper than those used for AFM. In any case, the strong similarity between the STM and AFM results suggests that the contrast observed in the nanometer scale images by STM (Figure 8c) is mainly of topographic origin. Thus, although local variations of electronic structure are also present to some extent within the nanosheet, they probably play only a secondary role in the features observed at such magnification. Thus, we can safely conclude that chemically reduced graphene oxide nanosheets display a smoothly undulated morphology even on an atomically flat substrate such as HOPG, probably as a result of the distortions induced on the carbon lattice by residual functional groups and structural defects.

Direct evidence for the presence of structural disorder in the chemically reduced nanosheets was obtained by atomic-scale STM imaging. Some representative results are shown in Figure 9. In general terms, these images are characterized by a complete lack of long-range atomic-scale order. Rather, atomic-sized spots arranged into different local domains are the dominant feature. At most, such domains constitute clearly ordered patterns a few nm large, whereas in other cases the local order of the atomic-sized spots is less evident or even absent. An example of a relatively large ordered domain can be seen in the bottom right part of Figure 9a, along with smaller domains in the same image. A line profile taken from the large domain (white line) is presented in Figure 9b. From this profile, a peak-to-peak distance between spots of ~0.22−0.24 nm was measured, which is very close to the ~0.25 nm periodicity observed in the triangular pattern that is typically obtained in the atomic-scale STM images of pristine, defect-free HOPG (Figure 9c). We note that not every area of the nanosheets investigated on the atomic scale displayed clearly ordered domains such as those seen in Figure 9a. In many cases, as mentioned before, the atomic-sized spots were not arranged into any recognizable domain (e.g., bottom part of Figure 9d) or were arranged into domains without evident periodicity (Figure 9e). Obviously, this is an indication that structural disorder in the chemically reduced nanosheets is not spatially uniform. On the contrary, local areas exhibiting a high degree of structural imperfection (Figure 9d and e) coexist with relatively ordered regions (Figure 9a). The structural disorder unveiled by STM on the reduced nanosheets (and also by Raman spectroscopy; Figure 4c) can in principle be attributed to the presence of oxygen functionalities covalently attached to the basal plane of the graphene sheet, which remain in significant quantities after chemical reduction (see XPS data), as well as to large numbers of atomic-scale defects within the carbon lattice itself, which were presumably created during the oxidation and/or reduction processes. At present, the exact nature of such defects in the graphene nanosheets is not known. One possibility is that they correspond to atomic vacancies, which would have originated via abstraction of carbon atoms by oxygen in the oxidation or reduction step, giving rise to volatile CO or CO_2. Isolated atomic vacancies on an otherwise defect-free graphitic surface are visualized by STM as defined protrusions between one and a few nanometers large,[51,64] but the STM signature of a very large concentration of vacancies, which would probably be the case here, has not been clearly established. Nevertheless, atomic-scale STM images reported for HOPG surfaces aggressively modified by microwave oxygen plasma treatment (which is known to proceed via atomic vacancy creation) revealed extremely disordered structures not very different from those obtained here for the chemically reduced nanosheets.[49] An alternative scenario to explain the presence of structural defects in the reduced graphene nanosheets would be a strong distortion (corrugation) of the carbon lattice as a result of the preparation of graphite oxide. Szabó et al. recently proposed a structural model for graphite oxide in which the carbon skeleton of the graphene layers becomes highly corrugated and deformed due to the grafting of large amounts of oxygen functional groups.[48] Corrugation of (unreduced) graphene oxide was evident in the AFM images obtained here (Figure 6c). It is plausible that such corrugation/deformation of the graphene lattice persists to a certain degree after removal of most of the oxygen by chemical reduction, as overcoming an energy barrier (and, therefore, some thermal annealing) would probably be required to resume a perfectly flat, pristine graphene structure from the corrugated one. In the present work, corrugation of the chemically reduced graphene oxide nanosheets was evident from the AFM images (Figure 6d) as well as from both the nanometer- and atomic-scale STM images (Figure 8c and 9). Corrugation/deformation of the carbon lattice would probably give rise to a distortion of the atomic-scale features seen in the STM images (Figure 9). From the previous discussion, it is reasonable to conclude that both atomic vacancies and corrugation of the carbon skeleton are possibly present in the chemically reduced graphene oxide nanosheets. We also note that an in-depth understanding of the atomic-scale features reported in Figure 9 would most probably require the assistance of some theoretical modeling. However, in the present case this could be a difficult task. Theoretical modeling of the STM images can be reasonably carried out

(64) Hahn, J. R.; Kang, H. *Phys. Rev. B* **1999**, *60*, 6007–6017.

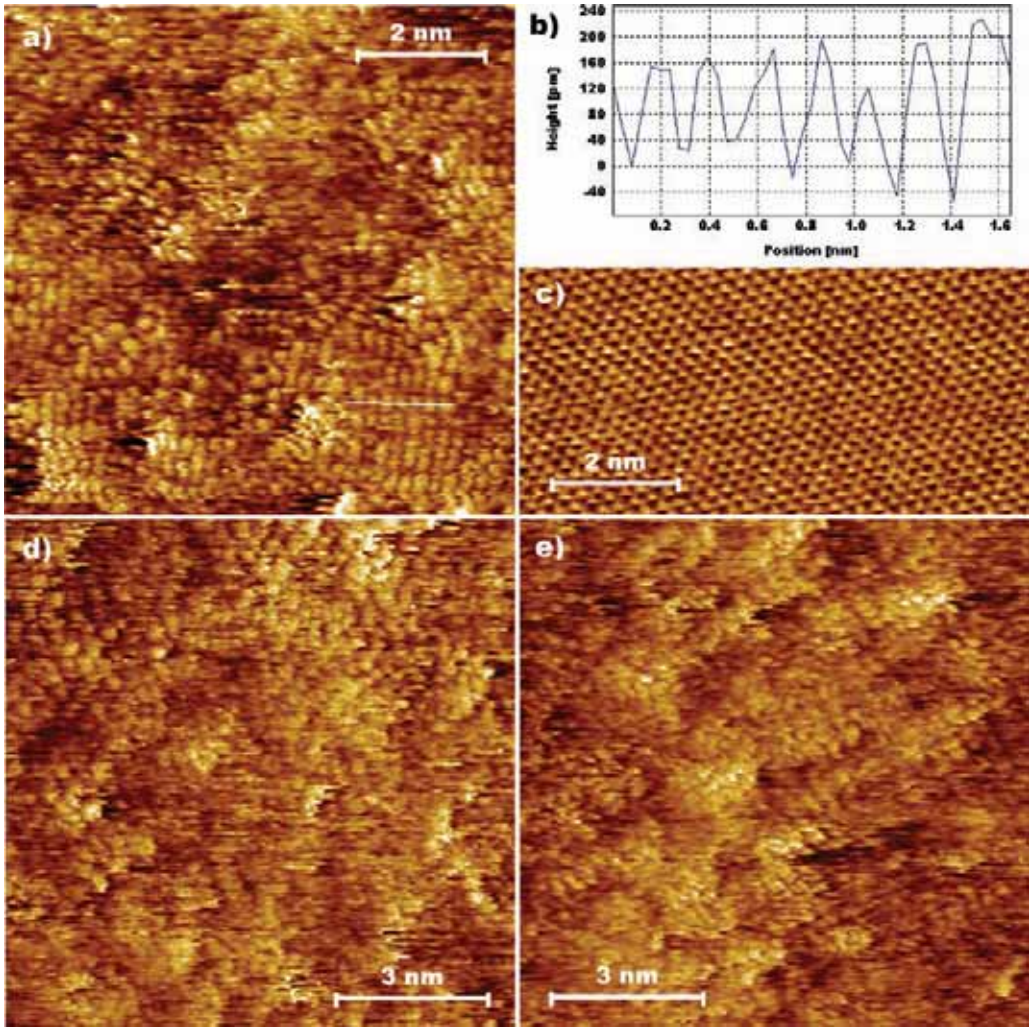

Figure 9. Typical atomic-scale STM images (a,d,e) of the basal plane of chemically reduced graphene oxide nanosheets. (b) Line profile taken along the white line marked in a. (c) Atomic-scale STM image of pristine, defect-free HOPG shown for comparison. Tunneling parameters: $I = 3$ nA, $V = 10$ mV (a); $I = 2$ nA, $V = 100$ mV (b); $I = 2$ nA, $V = 50$ mV (c); $I = 3$ nA, $V = 50$ mV (d).

for isolated, individual atomic-scale defects,[65] so that simulated STM images of potential defect structures can be compared with the experimental ones. However, the investigated graphene nanosheets presumably contain several different types of unknown defects, which are present in unknown (but very high) densities and with unknown spatial distributions. As defect type, density, and spatial distribution are all known to affect the atomic-scale STM images of graphitic surfaces,[66] the modeling task could become exceedingly arduous.

Finally, the detailed structure of the edges of the chemically reduced nanosheets was also investigated by STM. For pristine graphene, especially in the form of nanoribbons, the edge structure has been shown to play an important role in its electronic properties.[37] In the present case of graphene nanosheets prepared as stable aqueous dispersions, the sheet edges are thought to be randomly decorated with carboxyl groups that favor the stability of the colloidal dispersion via electrostatic repulsion.[13,26] Furthermore, taking into account that (1) the basal surface of the graphene nanosheets was highly disordered on the atomic scale (Figure 9) and (2) the cutting of the nanosheets during sonication is a rather uncontrolled process, we expect the nanosheet edges to be atomically rough and ill-defined. This is confirmed by the images of Figure 10. Figure 10a shows a nanometer-scale STM image of a nanosheet edge. As discussed previously in connection with the AFM images, the edges appear smooth and straight at this relatively low magnification. However, as illustrated in Figure 10b (graphene nanosheet: left; HOPG substrate: right), the edge profile is rather rough on the atomic scale, indicating that even the straight sections of the sheet edge (Figure 10a) do not possess a well-defined crystallographic orientation. Figure 10c presents an atomic-scale image of a nanosheet corner, exhibiting a very disordered, ill-defined structure that contrasts with the crystallinity of the HOPG substrate surrounding it. This is further highlighted in the line profile of Figure 10d, which was taken along the white line in Figure 10c: the periodicity observed over the HOPG substrate (left part of the profile) is completely lost when moving onto the nanosheet (right part). It will be

(65) Amara, H.; Latil, S.; Meunier, V.; Lambin, Ph.; Charlier, J.-C. *Phys. Rev. B* **2007**, *76*, 115423.
(66) Ruffieux, P.; Melle-Franco, M.; Gröning, O.; Bielmann, M.; Zerbetto, F.; Gröning, P. *Phys. Rev. B* **2005**, *71*, 153403.

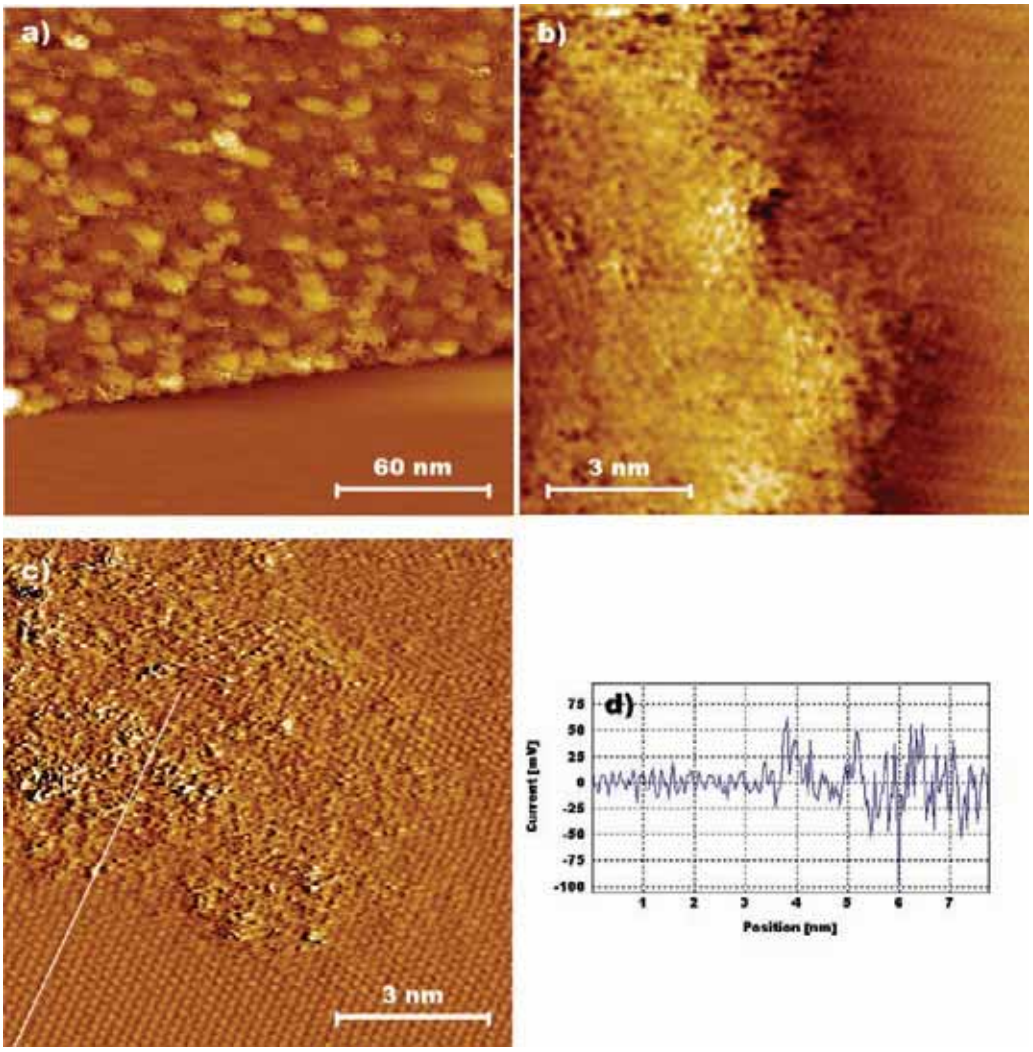

Figure 10. STM images of the edges of chemically reduced graphene oxide nanosheets: Nanometer scale image showing the smooth, straight edge of a nanosheet (a). Atomic-scale images of a nanosheet edge (b) and a nanosheet corner (c). Image c is a current STM image. (d) Line profile taken along the white line marked in c. Tunneling conditions: $I = 0.5$ nA, $V = 100$ mV (a); $I = 3$ nA, $V = 20$ mV (b); $I = 3.5$ nA, $V = 15$ mV (c).

interesting to see how these structures evolve and graphitic order is restored when the nanosheets are subjected to heat treatment, which will be the subject of future studies.

4. Conclusions

AFM and STM have afforded a direct visualization of the nanometer-scale morphology and atomic-scale structure of graphene nanosheets produced by chemical reduction of graphene oxide dispersions. In general terms, we can conclude that the structure of these chemically derived nanosheets is significantly different from that of pristine graphene prepared by micromechanical cleavage of bulk graphite. Even when deposited on an atomically flat substrate such as graphite, the former display an undulated, globular morphology that can be attributed to distortions of the carbon skeleton induced by the strong oxidation employed to produce such type of graphene. Atomic-scale STM imaging provided direct evidence of the lattice distortion in these graphene nanosheets, as long-range periodicity was never seen. Only ordered domains a few nanometers large could be identified. Such observation was consistent with the results obtained by Raman spectroscopy, which also indicated the presence of considerable structural disorder. Atomically rough and ill-defined nanosheet edges were also visualized by STM. Although they possess an extremely low electrical conductivity, the unreduced graphene oxide nanosheets could be imaged by STM, but only working with tunneling currents in the pA regime. In this case, the sheets appeared sometimes with inverted contrast in the images. Finally, phase imaging in the attractive regime of tapping-mode AFM could be employed to discriminate between the unreduced and chemically reduced graphene oxide nanosheets. Significant differences in hydrophilicity between the two samples that result from distinct oxygen levels probably allow such discrimination to be made.

Acknowledgment. Partial funding of this work by MEC (Project CTQ2005-09105-C04-02), CSIC (I3 Project 200680I198), and MICINN (Project MAT 2008-05700) is gratefully acknowledged. P.S.-F. also acknowledges receipt of an I3P predoctoral contract from CSIC.

CARBON 48 (2010) 2644–2673

Determining the thickness of chemically modified graphenes by scanning probe microscopy

*P. Solís-Fernández, J.I. Paredes *, S. Villar-Rodil, A. Martínez-Alonso, J.M.D. Tascón*

Instituto Nacional del Carbón, CSIC, Apartado 73, 33080 Oviedo, Spain

ARTICLE INFO

Article history:
Received 19 October 2009
Accepted 19 March 2010
Available online 25 March 2010

ABSTRACT

The thickness of unreduced and chemically reduced graphene oxide sheets deposited on different substrates was measured by different scanning probe microscopy (SPM) variants. Inaccurate and inconsistent results are obtained when thickness is derived as a sheet-to-substrate height, which is the typically employed approach to determine such a parameter. Measuring overlapped regions between different sheets leads to more realistic thickness values, which clearly reflect, for example, the removal of oxygen functionalities from graphene oxide following chemical reduction. The results underline the precautions that are required to draw valid conclusions from SPM-derived thickness data of chemically modified graphenes.

During the last 5 years of relentless development in the preparation and applications of graphene, scanning probe microscopy (SPM), and in particular atomic force microscopy (AFM), has become the technique of choice to ascertain the presence and measure the thickness of individual sheets in graphene samples [1]. The thickness of the sheets is normally evaluated by measuring their height relative to the supporting substrate [2–5]. However, it has been recognized that such sheet-to-substrate procedure can lead to artifactual values and that a more reliable determination is provided by measuring folded (overlapped) regions within (between) the sheets [3], but this sheet-to-sheet approach is seldom adopted by researchers. It is thus not surprising to find some apparently conflicting thickness data in the literature. This is the case with unreduced and chemically reduced graphene oxide, the two most common forms of chemically modified graphene (CMG). For the unreduced material, sheet thicknesses of ~1 nm are typically documented [6]. Such value is larger than that of pristine graphene (0.34 nm), and has been attributed to the presence of structural distortions and oxygen groups on both sides of the sheet [6]. However, the reported sheet thickness following chemical reduction is also about 1 nm [2], which is unreasonable as most of the oxygen originally present on graphene oxide is removed upon reduction, and therefore thinner sheets should be expected. In all these cases, sheet thickness was measured as a sheet-to-substrate height, suggesting that such values could be very imprecise.

Here, we provide a comprehensive evaluation of the thickness of individual graphene oxide sheets, both unreduced and chemically reduced. We show that rather discordant data are obtained with different substrates and SPM variants, including different AFM modes and scanning tunnelling microscopy (STM), when thickness is derived as a sheet-to-substrate height. This problem is eliminated by measuring overlapped regions between different sheets, leading to consistent thickness values.

Graphene oxide and chemically reduced graphene oxide were prepared as aqueous dispersions following previously reported procedures [2,7] (see Supplementary material for experimental details on their synthesis and characterization, as well as the results of their chemical analysis). For investigation by SPM, the dispersions were deposited onto different substrates: (i) highly oriented pyrolytic graphite (HOPG), (ii) mica, (iii) Si wafer with a 200 nm-thick layer of SiO_2, and (iv) borosilicate glass slide. HOPG and mica are atomically flat (rms roughness values of 0.03 and 0.04 nm, respectively, for $1 \times 1\ \mu m^2$ images), whereas SiO_2/Si and glass slide are slightly rough (rms roughness of 0.20–0.27 and 0.15–0.19 nm, respectively), which makes the evaluation of heights less accurate with the latter. This is exemplified in the images and line profiles of Fig. 1 for graphene oxide sheets deposited onto HOPG (a) and SiO_2/Si (b), which were visualized by tapping mode AFM (i.e., amplitude modulation AFM) in the attractive regime (see Supplementary material for an explanation of this regime), as well as for chemically reduced sheets deposited on HOPG and visualized by contact mode AFM (c). For this reason, the measurements were preferentially carried out on HOPG and mica. Depending on the volume of dispersion deposited onto the substrate, samples with varying densities of sheets could be obtained, in particular samples with large

* *Corresponding author*: Fax: +34 985 29 76 62.
E-mail address: paredes@incar.csic.es (J.I. Paredes).
0008-6223/$ - see front matter
doi:10.1016/j.carbon.2010.03.033

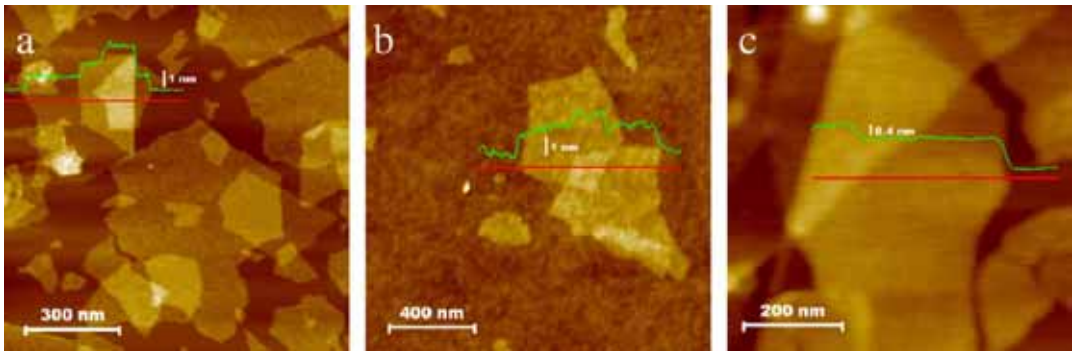

Fig. 1 – (a) and (b) Tapping mode AFM images recorded in the attractive regime of graphene oxide sheets deposited onto HOPG (a) and SiO_2/Si (b). (c) Contact mode AFM image of chemically reduced graphene oxide sheets on HOPG. For every image, a representative line profile (green) obtained along the marked red line is shown. (For interpretation of the references to colour in this figure legend, the reader is referred to the web version of this article.)

numbers of overlapping sheets (Fig. 1). For a given substrate, the sheets displayed uniform apparent heights (relative to the substrate), implying that the dispersions are constituted by fully exfoliated, single-layer objects [6], which facilitates a statistical determination of their thickness.

To determine sheet heights from the SPM images in a statistically meaningful manner, height histograms were used instead of the more common single or averaged line profiles. This is exemplified in Fig. 2 for a graphene oxide sheet deposited onto HOPG and visualized by tapping mode AFM in the attractive regime, where the histogram shown in (b) for the area within the green rectangle in (a) indicates that the apparent height of this sheet relative to the substrate is about 0.9 nm (derived as the peak-to-peak separation in the histogram). When conducting this approach over many sheets with the different substrates and SPM modes, clear trends became evident. First, the sheet-to-substrate height was both substrate- and SPM mode-dependent. For a given SPM mode, different substrates yielded different values of sheet-to-substrate height, e.g., 0.9–1.1 (HOPG), 1.1–1.2 (mica), 1.2–1.6 (SiO_2/Si) and 1.6–1.9 (glass slide) nm for graphene oxide sheets imaged in the attractive regime of tapping mode AFM. Similarly scattered values were obtained when measuring sheet-to-substrate heights with different SPM modes over a given substrate, e.g., 0.9–1.1 (tapping mode AFM, attractive regime), 1.1–1.3 (tapping mode AFM, repulsive regime) and 1.4–1.7 (contact mode AFM) nm for the case of graphene oxide sheets on HOPG. Second, the sheet-to-sheet height values, determined from overlapping sheets, were remarkably uniform for each type of CMG when data obtained with the different SPM modes and substrates were compared. To illustrate this result, Table 1 summarizes the sheet-to-substrate and sheet-to-sheet height values derived for unreduced and chemically reduced graphene oxide sheets on HOPG with the different SPM variants. While the sheet-to-substrate values were quite dependent on the SPM mode employed, their sheet-to-sheet counterparts clearly tended to cluster within a much more limited range of values, which were ~0.9–1.1 and about 0.5–0.7 nm for unreduced and chemically reduced graphene oxide, respectively.

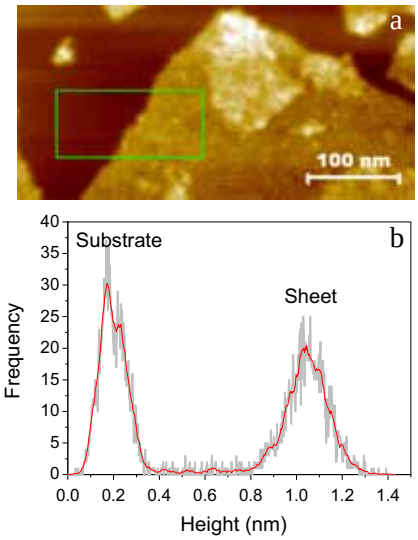

Fig. 2 – Determination of sheet height with height histograms derived from the SPM images. (a) Tapping mode AFM image (attractive regime) of a graphene oxide sheet on HOPG. (b) Typical height histogram obtained from the region within the green rectangle in (a). The separation between the two peaks (~0.9 nm) provides the height of the sheet relative to the substrate. (For interpretation of the references to colour in this figure legend, the reader is referred to the web version of this article.)

These results provide indication that, contrary to common practice, the thickness of CMGs cannot be obtained as a sheet-to-substrate height value. Such observation can be understood with the following considerations. First, the signal measured and employed in SPM to record the height images (e.g., cantilever oscillation amplitude in tapping mode AFM, cantilever static deflection in contact mode AFM, or tunnelling current in STM) is based on different types of tip-sample interaction for the different SPM variants, and second, the details of a certain type of interaction are typically material-dependent [8]. To record a height image, the SPM system places the tip at a certain distance from the sample surface

Table 1 – Sheet-to-substrate and sheet-to-sheet heights (in nm) measured for unreduced (GO) and chemically reduced (CRGO) graphene oxide sheets deposited on HOPG with different SPM variants. Due to the electrically non-conductive nature of the unreduced sheets, STM data for this material are not provided.

		Tapping AFM			
		Attractive	Repulsive	Contact AFM	STM
Sheet-to-substrate	GO	0.9–1.1	1.1–1.3	1.4–1.7	–
	CRGO	0.9–1.1	0.9–1.0	1.3–1.5	0.4–0.6
Sheet-to-sheet	GO	0.9–1.1	0.9–1.1	1.0–1.1	–
	CRGO	0.5–0.6	0.5–0.7	0.5–0.6	0.6–0.8

so that the corresponding measured signal equals a given, user-selectable value. Then, the vertical position of the tip is adjusted to keep that value constant as the sample surface is rastered and plotted to obtain a 3D rendering of the surface, i.e., a height image. Because the detailed characteristics of the tip-sample interaction depend on the properties of the specimen being probed, the tip-sample distance required to attain a given value of a specific SPM signal will differ for materials of different nature. Thus, for surfaces with regions of different characteristics (e.g., the CMG sheets and the substrate), a height offset will be generated between such regions that will add to the actual surface topography in the recorded height images, so the images will be artifactual to some extent. This effect is found, e.g., in the STM imaging of atomic vacancies on graphite. The vacancy induces a change in the electronic properties of a small area around it, so that the affected area is visualized as an apparent protrusion by STM, even though its topography remains essentially flat [9]. Height artifacts have also been reported by AFM on heterogenous surfaces [10]. In the present case, the appearance of a height offset between the sheets and substrate implies that the sheet-to-substrate height will depend on both the substrate and SPM mode employed, as it was indeed observed, and will be usually different to the actual thickness of the sheet. By contrast, within areas constituted by a single component (for example, when measuring sheet-to-sheet heights), no offset will arise and the height image will simply reflect its actual topography (e.g., actual sheet thickness).

One of the factors that may be affecting the measurement of sheet-to-substrate heights is the presence of water layers on the sample surface, because the different SPM modes respond differently to the surface water layer and the different materials probably have water layers of different thickness. For example, STM is thought to be essentially insensitive to the presence of water layers when working under ambient conditions, whereas non-invasive or little invasive AFM variants, such as tapping mode AFM, are known to be able to detect the nanometer-scale structure of water layers adsorbed on solid surfaces [11]. Similarly, the structure and thickness of water layers depends on the hydrophobic/hydrophilic character of the surface being probed. For this reason, in our measurements water will probably give rise to height offsets between substrate and CMG sheets, whose magnitude will depend on the substrate and SPM variant being used. Another point worth discussing is the possible presence of salts on the CMG sheets and their effect on the height measurements. In the production of graphite oxide, we used potassium permanganate and, in a smaller quantity, sodium nitrate. Although the products were thoroughly washed with water before being used, it would not be surprising that some remnants of these salts have remained in the samples. However, analysis by X-ray photoelectron spectroscopy (XPS) did not detect any potassium or sodium, implying that they are not present in significant quantities (see Supplementary material). Thus, we conclude that salts are not present in significant amounts so as to affect our measurements.

The type of problem in the measurement of heights discussed here has also been recently highlighted by Nemes-Incze et al. [3], who measured the thickness of single-layer and few-layer flakes of micromechanically cleaved (pristine) graphene on SiO_2/Si substrates with tapping mode AFM. These authors showed that the thickness data obtained through the sheet-to-substrate approach were generally artifactual, although they were able to identify a range of imaging parameters (in particular, free amplitude of cantilever oscillation) under which the height offset could be eliminated, providing an accurate measure of actual flake thickness via sheet-to-substrate heights, at least for pristine graphene on SiO_2/Si. Such information is very useful to evaluate the thickness of micromechanically prepared graphene samples, because they are usually produced in extremely low numbers on SiO_2/Si as isolated, non-overlapped objects. However, the CMG sheets considered here are produced and can be deposited onto substrates in very large quantities (e.g., Fig. 1a), so the sheet-to-sheet approach can be readily used instead of relying on the sheet-to-substrate method with a specific set of tapping mode AFM imaging parameters.

From the results of Table 1, we conclude that the actual thickness of unreduced graphene oxide is ~0.9–1.1 nm, which is reasonable because the carbon skeleton of the sheets is thought to be both structurally distorted and heavily decorated with oxygen on both sides [6]. After chemical reduction, sheet thickness decreases to ~0.5–0.7 nm, but not to the value of 0.34 nm characteristic of pristine, oxygen-free graphene. Such result is consistent, taking into account that a significant fraction of oxygen remains on the sheets after chemical reduction (see Supplementary material). Also, the error introduced when measuring sheet thickness as a sheet-to-substrate height is typically no more than a few to several tenths of nm (Table 1). Although such error would not be critical for objects down to several nm thick, it proves crucial for these atomically thin sheets.

In conclusion, we have shown that determining the thickness of CMG sheets with SPM by the widely used approach of measuring sheet-to-substrate heights leads to inaccurate and inconsistent results. More realistic thickness values can be

obtained by evaluating sheet-to-sheet heights from overlapping sheets. We could thus ascertain that the thickness of graphene oxide sheets is significantly decreased following chemical reduction, consistent with the removal of a large fraction of its oxygen groups. Thickness data are frequently employed to infer certain characteristics for CMGs [5]. The present results indicate that valid conclusions in this regard can only be attained if the sheet-to-sheet approach is adopted to evaluate such a parameter.

Acknowledgements

P.S.-F. acknowledges receipt of an I3P pre-doctoral contract from CSIC. Financial support by the Spanish MICINN (Project MAT2008-05700) and PCTI del Principado de Asturias (Project IB09-151) is gratefully acknowledged.

Appendix A. Supplementary material

Supplementary data associated with this article can be found, in the online version, at doi:10.1016/j.carbon.2010.03.033.

REFERENCES

[1] Rao CNR, Sood AK, Subrahmanyam KS, Govindaraj A. Graphene: the new two-dimensional nanomaterial. Angew Chem Int Ed 2009;48(42):7752–77.
[2] Li D, Müller MB, Gilje S, Kaner RB, Wallace GG. Processable aqueous dispersions of graphene nanosheets. Nat Nanotechnol 2008;3(2):101–5.
[3] Nemes-Incze P, Osváth Z, Kamarás K, Biró LP. Anomalies in thickness measurements of graphene and few layer graphite crystals by tapping mode atomic force microscopy. Carbon 2008;46(11):1435–42.
[4] Vallés C, Drummond C, Saadaoui H, Furtado CA, He M, Roubeau O, et al. Solutions of negatively charged graphene sheets and ribbons. J Am Chem Soc 2008;130(47):15802–3.
[5] Tung VC, Allen MJ, Yang Y, Kaner RB. High-throughput solution processing of large-scale graphene. Nat Nanotechnol 2009;4(1):25–9.
[6] Stankovich S, Dikin DA, Piner RD, Kohlhaas KM, Kleinhammer A, Jia Y, et al. Synthesis of graphene-based nanosheets via chemical reduction of exfoliated graphite oxide. Carbon 2007;45(7):1558–65.
[7] Paredes JI, Villar-Rodil S, Solís-Fernández P, Martínez-Alonso A, Tascón JMD. Atomic force and scanning tunnelling microscopy imaging of graphene nanosheets derived from graphite oxide. Langmuir 2009;25(10):5957–68.
[8] Magonov SN, Whangbo M-H. Surface analysis with STM and AFM. Weinheim: VCH; 1996.
[9] Paredes JI, Solís-Fernández P, Martínez-Alonso A, Tascón JMD. Atomic vacancy engineering of graphitic surfaces: controlling the generation and harnessing the migration of the single vacancy. J Phys Chem C 2009;113(23):10249–55.
[10] Kühle A, Sørensen AH, Zandbergen JB, Bohr J. Contrast artifacts in tapping tip atomic force microscopy. Appl Phys A 1998;66(1):S329–32.
[11] Verdaguer A, Sacha GM, Bluhm H, Salmeron M. Molecular structure of water at interfaces: wetting at the nanometer-scale. Chem Rev 2006;106(4):1478–510.

Supplementary Content for

Determining the thickness of chemically modified graphenes by scanning probe microscopy

P. Solís-Fernández, J.I. Paredes, S. Villar-Rodil, A. Martínez-Alonso, J.M.D. Tascón

Instituto Nacional del Carbón, CSIC, Apartado 73, 33080 Oviedo, Spain

Experimental details

Graphene oxide and chemically reduced graphene oxide were prepared as aqueous dispersions following previously reported procedures [1,2], which consisted in (i) synthesis of graphite oxide by the Hummers method starting with natural graphite powder, (ii) exfoliation and dispersion of the graphite oxide material in water by ultrasonication and centrifugation, yielding the graphene oxide dispersion, and (iii) chemical reduction of the dispersion prepared in (ii) with hydrazine monohydrate, to obtain an aqueous dispersion of chemically reduced graphene oxide. The dispersions were prepared at concentrations of ~0.1 mg mL^{-1} and then diluted by a factor of 10 before being drop-cast (a few to several tens of μL) and allowed to dry onto different pre-heated (~60 ºC) substrates for AFM and STM analysis. The latter technique was only employed with electrically conductive substrates (i.e., graphite).

AFM and STM images were recorded under ambient conditions with a Nanoscope IIIa Multimode apparatus (Veeco Instruments). STM imaging was accomplished with mechanically prepared Pt/Ir (80/20) tips using tunnelling parameters of 100 mV (bias voltage) and 1 nA (tunnelling current). AFM imaging was carried out both in the contact and tapping modes of operation. Tapping mode AFM should be more properly referred to as amplitude modulation AFM, although the former term is much more widely employed. Likewise, it has been well established that tapping mode/amplitude modulation AFM can be operated under two well-defined tip-sample interaction regimes: attractive and repulsive [3-5]. We stress that working in the attractive regime is not equivalent to working in a non-contact mode. In the attractive regime, the average force acting on the oscillating tip is attractive, even though the tip may experience repulsive forces at the lowest point of its oscillation cycle. In the non-contact mode, by contrast, the tip always experiences an attractive force over its entire oscillation cycle (i.e., it never touches the sample surface). Setting proper imaging parameters for working in the more stringent non-contact mode typically requires the assistance of simulations [6], which we have not carried out here. Triangular Si_3N_4 cantilevers (spring constant ~0.38 N m^{-1}) and rectangular Si cantilevers (spring constant ~40 N m^{-1}; resonance frequency ~250-300 kHz) were employed for the contact and tapping modes, respectively. Tapping mode AFM was accomplished both in the attractive and the repulsive regime. The operating regime was established by setting the free (A_0) and

setpoint (A_{sp}) amplitudes of cantilever oscillation to proper values with the assistance of amplitude and phase versus distance curves [3-5]. To avoid the introduction of artifactual height data as a result of switching between the two interaction regimes [7], A_0 and A_{sp} were carefully selected so that the interaction of the tip was set to the same regime with both the substrate and the chemically modified graphene sheets.

Further characterization of the prepared materials was performed by UV-vis absorption spectroscopy (double-beam Helios α spectrophotometer, from Thermo Spectronics) and X-ray photoelectron spectroscopy (XPS; SPECS spectrometer with monochromatic Al Kα X-ray source at 100 W and 10^{-7} Pa).

Chemical analysis of the samples

UV-vis spectra of the unreduced and chemically reduced dispersions (Fig. S1a), together with the XPS data of the same samples processed into films (Fig. S1b and c) illustrate the chemical identity of graphene oxide and its transformation upon chemical reduction. The UV-vis spectrum of the unreduced dispersion (orange plot in Fig. S1a) exhibits a maximum at 231 nm, assigned to $\pi \rightarrow \pi^*$ transitions of aromatic C-C bonds, with a shoulder at ~300 nm, ascribed to $n \rightarrow \pi^*$ transitions of C=O bonds [1,8]. After reduction (black plot), the maximum red-shifts to about 270 nm and the overall absorption in the 300-1000 nm range increases, suggesting that electronic conjugation has been restored, at least to some extent, within the carbon framework of the graphene sheets as a result of deoxygenation. Such assumption is confirmed by XPS: the spectra of graphene oxide and its reduced counterpart (Fig. S1b and c, respectively) reveal both a significant drop in the O1s band intensity in the survey spectrum and a dramatic change in the shape of the high resolution C1s band (insets to Fig. S1b and c) following chemical reduction. From the high resolution C1s band, we notice a large decrease in the contribution of the components at higher binding energies, which correspond to more oxidized forms of carbon. We note, however, that the chemically reduced material still contains a significant amount of oxygen (O/C ratio of 0.16, compared to 0.43 for unreduced graphene oxide), implying that it cannot be considered pristine graphene, but rather a form of chemically modified graphene. Likewise, we do not believe that salts left over from the preparation of graphite oxide are present in significant quantities in our samples. Such salts should be mainly made of potassium and sodium. However, our XPS analysis was not able to detect any potassium or sodium. For example, potassium can be readily detected by the presence of two bands in the 292-296 eV range of binding energies [9]. If one looks at the high resolution XPS spectrum of graphite oxide provided as the inset to Fig. S1(b), there is not even a hint of bands at such binding energies. Thus, we conclude that salts are not present in significant amounts so as to affect our measurements.

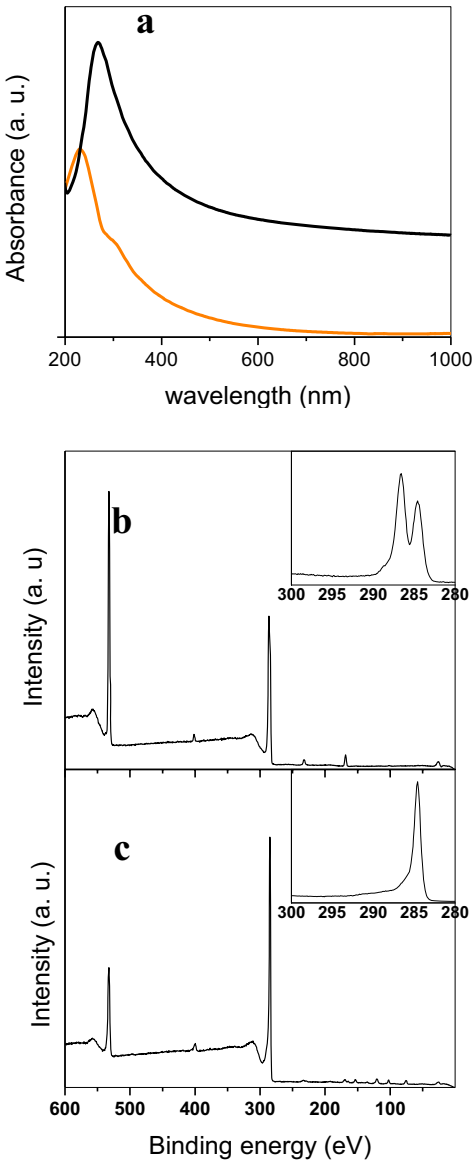

Fig. S1. (a) UV-vis absorption spectra of unreduced (orange plot) and chemically reduced (black plot) graphene oxide dispersions in water. (b,c) XPS survey spectra of unreduced (b) and chemically reduced (c) graphene oxide films with their respective high-resolution C1s spectra shown as insets.

References

[1] Li D, Müller MB, Gilje S, Kaner RB, Wallace GG. Processable aqueous dispersions of graphene nanosheets. Nat Nanotech 2008; 3(2):101-5.
[2] Paredes JI, Villar-Rodil S, Solís-Fernández P, Martínez-Alonso A, Tascón JMD. Atomic force and scanning tunnelling microscopy imaging of graphene nanosheets derived from graphite oxide. Langmuir 2009; 25(10):5957-68.
[3] García R, San Paulo A. Attractive and repulsive tip-sample interaction regimes in tapping-mode atomic force microscopy. Phys Rev B 1999; 60(7):4961−7.
[4] James PJ, Antognozzi M, Tamayo J, McMaster TJ, Newton JM, Miles MJ. Interpretation of contrast in tapping mode AFM and shear force microscopy. A study of Nafion. Langmuir 2001; 17(2):349-60.
[5] Paredes JI, Villar-Rodil S, Tamargo-Martínez K, Martínez-Alonso A, Tascón JMD. Real-time monitoring of polymer swelling on the nanometer scale by atomic force microscopy. Langmuir 2006; 22(10):4728-33.
[6] Lui CH, Liu L, Mak KF, Flynn GW, Heinz TF. Ultraflat graphene. Nature 2009; 462:339-41.
[7] Nemes-Incze P, Osváth Z, Kamarás K, Biró LP. Anomalies in thickness measurements of graphene and few layer graphite crystals by tapping mode atomic force microscopy. Carbon 2008; 46(11):1435-42.
[8] Paredes JI, Villar-Rodil S, Martínez-Alonso A, Tascón JMD. Graphene oxide dispersions in organic solvents. Langmuir 2008; 24(19):10560-4.
[9] Park S, An S, Piner RD, Jung I, Yang D, Velamakanni A, Nguyen ST, Ruoff RS. Aqueous suspension and characterization of chemically modified graphene sheets. Chem Mat 2008; 20(21): 6592-4.

4.3 Comportamiento frente a oxidación de grafeno proveniente de óxido de grafito

Artículo VI

Enviado para publicación: "*Oxidation behavior of chemically derived graphene*"

En materiales en los que la relación entre área superficial y volumen resulta muy elevada, el estudio de los fenómenos tanto físicos como químicos que ocurren en la superficie resulta de una importancia crucial. El caso límite lo encontramos en los materiales puramente bidimensionales como es el grafeno. En un material como el rGO confluye, aparte de la citada bidimensionalidad, la gran cantidad de defectos estructurales y grupos superficiales oxigenados que posee, lo que en teoría incrementa enormemente la reactividad de estas láminas. Esto se ve confirmado por los análisis termogravimétricos efectuados, que muestran que efectivamente el rGO es mucho más reactivo que el grafito prístino de partida. Se sabe que los cambios sufridos durante la preparación mediante oxidación afectan notablemente a las características de las láminas de grafeno, por lo que la motivación en el estudio de los efectos de las oxidaciones es doble. Por un lado se trata de conseguir una modificación controlada de las propiedades de las láminas. En este contexto resulta interesante conocer los efectos de la oxidación, de cara a la implementación de las láminas en determinadas aplicaciones que requieran características muy específicas. También es posible que la oxidación produzca una degradación en las láminas que las inutilice para ciertas aplicaciones. En este caso también resulta interesante conocer cómo son dichos efectos, así como la estabilidad que poseen las láminas bajo atmósferas oxidantes.

Las oxidaciones llevadas a cabo se pueden englobar en dos tipos bien diferenciados. Por un lado están las oxidaciones de tipo global, en las cuales la totalidad de la superficie de las láminas se ve afectada. Por otro lado, se efectuó un tipo de oxidación local en la que se oxidan regiones nanométricas de la muestra de manera controlada. Los diferentes métodos de oxidación empleados poseen importancia desde el punto de vista tecnológico.

a) Oxidaciones globales:

Se emplearon diferentes técnicas de oxidación, en las cuales las especies activas que participan en la oxidación son distintas: tratamientos térmicos en aire (oxígeno molecular), tratamientos en ozono generado mediante radiación ultravioleta (principalmente ozono, aunque también oxígeno atómico) y tratamientos en plasma de microondas (principalmente oxígeno atómico), en orden decreciente de selectividad química y creciente de reactividad. Las imágenes obtenidas mediante AFM en modo tapping permitieron seguir la evolución de las oxidaciones. Lo primero que mostraron las imágenes es que la superficie de las láminas no se modifica uniformemente a escala nanométrica. Las primeras evidencias

de la oxidación muestran zonas que son mucho más atacadas que las zonas que las rodean, dando lugar a la formación de pequeños agujeros en las láminas. Conforme avanza el tratamiento, estos agujeros continúan creciendo hasta que se fusionan entre sí, quedando de las láminas sólo pedazos inconexos. Estas diferencias locales en la reactividad confirman el modelo actual que se tiene del rGO, según el cual está compuesto de zonas de grafeno de unos pocos nm esencialmente perfectas rodeadas de parches con gran cantidad de defectos y funcionalidades oxigenadas. Son estas últimas zonas las que se oxidan preferentemente, debido al incremento en la reactividad provocado por los defectos. Por el contrario, las zonas perfectas son comparativamente menos reactivas y resultan menos alteradas por la oxidación. Además de la formación de agujeros se observa una disminución en el grosor de las láminas, especialmente marcada en la oxidación mediante aire. En este caso, se llegan a obtener para tiempos intermedios láminas inconexas con grosores aproximados de ~0.3–0.4 nm, muy cercanos al valor teórico atribuido al grafeno perfecto. De nuevo, estas observaciones apoyan la idea del rGO como un mosaico de regiones con dos reactividades diferentes. Los defectos estructurales provocan una ondulación de las zonas defectuosas frente a las zonas sin defectos, que permanecen esencialmente planas. Así, si la oxidación tiene lugar preferentemente en zonas con defectos, es de esperar que el grosor de la lámina disminuya. Al final de las oxidaciones se llega en todos los casos a una desintegración casi total del material, permaneciendo sólo pequeños restos esparcidos sobre el substrato.

El mecanismo de oxidación propuesto implica la adsorción de la especie activa preferencial o exclusivamente (dependiendo del tipo de oxidación y de la reactividad de la especie) sobre los dominios "defectuosos". Se crea así un grupo oxigenado que finalmente se desorbe como CO o CO_2, arrancando átomos de carbono en el proceso. La existencia del proceso de adsorción se demuestra por la disminución de la conductividad de las láminas (evidenciada por STM) tras tratamientos cortos que no provocan modificaciones morfológicas apreciables. Es decir, se ha quimisorbido oxígeno, lo que explica la disminución de la conductividad, pero aún no ha tenido lugar la desorción.

Tanto los espectros XPS, como experimentos complementarios midiendo grosores con AFM confirmaron la reactividad creciente prevista de las especies activas: oxígeno molecular < ozono < oxígeno atómico.

b) Oxidación local:

Para la oxidación local se empleó la litografía STM, que aprovecha la gran precisión de las microscopías de proximidad para modificar localmente pequeñas áreas siguiendo patrones predeterminados. El empleo de esta técnica sobre HOPG permite el ataque de átomos de carbono de una manera controlada. Esto se consigue aumentando el voltaje, V_b, por encima de un valor umbral, de modo que se sobrepasa la energía de activación de la reacción de oxidación. En el caso del rGO, el proceso es ligeramente distinto. Por un lado, la energía umbral necesaria es menor que en el caso del HOPG, en una clara indicación de la mayor reactividad del material. Para valores muy altos de V_b se

produce una oxidación totalmente incontrolada, dando lugar a la desintegración de grandes zonas de la lámina. Para valores menores de V_b dentro de un determinado rango, se consigue producir oxidaciones controladas, y las observaciones mediante STM sugieren que dichas oxidaciones no involucran el arranque de material carbonoso, al contrario de lo que sucede en el HOPG. Estas zonas presentan una conductividad menor que la de las zonas no oxidadas, por lo que aparecen como depresiones aparentes (no topográficas) en las imágenes. La disminución local de la conductividad está ligada a la introducción de funcionalidades oxigenadas, pero las energías involucradas no son lo suficientemente elevadas como para que se produzca una posterior desorción del oxígeno como CO o CO_2. Este tipo de oxidación local es interesante desde un punto de vista tecnológico en potenciales aplicaciones que requieran de una precisión nanométrica en la oxidación, como puede ser la fabricación de componentes electrónicos.

Oxidation behavior of chemically derived graphene

(Enviado para publicación)

P. Solís-Fernández,[1] J.I. Paredes,[1] S. Villar-Rodil,[1] L. Guardia,[1] M.J. Fernández-Merino,[1] G. Dobrik,[2] L.P. Biró,[2] A. Martínez-Alonso,[1] J.M.D. Tascón[1]

[1]*Instituto Nacional del Carbón, CSIC, Apartado 73, 33080 Oviedo, Spain*

[2]*Research Institute for Technical Physics and Materials Science, H-1525 Budapest, Hungary*

The oxidation and etching of chemically derived graphene (CDG) by thermal oxidation in air, microwave oxygen plasma, ultraviolet-generated ozone and scanning tunneling microscopy (STM) lithography have been investigated. This type of graphene exhibited a higher reactivity towards oxidation than that of pristine graphite (taken as a reference carbon material), which could be related to its intrinsically defective structure. Etching of CDG as a result of thermal oxidation in air was started at as low a temperature as 400 °C, compared with ~500 °C for graphite, indicating that the defects present on the former are different in nature to those found on the surface of pristine graphite. The morphological evolution of individual CDG sheets upon oxidative attack was consistent with the sheets being essentially a patchwork of minute domains (a few to several nanometers large) with two distinct reactivities, higher (lower) reactivity associated to defective (defect-free) domains. The introduction of oxygen functional groups on the basal plane of CDG was revealed directly by X-ray photoelectron spectroscopy and indirectly through STM. STM lithography enabled discrimination between oxidation proper (introduction of oxygen groups) and etching (desorption of the groups as CO or CO_2) of the CDG sheets through control of the applied bias voltage. The former was visualized in the STM images as locally depressed features of electronic origin, whereas etching led to the generation of actual trenches on the sheets. Taken together, the present results provide insight into the reactivity of CDG and suggest potential practical applications involving controlled oxidation of this type of graphene.

1. Introduction

As a novel two-dimensional material with unique attributes, graphene has attracted in recent years enormous interest from the research community.[1,2] A significant fraction of this interest is focused on chemically derived graphene (CDG), which is the name usually given to single-layer sheets prepared by exfoliation and subsequent reduction of graphite oxide. In addition to attractive mechanical, electrical or optical properties, this type of graphene exhibits several advantages with respect to graphenes manufactured by other methods: 1) its production is simple, scalable and cost-effective, 2) the material is dispersible in a variety of solvents, including water, which facilitates its further manipulation and processing, and 3) it displays versatility toward chemical functionalization.[3-5] These

characteristics make CDG a strong candidate for use in a number of technological applications, including composite materials,[6-8] transparent conductors,[9-11] supercapacitors[12,13] or molecular sensors.[14,15]

One relevant aspect of CDG concerns its chemical reactivity, and in particular its reactivity towards oxidation. In contrast to nearly ideal forms of graphene, such as those produced by micromechanical cleavage of pristine graphite, the carbon framework of CDG sheets contains a significant amount of structural defects and residual oxygen functional groups inherited from their preparation process.[4,16-18] As a result, many properties of CDG, including its oxidation behavior, are expected to differ significantly from those of pristine, defect-free graphene, and therefore deserve specific attention.

An in-depth knowledge of the oxidation behavior of CDG is important not only from a practical point of view (e.g., to evaluate its stability under oxidizing environments), but also from a fundamental science perspective. Carbon oxidation has long been a topic of scientific and technological relevance,[19-27] but to the best of our knowledge, oxidation studies on CDG have not yet been reported in the literature. Due to its special structural features, we can expect the evolution of CDG upon oxidation to be distinct from that exhibited by the majority of carbon materials that have been investigated in the past. Various types of oxidation have been used as a means to manipulate materials directly related to CDG (e.g., unreduced graphene oxide), which afforded the preparation of several structures therefrom, such as nanoribbons and nanotubes.[28,29] Oxidative etching has also been very recently employed as a means of fine-tuning the width of pristine graphene nanoribbons below 10 nm.[30]

In the work reported here, we investigate the behavior of CDG toward different gas-phase oxidation treatments. Oxidation was carried out in air at high temperature as well as by microwave (MW) oxygen plasma and ultraviolet-generated ozone (UVO). The effect of oxidation was investigated both on individual CDG sheets and on thin films of this material using mainly atomic force and scanning tunneling microscopy (AFM/STM) and X-ray photoelectron spectroscopy (XPS). In general terms, we find CDG to be extremely sensitive to the investigated oxidizing environments, which should be taken into account when considering certain applications for this type of graphene. In addition, we demonstrate that CDG sheets can be controllably re-oxidized on a local scale by means of STM lithography, thus opening the prospect of patterning oxidized regions on CDG with nanometric resolution.

2. Experimental

CDG was produced in the form of stable aqueous dispersions using graphite oxide and following previously reported procedures.[18,31] Briefly, graphite oxide was prepared from natural graphite powder (Fluka 50870) by the Hummers method[32] and exfoliated in water via sonication to yield a stable, homogeneous suspension of graphene oxide sheets. This suspension was then chemically reduced under basic conditions with hydrazine monohydrate, resulting in the final CDG dispersion that was used

in the subsequent experiments. Oxidation of CDG was investigated both on individual sheets and on macroscopic films. In the former case, samples were prepared by drop-casting the CDG suspension onto pre-heated (~50-60 °C), freshly cleaved highly oriented pyrolytic graphite (HOPG) or SiO_2/Si substrates. Such procedure is known to afford large numbers of isolated sheets on both substrates.[33] The films were produced either in the form of free-standing paper-like materials or as ultrathin coatings supported onto SiO_2/Si substrates. The paper-like films were obtained via vacuum filtration of the CDG suspension through Anodisc membrane filters 47 mm in diameter and 0.2 μm of pore size (Whatman).[31] The ultrathin coatings were prepared by heating the aqueous CDG suspension at 95 °C until most of the water evaporated and a continuous film formed on the liquid surface.[34] This floating film was then contacted downside with the SiO_2/Si substrate and allowed to dry.

The CDG samples were subjected to oxidation in air at high temperature, to MW oxygen plasma treatment and to UVO oxidation. Thermal oxidation in air was carried out in a horizontal quartz reactor with an internal diameter of 20 mm. The samples were first heated under flowing Ar (100 mL min^{-1}) at 20 °C min^{-1} until the desired oxidation temperature was reached, after which the Ar flow was switched to a flow of synthetic air (50 mL min^{-1}). Upon completion of the oxidation step, the samples were allowed to cool down to room temperature, again under an Ar flow. The temperature inside the reactor was measured with a Pt/Rh thermocouple placed close to the sample. Different temperatures and treatment times were investigated. MW oxygen plasma treatments were accomplished in a Technics Plasma 200-G apparatus. In this device, MW radiation (2.45 GHz) is generated by a magnetron and transferred through a waveguide to a quartz chamber that contains the samples and is filled with O_2 (99.999 % pure), where the oxygen plasma is activated. The working pressure in the chamber was set to 1.0 mbar and the effect of MW power and treatment time was studied. UVO oxidation was performed on a Jelight UVO cleaner model 42. UV radiation is generated by a low pressure mercury vapor grid lamp placed on the top of the stainless steel treatment chamber. The lamp radiates mainly at 184.9 and 253.7 nm wavelengths, the latter being the most intense, delivering a total power per unit area of 42 mW cm^{-2}.

AFM and STM characterization of the samples as well as STM lithography were carried out under ambient conditions with a Nanoscope IIIa Multimode apparatus, from Veeco Instruments. AFM imaging was accomplished in amplitude modulation, usually referred to as tapping mode, and more specifically in the attractive regime of tip-sample interaction. It is well-known that amplitude-modulation AFM can be operated under two distinct tip-sample interaction regimes: attractive and repulsive.[35-39] The former regime is preferable over the latter for the visualization of delicate structures. This is because perturbation of such structures by the tip is mostly avoided, which is not necessarily the case when working in the repulsive regime.[36,37] As will be seen below, oxidation of the CDG sheets led in some cases to the development of extremely fragile features that could only be imaged in the attractive

regime, which was established by setting proper values of the free and setpoint amplitudes of cantilever oscillation.[37] Rectangular silicon cantilevers with spring constant ~40 N m^{-1} and resonance frequencies between 250 and 350 kHz were employed. STM imaging was performed in the constant current mode (variable height) using mechanically prepared Pt/Ir (90/10) tips. The STM equipment included a low-current converter to allow operation with tunneling currents down to the pA regime, which proved to be necessary in some cases as noted below. Local oxidation of the CDG sheets via STM lithography was carried out with Pt/Ir tips like reported previously in the case of etching graphene nanoribbons,[40] working at significantly higher bias voltages than those normally employed for imaging (e.g., ~1600 vs. ~100 mV; sample always positive with respect to tip). Likewise, the tunneling current was increased (e.g. 1.5 vs. 1 nA) to keep the STM tip close to the sample surface. Local oxidation was typically performed at a temperature of 23-25 °C and a relative humidity of ~70% along straight lines, moving the STM tip at a controlled speed of 1 nm s^{-1}.

Additional characterization was carried out by means of thermogravimetric analysis (TGA), Raman spectroscopy and X-ray photoelectron spectroscopy (XPS). TGA was accomplished with an SDT Q600 thermobalance (TA Instruments) under either argon or synthetic air flow (100 mL min^{-1}) at a heating rate of 10 °C min^{-1} and using Pt crucibles. Raman spectra were recorded on a Horiba Jobin-Yvon LabRam instrument at a laser excitation wavelength of 532 nm. XPS was performed on a SPECS system at 10^{-7} Pa with a monochromatic Al Kα X-ray source at 100 W. Surface composition (atomic %) was determined from the integrated intensities of the main peaks that were found in the survey spectra.

3. Results and discussion

CDG obtained by chemical reduction of graphene oxide is known to contain a significant amount of residual oxygen functional groups and structural defects on its basal plane inherited from the preparation process.[4,16-18] Previous studies have also determined that gas-phase oxidation of graphite surfaces takes place preferentially on defected areas (atomic vacancies, step edges, etc) over structurally perfect ones owing to the higher reactivity of the former.[21,23,41,42] Therefore, we can expect CDG to generally exhibit an increased reactivity towards oxidation in relation to pristine graphitic structures. Fig. 1a and b shows the thermogravimetric (TG) and differential thermogravimetric (DTG) plots, measured under both argon and air flow, of the starting natural graphite powder and the CDG material obtained thereof, respectively. For the starting graphite under argon flow (blue plots in Fig. 1a), there is barely mass loss in the whole temperature range up to 900 °C, indicative of a pristine material essentially devoid of oxygen-containing or any other type of functional group. Under air flow (red plots in Fig. 1a), almost all the mass is lost in the temperature range between 700 and 850 °C, which can be attributed to gasification of the material in the form of CO and CO_2 as a result of reaction with O_2. By contrast, for CDG gasification occurs in a lower temperature range (550-650 °C; red plots in Fig. 1b), which is clearly an indication of enhanced reactivity towards oxidation compared to pristine graphite. As

noticed from Fig. 1b, CDG also exhibits a mass loss (~5%) below 100 °C, attributed to desorption of physisorbed water, and a slower, steady mass loss of ~10-15% between 100 and 550 °C, which is ascribed to the removal of some of its residual oxygen functionalities. The defective nature of CDG, which is presumably responsible of the enhanced reactivity reported in Fig. 1b, becomes apparent in its Raman spectrum (Fig. 1c, bottom). Such spectrum displays a strong D band, which is located at ~1350 cm^{-1} and can be related to the presence of a significant amount of structural disorder in the carbon skeleton of CDG.[16-18] For comparison, the D band is very weak in the spectrum of the starting pristine graphite (Fig. 1c, top), indicating an essentially defect-free graphitic structure.

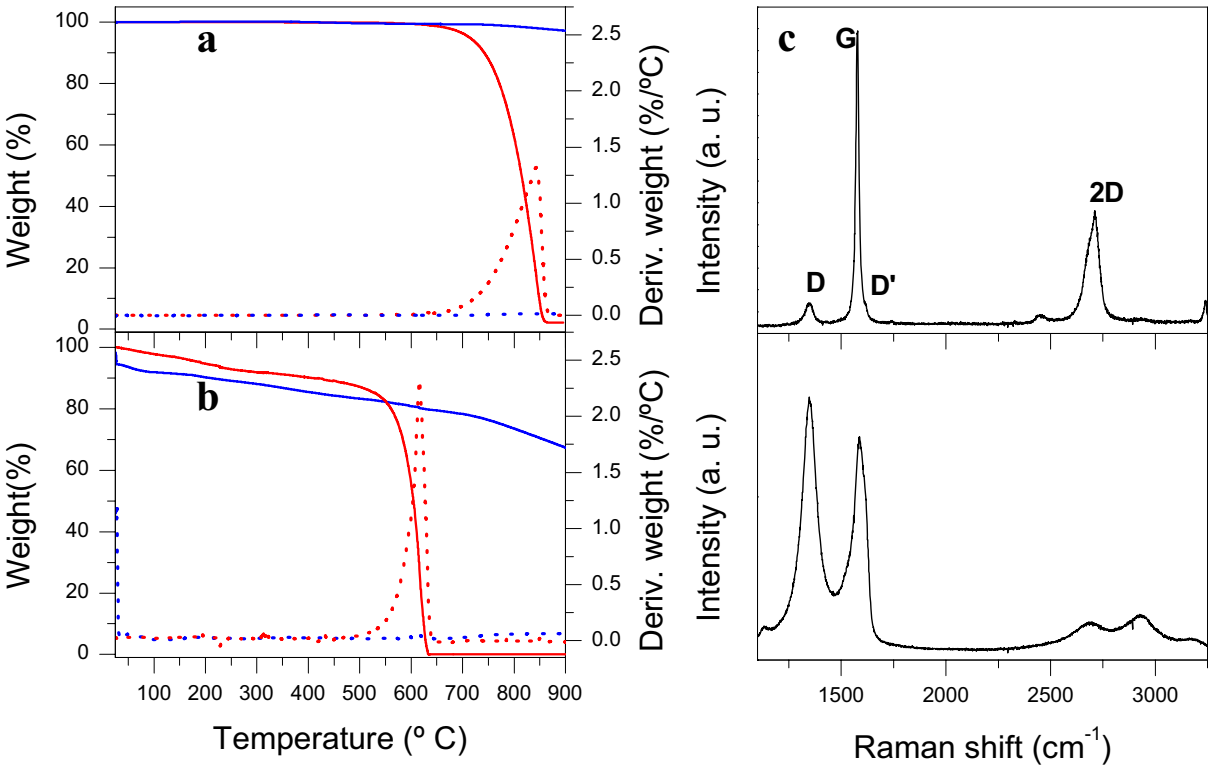

Figure 1 – (a,b) TG (solid curves) and DTG (dotted curves) plots in argon (blue) and air (red) atmosphere for the starting natural graphite (a) and CDG (b). (c) Raman spectra for the starting natural graphite (top) and CDG (bottom).

To provide further insight into the oxidation behavior of CDG, the modification of individual sheets upon the different oxidative treatments was investigated. Fig. 2a shows a representative AFM image of several isolated, as-prepared CDG sheets before oxidation, deposited onto HOPG. A characteristic line profile taken along the marked white line is also presented superimposed on the image. The apparent thickness of the sheets (measured as their height relative to the HOPG substrate) is about 1 nm, consistent with the sheets corresponding to single-layer objects.[18,31,33] At this magnification, the sheets appear rather featureless and flat. However, higher resolution imaging (inset to Fig. 2a) revealed that the sheets possess a slightly corrugated morphology, with typical lateral feature sizes and height variations of 5-10 nm and a few tenths of nanometer, respectively. Taking into account that the

supporting HOPG substrate is atomically flat, we conclude that the observed corrugated morphology has an intrinsic origin; i.e., it is related to the presence of structural distortions within the carbon lattice and residual oxygen groups that displace the carbon atoms out of their originally planar arrangement, but not to deformations induced by the substrate.[18]

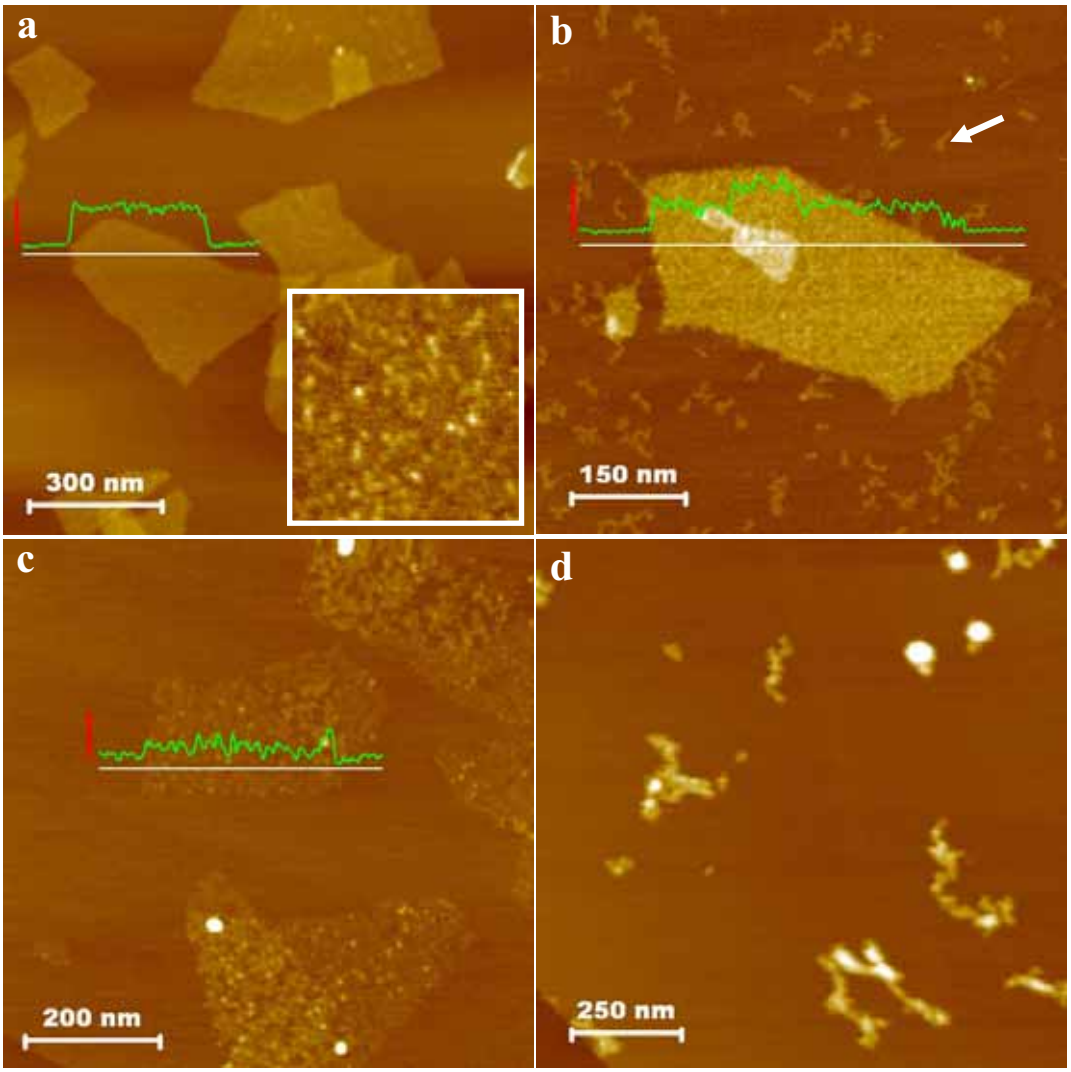

Figure 2 – (a) AFM image of the starting, as-prepared CDG sheets deposited onto HOPG. Inset: higher resolution AFM image (125 × 125 nm2) showing the nanometer-scale morphology of an individual sheet. (b-d) AFM images of CDG sheets onto HOPG following thermal oxidation in air at 400 °C for 30 (b), 60 (c) and 110 min (d). Representative line profiles, taken along the marked white lines, are superimposed on the images in (a-c). The vertical red bars correspond to 1 nm in the line profiles.

Morphological changes to the CDG sheets as a result of thermal oxidation in air were observed to come about at as low a temperature as 400 °C. As far as could be judged from AFM imaging, treatments below 400 °C did not lead to any noticeable modification of the as-prepared CDG sheets. By contrast, thermal oxidation-induced etching of the surface of bulk graphite is well known to start only at temperatures above 500 °C at defect sites,[21] whereas that of pristine graphene prepared by micromechanical cleavage of graphite onto SiO_2/Si substrates takes place at 450 °C.[26] Fig. 2b illustrates

the initial changes experienced by individual CDG sheets upon air oxidation at 400 °C, which were observable after a 30 min treatment. First, the apparent thickness of the sheets has decreased slightly (~0.7 vs. ~1 nm) and their corrugation has increased substantially, as noticed by inspecting line profiles. Second, very small and flat isolated objects (e.g., white arrow in Fig. 2b) were observed relatively often around the sheets. Such objects exhibited an apparent height of about 0.3 nm and an irregular shape, although it was usually elongated or branched with typical widths approximately between 5 and 15 nm. Taking into account the widening effect of features in AFM images due to the finite size of the tips employed (tip radii of 5-10 nm in the present case), we infer that the actual width of many of these objects should be just a few nm [43]. Control experiments on bare HOPG substrates did not reveal the presence of this type of feature following oxidation treatments at 400 °C or any other temperature. Consequently, its observation on HOPG surfaces covered with CDG sheets must be related with the oxidation process of the latter. Fig. 2c shows a typical AFM image of the sheets following a longer (60 min) oxidation in air at 400 °C. The sheets are still clearly visible on the HOPG substrate, but significantly, their apparent thickness has further decreased to a value of ~0.3-0.4 nm, and they display a somewhat discontinuous appearance (see line profile in Fig. 2c). The fact that the apparent thickness of the CDG sheets decreases with oxidation time seems to be at odds with the idea that they correspond to single-layer objects and requires some explanation, which will be given in the discussion below. Finally, after a sufficiently long oxidation at 400 °C (e.g., 110 min, Fig. 2d), the sheets are no longer visible and only some irregular features a few nm high, interpreted as remnants of the sheets, are left on the HOPG surface. Oxidation at higher temperatures (e.g., 500 °C, images not shown) followed a similar pattern to that observed at 400 °C, except that changes to the sheets took place at a much faster pace.

Fig. 3a-d shows the evolution of CDG sheets exposed to MW oxygen plasma at a power of 40 W for different times. For the shortest treatment time investigated (4 s), no obvious changes in the nanometer-scale morphology of the sheets were noticed by AFM (images not shown). Morphological changes were observed after 8 s of plasma exposure (Fig. 3a) in the form of an increased corrugation (compare line profiles from Fig. 2a and 3a), which reflected the presence of segregated areas with distinct heights (see, e.g., the sheet in the center of Fig. 3a). The next step in the etching process was the emergence of rounded and elongated pits within the sheets, as can be noticed in Fig. 3b for a 12 s plasma exposure, some of which are indicated by white arrows. Subsequently, the pits tended to grow in number as well as to expand and coalesce, giving rise to a structure of tiny patches of isolated material (e.g., Fig. 3c for a 24 s treatment), and finally to a residue of the original sheets (Fig. 3d, 60 s). We note that during this etching process, the apparent thickness of the CDG sheets also tended to decrease, although not as markedly as in the case of thermal oxidation in air. Likewise, the etching behavior of the CDG sheets only changed quantitatively, but not qualitatively, when different plasma powers were used, i.e., higher powers induced faster etching but no new features appeared. Such trend can be distinctly noticed by comparing Fig. 3e, which corresponds to a 10 s plasma treatment at 80 W,

with Fig. 3b (12 s at 40 W), the former generating more and wider pits than the latter for a shorter exposure time. The images of Fig. 3 also provide clear indication that etching of the CDG sheets is much faster than that of the HOPG surface: the latter appears hardly modified even after the individual CDG sheets have been etched away almost completely (Fig. 3d). To provide some quantitative comparison, we determined the etching rate of ultrathin (~100 nm) CDG films supported onto SiO_2/Si substrates. This was accomplished by measuring the reduction in thickness of the film via AFM upon consecutive plasma treatments at a given power (100 W). Assuming the actual thickness of a CDG monolayer to be about 0.5 nm,[33] an etching rate of ~15 monolayers of CDG per min was obtained, compared with a rate of ~1 monolayer per min previously determined in the case of HOPG.[44]

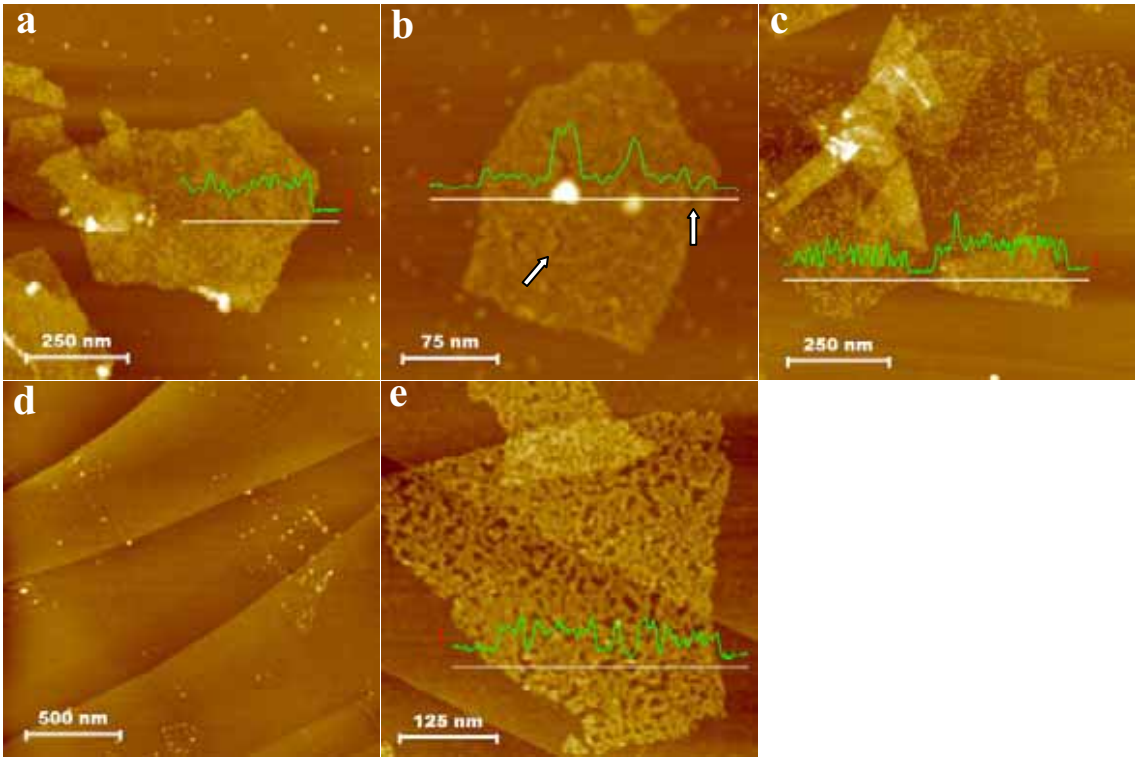

Figure 3 – AFM images of CDG sheets after exposure to MW oxygen plasma for 8 (a), 12 (b), 24 (c) and 60 s (d) at a plasma power of 40 W, and 10 s at a plasma power of 80 W (e). Representative line profiles superimposed on the images are given in (a-c and e). The profiles were taken along the marked white lines. The vertical red bars correspond to 1 nm in the line profiles.

The etching of CDG sheets by UVO exposure (Fig. 4) exhibited traits that were already present either on thermally oxidized or on plasma treated samples. UVO oxidation led to a remarkable reduction in the apparent thickness of the sheets (down to about 0.5 nm) together with the development of a number of rounded features at short exposure times (e.g., 1 min, Fig. 4a), extended treatment times inducing the progressive disintegration of the thinned sheets through generation of pits (e.g., Fig. 4b for a 5 min treatment). We note that some of the structures generated by this and the previous oxidations could only be imaged working specifically in the attractive regime of amplitude-modulation AFM, which is extremely gentle. Such regime was established by setting proper values of free and set-point

amplitudes of cantilever oscillation.[35,37,38] In particular, stable operation in the attractive regime required the use of relatively small free oscillation amplitudes (for instance, 10-30 nm). The use of larger free amplitudes (e.g., 100 nm), which are customary in amplitude-modulation AFM, did not allow the imaging of many of the reported structures, since they were easily wiped out by the AFM tip. In a few cases, even operation in the attractive regime did not avoid perturbation of delicate structures after repeated scanning of the same area, as exemplified in the insets to Fig. 4b.

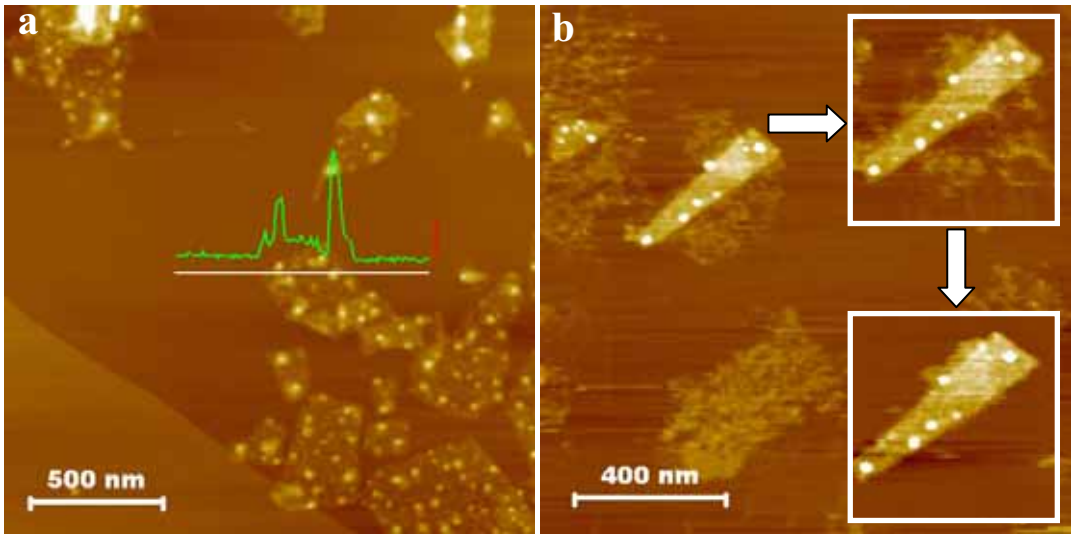

Figure 4 – AFM images of CDG sheets on HOPG following UVO treatment for 1 (a) and 5 min (b). A representative line profile, taken along the marked white line, is given in (a). The vertical red bar corresponds to 1 nm in the line profile. Insets to (b): repeated scanning of the same sheet, even in the attractive regime of amplitude modulation AFM, led to the removal of extremely loose oxidized material.

The reactivity towards oxidation of carbon materials is well known to be closely related to their particular structure.[45,46] Therefore, to rationalize and interpret the oxidation behavior of CDG sheets reported above, we first have to consider the structure of this type of graphene in some detail, which is expected to differ considerably from that of pristine graphene prepared, e.g., by micromechanical cleavage of bulk graphite. Although a comprehensive understanding of the atomic structure of CDG produced by chemical reduction of graphene oxide is still missing, some recent work has shed some light on this question. Using high resolution transmission electron microscopy (HR-TEM), Gómez-Navarro et al have concluded that chemically reduced graphene oxide sheets consist of essentially defect-free graphene areas interspersed with highly defective regions, both of which possess lateral dimensions of just a few nanometers.[47] The carbon lattice within the defective regions, as well as in their immediately surrounding areas, was shown to display strong local deformations, including out-of-plane distortions, which are probably the origin of the smoothly corrugated morphology observed for the as-prepared CDG sheets (Fig. 2a, inset). The defect areas were also interpreted as arising from highly oxidized sections in the graphene oxide sheets before chemical reduction. Therefore, it is reasonable to assume that the residual oxygen groups remaining on the CDG sheets following the reduction step[16,18,31] will be mostly located on such defective regions. As a result of the local structural distortions, the carbon atoms

in the defective regions will exhibit a certain sp^3 orbital character and π-orbital misalignment, and thus will be significantly strained, making them more reactive than those from the defect-free areas.[48,49] Consequently, a CDG sheet can be thought of as an intimate mixture of areas with two distinct reactivities: a high chemical reactivity would be associated to the defective areas, whereas the defect-free regions would exhibit a comparatively low reactivity. In turn, such observation implies that oxidative etching of the sheets will take place preferentially on the defect regions.

The etching of the surface of bulk graphite via oxidation with molecular oxygen is a thermally activated process that requires temperatures of at least ~500 °C and proceeds exclusively at defect sites (provided that the temperature is below ~700 °C).[21,23] For the CDG sheets investigated here, etching induced by thermal oxidation was observed to start at a lower temperature (400 °C, Fig. 2), which we attribute to the fact that the defects present on this material are of a different nature to those characteristic of the graphite surface. On the surface of bulk graphite, the defects are essentially edge carbon atoms, whether in the form of atomic vacancies or as part of, e.g., step edges[21,23,50,51]. On the other hand, according to the HR-TEM studies mentioned above, the defective regions of CDG are not believed to be constituted by edge carbon atoms, but instead by carbon atoms bonded to three neighboring carbons in distorted topologies, including carbon pentagons and heptagons.[47] Such observation is further supported by previous atomic-scale STM investigations, which revealed a distorted carbon lattice but not edge carbon atoms (e.g., holes) within the CDG sheets.[18] Considering that etching of carbon with molecular oxygen to yield volatile species, such as CO or CO_2, requires the overcoming of an activation barrier, it is reasonable to expect that the magnitude of such barrier will be somewhat different at defects of different type, just as the oxidative attack at, e.g., a vacancy has a different (lower) barrier to that of attack on the pristine basal surface.[52] Consequently, we can also expect that the temperature at which etching is first observed will be different for CDG and graphite, as it was indeed the case.

The main features of the oxidative etching of CDG reported above can be accounted for on the basis of the preceding discussion. Oxidation by air at 400 °C will take place selectively at the defective regions that make the CDG sheets to be smoothly corrugated. As oxidation proceeds, the higher-lying, defective regions should be progressively removed, leaving behind the relatively flat, defect-free graphene areas, which should lead to an apparent thinning of the sheets. Such behavior was actually observed in the experiments (Fig. 2). In particular, the evolution of the sheets into somewhat discontinuous structures with an apparent thickness of 0.3-0.4 nm after a 60 min oxidation (Fig. 2c) can be interpreted to be the result of the complete (or almost complete) removal of the defect regions. Thus, the sheets seen in Fig. 2c can be thought of as a porous mesh constituted by tiny fragments of more or less pristine graphene. The fact that the apparent thickness of these sheets (measured as a height relative to the HOPG substrate) matches that of the uppermost layer of graphite surfaces or the

interlayer distance in graphite (0.34 nm) supports such interpretation. Some of these minute graphene fragments are probably not too tightly connected to their neighbors, so that a few of them could easily detach from the periphery of the sheets during the oxidative treatment. At the high temperatures employed for oxidation (400 °C and above), the detached fragments could either desorb from or migrate across the HOPG surface, in the latter case possibly to coalesce with other graphene fragments. We believe that the isolated objects that were observed in the images (Fig. 2b) correspond to these detached and coalesced graphene fragments, as their apparent thickness (~0.3 nm) was very similar to that of the CDG sheets after selective removal of their defective regions (Fig. 2c). It is also conceivable that upon sufficiently long oxidation times at 400 °C (e.g., 110 min, Fig. 2d), the loose connections between the pristine graphene fragments will be etched away, and the thermal energy of the liberated fragments will cause the porous mesh to disintegrate. Some of these fragments could then re-aggregate in a random fashion, yielding the type of structures observed in Fig. 2d. Very recently, the oxidative cutting of (unreduced) graphene oxide sheets into molecular fragments has also been shown to be possible via sonication in acid.[29] In that case, the molecular fragments could be subsequently re-assembled to yield carbon nanostructures, such as nanotubes and nanoparticles. In the present case, at higher oxidation temperatures (e.g., 500 °C, images not shown), the size and number of re-aggregated structures decreased significantly, which can be attributed to the consumption of the graphene fragments through attack at their edges.

The evolution of CDG sheets exposed to MW oxygen plasma (Fig. 3) and UVO (Fig. 4) can also be readily understood bearing in mind the preceding discussion and previous studies that revealed the effect of such oxidation treatments on graphite as a model carbon surface.[41,42,44] In both cases, attack is dominated by highly reactive species (atomic oxygen and ozone) and takes place at defect sites as well as perfect sites of basal planes, although there is a significant selectivity towards the former. Consequently, MW oxygen plasma- and UVO-induced etching will occur preferentially on the defective domains of the CDG sheets, which will be removed faster than the pristine graphene areas. Again, such process should lead to a reduction in the apparent thickness of the sheets, as it was indeed noticed in Figs. 3 and 4. However, contrary to the case of thermal oxidation at 400 °C, once the edges of the pristine graphene fragments become exposed, they should also be etched away.[41,42] Therefore, holes are expected to develop throughout the sheets and progressively grow with treatment time (e.g., Fig. 3b and e), until isolated patches (Fig. 3c) and finally some residue of the sheets (Fig. 3d) are left. We note that both MW oxygen plasma and UVO treatments are carried out at, or close to, room temperature, particularly for the short exposure times investigated.[42,53] Thus, unlike thermal oxidation, the isolated graphene fragments generated during plasma and ozone oxidation will exhibit low or even no mobility, so that the sheets should be seen to disintegrate progressively. Fig. 3c and d provides clear indication of this point.

We have interpreted the etching behavior of CDG sheets on the basis of the implicit assumption that such behavior was exclusively dominated by intrinsic factors, i.e., by the large amount of structural defects present on the sheets as a result of their preparation process. However, possible effects of the supporting substrate should also be considered. In the case of pristine, micromechanically cleaved graphene, its structure is known to be significantly influenced by the substrate. More specifically, this type of graphene exhibits nanoscale corrugations when deposited onto atomically rough supports (e.g., SiO_2/Si).[54] By contrast, such corrugations are completely absent on an atomically smooth substrate such as mica or hexagonal boron nitride.[38,55] The structural deformations may be a source of enhanced chemical reactivity for graphene samples supported on rough substrates.[26,55] In the present work, the oxidation experiments of CDG reported above were carried out using atomically flat HOPG substrates, which are not expected to bring about additional (extrinsic) distortions to the sheets. Therefore, to determine the possible influence of extrinsic corrugations on the oxidation behavior of the CDG sheets, additional experiments were carried out using a rough substrate (SiO_2/Si) instead of HOPG (results not shown). For example, it was observed that the evolution of the sheets on SiO_2/Si with exposure time to MW oxygen plasma was very similar to that documented on HOPG in Fig. 3, even though the sheets are significantly more corrugated when supported on the former substrate.[33] Hence, although some contribution from the substrate cannot be completely ruled out, we conclude that the etching behavior of CDG is mostly dominated by its own defective nature.

The attack of CDG via the investigated gas-phase oxidations can be essentially envisaged to proceed through a two-step process. The first step (oxidation proper) would be the chemisorption of molecular oxygen (for thermal oxidation in air) or atomic oxygen/ozone (for MW oxygen plasma and UVO) exclusively, or at least preferentially, onto the defective domains of this type of graphene. The functional group that is subsequently formed on the basal plane of the sheet might be an endoperoxide in the case of molecular oxygen[56] or an epoxide in the case of atomic oxygen/ozone.[57,58] The second step (etching) would involve desorption of the functional group as CO or CO_2, thus removing a carbon atom from the CDG lattice. The successive iteration of these two basic steps should lead to the modification of the CDG sheets as observed in the AFM images of Figs. 2 to 4. However, such images only provide direct indication of the occurrence of the second step in the process (removal of carbon atoms), but not of the first one (adsorption of oxygen species). To gather evidence that the first step was also actually taking place, further experiments were accomplished.

We noted previously that, as visualized by AFM, MW oxygen plasma treatment of CDG at 40 W for 4 s did not bring about any noticeable morphological modifications to the individual sheets. Nonetheless, STM experiments suggested that very subtle changes did in fact take place. The starting, as-prepared CDG sheets on HOPG could be readily imaged by STM under a wide range of tunneling conditions, in particular those that are typical of highly conductive carbon materials (e.g., tunneling

currents in the nA regime and bias voltages of a few tens of mV).[18] By contrast, the same sheets after a 4s MW oxygen plasma treatment could not be studied under such conditions, but instead were easily moved and swept away by the probing STM tip. This result suggests that the sheets become significantly less conducting after the 4 s plasma treatment. As a matter of fact, they could only be visualized by STM using very low tunneling currents (~1 pA), which is a typical feature of specimens of very low electrical conductivity; for instance, the heavily oxygenated, unreduced graphene oxide sheets.[18] Even though there is decrease in conductivity, the low-current STM images did not exhibit any morphological changes in the CDG sheets before and after the MW plasma treatment, as shown in Fig. 5. We interpret that some atomic oxygen from the plasma has already chemisorbed onto the basal surface of the CDG sheets to form epoxide groups after a 4 s exposure, but these groups have not yet desorbed as CO/CO_2 in any significant amounts, i.e., etching has not yet taken place. However, the increased amount of oxygen on the CDG sheets would be responsible for their diminished conductivity. Such interpretation is supported by very recent theoretical calculations by Leconte *et al*, which predicted a drastic reduction in the electrical conductivity of graphene covered with just a few percent (4 %) of epoxide groups.[59] A similar behavior to the one reported for MW oxygen plasma was observed in the case of oxidation by UVO, but not for thermal oxidation in air. Because molecular oxygen is generally much less reactive than atomic oxygen and ozone, it is likely that the amount of oxygen groups present on the (disrupted) basal plane of the CDG sheets as a result of chemisorption of the former will be very limited, so that their conductivity would not be severely affected.

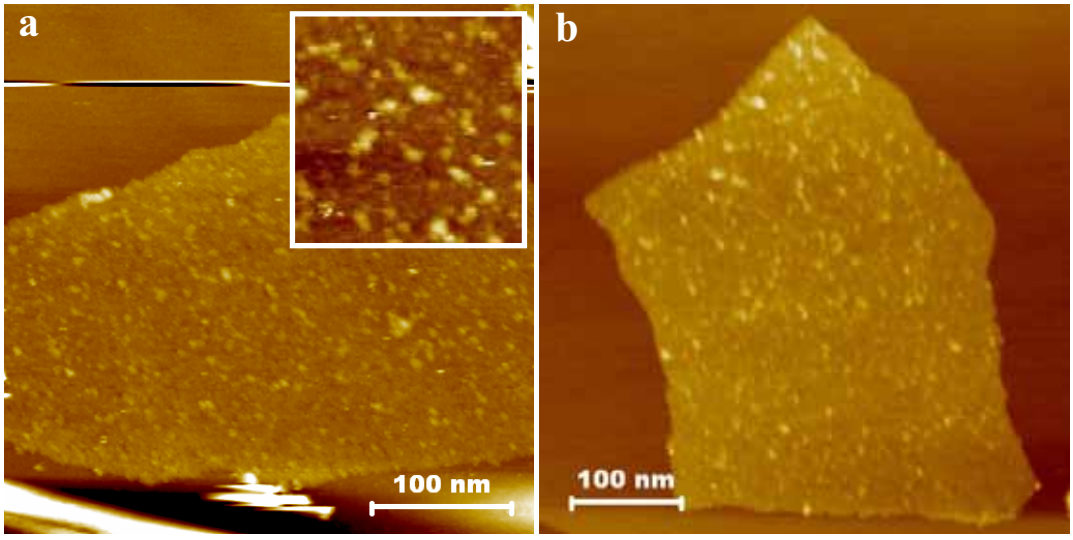

Figure 5 – Low-current STM images (1 pA, 1000 mV) of CDG sheets after MW oxygen plasma exposure at a power of 40 W during 4 s (a) and before oxygen plasma exposure (b). Inset to (a): detailed morphology (80 × 80 nm2 image) of a plasma-treated sheet.

XPS investigations provided spectroscopic confirmation of the previous hypothesis. Paper-like films oxidized for longer periods than their individual sheet counterparts were used as specimens for XPS analysis, as a significant modification of sample composition is needed to allow detection by this

technique. The XPS survey spectra (not shown) yielded O/C atomic ratios for films subjected to MW oxygen plasma (2 min, 40 W) and UVO (30 min) of ~0.32 and ~0.16, respectively, which were larger than the value measured on thermally oxidized samples at 400 °C for 1 h (0.08). Such results confirm that the amount of functional groups resulting from thermal oxidation in air is small compared with oxidation by UVO and especially MW plasma. Furthermore, high resolution spectra for the C1s and O1s core levels (Fig. 6a and b, respectively) show that thermal oxidation in air yields the lowest content of hydroxyl/ether/epoxide/peroxide groups, which are believed to be the species created upon basal plane oxidation of graphite/graphene.[60] Indeed, the normalized C1s spectra (Fig. 6a) reveal that the amount of carbon singly bonded to oxygen (binding energy of ~286.5 eV[61] indicated by a red vertical line in Fig. 6a) in thermally oxidized CDG is the lowest in the series and largest for MW oxygen plasma-treated CDG. This result is consistent with the expected differences in reactivities of graphitic carbon towards these oxidizing agents, which are supposed to be in the following order: molecular oxygen < ozone < atomic oxygen. The information attained from the O1s spectra is in agreement with these findings. The O1s band was peak-fitted into four components (Fig. 6b), which were assigned to the following species:[62,63] doubly bonded oxygen (~531.1 eV); singly bonded oxygen in alcohols, ethers, and peroxides (~532.1

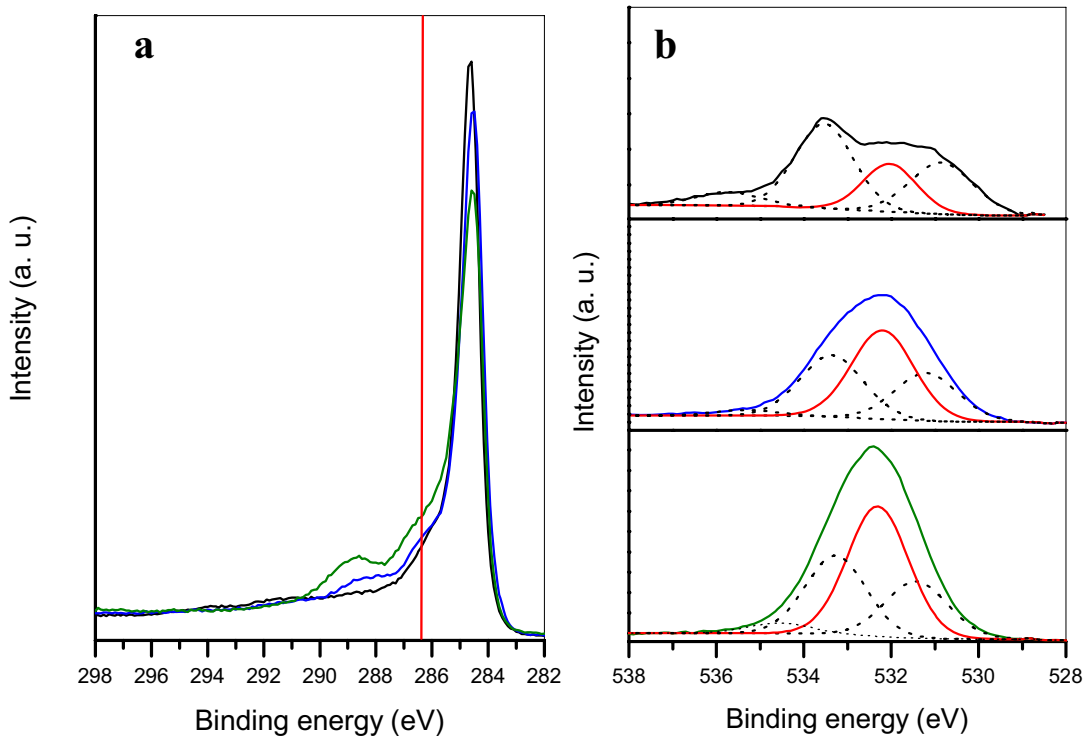

Figure 6 – (a) Normalized high-resolution core level C1s XPS spectra of CDG following thermal oxidation in air at 400 °C (black), UVO oxidation (blue) and MW oxygen plasma treatment (green). The vertical red line indicates the binding energy corresponding to carbon singly bonded to oxygen. (b) High-resolution core level O1s XPS spectra of CDG subjected to thermal oxidation in air at 400 °C (top/black), UVO oxidation (middle/blue) and MW oxygen plasma treatment (bottom/green). The spectra were peak-fitted into three or four components, which are drawn with dotted lines except the one corresponding to hydroxyl/ether/epoxide/peroxide moieties, which is highlighted by a red contour.

eV); singly bonded oxygen in acids, esters, and hydroperoxides (~533.4 eV); and peroxyacid, peroxyester and/or charge effect (~535 eV). Again, the component corresponding to singly bonded oxygen (red contour in Fig. 6b) increases with the reactivity of the oxidizing agent.

Local oxidation of the CDG sheets by STM lithography was also investigated. In the case of HOPG, it has been established that STM lithography, when carried out under ambient conditions, can be used to etch pre-determined surface patterns (e.g., trenches or holes).[40,64-66] This STM-induced etching is thought to proceed through an electrochemical reaction involving the water meniscus formed between tip and sample: water molecules and protons are reduced at the STM tip (for positive sample bias voltages) and carbon atoms are etched away at the HOPG surface as a result of oxidation with water molecules.[64,65] The activation energy associated to etching of the graphite surface is effectively modulated by the bias voltage applied between tip and sample, higher voltages leading to lower activation energies. When the bias voltage is raised above a certain threshold value, typically a few volts, the activation energy becomes sufficiently small, so that etching of the HOPG surface takes place.[65]

Lithography experiments were usually performed along 100 nm long straight lines at a tip scanning speed of 1 nm s^{-1}, which required bias voltages above 2 V to generate trenches on HOPG. For instance, working at 2.2-2.4 V and 2.2 nA, monolayer deep and ~6 nm wide trenches could be produced (Fig. 7a). By contrast, the same etching conditions proved to be extremely aggressive when the experiments were done on CDG sheets. In the latter case, a very large fraction of the sheet was removed and a trench was generated on the underlying HOPG substrate (images not shown). For voltages between ~1.7 and 2 V, uncontrolled etching of CDG was also observed, but the graphite surface was not etched (Fig. 7b and c). These results indicate that the activation energy for etching CDG is lower than that for HOPG, consistent with their expected different reactivities. However, for bias voltages in the range ~1.4-1.8 V (using tunneling currents of 1.45 nA) reproducible and controllable features could be generated on the CDG sheets, as exemplified in Fig. 7d and e. They were imaged by STM as depressions ~10 nm wide (Fig. 7e) and could not be created at voltages below 1.4 V. Significantly, such features do not appear to be of topographic nature, i.e., they are not physical trenches carved on the sheets for the following reasons. First, the apparent depth of the feature in Fig. 7e is about 1 nm, considerably larger than the measured height of the sheet relative to the HOPG substrate (~0.5 nm). It is very unlikely that this value is due to etching of the HOPG surface, as bias voltages below 2 V are not large enough to induce any modification on this material (see, e.g., Fig. 7c). Second, detailed inspection of the STM-modified area in Fig. 7d and e revealed that its morphology was largely retained after modification. This observation is not consistent with the creation of an actual trench (removed material). Third, the apparent depth of the features generated at 1.4-1.8 V was dependent on the tunneling parameters employed during image acquisition (higher tunneling resistances leading to smaller apparent depths).

Such behaviour is not observed for actual trenches/holes produced either on HOPG (Fig. 7a) or on CDG (Fig. 7c).

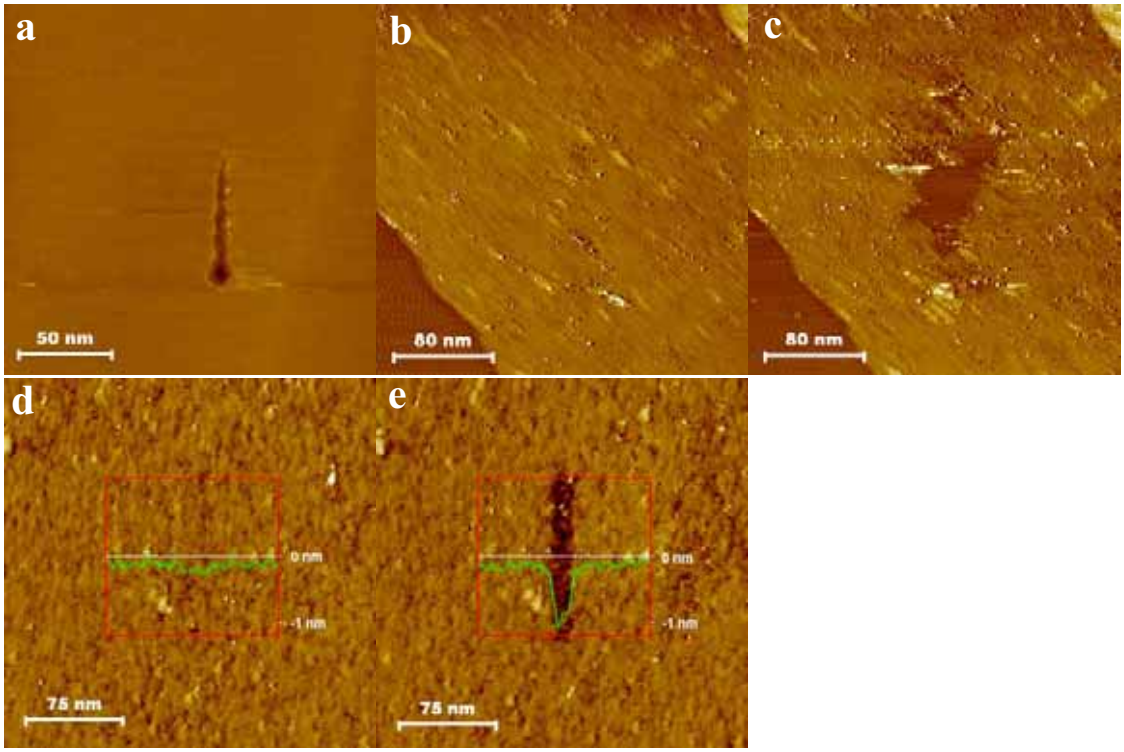

Figure 7 – STM lithography of HOPG (a) and CDG (b-e). In all cases, the experiments were done by moving the STM tip along a straight line (100 nm long) from bottom to top in the images at positive sample bias voltages. (a) Monolayer deep, ⍰6 nm wide trench etched on HOPG at a bias voltage of 2.2 V. (b,c) CDG sheet before (a) and after (b) a lithography experiment at a bias voltage of 1.7 V. The sheet was locally etched away [compare the depth of the etched area with that of the underlying HOPG substrate in the bottom left corner of (c)], yielding an unpredictable pattern rather than a straight line. (d,e) CDG sheet before (d) and after (e) a lithography experiment at 1.6 V. A straight, depressed feature ⍰10 nm wide with an apparent depth of about 1 nm [see averaged line profile as an inset to (e)] was generated.

It is well known that both topography and electronic structure contribute to image contrast in STM.[67] Since the feature observed in Fig. 7e is not topographic, we conclude that it must have an electronic origin and therefore should be ascribed to a region of diminished local electrical conductivity compared with the surrounding, unmodified areas of the CDG sheet. It is then reasonable to attribute the decreased conductivity to the introduction of oxygen species, probably in the form of epoxide or hydroxyl groups, during the lithographic process at 1.4-1.8 V, i.e., the feature can be ascribed to a controlled, local re-oxidation (but not etching) of the sheet. This interpretation is supported by the work reported by Leconte *et al* referred to beforehand[59] and also by recent experimental and theoretical studies suggesting that two-dimensional clusters of sub-surface oxygen atoms attached in epoxy positions to the surface graphene in graphite are detected by STM as depressed features similar to those observed here in Fig. 7e.[68]

As mentioned before, the gas-phase oxidative attack of CDG is a two-step process. Similarly, the STM-induced attack of graphite and CDG should consist of two sequential steps: (1) dissociation of physisorbed water molecules to form surface oxygen groups (oxidation step) and (2) desorption of the oxygen groups as CO/CO_2 (etching step),[65] each reaction having its own activation energy. The lithography experiments reported here suggest that, for a given bias voltage, the activation energy associated to reaction (1) on CDG is smaller than that of reaction (2). Thus, there should be a voltage range (measured to be 1.4-1.8 V) for which the activation energy of (1) becomes sufficiently small and the corresponding reaction (formation of surface oxygen groups) takes place, but the activation energy of (2) is not yet small enough, so that etching does not proceed (Fig. 7e). For higher bias voltages both reaction (1) and (2) occur, and etching comes about effectively (Fig. 7c). In the case of HOPG, oxidation and etching could not be discriminated on the basis of the applied bias voltage. Either etching was created or the HOPG surface remained apparently intact (above and below the threshold voltage, respectively), but no oxidized patterns could be ever observed in the recorded STM images. Possible reasons to explain such finding could be that the activation energies of reactions (1) and (2) on pristine graphite are very similar, or that the surface oxygen groups formed on graphite are less stable than their CDG counterparts, so that they could easily desorb from or migrate across the graphite surface as a result of interaction with the STM tip during imaging.

In addition to increasing our fundamental insight into the reactivity of CDG, the preceding results could prove useful in some practical uses. For example, the patterning of areas with different levels of oxidation, and therefore different local conductivities, can in principle be achieved on CDG using STM. This method is complementary to the one documented very recently by Wei *et al* with a view to application in graphene devices.[69] These authors used a heated AFM tip to generate reduced patterns on graphene oxide films, whereas in our case oxidized patterns are produced on reduced graphene oxide. A similar resolution (~10 nm) was achieved with both methods. Likewise, several recent reports based on theoretical simulations have put forward the use of porous graphene as a highly efficient membrane for molecular sieving of gases or water filtration applications.[70-72] However, the practical implementation of porous graphene membranes has not yet been achieved. Considering the potential for mass production of CDG and the fact that selective etching of its defective domains by oxidation should lead to the opening of a very large number of tiny pores (just a few nm in diameter or even below), the use of controlled oxidations of CDG (for instance, thermal oxidation in air at 400 °C for several minutes or MW oxygen plasma for just a few seconds) could offer a convenient approach toward practical graphene membranes.

4. Conclusions

The present work has provided a detailed knowledge about the global (gas-phase) and local (STM-induced) oxidation behavior of CDG. AFM imaging of individual CDG sheets deposited onto pristine

graphite indicated that etching by the different oxidation treatments proceeds at a much faster pace on the sheets compared to the graphite surface, which is indicative of their higher reactivity. Under controlled conditions, the oxidative attack was seen to take place selectively (for thermal oxidation in air) or at least preferentially (for MW oxygen plasma and UVO) at a very large number of locations several nanometers apart from each other on the CDG sheets. This behavior is thought to reflect the segregated structure of essentially defect-free regions interspersed with highly defective domains that this type of graphene possesses on the nanometer level, the latter being much more reactive and therefore selectively/preferentially attacked. XPS showed evidence of the introduction of oxygen groups on the basal plane of the CDG sheets, revealing differences between the various oxidation treatments that generally bore correspondence with the expected reactivity of the oxidizing agents (molecular oxygen, ozone, atomic oxygen). Local oxidation experiments with STM lithography allowed discriminating (through applied bias voltage) between oxidation itself and the subsequent etching of the oxidized patterns, which was not possible in the case of pristine graphite. Finally, the knowledge afforded here could be useful with a view to some applications, e.g. in the development of practical porous graphene membranes from CDG.

Acknowledgements

Financial support from the Spanish MICINN (Project MAT2008-05700) and PCTI del Principado de Asturias (Project IB09-151) is gratefully acknowledged. The work in Hungary was supported by OTKA-NKTH grant 67793. M.J.F.-M. thanks the receipt of a pre-doctoral contract (FPI) from MICINN. L.G. and P.S.-F. acknowledge CSIC for the receipt of post-doctoral (JAE-Doc) and pre-doctoral (I3P) contracts, respectively.

References

(1) Geim, A. K.; Novoselov, K. S. *Nat. Mater.* **2007**, *6*, 183-191.

(2) Geim, A. K. *Science* **2009**, *324*, 1530-1534.

(3) Park, S.; Ruoff, R. S. *Nat. Nanotechnol.* **2009**, *4*, 217-224.

(4) Eda, G.; Chhowalla, M. *Adv. Mater.* **2010**, *22*, 2392-2415.

(5) Compton, O. C.; Nguyen, S. T. *Small* **2010**, *6*, 711-723.

(6) Stankovich, S.; Dikin, D. A.; Dommett, G. H. B.; Kohlhaas, K. M.; Zimney, E. J.; Stach, E. A.; Piner, R. D.; Nguyen, S. T.; Ruoff, R. S. *Nature* **2006**, *442*, 282-286.

(7) Ramanathan, T.; Abdala, A. A.; StankovichS; Dikin, D. A.; Herrera Alonso, M.; Piner, R. D.; Adamson, D. H.; Schniepp, H. C.; Chen, X.; Ruoff, R. S.; Nguyen, S. T.; Aksay, I. A.; Prud'Homme, R. K.; Brinson, L. C. *Nat. Nanotechnol.* **2008**, *3*, 327-331.

(8) Villar-Rodil, S.; Paredes, J. I.; Martinez-Alonso, A.; Tascon, J. M. D. *J. Mater. Chem.* **2009**, *19*, 3591-3593.

(9) Eda, G.; Fanchini, G.; Chhowalla, M. *Nat. Nanotechnol.* **2008**, *3*, 270-274.

(10) Wu, J.; Agrawal, M.; Becerril, H. c. A.; Bao, Z.; Liu, Z.; Chen, Y.; Peumans, P. *ACS Nano* **2010**, *4*, 43-48.

(11) Wang, S. J.; Geng, Y.; Zheng, Q.; Kim, J.-K. *Carbon* **2010**, *48*, 1815-1823.

(12) Stoller, M. D.; Park, S.; Zhu, Y.; An, J.; Ruoff, R. S. *Nano Lett.* **2008**, *8*, 3498-3502.

(13) Wang, Y.; Shi, Z.; Huang, Y.; Ma, Y.; Wang, C.; Chen, M.; Chen, Y. *J. Phys. Chem. C* **2009**, *113*, 13103-13107.

(14) Robinson, J. T.; Perkins, F. K.; Snow, E. S.; Wei, Z.; Sheehan, P. E. *Nano Lett.* **2008**, *8*, 3137-3140.

(15) Fowler, J. D.; Allen, M. J.; Tung, V. C.; Yang, Y.; Kaner, R. B.; Weiller, B. H. *ACS Nano* **2009**, *3*, 301-306.

(16) Stankovich, S.; Dikin, D. A.; Piner, R. D.; Kohlhaas, K. A.; Kleinhammes, A.; Jia, Y.; Wu, Y.; Nguyen, S. T.; Ruoff, R. S. *Carbon* **2007**, *45*, 1558-1565.

(17) Gómez-Navarro, C.; Weitz, R. T.; Bittner, A. M.; Scolari, M.; Mews, A.; Burghard, M.; Kern, K. *Nano Lett.* **2007**, *7*, 3499-3503.

(18) Paredes, J. I.; Villar-Rodil, S.; Solís-Fernández, P.; Martínez-Alonso, A.; Tascón, J. M. D. *Langmuir* **2009**, *25*, 5957-5968.

(19) Yang, R. T. *Chem. Phys. Carbon* **1984**, *19*, 163-210.

(20) McKee, D. W. *Chem. Phys. Carbon* **1991**, *23*, 173-232.

(21) Chang, H.; Bard, A. J. *J. Am. Chem. Soc.* **1991**, *113*, 5588-5596.

(22) Ngo, T.; Snyder, E. J.; Tong, W. M.; Williams, R. S.; Anderson, M. S. *Surf. Sci.* **1994**, *314*, L817-L822.

(23) Lee, S. M.; Lee, Y. H.; Hwang, Y. G.; Hahn, J. R.; Kang, H. *Phys. Rev. Lett.* **1999**, *82*, 217-220.

(24) Kinoshita, H.; Umeno, M.; Tagawa, M.; Ohmae, N. *Surf. Sci.* **1999**, *440*, 49-59.

(25) Hahn, J. R. *Carbon* **2005**, *43*, 1506-1511.

(26) Osváth, Z.; Darabont, A.; Nemes-Incze, P.; Horváth, E.; Horváth, Z. E.; Biró, L. P. *Carbon* **2007**, *45*, 3022-3026.

(27) Liu, L.; Ryu, S.; Tomasik, M. R.; Stolyarova, E.; Jung, N.; Hybertsen, M. S.; Steigerwald, M. L.; Brus, L. E.; Flynn, G. W. *Nano Lett.* **2008**, *8*, 1965-1970.

(28) Zhou, X.; Lu, G.; Qi, X.; Wu, S.; Li, H.; Boey, F.; Zhang, H. *J. Phys. Chem. C* **2009**, *113*, 19119-19122.

(29) Wang, S.; Tang, L. A. l.; Bao, Q.; Lin, M.; Deng, S.; Goh, B. M.; Loh, K. P. *J. Am. Chem. Soc.* **2009**, *131*, 16832-16837.

(30) Wang, X.; Dai, H. *Nat. Chem.* **2010**, *2*, 661-665.

(31) Li, D.; Muller, M. B.; Gilje, S.; Kaner, R. B.; Wallace, G. G. *Nat. Nanotechnol.* **2008**, *3*, 101-105.

(32) Hummers, W. S.; Offeman, R. E. *J. Am. Chem. Soc.* **1958**, *80*, 1339-1339.

(33) Solís-Fernández, P.; Paredes, J. I.; Villar-Rodil, S.; Martínez-Alonso, A.; Tascón, J. M. D. *Carbon* **2010**, *48*, 2657-2660.

(34) Chen, C.; Yang, Q.-H.; Yang, Y.; Lv, W.; Wen, Y.; Hou, P.-X.; Wang, M.; Cheng, H.-M. *Adv. Mater.* **2009**, *21*, 3007-3011.

(35) Garcia, R.; San Paulo, A. *Phys. Rev. B* **1999**, *60*, 4961-4967.

(36) San Paulo, A.; García, R. *Biophys. J.* **2000**, *78*, 1599-1605.

(37) Paredes, J. I.; Villar-Rodil, S.; Tamargo-Martinez, K.; Martinez-Alonso, A.; Tascon, J. M. D. *Langmuir* **2006**, *22*, 4728-4733.

(38) Nemes-Incze, P.; Osváth, Z.; Kamarás, K.; Biró, L. P. *Carbon* **2008**, *46*, 1435-1442.

(39) Lui, C. H.; Liu, L.; Mak, K. F.; Flynn, G. W.; Heinz, T. F. *Nature* **2009**, *462*, 339-341.

(40) Tapasztó, L.; Dobrik, G.; Lambin, P.; Biró, L. P. *Nat. Nanotechnol.* **2008**, *3*, 397-401.

(41) Paredes, J. I.; Martinez-Alonso, A.; Tascon, J. M. D. *Langmuir* **2002**, *18*, 4314-4323.

(42) Solís-Fernández, P.; Paredes, J. I.; Cosío, A.; Martínez-Alonso, A.; Tascón, J. M. D. *J. Colloid Interface Sci.* **2010**, *344*, 451-459.

(43) Li, X.; Wang, X.; Zhang, L.; Lee, S.; Dai, H. *Science* **2008**, *319*, 1229-1232.

(44) Paredes, J. I.; Martínez-Alonso, A.; Tascón, J. M. D. *Langmuir* **2007**, *23*, 8932-8943.

(45) Lahaye, J.; Ehrburger, P. (Eds.), Fundamental issues in control of carbon gasification reactivity, Kluwer Academic Publishers, Dordrecht, 1991.

(46) Cuesta, A.; Martínez-Alonso, A.; Tascón, J. M. D. *Carbon* **2001**, *39*, 1135-1146.

(47) Gómez-Navarro, C.; Meyer, J. C.; Sundaram, R. S.; Chuvilin, A.; Kurasch, S.; Burghard, M.; Kern, K.; Kaiser, U. *Nano Lett.* **2010**, *10*, 1144-1148.

(48) Haddon, R. C. *Science* **1993**, *261*, 1545-1550.

(49) Niyogi, S.; Hamon, M. A.; Hu, H.; Zhao, B.; Bhowmik, P.; Sen, R.; Itkis, M. E.; Haddon, R. C. *Acc. Chem. Res.* **2002**, *35*, 1105-1113.

(50) Giunta, P. L.; Kelty, S. P. *J. Chem. Phys.* **2001**, *114*, 1807-1812.

(51) Kobayashi, Y.; Fukui, K.-i.; Enoki, T.; Kusakabe, K. *Phys. Rev. B* **2006**, *73*, 125415.

(52) Xu, S. C.; Irle, S.; Musaev, D. G.; Lin, M. C. *J. Phys. Chem. C* **2007**, *111*, 1355-1365.

(53) Paredes, J. I.; Martínez-Alonso, A.; Tascón, J. M. D. *J. Mater. Chem.* **2000**, *10*, 1585-1591.

(54) Ishigami, M.; Chen, J. H.; Cullen, W. G.; Fuhrer, M. S.; Williams, E. D. *Nano Lett.* **2007**, *7*, 1643-1648.

(55) Dean, C. R.; Young, A. F.; Meric, I.; Lee, C.; Wang, L.; Sorgenfrei, S.; Watanabe, K.; Taniguchi, T.; Kim, P.; Shepard, K. L.; Hone, J. *Nat. Nanotechnol.* **2010**, *5*, 722-726.

(56) Seip, M.; Brauer, H. D. *J. Am. Chem. Soc.* **1992**, *114*, 4486-4490.

(57) Lamoen, D.; Persson, B. N. J. *J. Chem. Phys.* **1998**, *108*, 3332-3341.

(58) Lee, G.; Lee, B.; Kim, J.; Cho, K. *J. Phys. Chem. C* **2009**, *113*, 14225-14229.

(59) Leconte, N.; Moser, J.; Ordejón, P.; Tao, H.; Lherbier, A. l.; Bachtold, A.; Alsina, F.; Sotomayor Torres, C. M.; Charlier, J.-C.; Roche, S. *ACS Nano* **2010**, *4*, 4033-4038.

(60) Lerf, A.; He, H.; Forster, M.; Klinowski, J. *J. Phys. Chem. B* **1998**, *102*, 4477-4482.

(61) Zhang, G.; Sun, S.; Yang, D.; Dodelet, J.-P.; Sacher, E. *Carbon* **2008**, *46*, 196-205.

(62) Clark, D. T.; Cromarty, B. J.; Dilks, A. *J. Polym. Sci. Polym. Chem. Ed.* **1978**, *16*, 3173-3184.

(63) Rosenthal, D.; Ruta, M.; Schlögl, R.; Kiwi-Minsker, L. *Carbon* **2010**, *48*, 1835-1843.

(64) McCarley, R. L.; Hendricks, S. A.; Bard, A. J. *J. Phys. Chem.* **1992**, *96*, 10089-10092.

(65) Hiura, H. *Appl. Surf. Sci.* **2004**, *222*, 374-381.

(66) Biró, L. P.; Lambin, P. *Carbon* **2010**, *48*, 2677-2689.

(67) Magonov, S. N.; Whangbo, M.-H. *Surface Analysis with STM and AFM*; VCH: Weinheim, 1996.

(68) Solís-Fernández, P.; Paredes, J. I.; López, M. J.; Cabria, I.; Alonso, J. A.; Martínez-Alonso, A.; Tascón, J. M. D. *J. Phys. Chem. C* **2009**, *113*, 18719-18729.

(69) Wei, Z.; Wang, D.; Kim, S.; Kim, S.-Y.; Hu, Y.; Yakes, M. K.; Laracuente, A. R.; Dai, Z.; Marder, S. R.; Berger, C.; King, W. P.; de Heer, W. A.; Sheehan, P. E.; Riedo, E. *Science* **2010**, *328*, 1373-1376.

(70) Jiang, D.-e.; Cooper, V. R.; Dai, S. *Nano Lett.* **2009**, *9*, 4019-4024.

(71) Suk, M. E.; Aluru, N. R. *J. Phys. Chem. Lett.* **2010**, *1*, 1590-1594.

(72) Schrier, J. *J. Phys. Chem. Lett.* **2010**, *1*, 2284-2287.

Conclusiones 5

Los resultados expuestos en la presente Memoria permiten extraer las siguientes conclusiones generales:

- Los estudios de los distintos tipos de oxidación de grafito ponen de relieve la existencia de dos mecanismos básicos de ataque (químico y físico) claramente diferenciados. La complementariedad de estos dos mecanismos permitiría, mediante combinaciones apropiadas de ambos, adecuar los tratamientos de oxidación a requerimientos específicos de cada aplicación.
- El mecanismo de oxidación mediante UVO presenta una elevada selectividad química, produciéndose el ataque de átomos de carbono preferentemente en posiciones no basales. Esto implica la formación de patrones típicos de ataque regido por fenómenos químicos: formación de agujeros en el grafeno superficial, surcos a partir de límites de grano, etc. Debido a la gran selectividad de los procesos involucrados, la mayor parte de la superficie expuesta mantiene intacta su estructura basal original.
- La oxidación de materiales grafíticos mediante plasma DBD muestra las características básicas de un ataque dominado por fenómenos físicos (bombardeo iónico), mediante los cuales se introducen defectos intersticiales bajo el grafeno superficial. El ataque por medio de este tipo de plasma está esencialmente exento de selectividad química.
- La combinación de las simulaciones teóricas y de los estudios STM de las muestras oxidadas en plasma DBD permitió investigar las características y naturaleza de un tipo de defecto nunca antes observado en materiales carbonosos, consistente en la presencia de agregados intersticiales de oxígeno. Debido a su electronegatividad, estos agregados provocan una disminución en la densidad local de estados electrónicos en el grafeno superficial, con lo que son observados como depresiones aparentes en imágenes STM.
- Para obtener valores precisos y consistentes del grosor de las láminas de GO y CMG mediante técnicas SPM, es necesario efectuar las medidas en regiones de láminas solapadas. De este modo, se evitan los problemas que surgen al estimar el grosor como altura de la lámina respecto al sustrato sobre el que está depositada.
- El estudio de las láminas de GO y CMG mediante técnicas SPM muestra que la estructura grafítica de ambas se encuentra altamente distorsionada debido a la presencia tanto de defectos estructurales como de grupos funcionales oxigenados. Es más, como sugieren los estudios de oxidación de CMG, la distorsión no es uniforme a escalas de unos pocos nm. Así, las láminas se componen de una amalgama de dos tipos de regiones diferenciadas: zonas en las que la presencia de defectos y funcionalidades es muy elevada, y zonas prístinas esencialmente carentes de defectos. Las primeras presentan una alta reactividad frente a oxidación, mientras que las segundas son relativamente poco reactivas.

Ello hace que, en conjunto, el CMG sea mucho más reactivo que el HOPG y que el grafeno prístino.

- Mediante litografía STM es posible oxidar localmente y de manera muy controlada CMG. Este proceso implica la introducción de funcionalidades oxigenadas evitando la extracción de material (ataque o *etching*), lo cual no es posible conseguir en estructuras grafíticas prístinas (HOPG).


Anexo 6

Durante el trabajo de Tesis Doctoral se generaron una serie publicaciones, no incluidas en la presente Memoria, aunque de temática íntimamente relacionada.

Paredes J.I., Solís-Fernández P., Martínez-Alonso A. and Tascón J.M.D., "*Atomic Vacancy Engineering of Graphitic Surfaces: Controlling the Generation and Harnessing the Migration of the Single Vacancy*," J. Phys. Chem. C **113**, 10249-10255 (2009).

Fernández-Merino M.J., Guardia L., Paredes J.I., Villar-Rodil S., Solís-Fernández P., Martínez-Alonso A. and Tascón J.M.D., "*Vitamin C Is an Ideal Substitute for Hydrazine in the Reduction of Graphene Oxide Suspensions*," J. Phys. Chem. C **114**, 6426-6432 (2010).

Guardia L., Fernández-Merino M.J., Paredes J.I., Solís-Fernández P., Villar-Rodil S., Martínez-Alonso A. and Tascón J.M.D., "*High-throughput production of pristine graphene in an aqueous dispersion assisted by non-ionic surfactants*," Carbon **49**, 1653-1662 (2011).

Aportaciones a congresos:

Solís-Fernández P., Paredes J.I., Martínez-Alonso A., Tascón J.M.D., "*Modificación superficial de grafito mediante plasma de descarga de barrera dieléctrica*", IX Reunión del Grupo Español del Carbón, Teruel (España), 22-24 Octubre 2007.

Solís-Fernández P., Paredes J.I., Martínez-Alonso A., Tascón J.M.D., "*Surface modification of graphite by dielectric barrier discharge plasma*", Carbon Conference 08, Nagano (Japón), 13-18 Julio 2008.

Solís-Fernández P., Paredes J.I., García-Cosío A., Martínez-Alonso A., Tascón J.M.D., "*A comparison of physical and chemical attacks in the oxidation of carbonaceous materials*", Carbon Conference 09, Biarritz (Francia), 14-19 Junio 2009.

Solís-Fernández P., Paredes J.I., Martínez-Alonso A., Tascón J.M.D., "*An investigation of the atomic-scale defects induced on graphite surfaces by dielectric barrier discharge plasma treatment*", Carbon Conference 09, Biarritz (Francia), 14-19 Junio 2009.

Paredes J.I., Villar-Rodil S., Solís-Fernández P., Guardia L., Fernández-Merino M.J., Martínez-Alonso A., Tascón J.M.D., "*SPM Imaging of graphene nanosheets derived from graphite oxide*", Cambridge CNT Symposium 09, Cambridge (Reino Unido), 13 Noviembre 2009.

P. Solís-Fernández, J.I. Paredes, M.J. López, I. Cabria, J.A. Alonso, A. Martínez-Alonso, J.M.D. Tascón, "*Estudio experimental y teórico de los defectos producidos en superficies grafíticas en tratamientos de plasma de descarga de barrera dieléctrica (DBD)*", X Reunión del Grupo Español del Carbón, Girona (España), 9-12 Mayo 2010.

P. Solís-Fernández, J.I. Paredes, S. Villar-Rodil, L. Guardia, M.J. Fernández-Merino, G. Dobrik, L.P. Biró, A. Martínez-Alonso, J.M.D. Tascón, "*Oxidación local y global de láminas de grafeno químicamente modificadas*", X Reunión del Grupo Español del Carbón, Girona (España), 9-12 Mayo 2010.

M.J. Fernández-Merino, L. Guardia, J.I. Paredes, S. Villar-Rodil, P. Solís Fernández, A. Martínez-Alonso, J.M.D. Tascón, "*Preparación de grafenos por reducción química de óxido de grafeno: efecto de los distintos reductores*", X Reunión del Grupo Español del Carbón, Girona (España), 9-12 Mayo 2010.